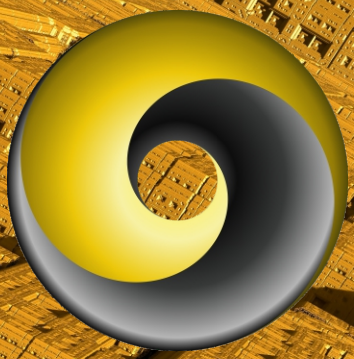

MATHMODEL'19

III INTERNATIONAL SCIENTIFIC CONFERENCE

11 - 14 DECEMBER, 2019, BOROVETS, BULGARIA

MATHEMATICAL MODELING

PROCEEDINGS

YEAR III ISSUE 1(3)/2019
ISSN (Print) 2535-0978
ISSN (Online) 2603-3003

Published by
SCIENTIFIC-TECHNICAL UNION of MECHANICAL ENGINEERING - INDUSTRY 4.0
Sofia, BULGARIA

III INTERNATIONAL SCIENTIFIC CONFERENCE

MATHEMATICAL MODELING

Year III **Volume 1/3** **DECEMBER 2019**

ISSN 2535-0978 (Print)
ISSN 2603-3003 (Online)

PROCEEDINGS

TEMATIC FIELDS
THEORETICAL FOUNDATIONS AND SPECIFICITY OF MATHEMATICAL MODELLING
MATHEMATICAL MODELLING OF TECHNOLOGICAL PROCESSES AND SYSTEMS

11 – 14 DECEMBER, 2019,
BOROVETS, BULGARIA

PUBLISHER:
SCIENTIFIC TECHNICAL UNION OF MECHANICAL ENGINEERING "INDUSTRY-4.0"

108, Rakovski Str., 1000 Sofia, Bulgaria
tel. (+359 2) 987 72 90,
tel./fax (+359 2) 986 22 40**,**
office@mathmodel.eu
www.mathmodel.eu

INTERNATIONAL EDITORIAL BOARD

Chairman:		
Prof. ANDREY FIRSOV Peter the Great St.Petersburg Polytechnic University		RU
Members:		
Abilmazhin Adamov, Prof.	L.N.Gumilyov Eurasian National University	KZ
Alexander Guts, Prof.	Omsk State University	RU
Alexei Zhabko, Prof.	Saint Petersburg State University	RU
Andrey Markov, Prof.	Baltic State Technical University	RU
Andrii Matviichuk, Prof.	Kyiv National Economics University	UA
Andrzej Nowakowski, Prof.	University of Lodz	PL
Anton Makarov, Dr.	Saint Petersburg State University	RU
Armands Gricans, Assoc. Prof.	Daugavpils University	LV
Artūras Dubickas, Prof.	Vilnius University	LT
Avinir Makarov, Prof.	Saint Petersburg State University of Industrial Technologies and Design	RU
Christo Boyadjiev, Prof.	Institute of Chemical Engineering, BAS	BG
Daniela Marinova, Dssoc. Prof.	Technical University of Sofia	BG
Dimitrios Poulakis, Prof.	Aristotle University of Thessaloniki	GR
Evgeniy Smirnov, Assoc. Prof.	Volgograd State Technical University	RU
Galia Angelova, Prof. DSc	Institute of Information and Communication Technologies, BAS	BG
Giovanni Borgioli, Assoc. Prof.	University of Florence	IT
Haskiz Coskun, Prof.	Karadeniz Technical University of Trabzon	TR
Idilia Bachkova, Prof.	University of Chemical Technology and Metallurgy	BG
Irena Stojkovska, Prof.	Ss. Cyril and Methodius University in Skopje	NM
Ivana Štajner-Papuga, Prof.	University of Novi Sad	RS
Kanagat Aldazharov, Assoc. Prof.	Kazakh Economics University	KZ
Karl Kunisch, Prof.	University of Graz	AT
Mahomed Agamirza ogly Dunyamalyev, Prof.	Azerbaijan Technical University	AZ
Marius Giuclea, Prof.	The Bucharest University of Economics Studies	RO
Mihail Okrepilov, Prof.	D.I. Mendeleyev Institute for Metrology (VNIIM)	RU
Milena Racheva, Assoc. Prof.	Technical University of Gabrovo	BG
Mohamed Kara, Dr.	Ferhat Abbas Sétif 1 University	DZ
Mohamed Taher El-mayah, Prof	MTI University	EG
Neli Dimitrova, Prof.	Institute of Mathematics and Informatics, BAS	BG
Nina Bijedic, Prof.	Dzemal Bijedic University of Mostar	BA
Oleg Obradović, Prof.	University of Montenegro	ME
Olga Pritomanova, Assoc. Prof.	Oles Honchar Dnipropetrovsk National University	UA
Özkan Öcalan, Prof.	Akdeniz University of Antalya	TR
Paşc Găvruţă, Prof.	Politehnic University of Timisoara	RO
Pavel Satrapa, Assoc. Prof.	Technical University of Liberec	CZ
Pavel Tvrdík, Prof.	Czech Technical University in Prague	CZ
Pavlina Yordanova, Assoc. Prof.	Shumen University	BG
Petr Trusov, Prof.	Perm State Technical University	RU
Rannveig Björnsdóttir, Prof.	University of Akureyri	IS
Roumen Anguelov, Prof.	University of Pretoria	ZA
Sándor Szabó, Dr. Prof.	University of Pécs	HU
Sashko Martinovski, Assoc. Prof.	St. Kliment Ohridski University of Bitola	NM
Sergey Bosnyakov, Prof.	Moscow Institute of Physics and Technology	RU
Sergey Kshevetskii, Prof.	Immanuel Kant Baltic Federal University	RU
Snejana Hristova, Prof.	University of Plovdiv	BG
Svetlana Lebed, Assoc. Prof.	Brest State Technical University	BY
Tomasz Szarek, Prof.	University of Gdansk	PL
Valeriy Serov, Prof.	University of Oulu	FI
Vasily Maximov, Prof.	Saint Petersburg State University of Industrial Technologies and Design	RU
Ventsi Rumchev, Prof.	Curtin University, Perth	AU
Veronika Stoffová, Prof.	University of Trnava	SK
Veselka Pavlova, Prof.	University of National and World Economy	BG
Viorica Sudacevschi, Assoc. Prof.	Technical University of Moldova	MD
Vladimir Janković, Prof.	University of Belgrade	RS
Vladislav Holodnov, Prof.	Saint Petersburg State Institute of Technology	RU
Vyacheslav Demidov, Prof.	Saint Petersburg State University of Industrial Technologies and Design	RU
Yordan Yordanov, Assoc. Prof.	University of Sofia	BG
Yuriy Kuznetsov, Prof.	Nizhny Novgorod State University	RU
Zdenka Kolar - Begović, Prof.	University of Osijek	HR

C O N T E N T S

THEORETICAL FOUNDATIONS AND SPECIFICITY OF MATHEMATICAL MODELLING

MATHEMATICAL MODELLING OF TECHNOLOGICAL PROCESSES AND SYSTEMS

ON THE ASYMPTOTIC IN TIME OF SOLUTIONS OF THE BOLTZMANN EQUATION IN THE CASE OF SOFT INTERMOLECULAR POTENTIALS

Prof. Dr.Tech.Sci. Andrei N. Firsov
Institute of Computer Science and Technology – Peter the Great Saint-Petersburg Polytechnic University, Russia
E-mail: anfirs@yandex.ru

Abstract: *The work is devoted to the mathematical problems of the analysis of asymptotic time behavior of solutions of the nonstationary Boltzmann equation. The proof of the fundamental difference between such behavior for the cases of "hard" and "soft" (in the sense of H. Grad) potentials of intermolecular interaction is given*

KEYWORDS: BOLTZMANN EQUATION, SOFT POTENTIALS, SOLUTIONS, ASYMPTOTIC IN TIME

1. Introduction

Behavior of the solutions of the Boltzmann equation

$$\frac{\partial F}{\partial t}+u\frac{\partial F}{\partial x}=Q(F,F);\ F|_{t=0}=F_0,\ x\in R_x^3,\ u\in R_u^3 \quad (1)$$

at large values of time are considered in most serious studies of this object. In fact, even Boltzmann expressed his thoughts on the possibility of rapid relaxation of an arbitrary initial distribution function to equilibrium. Many physicists now adhere to this conclusion, although the evidence they use is often far from mathematical perfection. The first serious analysis of these issues was carried out by Carleman [1] as early as the 30s of the XX century, and then only after 30 years was continued by many researchers. A fairly complete review of the results is contained in [2, 3]. In the aspect that interests us, their essence is that for solution *F* of problem (1), an inequality of the form

$$N(F-F_M)\le C_0 p(t) \quad (2)$$

is true, where *N* – suitable norm in the space of functions depending on speed u and radius-vector x (so $N(F)$ – is time dependent function); C_0 – is a constant, depending possibly on the initial distribution $F_0(x,u);\ F_M=F_M(|u|)$ – Maxwell distribution; the behavior of functions $p(t)$ essentially depends, on the one hand, on the class of function spaces in which a solution is sought, and on the other, on the properties of the collision operator $Q(F,F)$, characterized by assumptions about the type of intermolecular interaction potential.

For "hard" "cut off in the corner" potentials $U\sim r^{-k}$, k > 5 the problem was investigated very actively; the main result is that the function $p(t)$ in (2) tends to zero with an infinite increase in time *t* either as a power law or as an exponent, depending on the degree of smoothness over the coordinates of the initial distribution, the boundedness (or not) of the spatial region and the rate of decrease $F_0(x,u)$ at $|u|,|x|\to\infty$. The presented results are well known [2, 3, 4, 5] (see also chapter 1 of [6]).

Since in what follows we will consider situations close to equilibrium, then, as usual, instead of a function *F*, we use $f=F_M^{-\frac{1}{2}}(F-F_M)$. Equation (1) goes over to

$$\frac{\partial f}{\partial t}+u\frac{\partial f}{\partial x}=L(f)+\nu(|u|)\Gamma(f,f);\ f_{t=0}=f(x,u) \quad (3)$$

(see, for example, [2, 3] and chapter 1 of [6]).

The result (2) in terms of a function f has the form

$$N(f)\le N_1(f_0)p(t), \quad (4)$$

where N_1 – a norm that is generally different from the norm N (the properties of a solution *f* generally speaking, worsen compared with the properties of the initial function f_0 – see Caflich's work [7]), and $p(t)\to 0$ at $t\to\infty$.

A characteristic feature of all the results discussed above is the uniform evolution of the solution to the equilibrium distribution function; in other words, "long-lived" initial distributions are absent.

Significantly poorer is set of facts concerning the case of "soft" potentials $U\sim r^{-k},\ 2<k<5.$ Here we have the results of Caflish [7], in obtaining which it was assumed that, first, there is a situation of the so-called "Grad box" with mirror-reflecting walls (i.e., the class of solutions periodic in coordinates is considered), and secondly, the initial distribution function is quite smooth and the difference $F-F_M$ decreases (in speed) exponentially fast.

2. The case of "soft" potentials

For further research, we introduce the following

Definition. Let us call by *an absolute degree of nonequilibrium of the Cauchy problem* for equation (3) the value

$$\mu=\lim_{T\to\infty}\sup_{f_0}\inf_{0\le t\le T}\left[N(f)/N(f_0)\right]$$

where f is a solution to problem (3) corresponding to the initial distribution f_0.

The result (4) therefore means that $\mu=0$.

The transition to "soft" potentials and the weakening of the conditions imposed on f_0, fundamentally change the picture of the asymptotic behavior of the solutions of equation (3).

Theorem. In the case of power-cut potential-power intermolecular interactions of the form $U\sim r^{-k}$, 2< k <5, for each $\varepsilon>0$ and each T>0 there is an initial distribution $f_0\in L_2(x,u)$, such that for the corresponding solution $f(x,u,t)$ of problem (3) we have the inequality

$$\inf_{0\le t\le T}\left[N(f)/N(f_0)\right]>1-\varepsilon$$

Here $N(f)$ means the norm of f in $L_2(x,u)$.

Thus, $\mu=1$ and, therefore, *there exist "long-living" initial disturbances*.

The core of the proof of this theorem is the properties of the solutions of the corresponding linearized problem (designations see in [8])

$$\frac{\partial f}{\partial t} = A(f); \quad f_{t=0} = f(x,u), \qquad (5)$$

where $A \equiv -u\frac{\partial}{\partial x} + L;\ L(f) = K(f) - \nu(|u|)f$.

Lemma 1. An operator A with a domain of definition

$$D(A) = \left\{ f(x,u,t) \,\middle|\, f, u_i \frac{\partial f}{\partial x_i} \in L_2(x,u)\ \forall t > 0 \right\}$$

generates in $L_2(x,u)$ a contracting semigroup of bounded linear operators $\{T(t,),t>0\}$ of the class C_0. (The terminology corresponds to that adopted in [9]; see also chapter 1 of [6]).

Proof. The operator $A_1 = iu\frac{\partial}{\partial x}$ is self-adjoint on $D(A_1) = D(A)$ and, therefore (see [10], Sec. X.8), the operator iA_1 generates a compressive semigroup of class C_0. Since under the conditions of the theorem the operator L turns out to be bounded, self-adjoint, dissipative, $D(L) \supset D(A)$ and $\forall \phi \in D(A)$

$$\|L(\phi)\| \le a\|iA_1(\phi)\| + \|L\| \cdot \|\phi\|;\ \|\cdot\|^2 \equiv \int |\cdot|^2\, dxdu$$

for an arbitrarily small number a, then, according to the lemma from Sec. X.8 of the book [10], the operator $A = iA_1 + L$ generates a compressive semigroup $\{T(t)\}$ of class C_0, i.e. equation (4) with $f_0 \in D(A)$ has the only solution $f \in D(A)$:

$$f = T(t) f_0;\ \|T(t)\| \le 1. \qquad (6)$$

The lemma is proved.

Lemma 2. $0 \in \sigma(A)$ – spectrum of A.

Proof. We shell show that $\lambda = 0$ is the point of the essential spectrum of operator A, i.e. there is a bounded noncompact sequence $f_n \in D(A)$, satisfying condition

$$\lim_{n\to\infty} (A - \lambda E) f_n = 0.$$

Let $\varepsilon_n > 0$ and $\varepsilon_n \to 0$, monotonously decreasing; let the numbers $\xi_n > 0$ are such that $\nu(\xi_n) = \varepsilon_n$ (such ξ_n exist due to the monotonic tendency to zero collision frequencies $\nu(|u|)$ at $|u| \to \infty$ for "soft" potentials; in particular $\xi_n \to 0$, monotonously increasing). Let further Ω_n – limited area in R_u^3, located entirely outside a sphere of radius ξ_n centered at the origin and such that $\int_{\Omega_n} |u|^2\, du \le 1$.

Let $\{\nu_n(u)\}$ – sequence of functions that are finite in the domains $\Omega_n \subset R_u^3$ with media lying in their respective areas Ω_n, and orthonormalized in $L_2(u)$ (orthogonality can be achieved, for example, by choosing disjoint areas Ω_n). We put further

$$\omega_n(x) = 2^{-\frac{1}{2}} (\pi n)^{-\frac{3}{4}} \exp\left(-\frac{|x|^2}{2n} \right).$$

Note that ν_n converges weakly to zero in $L_2(u)$, and

$$\int |\omega_n(x)|^2 dx; \quad \int \left| \frac{\partial \omega_n}{\partial x_i} \right|^2 dx \xrightarrow[n\to\infty]{} 0.$$

Let $f_n = \nu_n(u)\omega_n(x)$. Obviously, $\{f_n\}$ is orthonormal sequence in $L_2(x,u)$. Let us rate

$$\|A(f_n)\| \le \left\| \nu_n u \frac{\partial \omega_n}{\partial x} \right\| + \|\nu_n \omega_n\| + \|\omega_n K(\nu_n)\|,$$

where $\|\cdot\|$ is a norm in $L_2(x,u)$. Given the choice of functions ν_n, ω_n, domains Ω_n and numbers ε_n, ξ_n we get

$$\|A(f_n)\| \to 0,\ n \to \infty.$$

Lemma 2 is proved.

Consequence. $\|T(t)\| = 1$.

Proof. By Theorem 16.3.1. and Lemma 16.3.2 from [9] we have

$$\|T(t)\| \ge \sup_{\lambda \in \sigma(A)} |\exp(t\lambda)|.$$

But according to the lemma 2, $0 \in \sigma(A)$ and therefore, $\|T(t)\| \ge 1$. On the other hand, by the lemma 1, $\|T(t)\| \le 1$, hence, $\|T(t)\| = 1$.

By virtue of (6), the statement of the main theorem is valid for the linearized equation (5). The proof of the main theorem for the nonlinear (but close to equilibrium) case is based on the technique developed in [4, 11] and the properties of solutions of equation (5) established above.

Comment. For a spatially homogeneous linearized equation, the formulation of the main result will slightly change, namely, for the semigroup $T(t) = \exp(tL)$ generated by a bounded (for "soft" potentials) operator L, there is a presentation

$$T(t) = \int_{\sigma(L)\setminus\{0\}} e^{t\lambda} dE_\lambda + \sum_{j=0}^{4} P_{\psi_j},$$

where P_{ψ_j} are projectors on one-dimensional subspaces of additive invariants ψ_j.

Denote the first term on the right-hand side of the last equality by $T_\perp(t)$. Then

$$f = T_\perp(t) f_0 + \sum_{j=1}^{4} a_j \psi_j.$$

Similarly, to the above, it is easy to show that $\|T_\perp(t)\| = 1$.

3. Conclusions

The work is devoted to the study of the stability of solutions of the linearized Boltzmann equation in the case of “soft” intermolecular interaction potentials (that is, power potentials with exponents less than 5). In this case, a fact of loss of stability of solutions is found that is very curious from a physical point of view: it turns out that there are initial perturbations that "live" for an arbitrarily long time!

Recall that for “hard” potentials (exponent greater than 5) this fact does not occur. We also note that the potential of Coulomb interactions is “soft”.

4. References

1. Carleman T. Problemes Mathematiques dans la Theorie Cinetique des Gaz. – Uppsala, 1957.

2. Maslova N.B. Solvability theorems for the nonlinear Boltzmann equation // Supplement II to the Russian translation of the book: Cercignani K. Theory and Applications of the Boltzmann Equation. – Moscow, 1978, p. 461-480 (in Russian)

3. Lebowitz J.L., Montroll E.W. (editors). Nonequilibrium Phenomena: The Boltzmann Equation. – North-Holland Publishing Company, 1983

4. Maslova N.B., Firsov A.N. On the General solvability of the Cauchy problem for the nonlinear Boltzmann equation. – Proceedings of the all-Union conference on partial differential equations. Publishing house of Moscow University, Moscow, 1978, p. 376 – 377 (in Russian)

5. Firsov A.N. On a Cauchy problem for the nonlinear Boltzmann equation. – Aerodynamics of rarefied gases, issue 8. Publishing House of Leningrad State University, Leningrad, 1976, p. 22 – 37 (in Russian)

6. Firsov A.N. Generalized mathematical models and methods for analyzing dynamic processes in distributed systems. – Publishing House of Polytechnic University, St. Petersburg, 2012 (in Russian)

7. Caflich R.E. The Boltzmann equation with a soft potential // Commun. Math. phys., 1980, v. 74, p. 71-95.

8. Grad H. Asymptotic theory of the Boltzmann equation, II. Rarefied Gas Dynamics, vol. I, Academic Press, New York, London, 1963, p. 26 – 59.

9. Hille E., Phillips R.S. Functional Analysis and Semi-Groups. – Providence, 1957.

10. Reed M., Simon B. Methods of Modern Mathematical Physics. Vol. II. – Academic Press, NY, San Francisco, London, 1975

11. Maslova N.B., Firsov A.N. Solution of the Cauchy problem for the Boltzmann equation. I. // Vestnik of Leningrad University, 1975, № 19, p. 83-88 (in Russian)

MODELING OF A CYLINDRICAL BODY MOTION ON A VIBRATING SURFACE

МОДЕЛИРОВАНИЕ ДВИЖЕНИЯ ЦИЛИНДРИЧЕСКОГО ТЕЛА ПО ВИБРИРУЮЩЕЙ ПОВЕРХНОСТИ

Doctor of Physical and Mathematics sciences, Prof. Ibrayev A.,
Candidate of Physical and Mathematics sciences, Assoc. Prof. Bersugir M.
Eurasian National University named after L.N.Gumilev, Nur-Sultan, Kazakhstan
E-mail: ibrayev.askar@mail.ru, bersugir68@mail.ru

Abstract: *The problems of continuous motion of a cylindrical body with a displaced center of mass along vibrating horizontal and inclined surfaces are considered.*

The analytical solutions of the motion equations were obtained by the method of partial discretization of nonlinear differential equations [1] *and graphs of changes in the rotation angles of a cylindrical body were constructed for various cases.*

KEY WORDS: *SOLID BODY, ROUGH SURFACE, AMPLITUDE, FREQUENCY, MOMENT OF INERTIA, DIFFERENTIAL EQUATIONS*

1. Introduction

Vibration processes are widespread in industrial and technological systems. Vibrations are significant in the processes of vibrational movement, transportation, and also used in part process technologies. In general, the dynamics of vibrating machines and mechanisms are widely studied. In studies of vibrational processes, modeling plays a significant role. In this case, models of various levels ща complexity are used. The indicated models are reduced to the description of nonlinear differential equations system, the analytical solutions of which present known difficulties. Therefore, the construction of their analytical solutions is very relevant.

2. Preconditions and means for resolving the problem

The movement of a cylindrical body occurs under the action of gravity and the reaction of the surface applied at a point P. Decompose the reaction into two components: vertical N and horizontal F (Fig. 1).

Let the surface perform translational rectilinear harmonic oscillations according to the law $\xi = A\sin(\omega t)$, directed at an angle β to the horizontal

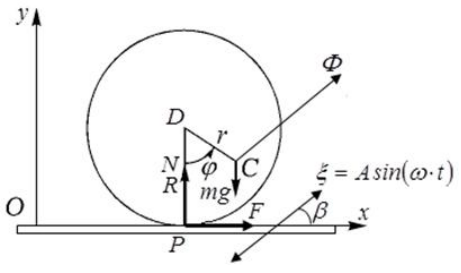

Fig.1 *The movement of a cylindrical body on a vibrating horizontal surface*

Here: A, ω – amplitude and frequency of oscillations; t –time. The inertial properties of the body are characterized by mass and moment of inertia relative to the center of mass *C*. We will set the position of the body by the x_C, y_C coordinates of the center of mass in the Oxy coordinate system associated with a rough surface and the rotation angle φ.

The interaction of a solid body with a surface occurs through the action of a normal reaction N and friction force F (rolling friction is neglected). Assume that friction obeys the Amonton-Coulomb law:

$$|F| \le f \cdot N,$$

where f is the coefficient of sliding friction. In this paper, we consider continuous motion, $N \ge 0$.

The body is also under the influence of gravity force mg. In relative motion, to all forces it is necessary to add the portable inertia force:

$$\Phi = m \cdot A \cdot \omega^2 \cdot \sin(\omega t).$$

Non-slip rolling of a cylindrical body with a displaced center of mass on a horizontal surface is described by differential equations system arising from general theorems on the motion of the center of mass and on the change in the kinetic moment [2,3]:

$$\begin{aligned} m\ddot{x}_C &= F + \Phi\cos\beta, \\ m\ddot{y}_C &= N - mg + \Phi\sin\beta, \\ J_C\ddot{\varphi} &= F(R - r\cos\varphi) - Nr\sin\varphi, \end{aligned} \tag{1}$$

where m – mass of a body; x_C, y_C – coordinate of center of mass *C* of the body; N – normal reaction of the surface; J_C – moment of inertia about an axis perpendicular to the surface of the body; φ – body rotation angle; R – cylinder radius; r – distance from the geometric center to the center of gravity of the body; g – gravitational acceleration.

Consider the system of differential equations (1) together with the initial conditions

$$t = 0: \quad \varphi = \varphi_0, \quad \dot{\varphi} = \dot{\varphi}_0. \tag{2}$$

For a more convenient recording, we consider positive the direction of the rotation angle counterclockwise. The coordinates of the center of mass *C* can be represented as:

$$x_C = x_D + r\sin\varphi; \qquad y_C = R - r\cos\varphi, \tag{3}$$

where $x_D, y_D = R$ – coordinates of the center of curvature *D*, $r = CD$.

When rolling without sliding, the instantaneous center of velocity is at the point of contact *P*, i.e. $\upsilon_P = 0$, or

$$\dot{x}_D = -\dot{\varphi}R; \qquad \dot{y}_D = 0. \tag{4}$$

Using (3), (4), find:

$$\ddot{x}_C = -\left(R - r\cos\varphi\right)\ddot{\varphi} - r\sin\varphi\cdot\dot{\varphi}^2;$$
$$\ddot{y}_C = r\sin\varphi\cdot\ddot{\varphi} + r\cos\varphi\cdot\dot{\varphi}^2. \tag{5}$$

The first two of the three differential equations of the body motion (1), taking into account (5), give the dependence of the components of the surface reaction on $\varphi, \dot{\varphi}$ и $\ddot{\varphi}$:

$$N = m\left[g + r\left(\sin\varphi\cdot\ddot{\varphi} + \cos\varphi\cdot\dot{\varphi}^2\right)\right] - mA\omega^2\sin(\omega t)\sin\beta,$$
$$F = -m\left[\left(R - r\cos\varphi\right)\ddot{\varphi} + r\sin\varphi\cdot\dot{\varphi}^2\right] - mA\omega^2\sin(\omega t)\cos\beta. \tag{6}$$

Substituting expressions (6) into the third of the differential equations of motion of the body (1), arrive at the equation describing the change in the rotation angle $\varphi(t)$:

$$\left[J_C + m\left(R^2 + r^2 - 2Rr\cos\varphi\right)\right]\ddot{\varphi} + mr\sin\varphi\left(R\dot{\varphi}^2 + g\right) +$$
$$+ mA\omega^2\sin(\omega t)\left[R\cos\beta - r\cos(\varphi - \beta)\right] = 0. \tag{7}$$

By entering the notation

$$f(t) = \frac{m}{J_C + m\left(R^2 + r^2 - 2Rr\cos\varphi\right)}, \tag{8}$$

obtain equations (7) in the form

$$\ddot{\varphi} + f(t)\left\{r\sin\varphi\left(R\dot{\varphi}^2 + g\right) + A\cdot\omega^2\cdot\sin(\omega t)\left[R\cos\beta - r\cos(\varphi - \beta)\right]\right\} = 0. \tag{9}$$

3. Results and discussion

The last equation in its final form is not integrated. To solve problem (9)-(2) using the method of partial discretization of nonlinear differential equations, obtain

$$\ddot{\varphi} = -\frac{1}{2}\sum_{i=1}^{n}\left(t_i + t_{i+1}\right)\Big\langle f(t_i)\Big\{r\sin\varphi(t_i)\left(R\dot{\varphi}(t_i)^2 + g\right) +$$
$$+ A\cdot\omega^2\cdot\sin(\omega t_i)\left[R\cos\beta - r\cos(\varphi(t_i) - \beta)\right]\Big\}\delta(t - t_i) -$$
$$- f(t_{i+1})\Big\{r\sin\varphi(t_{i+1})\left(R\dot{\varphi}(t_{i+1})^2 + g\right) + A\cdot\omega^2\cdot\sin(\omega t_{i+1})\times$$
$$\times\left[R\cos\beta - r\cos(\varphi(t_{i+1}) - \beta)\right]\Big\}\delta(t - t_{i+1})\Big\rangle, \tag{10}$$

where $\delta(t)$ – Delta Dirac function.
The general solution of equation (10) has the expression

$$\dot{\varphi}(t) = C_1 - \frac{1}{2}\sum_{i=1}^{n}\left(t_i + t_{i+1}\right)\Big\langle f(t_i)\Big\{r\sin\varphi(t_i)\left(R\dot{\varphi}(t_i)^2 + g\right) +$$
$$+ A\cdot\omega^2\cdot\sin(\omega t_i)\left[R\cos\beta - r\cos(\varphi(t_i) - \beta)\right]\Big\}H(t - t_i) -$$
$$- f(t_{i+1})\Big\{r\sin\varphi(t_{i+1})\left(R\dot{\varphi}(t_{i+1})^2 + g\right) + A\cdot\omega^2\cdot\sin(\omega t_{i+1})\times$$
$$\times\left[R\cos\beta - r\cos(\varphi(t_{i+1}) - \beta)\right]\Big\}H(t - t_{i+1})\Big\rangle, \tag{11}$$

where $H(t)$ – Heaviside function, C_1 – arbitrary integration constant.
Using the initial conditions (2), we have

$$\dot{\varphi}(t) = \dot{\varphi}_0 - \frac{1}{2}\sum_{i=1}^{n}\left(t_i + t_{i+1}\right)\Big\langle f(t_i)\Big\{r\sin\varphi(t_i)\left(R\dot{\varphi}(t_i)^2 + g\right) +$$
$$+ A\cdot\omega^2\cdot\sin(\omega t_i)\left[R\cos\beta - r\cos(\varphi(t_i) - \beta)\right]\Big\}H(t - t_i) -$$
$$- f(t_{i+1})\Big\{r\sin\varphi(t_{i+1})\left(R\dot{\varphi}(t_{i+1})^2 + g\right) + A\cdot\omega^2\cdot\sin(\omega t_{i+1})\times$$
$$\times\left[R\cos\beta - r\cos(\varphi(t_{i+1}) - \beta)\right]\Big\}H(t - t_{i+1})\Big\rangle. \tag{12}$$

The general solution of equation (12) has the expression

$$\dot{\varphi}(t) = \dot{\varphi}_0 t + C_2 - \frac{1}{2}\sum_{i=1}^{n}\left(t_i + t_{i+1}\right)\Big\langle f(t_i)\Big\{r\sin\varphi(t_i)\left(R\dot{\varphi}(t_i)^2 + g\right) +$$
$$+ A\cdot\omega^2\cdot\sin(\omega t_i)\left[R\cos\beta - r\cos(\varphi(t_i) - \beta)\right]\Big\}(t - t_i)H(t - t_i) -$$
$$- f(t_{i+1})\Big\{r\sin\varphi(t_{i+1})\left(R\dot{\varphi}(t_{i+1})^2 + g\right) + A\cdot\omega^2\cdot\sin(\omega t_{i+1})\times$$
$$\times\left[R\cos\beta - r\cos(\varphi(t_{i+1}) - \beta)\right]\Big\}(t - t_{i+1})H(t - t_{i+1})\Big\rangle. \tag{13}$$

With taking into account the initial conditions (2), the solution of equation (13) will have the form

$$\varphi(t) = \dot{\varphi}_0 t + \varphi_0 - \frac{1}{2}\sum_{i=1}^{n}\left(t_i + t_{i+1}\right)\Big\langle f(t_i)\Big\{r\sin\varphi(t_i)\left(R\dot{\varphi}(t_i)^2 + g\right) +$$
$$+ A\cdot\omega^2\cdot\sin(\omega t_i)\left[R\cos\beta - r\cos(\varphi(t_i) - \beta)\right]\Big\}(t - t_i)H(t - t_i) -$$
$$- f(t_{i+1})\Big\{r\sin\varphi(t_{i+1})\left(R\dot{\varphi}(t_{i+1})^2 + g\right) + A\cdot\omega^2\cdot\sin(\omega t_{i+1})\times$$
$$\times\left[R\cos\beta - r\cos(\varphi(t_{i+1}) - \beta)\right]\Big\}(t - t_{i+1})H(t - t_{i+1})\Big\rangle. \tag{14}$$

In accordance with equation (14), expressions of the rotation angle $\varphi(t_k)$ and the angular velocity $\dot{\varphi}(t_k)$ of the body at times t_k will be:

$$\varphi(t_1) = \dot{\varphi}_0 t_1 + \varphi_0;$$
$$\dot{\varphi}(t_1) = \dot{\varphi}_0 - \frac{1}{2}(t_1 + t_2)f(t_1)r\sin\varphi(t_1)\left(R\dot{\varphi}(t_1)^2 + g\right) +$$
$$+ A\cdot\omega^2\cdot\sin(\omega t_1)\left[R\cos\beta - r\cos(\varphi(t_1) - \beta)\right];$$
$$\varphi(t_2) = \dot{\varphi}_0 t_2 + \varphi_0 - \frac{1}{2}(t_1 + t_2)f(t_1)\Big\{r\sin\varphi(t_1)\left(R\dot{\varphi}(t_1)^2 + g\right) +$$
$$+ A\cdot\omega^2\cdot\sin(\omega t_1)\left[R\cos\beta - r\cos(\varphi(t_1) - \beta)\right]\Big\}(t_2 - t_1);$$
$$\dot{\varphi}(t_2) = \dot{\varphi}_0 - \frac{1}{2}(t_1 + t_2)f(t_1)\Big\{r\sin\varphi(t_1)\left(R\dot{\varphi}(t_1)^2 + g\right) + A\cdot\omega^2\cdot\sin(\omega t_1)\Big\} +$$
$$+ \left[R\cos\beta - r\cos(\varphi(t_1) - \beta)\right] - \frac{1}{2}(t_3 - t_1)f(t_2)\Big\{r\sin\varphi(t_2)\left(R\dot{\varphi}(t_2)^2 + g\right) +$$
$$+ A\cdot\omega^2\cdot\sin(\omega t_2)\left[R\cos\beta - r\cos(\varphi(t_2) - \beta)\right]\Big\};$$
$$\varphi(t_3) = \dot{\varphi}_0 t_3 + \varphi_0 - \frac{1}{2}(t_1 + t_2)f(t_1)\Big\{r\sin\varphi(t_1)\left(R\dot{\varphi}(t_1)^2 + g\right) +$$
$$+ A\cdot\omega^2\cdot\sin(\omega t_1)\left[R\cos\beta - r\cos(\varphi(t_1) - \beta)\right]\Big\}(t_3 - t_1) -$$
$$- \frac{1}{2}(t_3 - t_1)f(t_2)\Big\{r\sin\varphi(t_2)\left(R\dot{\varphi}(t_2)^2 + g\right) + A\cdot\omega^2\cdot\sin(\omega t_2)\times$$
$$\times\left[R\cos\beta - r\cos(\varphi(t_2) - \beta)\right]\Big\}(t_3 - t_2) - \frac{1}{2}(t_4 - t_2)f(t_3)\times$$
$$\times\Big\{r\sin\varphi(t_3)\left(R\dot{\varphi}(t_3)^2 + g\right) + A\cdot\omega^2\cdot\sin(\omega t_3)\times$$
$$\times\left[R\cos\beta - r\cos(\varphi(t_3) - \beta)\right](t_3 - t_2)\Big\};$$

$$\dot{\varphi}(t_3)=\dot{\varphi}_0-\frac{1}{2}(t_1+t_2)f(t_1)\{r\sin\varphi(t_1)(R\dot{\varphi}(t_1)^2+g)+$$

$$+A\cdot\omega^2\cdot\sin(\omega t_1)[R\cos\beta-r\cos(\varphi(t_1)-\beta)]\}-$$

$$-\frac{1}{2}(t_3-t_1)f(t_2)\{r\sin\varphi(t_2)(R\dot{\varphi}(t_2)^2+g)+A\cdot\omega^2\cdot\sin(\omega t_2)\times$$

$$\times[R\cos\beta-r\cos(\varphi(t_2)-\beta)]\}-\frac{1}{2}(t_4-t_2)f(t_3)\times$$

$$\times\{r\sin\varphi(t_3)(R\dot{\varphi}(t_3)^2+g)+A\cdot\omega^2\cdot\sin(\omega t_3)\times$$

$$\times[R\cos\beta-r\cos(\varphi(t_3)-\beta)].$$

Using the method of mathematical induction, construct analytical expressions of the rotation angle $\varphi(t_k)$ and the angular velocity $\dot{\varphi}(t_k)$ at an arbitrary point $k=\overline{1,n}$:

$$\varphi(t_k)=\dot{\varphi}_0t_k+\varphi_0-\frac{1}{2}(t_1+t_2)f(t_1)\{r\sin\varphi(t_1)(R\dot{\varphi}(t_1)^2+g)+$$

$$+A\cdot\omega^2\cdot\sin(\omega t_1)[R\cos\beta-r\cos(\varphi(t_1)-\beta)]\}(t_k-t_1)-$$

$$-\frac{1}{2}\sum_{i=2}^{k}(t_{i+1}-t_{i-1})f(t_i)\{r\sin\varphi(t_i)(R\dot{\varphi}(t_i)^2+g)+$$

$$+A\cdot\omega^2\cdot\sin(\omega t_i)[R\cos\beta-r\cos(\varphi(t_i)-\beta)]\}(t_k-t_i),$$

(15)

$$\dot{\varphi}(t_k)=\dot{\varphi}_0-\frac{1}{2}(t_1+t_2)f(t_1)\{r\sin\varphi(t_1)(R\dot{\varphi}(t_1)^2+g)+$$

$$+A\cdot\omega^2\cdot\sin(\omega t_1)[R\cos\beta-r\cos(\varphi(t_1)-\beta)]\}-$$

$$-\frac{1}{2}\sum_{i=2}^{k}(t_{i+1}-t_{i-1})f(t_i)\{r\sin\varphi(t_i)(R\dot{\varphi}(t_i)^2+g)+$$

$$+A\cdot\omega^2\cdot\sin(\omega t_i)[R\cos\beta-r\cos(\varphi(t_i)-\beta)]\}.$$

Figure 2 presents graphs of changes of the rotation angle $\varphi(t)$ of a cylindrical body located on a horizontal surface. System parameters correspond to the values: $m=50\,kg$, $\beta=0{,}524\,rad$, $R=0{,}5\,m$, $\varphi(0)=0{,}175\,rad$, $\dot{\varphi}(0)=0$.

In this case, the center of mass of the cylindrical body is offset from the geometric center by half the radius, i.e. $r=0{,}25\,m$.

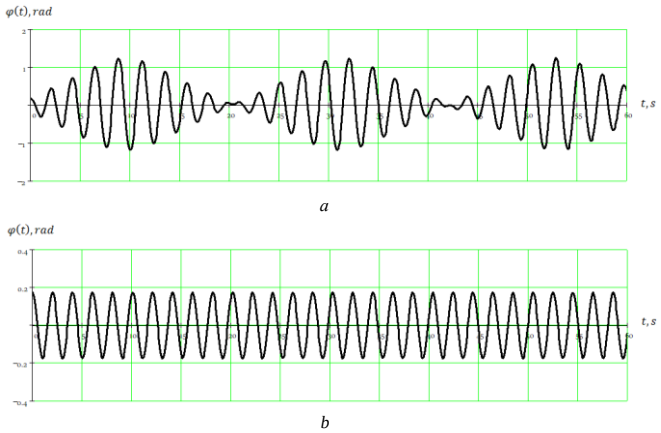

Fig.2 *Graphs of changes of the rotation angle* $\varphi(t)$:
a) at $A=0{,}1\,m$, $\omega=3\ rad/s$; *b) at* $A=0{,}001\,м$, $\omega=10\ rad/s$

From graph *2a* it follows that the nature of the beating occurs with the corresponding parameters $A=0{,}1\,m$, $\omega=3\ rad/s$.

Figure *2b* shows a graph of changes $\varphi(t)$ at $A=0{,}001\,m$, $\omega=10\ rad/s$. As follows from this graph, the fluctuations of the rotation angle $\varphi(t)$ obeys the harmonic law and has an established character. It should be noted that when $r<0{,}25\,m$, the period of oscillation of the rotation angle increases, when $r>0{,}25\,m$ the period decreases.

Consider the motion of a cylindrical solid with a displaced center of mass along a vibrating inclined surface (Fig. 3).

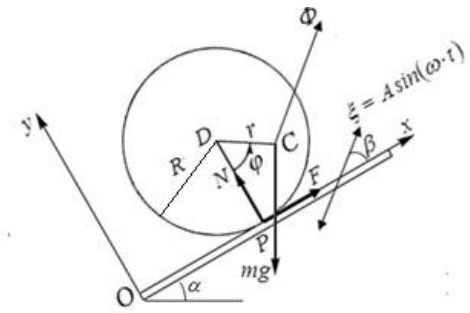

Fig.3 *The motion of a cylindrical solid on a vibrating inclined surface*

In this case, the system of differential equations (1) takes the following form

$$m\ddot{x}_C=F+\Phi\cos\beta-mg\sin\alpha,$$

(16) $$m\ddot{y}_C=N+\Phi\sin\beta-mg\cos\alpha,$$

$$J_C\ddot{\varphi}=F(R-r\cos\varphi)-Nr\sin\varphi.$$

After some transformations, from the system of differential equations (16) obtain the values of the surface reaction components from $\varphi,\dot{\varphi}$ и $\ddot{\varphi}$ in the form

$$N=mr(\sin\varphi\cdot\ddot{\varphi}+\cos\varphi\cdot\dot{\varphi}^2)-mA\omega^2\sin(\omega t)\sin\beta+mg\cos\alpha,$$

(17)

$$F=-m[(R-r\cos\varphi)\ddot{\varphi}+r\sin\varphi\cdot\dot{\varphi}^2]-mA\omega^2\sin(\omega t)\cos\beta+mg\sin\alpha.$$

Substituting expressions (17) into the third of the system of differential equations of body motion (16) and introducing the notation (8), obtain the expression for the change in the rotation angle $\varphi(t)$ in time:

$$\ddot{\varphi}+f(t)\{rR\sin\varphi\dot{\varphi}^2-g[R\sin\alpha-r\sin(\varphi+\alpha)]+A\cdot\omega^2\cdot\sin(\omega t)\times$$

(18)

$$\times[R\cos\beta-r\cos(\varphi-\beta)]\}=0.$$

Similarly, by the above method, obtain an analytical solution in the form:

$$\varphi(t)=\dot{\varphi}_0t+\varphi_0-\frac{1}{2}\sum_{i=1}^{n}(t_i+t_{i+1})\langle f(t_i)\{rR\sin\varphi(t_i)\dot{\varphi}^2(t_i)+A\omega^2\times$$

$$\times\sin(\omega t_i)[R\cos\beta-r\cos(\varphi(t_i)-\beta)]-g[R\sin\alpha-r\sin(\varphi(t_i)+\alpha)]\}\times$$

(19) $$\times(t-t_i)H(t-t_i)-f(t_{i+1})\{rR\sin\varphi(t_{i+1})\dot{\varphi}^2(t_{i+1})+A\omega^2\sin(\omega t_{i+1})\times$$

$$\times[R\cos\beta-r\cos(\varphi(t_{i+1})-\beta)]-g[R\sin\alpha-r\sin(\varphi(t_{i+1})+\alpha)]\}\times$$

$$\times(t-t_{i+1})H(t-t_{i+1})\rangle.$$

Using the same transformations, define the expressions of the rotation angle $\varphi(t_k)$ and the angular velocity $\dot{\varphi}(t_k)$ of the body at times t_k in the following form

$$\varphi(t_k)=\dot{\varphi}_0 t_k+\varphi_0-\frac{1}{2}(t_1+t_2)f(t_1)\{rR\sin\varphi(t_1)\dot{\varphi}^2(t_1)+$$

$$+A\omega^2\sin(\omega t_1)[R\cos\beta-r\cos(\varphi(t_1)-\beta)]-$$

$$-g[R\sin\alpha-r\sin(\varphi(t_1)+\alpha)]\}(t_k-t_1)-\frac{1}{2}\sum_{i=2}^{k}(t_{i+1}-t_{i-1})f(t_i)\times$$

$$\times\{rR\sin\varphi(t_i)\dot{\varphi}^2(t_i)+A\omega^2\sin(\omega t_i)[R\cos\beta-r\cos(\varphi(t_i)-\beta)]-$$

$$-g[R\sin\alpha-r\sin(\varphi(t_i)+\alpha)]\}(t_k-t_i),$$

(20)

$$\dot{\varphi}(t_k)=\dot{\varphi}_0-\frac{1}{2}(t_1+t_2)f(t_1)\{rR\sin\varphi(t_1)\dot{\varphi}^2(t_1)+A\omega^2\sin(\omega t_1)\times$$

$$\times[R\cos\beta-r\cos(\varphi(t_1)-\beta)]-g[R\sin\alpha-r\sin(\varphi(t_1)+\alpha)]\}-$$

$$-\frac{1}{2}\sum_{i=2}^{k}(t_{i+1}-t_{i-1})f(t_i)\{rR\sin\varphi(t_i)\dot{\varphi}^2(t_i)+A\omega^2\sin(\omega t_i)\times$$

$$\times[R\cos\beta-r\cos(\varphi(t_i)-\beta)]-g[R\sin\alpha-r\sin(\varphi(t_i)+\alpha)]\}(t_k-t_i).$$

Figure 3 shows the case when the inclination of the vibrating surface makes an angle with the horizontal: $\alpha=0{,}130\,rad$, other parameters correspond to the values indicated in the previous case.

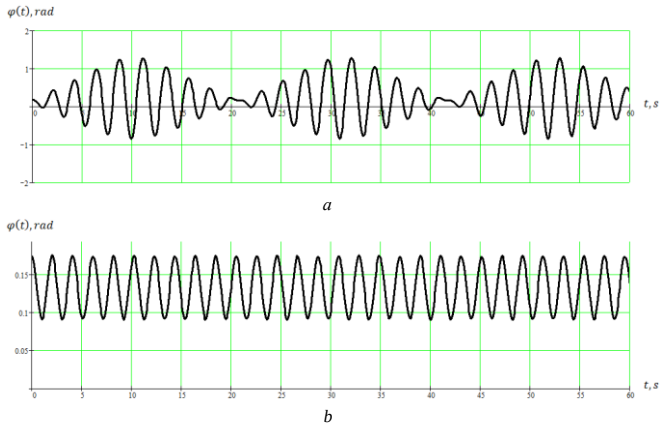

Fig.3 *Graphs of changes of the rotation angle* $\varphi(t)$:
a) at $A=0{,}1\,m$, $\omega=3\ rad/s$; *b) at* $A=0{,}001\,м$, $\omega=10\ rad/s$

As can be seen from graph *3a*, oscillations having the nature of a beating are preserved.

As follows from graph *3b*, the oscillations are harmonic, but due to the angle of inclination of the plane, the graph has the form of an offset.

The research results show and this is evident from the graphs.

5. Conclusion

The problems of continuous motion of a cylindrical body with a displaced center of mass along vibrating horizontal and inclined surfaces are considered.

The analytical solutions of the motion equations are obtained by the method of partial discretization of nonlinear differential equations.

Graphs of changes of the rotation angles $\varphi(t)$ of a cylindrical body are constructed for various cases of changing the system parameters.

In particular, changes were made to the distances of the displacement of the center of mass from the geometric center within $r=0{,}1m$ до $r=0{,}4m$.

It has been established that the nature of the oscillatory processes when the center of mass of the cylindrical body is displaced from the geometric center is significantly affected by the amplitude and frequency of the oscillations.

It is shown that changes in the angle of inclination of the vibrating surface do not significantly affect the rotation angle of the body.

6. Literature

1. Tyurehodzhaev A.N. *Analytical solutions of nonlinear equations and differential equations with variable coefficients.* Proceedings of the «Actual Problems of Mechanics and Engineering» IV International Scientific Conference, II, Almaty, 40-57 (2014).

2. Yelisseyev A.V., Selviskiy V.V., Yelisseyev S.V. Dynamics of vibrational interactions of elements of technological systems, taking into account unstable bonds: monograph. – Irkutsk: IrSTU, 2015. – 400 p.

3. Markeev A.P. Theoretical Mechanics: A manual for Universities. - Moscow: CheRo, 1999.

APPLICATION OF PERSISTENT HOMOLOGY ON BIO-MEDICAL DATA – A CASE STUDY

Eng. Sekuloski, P., Ass. Prof. Dr. Dimitrievska Ristovska, V.
Faculty of Computer Science and Engineering, "Ss. Cyril and Methodius" University, Skopje, Macedonia
petar.sekuloski@finki.ukim.mk, vesna.dimitrievska.ristovska@finki.ukim.mk,

Abstract: In this paper we introduce, analyze and apply persistent homology, one of the main algorithms of TDA, on some real data sets from the bio-medical field. Topological data analysis (TDA) is a field which is a synergy between mathematics, data science and computer science. The main goal of TDA is studying the shape of data using topological techniques. TDA proposes new algorithms that deal with these problems based on tools or concepts from algebraic topology and pure mathematics. We analyze the results and give a topological characterization of the dataset and propose to use them in future work.

Keywords: PERSISTENT HOMOLOGY, TOPOLOGICAL DATA ANALYSIS, ALGEBRAIC TOPOLOGY, DATA SCIENCE, COMPUTATIONAL TOPOLOGY

1. Introduction

Topology is a mathematical field that studies properties of topological spaces, such as connectedness and compactness, invariant of continuous deformations. Algebraic topology studies topological spaces using techniques from algebra by associating algebraic objects such as groups with topological spaces. One of the main tools of algebraic topology is homology. Homology is a mathematical tool which associates sequences of algebraic objects with topological spaces. One way to study a topological space is to find and compute its homology groups. The motivation behind defining homology groups was that two shapes can be distinguished by examining their holes. For example, a disk is different from a circle, or a disk is not a circle, because the disk is solid while the circle has a hole through it. Homology groups are set of invariants of a topological space. These invariants characterize the topological space. The number of structures for some dimension k is the rank of the k-dimensional homology group of the topological space. The number of such structures is known as a Betti number (β_k) of dimension k.

The main idea of Topological Data Analysis is application of these mathematical concepts on real data. Persistent homology is an algorithm from TDA that use homology as main idea. The algorithm computes topological features of a space.

2. Mathematical Background

The starting point is to construct a topological space from a given dataset. We will define some necessary mathematical concepts.

Definition 1. A $\boldsymbol{k}$-simplex is a convex hull of $\boldsymbol{k+1}$ affinely independent points $\boldsymbol{S} = \{\boldsymbol{x_0}, \boldsymbol{x_1}, , \dots, \boldsymbol{x_k}\} \subseteq \mathbb{R}^{\boldsymbol{d}}$. The points of S are vertices of the simplex**.**

The low dimensional simplices (plural: simplices or simplexes) have special names:

- a 0-simplex is called a *vertex;*
- a 1-simplex is called *an edge;*
- a 2-simplex is called *a triangle:*

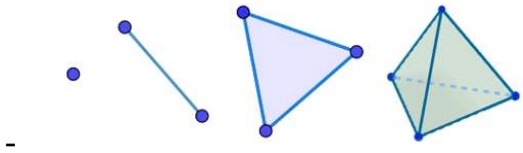

Figure 1. 0-simplex 1-simplex, 2-simplex, 3-simplex

Definition 2. Let σ be a k-simplex defined $\boldsymbol{on\ S} = \{\boldsymbol{x_0}, \boldsymbol{x_1}, , \dots, \boldsymbol{x_k}\}$. A simplex $\boldsymbol{\tau}$ defined by $\boldsymbol{T} \subseteq \boldsymbol{S}$ is a face of $\boldsymbol{\sigma}$ and has $\boldsymbol{\sigma}$ as a coface. The relationship is denoted with $\boldsymbol{\sigma} \geq \boldsymbol{\tau}$ and $\boldsymbol{\tau} \leq \boldsymbol{\sigma}$.

Definition 3. Let K be a set. Simplicial complex S is a collection of subsets of $\boldsymbol{K}$ called simplices such that:

1. For all $\boldsymbol{x} \in \boldsymbol{K}, \{\boldsymbol{x}\} \in \boldsymbol{S}$.
2. If $\tau \subseteq \sigma \in$ S, then $\tau \in$ S.

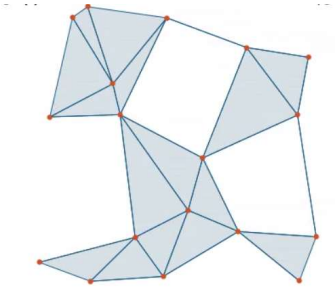

Figure 2. An example of a simplicial complex

We call the sets {x} the vertices of K. **Definition 3** gives a more abstract definition of simplicial complex that can be applied to a data where vertices will be the data points. Topological invariants of the space, such as holes and number of connected components, can be computed from a simplicial complex, see Figure 2. One of the key ideas of TDA is to construct a simplicial complex from a dataset. There are a few ways to construct such a simplicial complex [1]. In other words simplicial complexes are high dimensional analogues of graphs. We will explain the steps of the process.

1. Construction of a topological space from a given point cloud

The open (metric) ball of radius $\varepsilon > 0$ centered at a point $m \in M$, usually denoted by $B(m; \varepsilon)$ is defined by

$B(m;\varepsilon) = \{n \in M \mid d(m,n) \leq \varepsilon\}$

formation of a connected component in the simplicial complex at

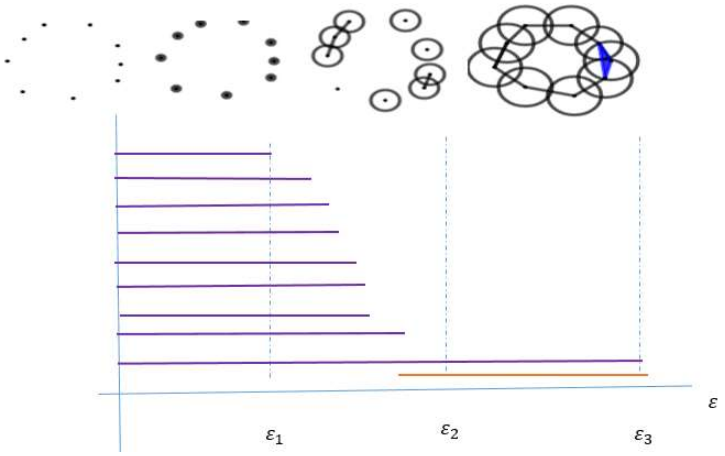

Figure 3. An example of Vietoris-Rips filtration of a space. There are different complexes for different values for ε. Violet horizontal lines shows barcodes in dimension 0 and orange line shows barcode for dimension 1.

Let $\boldsymbol{M}$ be a point cloud in $\mathbb{R}^{\boldsymbol{d}}$ and $\boldsymbol{\varepsilon > 0}$. The $\boldsymbol{\varepsilon}$ −neighborhood of the point cloud $\boldsymbol{M}$ is the set $\boldsymbol{S(m;\varepsilon)}$, defined as

$$\boldsymbol{S(m;\varepsilon) = \bigcup_{m \in M} B(m,\varepsilon), \qquad \varepsilon \geq 0.}$$

It is known that every $\boldsymbol{\varepsilon}$ −neighborhood is a topological space. PH gives a summary of a sequence of such topological spaces for different values for $\boldsymbol{\varepsilon}$. The key idea here is to see how topological characteristics are changing and which features are the same as $\boldsymbol{\varepsilon}$ increases.

2. Construction of a simplicial complex from topological space

In our experiments we will use Vietoris-Rips complexes. For a given point cloud $\boldsymbol{M}$ and $\boldsymbol{\varepsilon \geq 0}$ we construct Vietoris-Rips complex denoted as $\boldsymbol{VR(M;\varepsilon)}$. $\boldsymbol{VR(M;\varepsilon)}$ is defined as:

$$\boldsymbol{VR(M;\varepsilon) = \bigcup_{n \geq 0} VR(M;\varepsilon)_n}$$

$$\boldsymbol{VR(M;\varepsilon)_n = \left\{(m_0,\dots,m_n) \middle| d(m_i m_j) \leq \varepsilon, \text{for all i, j} \in \{1,2,\dots,n\}\right\}}$$

Note that $\boldsymbol{VR(M;\varepsilon)_n}$ is the set of all n-simplexes of the simplicial complex. The simplicial complex constructed from the topological space is the approximation of the topological space. Hence, every simplicial complex is a topological space which is why we can analyze its topological features.

3. Computing and representing homology groups

Linear algebra is used for computing homology groups of a given simplicial complex. The $\boldsymbol{k^{th}}$ homology group $\boldsymbol{H_k}$(S) of a simplicial complex $\boldsymbol{S}$ is defined as abelian quotient group. The rank of the $\boldsymbol{H_k}$, $\boldsymbol{rank(H_k(S))}$, is called $\boldsymbol{k^{th}}$ Betti number of $\boldsymbol{S}$. It gives a measure of the number of k-dimensional holes in S. The homology groups are computed for every simplicial complex derived from the topological space for each $\boldsymbol{\varepsilon}$. Thus, by increasing $\boldsymbol{\varepsilon}$ we can trail elements of homology groups of the corresponding complex $\boldsymbol{VR(M;\varepsilon)}$. We can visualize the existence of homology groups as $\boldsymbol{\varepsilon}$ increases using a persistent barcode. Persistent barcode is a topological summary of a topological space. When an element shows at some $\boldsymbol{\varepsilon}$, we say that an element is born and denote that $\boldsymbol{\varepsilon}$ as $\boldsymbol{\varepsilon_{birth}}$. When the element disappears at some $\boldsymbol{\varepsilon}$ (it is mapped to 0), we say that the element has died and we denote that $\boldsymbol{\varepsilon}$ as $\boldsymbol{\varepsilon_{death}}$. Every element is represented with a "bar" (a line in the persistent barcode) on the interval [$\boldsymbol{\varepsilon_{birth}}$. $\boldsymbol{\varepsilon_{death}}$). For example, in $\boldsymbol{H_0}$, this will correspond to the $\boldsymbol{\varepsilon_{birth}}$ and connecting that component with others in a way that they will form a circle in $\boldsymbol{\varepsilon_{death}}$, see Figure 3. If we observe the Figure 3, we can see that the orange line is a bar which corresponds to an element of a homology group of dimension 1, which appears near $\boldsymbol{\varepsilon_2}$. It clearly be seen that there is one circle at the last simplex. Also, we can see that near $\boldsymbol{\varepsilon_2}$ there is one violet line which means that we have one connected component which corresponds with the given simplex.

3. Diabetes datasets

For this case study we picked two diabetes datasets. First dataset is the Miller-Reaven dataset. Reaven and Miller (1979) examined the relationship among blood chemistry measures of glucose tolerance and insulin in 145 non-obese adults [10]. They used the PRIM9 system to visualize the data in 3D, and discovered a peculiar pattern that looked like a large blob with two wings in different directions. In this dataset, the data is split up in three categories. Data from non-diabetic patients, data from patients with diabetes classified as overt and data from patients with diabetes classified as chemical diabetes. Overt diabetes is the most advanced stage, characterized by elevated fasting blood glucose concentration and classical symptoms. Preceding overt diabetes is the latent or chemical diabetic stage, with no symptoms of diabetes but demonstrable abnormality of oral or intravenous glucose tolerance. There are 145 observations on the following 6 variables:

relwt

relative weight, expressed as the ratio of actual weight to expected weight, given the person's height, a numeric vector

glufast

fasting plasma glucose level, a numeric vector

glutest

test plasma glucose level, a measure of glucose intolerance, a numeric vector

instest

plasma insulin during test, a measure of insulin response to oral glucose, a numeric vector

sspg

steady state plasma glucose, a measure of insulin resistance, a numeric vector

group

diagnostic group, a factor with levels Normal, Chemical_Diabetic, Overt_Diabetic.

4. Preliminary results and discussion

First, we apply persistent homology for each diabetic group of data. For the Chemical_Diabetic group the results are given in Figure 4 and for Overt_Diabetic group the results are given in Figure 5.

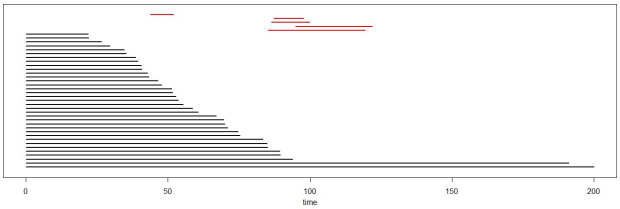

Figure 4. Persistent barcode for the Chemical_Diabetic group

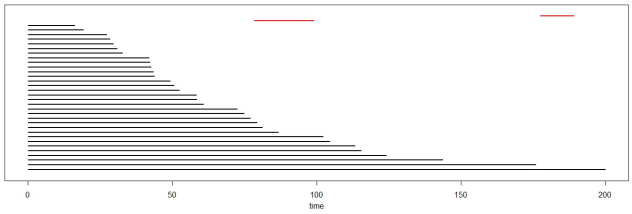

Figure 5. Persistent barcode for the Overt_Diabetic group

We can see that the persistent barcodes are different. In Figure 4, the persistent barcode has more red bars, which means that there are more circles in the simplex constructed from the data for the Chemical_Diabetic group. In this case, there is significant topological difference in the simplexes which means the shape of the data of the two groups is different. A question that arises here is which physical or real factor makes the difference? These factors may be crucial for better understanding the different types of diabetes.

Next, we apply persistent homology on both the diabetic group and the non-diabetic group. The results are given in Figure 6 and Figure 7.

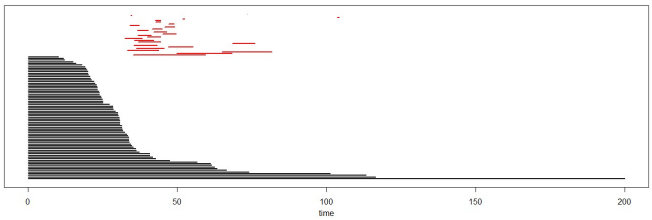

Figure 6. Persistent for non-diabetic group

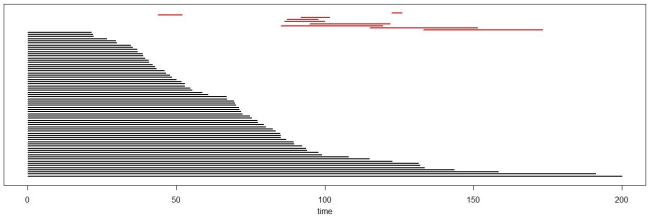

Figure 7. Persistent for diabetic groups

According to the barcodes in Figure 6 and Figure 7, we can conclude that topological characteristics in the data of diabetic and non-diabetic groups are obvious. In the second persistent barcode, there are circles which are present most of the time.

We apply persistent homology on the second dataset which contains data from diabetic and non-diabetic patients. This dataset is originally from the National Institute of Diabetes and Digestive and Kidney Diseases. The objective of the dataset is to diagnostically predict whether or not a patient has diabetes based on certain diagnostic measurements included in the dataset. Several constraints were placed on the selection of these instances from a larger database. In particular, all patients in this dataset are females at least 21 years old and of Pima Indian heritage. The results are given in Figure 8 and Figure 9.

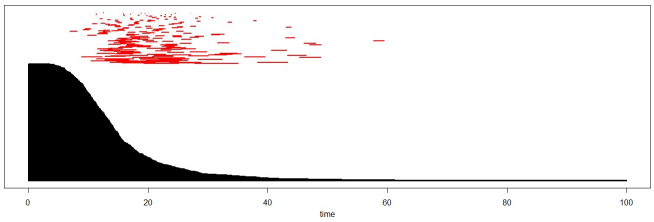

Figure 8. Persistent barcode for non-diabetic data

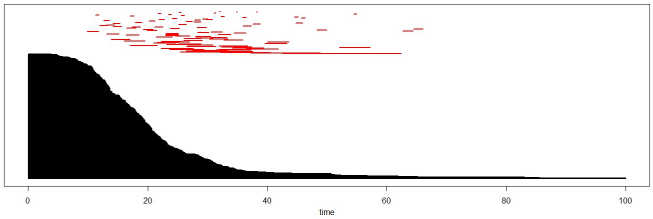

Figure 9. Persistent barcode for diabetic data

5. Further work and application in bio-medical field

The main goal is to link the differences of the topological characterizations of the two types of diabetes to real factors. Persistent homology, and in general, TDA, can be applied in the bio-medical field in many areas. The application of statistics allowed significant progress in understanding diseases. Knowing that, and the fact that TDA gives a new way of analyzing the data, specifically, analyzing the shape of the data, we think that TDA will be useful for medicine. It can be used to see how one factor changes the topological characteristics of the topological space underneath the given data, and how it is related to a disease. If we work in three dimensional Euclidean space, we may find some structural deformations of a system in the body. For example, to observe the deformations of the vasculature of some organ or tissue. In the future, we will investigate how persistent homology can be applied to characterize retinal and liver vasculature networks. TDA can also be applied on big data from the healthcare field.

6. Acknowledgement

This work was partially financed by the Faculty of Computer Science and Engineering at the “Ss. Cyril and Methodius University”, Skopje.

References

[1] H. Edelsbrunner, “Persistent homology: theory and practice”, 2014.

[2] Gunnar Carlsson, “Topology and data”. Bulletin of the American Mathematical Society. 46 (2), 2009, pp. 255–308.

[3] J. R. Munkres, Topology. vol. 2. Upper Saddle River: Prentice Hall, 2000

[4] llen Hatcher, Algebraic topology. Cambridge University Press, 2002

[5] G. Carlsson, A. Zomorodian, A. Collins, L. Guibas, J. (2005-12-01). "Persistence barcodes for shapes". International Journal of Shape Modeling.

[6] Brittany Terese Fasy, Jisu Kim, Fabrizio Lecci, and Clément Maria. “Introduction to the r package tda. “, arXiv preprint arXiv:1411.1830, 2014.

[7] https://s3.amazonaws.com/cdn.ayasdi.com/wp-content/uploads/2018/11/12131418/TDA-Based-Approaches-to-Deep-Learning.pdf

[8] https://en.wikipedia.org/wiki/Fluoroscopy

[9] Ulrich Bauer and Michael Lesnick.” Induced matchings of barcodes and the algebraic stability of persistence. In Proceedings of the thirtieth annual symposium on Computational geometry”, p. 355, 2014.

[10] Reaven, G. M. and Miller, R. G. (1979). An attempt to define the nature of chemical diabetes using a multidimensional analysis. Diabetologia, 16, 17-24.

[11] A. J. Zomorodian, Topology for Computing, Cambridge, 2005

[12] J. Nicponski and J.-H. Jung, Topological data analysis of vascular disease: A theoretical framework, BioRxiv, (2019), p. 637090.

[13] D. Cohen-Steiner, H. Edelsbrunner, and J. Harer, Stability of persistence diagrams, Discrete & Computational Geometry, (2007), pp. 103–120

[14] A. Zomorodian and G. Carlsson, Computing persistent homology, Discrete & Computational Geometry, 33 (2005), pp. 249–274

ENHANCED ASYNCHRONY IN THE VECTORIZED CONEFOLD ALGORITHM FOR FLUID DYNAMICS MODELLING

Perepelkina A. Ph. D., Levchenko V. Ph.D.
Keldysh Institute of Applied Mathematics, Miusskaya sq. 4, Moscow, Russia
Email: mogmi@narod.ru, lev@keldysh.ru

Abstract: *The application of a rigorous CFD method and an all-encompassing algorithmic performance optimization method can make possible the CFD simulation of the extremely large-scale problems, which allows simulation of either larger systems, or more detailed simulation of systems that are already simulated. The CFD code has to show both efficient one-node performance and excellent parallel scaling. The record breaking performance on one node has been achieved before with application of the LRnLA algorithm and making use of many core parallelism as well as the vectorization. In the current work, the algorithm is extended for many-node parallelism. The algorithms is characterized by high parallelization degree, small number of node communication events, and may be concisely described and programmed on the base of the previously implemented one-node solution, which is a rare feature among the algorithms with temporal blocking in all four of the spatial and time dimensions.*

Keywords: LATTICE BOLTZMANN METHOD, PARALLEL ALGORITHMS, LRNLA, CONEFOLD, CFD

1. Introduction

The mathematical modelling of fluids is used for industrial design problems, disaster prevention, exploration for oil and gas, as well as in the medical applications. The CFD problems are computationally heavy, and comprise a large portion of the supercomputer load. To make the large-scale modelling cheaper, accessible to more scientists, and to make extreme scale modelling possible, we develop algorithms that raise the efficiency of the parallel implementation of the numerical schemes higher than the memory bound limit.

Among the CFD schemes the Lattice Boltzmann Method [14] has the advantage of high stencil locality. It is highly parallelizable, and the speedup from using the hybrid computers is achieved by many authors. The method has its range of stability, and there are extensions that allow for more stability in simulation of high Reynolds numbers. However, the extensions of the method may complicate the simulation so that it may be comparable in amount of computation to the Navier-Stokes discretization schemes. We promote the other way to extend the range of possible applications: by making the computer implementation of a simple scheme more efficient, larger meshes may be simulated in reasonable time. This way, the robustness of the method is gained by highly detailed mesh..

Indeed, high performance LBM codes [1,2,6,7,8,12,13] use the most basic variations of the method. In our work we achieved the record breaking performance on multi-core CPU [6,10] and high-end GPU [6,7]. These results were obtained by applying the LRnLA algorithms [4,5] that allow traversal in both space and time to enhance the locality of data access and take advantage of the computer memory hierarchy to gain more calculation performance. The approach of space-time decomposition of the problem has been used in LBM codes by other authors to conceal data copy in parallel simulation [13] and to overcome some of the memory bottlenecks [8]. In CFD LRnLA algorithms are also applied for the RKDG method [3].

In this paper we extend our previous algorithm to make the multi-node simulation possible.

2. Methods

In LBM [14], the simulation domain is split into Nx×Ny×Nz cubic cells. In each cell, the probability distribution function is known for a set of discrete velocities $\vec{c}_{ijk}$. The specific method is denoted by a word like D3Q19, where the first number is the dimensionality of the model and the second number is the number of velocities. Discrete velocities are chosen as vectors that point from the center of the cell to the centers of its neighbors, and a zero velocity. In D3Q27, there is a set of vectors that point to each cell in a 3×3×3 cube. In D3Q19, the longest vectors of D3Q27 are pruned.

For each velocity the update rule for its Distribution Function (DF) is split into two sub-steps: the streaming step $f_{ijk}(\vec{r}_{ijk}, t+\Delta t) \leftarrow f_{ijk}(\vec{r}_{000}, t)$, and the collision step after: $f_{ijk} \leftarrow f_{ijk} - (f_{ijk} - f_{ijk}^{eq})/\tau$; i, j, k = -1, 0, 1 while $i^2+j^2+k^2<3$for D3Q19.

Streaming copies the f_{ijk} from cell with coordinates r_{000} to the cell with the relative position $\vec{r}_{ijk} = \vec{r}_{000} + \vec{c}_{ijk}\Delta t$, $\vec{c}_{ijk} = (i, j, k)$. The collision operates with the DF in the same cell. The expression for the equilibrium DF f_{ijk}^{eq} is taken as the most commonly used second-order polynomial in $\vec{u} = \sum_{ijk} f_{ijk}\vec{c}_{ijk} / \sum_{ijk} f_{ijk}$ [14] to make the performance comparison easier, but any expression that operates on the data inside one LBM cell may be used in the current implementation.

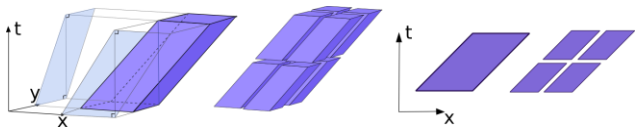

Fig. 1 *ConeFold algorithm in 2D1T and 1D1T*

For the implementation, we start from our previous work documented in [10]. The reader may refer to the texts for information of algorithm construction, data structure, details on the vectorization method. These are summarized below.

2.1 ConeFold

The algorithm operates recursively on a Z-curve array, which is a cube with linear size of $N=2^{MaxRank}$, where MaxRank is an integer number. Between the synchronization steps in time t=0 and t=N the dependency graph is subdivided recursively (Fig. 1) until an elementary update of one cell.

The procedure is implemented with recursive templates in C++. There are special cases for the inside of the domain, left and right boundaries, the decomposition in 1D1T is shown in Fig. 2 [11]. For 2D1T and 3D1T the treatment of all corners is necessary, and the coding similar to a direct product, since the description of ConeFold may be split by coordinates. For example, in 3D1T at x=N, y=N, z=0 the code is XXI.

In 1D1T case, at maximal rank, two ConeFold should be executed: X and I. Each of them will recursively call ConeFolds of smaller rank (Fig. 2). In 3D1T, after XXX, three ConeFolds may be executed in parallel (XXI, XIX, IXX), as well as the next three (IIX, IXI,XII). The last one is III.

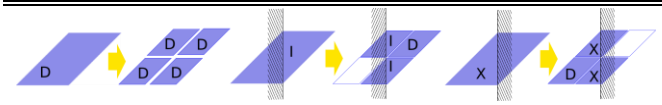

Fig. 2 *ConeFold decomposition and codes near the boundaries in 1D1T*

2.2 Streaming algorithm

The smallest ConeFold is an LRnLA cell. Its base is one data structure cell. Two of the streaming algorithms allow for only one LBM node to be put in this structure: EsoTwist [1] and the special swap algorithm used in our previous work [10]. Here we have implemented EsoTwist for further comparison of the methods. In EsoTwist, in the LRnLA cell the data that is saved is put in place of the data that was read for its execution. This prevents data race condition when parallelism is implemented with stepwise algorithms. In ConeFold, this advantage is not used. However, at smaller scales, this may lead to better data locality.

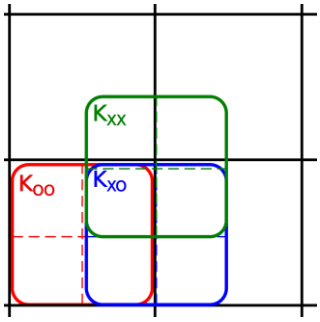

Fig. 3 *Implementation of ConeTur with vectorized ConeFold*

2.3 AVX vectorization

The AVX2/AVX512 vectorization is implemented by putting 8 float/double values into each DF in a cell. At the same time, the size of the domain is doubled in each direction.

To return to 1D1T illustration, let the vector length be equal to 2, not 8. These two values are from cells *ix* and *2N-ix-1* in the domain. It may be visualized as if the *2N* cell domain is 'folded', the ends are 'glued' and we get a 'ring' of cells. First N cells are in the natural order, the next N cells are mirrored. The LBM scheme is also mirrored. The ConeFold is executed on a cube of N cells, which contain the vectors of natural and mirrored data. This way, the calculation inside the domain with scalars for the N size domain and the calculation in the with vectors for the 2N domain are indistinguishable. The mirroring is implemented only by introducing {1,-1} constant vectors into the numerical scheme. At X and I ConeFold, the mirrored and natural domains are linked by the vector shuffle operations. This is generalized to 3D, where the vector length is 8, the domain size is 2N×2N×2N, and some areas are mirrored by several axes.

This kind of implementation of periodic boundary with wavefront blocking is also suggested in [9].

3. Multi-node parallelism

In the current work we explore the ability to make a many-node implementation of the code.

There is a certain issue with multi-node parallelism of the 3D1T ConeFold, especially prominent when the number of nodes is high. Let us consider a simulation domain, made up of Bx×By×Bz cubes. The cubes may be passed to different nodes, and each node would start the ConeFold with MaxRank, treating the cube as a base. The maximal degree of parallelism can be estimated as a number of cubes on the 3D diagonal cross-section of the domain.

On the other hand, other types of space-time traversal algorithms allow more parallelism, such as diamond tiling [15] or ConeTur [4, 5], or earlier version of the LRnLA algorithms. In 2D1T subdivision, which we choose for the demonstration since it can illustrate some complexity of higher dimensions by using 3D shapes, the tiling is obtained with octahedra and two types of tetrahedra. In our work, the ConeFold is favoured since it is simpler for the programmer to write and for the compiler to optimize, and produces a clean and comprehensible code due to the use of the common recursive C++ templates. The number templates types is equal to 3^D, due to the fact that the special treatment is required for the boundary of the domain. If ConeTur is used, in 3D1T there are 2^D types of shapes, and each shape has to be specified in the variants that describe each of the 3^D-1 boundary types.

The use of 'folding' of the domain which has already helped with vectorization and application of the periodic boundaries can be used in this case as well, for the purpose of simplifying the implementation of ConeTur.

In 2D1T illustration (Fig. 3), which is easily generalized to 3D1T, let us take the area of 2×2 cubes K_{OO}, and fold them to make a vectorized cube K_V. If only the first ConeFold XX is executed on K_V, it is equivalent to the execution of the 2D1T pyramid on the K_{OO} base. The data from K_V is returned to the main array. Then 2×2 cubes K_{OX}, are folded into K_V, and ConeFold IX is executed on it. This fills in the tetrahedron between the pyramids in the X direction. The same is performed in the Y axis, and then for K_{XX}. At this point every cell is updated up to the synchronization instant.

Thus, ConeTur is executed by 'refolding' of the ConeFold. The synchronization between nodes, in case the pyramids and the tetrahedra are distributed between different nodes, is performed 2^D times per N time steps.

4. Performance analysis

We have implemented the described algorithm, namely, the 'unfolding' and 'folding' the data cubes. On one node, in the Bx×By×Bz cubes domain, one vectorized cube is formed, processed, and unfolded repeatedly to update all cubes on the node. At the boundary, in case there is a part of domain that is processed by another node, the necessary amount of data is sent by MPI. Otherwise, the one-node domain is treated as periodic.

The important metric for the performance analysis is the slowdown due to the vector copy operations. Thus, we have tested the code with and without the 'refolding' introduction and compared the results on different processors.

The test was performed on one node with N=256, Bx×Bx×Bx = 2×2×2, D3Q19. The performance is compared with the previously published results [10]. Since the results do not differ much, we conclude that the data copy, which is introduced with the new algorithm, does no significant impact on the performance.

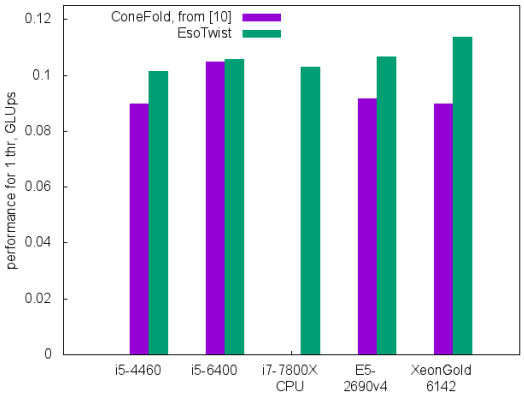

Fig. 4 *Performance comparison against the previous solution*

5. Conclusion

We have introduced the extension of the vectorized ConeFold algorithm for the supercomputer fluid simulation with the Lattice Boltzmann Method. The ConeTur algorithm, that has been difficult to implement in 3D1T before, has been implemented by reshuffling the data structure in the code based on ConeFold. This solution leads to a comprehensible code for fluid simulation, where the space-time decomposition is used for 3 levels of parallelism: vectorization, multi-core and multi-node.

We see that the introduction of the 'refolding' algorithm has not presented significant slowdown. The current results are even higher than the reported ones, which is probably due to small optimization of the code and compiler options.

The introduced algorithm may be applied to other hydrodynamic schemes with cube stencil, and for similar schemes of other numerical methods.

The work is supported by the Russian Science Foundation (project #18-71-10004).

6. Literature

1. Geier, M., Schönherr, M.: Esoteric twist: an efficient in-place streaming algorithmus for the lattice boltzmann method on massively parallel hardware. Computation 5(2), 19 (2017)

2. Godenschwager, C., et al.: A framework for hybrid parallel flow simulations with a trillion cells in complex geometries. In: Proceedings of the International Conference on High Performance Computing, Networking, Storage and Analysis. p. 35. ACM (2013)

3. Korneev B., Levchenko V. Numerical simulation of increasing initial perturbations of a bubble in the bubble–shock interaction problem // Fluid Dynamics Research. – 2016. – V. 48. – No. 6. – P. 061412.

4. Levchenko, V. D. Asynchronous parallel algorithms as a way to archive effectiveness of computations. J. of Inf. Tech. and Comp. Systems 1 (2005): 68.

5. Levchenko V., Perepelkina A. Locally recursive non-locally asynchronous algorithms for stencil computation // Lobachevskii Journal of Mathematics. – 2018. – V. 39. – No. 4. – P. 552-561.

6. Levchenko, V., et al. GPU Implementation of ConeTorre Algorithm for Fluid Dynamics Simulation." International Conference on Parallel Computing Technologies. Springer, Cham, 2019.

7. Levchenko V., et al. LRnLA Lattice Boltzmann Method: A Performance Comparison of Implementations on GPU and CPU. In: Sokolinsky L., Zymbler M. (eds) Parallel Computational Technologies. PCT 2019. Communications in Computer and Information Science, vol 1063. Springer, Cham

8. Nguyen, A., et al.: 3.5-D blocking optimization for stencil computations on modern CPUs and GPUs. In: High Performance Computing, Networking, Storage and Analysis (SC), pp. 1–13. IEEE (2010).

9. Osheim, Nissa, et al. "Smashing: Folding space to tile through time." International Workshop on Languages and Compilers for Parallel Computing. Springer, Berlin, Heidelberg, 2008.

10. Perepelkina, A., Levchenko, V.: LRnLA algorithm ConeFold with non-local vectorization for LBM implementation. Commun. Comput. Inf. Sci. 965, 101–113 (2019)

11. Perepelkina, A.Y., Levchenko, V.D., Goryachev, I.A.: Implementation of the kinetic plasma code with locally recursive non-locally asynchronous algorithms. In: Journal of Physics: Conference Series. vol. 510, p. 012042. IOP Publishing (2014)

12. Riesinger, C., Bakhtiari, A., Schreiber, M., Neumann, P., Bungartz, H.J.: A holistic scalable implementation approach of the lattice Boltzmann method for CPU/GPU heterogeneous clusters. Computation 5(4), 48 (2017)

13. Shimokawabe, T., Endo, T., Onodera, N., Aoki, T.: A stencil framework to realize large-scale computations beyond device memory capacity on GPU supercomputers. In: Cluster Computing (CLUSTER). pp. 525–529. IEEE (2017)

14. Succi, S.: The Lattice Boltzmann Equation: for Fluid Dynamics and Beyond. Oxford University Press, Oxford (2001)

15. Orozco, Daniel, and Guang Gao. Diamond tiling: A tiling framework for time-iterated scientific applications. CAPSL Technical Memo 091, 2009.

МАТЕМАТИЧЕСКАЯ МОДЕЛЬ СИСТЕМЫ АНАЛИТИКИ ПОВЕДЕНИЯ ПОЛЬЗОВАТЕЛЕЙ ДЛЯ ОБЛАЧНЫХ СЕРВИС ПРОВАЙДЕРОВ

MATHEMATICAL MODEL FOR CLOUD PROVIDERS' USER BEHAVIORAL ANALYTICS SYSTEM'S

Проф., д т.н. Адамов А.А., докторант Тынымбаев Б.А.
Механико-математический факультет – Евразийский национальный университет, Казахстан.
Adam1955@mail.ru, tynymbaevba@gmail.com

Abstract: *In this work presented mathematical model of user behavior analytical system for cloud service providers. User behavioral analysis systems include three main components: methods, data and threat detection scenarios. The work describes these components, as well as their application to a potential UEBA class system. The data is taken from the logs of cloud service provider. The novelty of the presented architecture is described in the methods for obtaining the necessary data. Methods for analysis use advanced analytics to study users, data: profiles, interests, public groups, publications, comments, and other parameters from the model of unsupervised learning model, the k-means method, remote functions, random forests, in-depth study, artificial intelligence. Moreover, artificial intelligence has become more commonly used in recent years by many vendors. Threat detection scenarios are a subjective component and are defined by the customer of the system. This work presents scenarios for detecting information security threats.*
KEYWORDS: *USER BEHAVORIAL ANALYTICAL SYSTEM, THREAT, SIEM, VULNERABILITIES, CLOUD, SERVICE, CYBERSECURITY.*

1. Введение. Системы класса UEBA

В данное время становятся всё более популярными услуги облачных сервис-провайдеров. Многие организации предпочитают пользоваться сторонними приложениями, не развивая парк технологий у себя. Сервисы, предоставляемые в облаках, могут быть различные, от услуг документооборота до предоставления финансовых услуг. Соответственно, вопросы обеспечения информационной безопасности могут быть различные по степени критичности, но при этом без ограничения общности можно считать наличие инструментов по обеспечению защищённости облаков обязательным.

Для предоставления качественных сервисов облачному провайдеру необходима постоянно развивающаяся система управления информационной безопасности, позволяющая гарантировать защищенность таких атрибутов информационной безопасности, как конфиденциальность, целостность и доступность. Если ранее, корпоративную сеть можно было обеспечить стандартными инструментами, такими как файервол, антивирусное программное обеспечение, системы класса SIEM, прокси-сервер, то сейчас наступает необходимость применения аналитических инструментов для обеспечения безопасности компаний, и тем более облачных сервисов. Одним из аналитических инструментов является система класса UEBA (user entity and behavioral analytics).

Риски информационной безопасности для облачных сервис-провайдеров – схожи с рисками для корпоративных сетей, и отличаются отдельными видами угроз. В работе [1] представлены примеры сценариев обнаружения угроз для облачных сервис-провайдеров.

ТАБЛИЦА 1. Сценарии обнаружения угроз.

Обнаружение компрометации учётной записи	Решение UEBA определяет ситуации, когда учётные данные были украдены и используются кем-то иным. Выявление использования учётной записи или злоупотребления учётной записи одни из примеров данного сценария.
Обнаружение скомпрометированного конечного устройства	Решение класса UEBA используется для обнаружения сетевых устройств, которые были скомпрометированы, заражены зловредными ПО или демонстрирующие подозрительное поведение.
Обнаружение утечки данных	UEBA также используется для выявления утечки данных. Неавторизованная или целенаправленная утечка данных может случиться даже в действиях авторизованного пользователя. В результате, данный сценарий сфокусирован на определении такого типа активности, которая необходима для выявления скомпрометированных учётных записей и конечных устройств.
Использование злонамеренно внутреннего доступа, включая привилегированные доступы	Инструменты UEBA могут быть использованы для выявления пользователей (и работники и доверенные третьи лица), злоупотребляющих своими привилегиями доступа, которые во многих случаях связаны с злонамеренным событием. Примеры типов активности с превышением привилегий или неавторизованного доступа к данным (к примеру, получение доступа к базе данных с персональной информацией) или в случае злоупотребления системными привилегиями (к примеру, создание новой пользовательской учётной записи или присваивание дополнительных привилегий в разрез политики безопасности).
Предоставление дополнительной информации и контекста для исследования	Технологии UEBA изучают много информации касательно пользователей и сущностей в организации в порядке для определения аномалий, связанных с угрозами. Эта информация используется аналитиками, выполняя сортировку предупреждений и расследованием инцидентов. Если аналитик подозревает, что конечная станция была скомпрометирована, например, он может использовать решение UEBA для получения информации о пользователях данной рабочей станции, их регулярное поведение и даже роль конечной станции в сети.

Разработка отдельных сценариев	Вендоры UEBA часто упоминают сценарии, где их решения используются в виде, отличающемся от оригинального назначения, начиная с обнаружения мошенничества до трекинга наркотиков в организациях здравоохранения. Свойство собирать отдельные данные и создавать типичные модели машинного обучения для тех сценариев достаточно важное.

2. *Пример использования системы UEBA*

Пункт CLD.12.4.5 стандарта ISO/IEC 27017 [2] определяет возможности провайдера, которые позволяют клиенту проводить мониторинг активности в облачной среде. Таким образом предоставляется возможность использования аналитических инструментов. В качестве тестового стенда в облачном сервис-провайдере Qazcloud использовалась система класса UEBA производителя IBM Qradar.

Согласно [3], основу системы UEBA составляют сценарии обнаружения угроз, наиболее критичные и значимые для любой организации. Для определения угроз, были использованы, в первую очередь, стандартные сценарии: обнаружение компрометации учётных записей пользователей, обнаружение скомпрометированного конечного устройства, обнаружение утечки данных, использование несанкционированного внутреннего доступа, включая привилегированные доступы, предоставление дополнительной информации и контекста для исследования. Кроме того, должны использоваться специфичные сценарии угроз, свойственные конкретному облачному провайдеру.

При тестировании используемой системы возникла следующая задача. Для каждого пользователя в настройках составляется порог рейтинга, при превышении которого, фиксируется событие аномального поведения, несвойственное нормальному поведению. Модель, используемая в системе, схожа с работой [4].

Рейтинг пользователя составляется на основе включенных, настроенных правилах детектирования аномального поведения пользователя, которых в системе насчитывается порядка 157. В таблице представлены правила с наибольшим количеством зафиксированных срабатываний.

ТАБЛИЦА 2. Правила детектирования аномального поведения.

Подключение пользователя в нетипичное время суток	После обучающего периода было установлена, что стандартные часы подключения пользователей с 9-00 до 19-00.
Соединение с зловредными веб-сайтами	Логи прокси-сервера, указывающие на попытки соединения с зловредными веб-сайтами
Повышение прав пользователя или группы пользователя	Предоставление записи файлов, вместе чтения.

В тестовой среде для 100 пользователей в рамках обучающего периода был выставлен порог в 20 баллов. Соответственно, согласно настройкам, при превышении указанного порога, система оповещала об инцидентах кибербезопасности для каждого пользователя. При внедрении системы в продуктивную среду для крупного облачного сервис-провайдера рассматриваемая система оказалась неэффективна. Система UBA получила для анализа и обработки порядка 23000 пользователей. Соответственно для указанного порога рейтинга пользователя в 20 баллов за период с 29 июня по 25 сентября 2019 года было сгенерировано 37 733 448 срабатываний правил, и 3265 событий превышения указанного порога. Соответственно, возникают сложности при обработке такого количества инцидентов, при этом для таких пользователей необходимо проводить обучающие курсы, повышать их осведомлённость.

Идея разделить пользователей на отдельные группы по типу поведения – естественна, однако разделить порядка 23000 облачных пользователей становится трудоёмкой задачей.

3. *Постановка задачи*

Основной задачей для любой системы аналитики поведения пользователей, является создание математической модели, способной решать комплекс необходимых задач, при этом генерируя как можно меньше ложных срабатываний.

Предлагается использование модели для анализа поведения пользователей и подсчёта рейтинга пользователей. Для данной модели будет поставлена задача избежать генерации большого количества инцидентов, на которые физически невозможно среагировать. Таким образом представляет интерес получение системы UEBA, которая позволяет гибкую настройку рейтингов пользователей.

Имеющиеся модели машинного обучения в системе – это модели на основе привязки пользователя к локальному ip адресу; соединенных сетевых портов в локальной сети; обнаруженных процессов в операционной системе Windows или Linux; проведённого времени в браузере на нерабочих сайтах; событиях приложения; соединений с рискованными веб-приложениями.

4. *Модель потенциальной системы класса UEBA*

В результате анализа использования системы UBA Qradar и готовых шаблонов моделей предлагается для потенциальной системы класса UEBA использование аналога рейтинга ЭЛО [5] для оценки поведения пользователя облачного сервис-провайдера. Рейтинг ЭЛО, который используется в шахматных соревнованиях. Формула рейтинга для оценки поведения пользователей:
вычисляется математическое ожидание количества баллов рейтинга, которое получит пользователь за день N в сравнении с предыдущим днём N-1 согласно следующей формуле:

$$E_N = \frac{1}{1+10^{\frac{R_N - R_{No}}{400}}},$$

где E_N – математическое ожидание количества баллов, которое наберёт пользователь за день N в сравнении с рейтингом ожидаемого поведения пользователя в данной группе, где R_N – рейтинг пользователя за день N.

Новый рейтинг пользователя считается по формуле

$$R_N = R_{n-1} + K * (S_N - E_N),$$

где K - значение которого равно 10 для опытных пользователей (рейтинг 2400 и выше), 20— для пользователей с рейтингом меньше, чем 2400 и 40 — для новых пользователей (первые 30 дней с момента регистрации). Как и во всех моделях, предполагающих случайную переменную, система оценки Эло уязвима к избирательным парам и непредставительным популяциям, что делает модель неточной. Указанные k-факторы не окончательные, в рамках будущих тестирований модели могут измениться, аналогично [6]

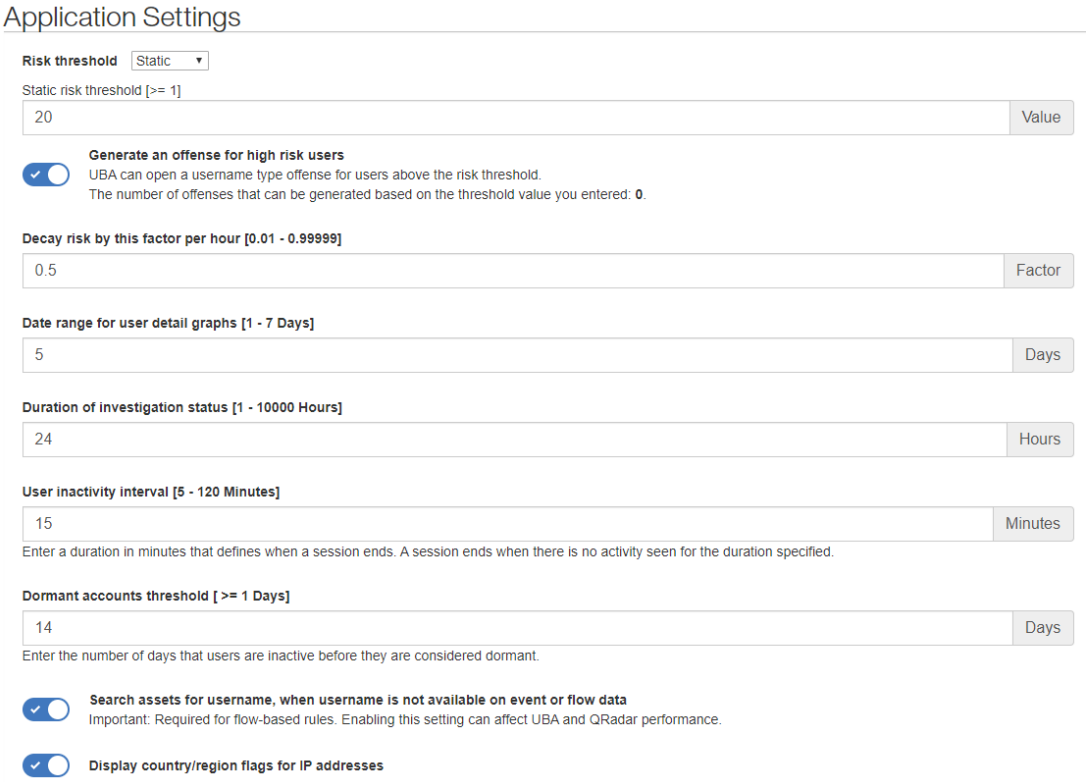

Рис. 1 *Настройки UBA IBM Qradar*

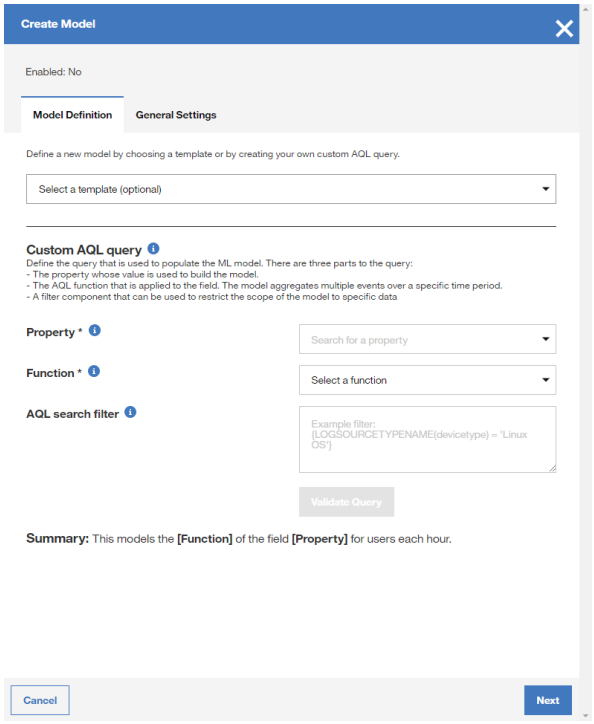

Рис. 2 *Создание собственной модели*

5. *Заключение*

Предложена модель подсчёта рейтинга поведения пользователей, которая может быть применима для большого количества пользователей. Данная модель так же позволяет разделять группы пользователей согласно уровням k-факторам. Разделение пользователей по группам позволяет быстрее реагировать на схожие типы инцидентов, а также проводить обучающие, корректирующие мероприятий по повышению осведомлённости пользователей.

6. *Литература*

1. Котенко И.В., Тынымбаев Б.А. Обзор решений класса UEBA - VIII Международная научно-техническая и научно-методическая конференция. Актуальные проблемы инфо-телекоммуникаций в науке и образовании Российской академии наук (27-28 Февраля, 2019) том 1, стр. 587.

2. ISO/IEC 27017 Extending ISO/IEC 27001 into the Cloud A Whitepaper.

3. Котенко И.В., Тынымбаев Б.А Архитектура перспективной системы UEBA для провайдеров облачных услуг - VIII Международная научно-техническая и научно-методическая конференция. Актуальные проблемы инфо-телекоммуникаций в науке и образовании Российской академии наук (27-28 Февраля, 2019) том 1, стр. 580.

4. Chen Z., Tian L., Lin Ch. Trust evaluation model of cloud user based on behavior data // International Journal of Distributed Sensor Networks, 2018, Vol. 14 (5).

5. Veisdal J. The mathematics of Elo Ratings. - Medium, September 2019,

6. Sonas J. The Sonas Rating formula – better than Elo? - Chess News, October, 2002.

MAPPER ALGORITHM AND IT'S APPLICATIONS

Ass.Prof. Dr. Dimitrievska Ristovska, V., Eng. Sekuloski, P.
Faculty of Computer Science and Engineering, "Ss. Cyril and Methodius" University, Skopje, Macedonia
vesna.dimitrievska.ristovska@finki.ukim.mk, petar.sekuloski@finki.ukim.mk,

Abstract: In this paper we analyze and apply one of the main algorithms of TDA (Topological Data Analysis), Mapper, on some real data sets. We use Mapper for visualization of a data sets, and we tend to get some insights if some key characteristics of the data are captured by the visualization and how they are connected with human perception of the data. Also, we will discuss if the visualization can make progress in further work.

Keywords: MAPPER ALGORITHM, TOPOLOGICAL DATA ANALYSIS, ALGEBRAIC TOPOLOGY, DATA SCIENCE, COMPUTATIONAL TOPOLOGY

1. Introduction

Topological data analysis (**TDA**), is an approach for analyzing data using techniques from topology. Extraction of an information from the datasets which are high-dimensional, incomplete or noisy, is a wide field for researchers and scientists in last few years. TDA provides a general framework to analyze such data in a manner that is insensitive to a particular metric. Beyond this, it inherits functors , a fundamental concept of modern mathematics, which allows it to adapt to new mathematical tools.

Mapper algorithm was developed by Singh, M´emoli, and Carlsson in [1], and it gives a multi-resolution, low dimensional picture of point cloud. It's highly customizable, and has a track record of revealing structure that some other methods, like clustering and "projection pursuit" methods miss.

Mapper algorithm is one of the most important tools used in TDA for data visualization. For **input**, it use:

-point cloud;

- "filter function;"

-covering of a metric space;

-clustering algorithm;

- various other parameters.

Output is a Graph (or higher simplicial complex) which is tend to capture the main topological aspects of the point cloud.

2. Mathematical preliminaries

We will introduce some mathematical concepts, in order to construct a topological space from given dataset.

Let $n \geq 1$ be an integer, let $[n] = \{0, \ldots, n\}$.

An **n-simplex** σ is the convex hull of $n + 1$ affinely independent vertices $S = \{v^i\}, i \in [n]$ in R^d where $d \geq n$.

A simplex τ defined by $T \subseteq S$ is called a face.

A simplicial complex K is a finite set of simplices which meet along faces, every one of which is in K.

Let e^0 denote the origin in R^n and e^i the i-th standard basis vector for R^n.

The **standard n-simplex** $\Delta^n \subset R^n$ is the convex hull of $\{e^i\} i \in [n]$. Given any subset $J \subseteq [n]$, let Δ^J be the face of Δ^n spanned by $\{e^j\} j \in J$. The points of S are vertices of the simplex.

As basic examples, the low dimensional simplices (plural:simplices or simplexes) have special names:

- a 0-simplex is called a *vertex;*
- a 1-simplex is called *edge;*
- a 2-simplex is called *triangle*
- a 3-simplex is called *tetrahedron*,
- a 4-simplex is called a *5-cell*.

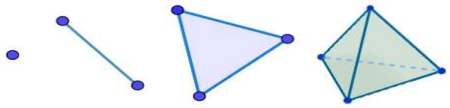

Figure 1. 0-simplex 1-simplex, 2-simplex, 3-simplex

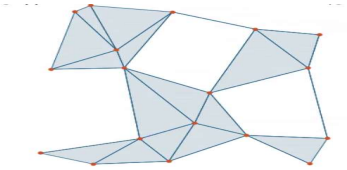

Figure 2. Example of simplicial complex

Topological invariants of the space, such as: holes and number of connected components, can be computed from a simplicial complex, see Figure 2. One of the basic idea of Topological Data Analysis is to construct a simplicial complex from a dataset, i.e. in one hand, simplicial complexes are high dimensional analogues of graphs, and in other hand simplicial complexes are approximation of the topological space.

3.Mapper algorithm

The algorithm works very simple: put bin data into overlapping bins, cluster each bin, create a graph where vertices = clusters and two clusters are connected by an edge if they have points in common.

Mapper algorithm (implementation)

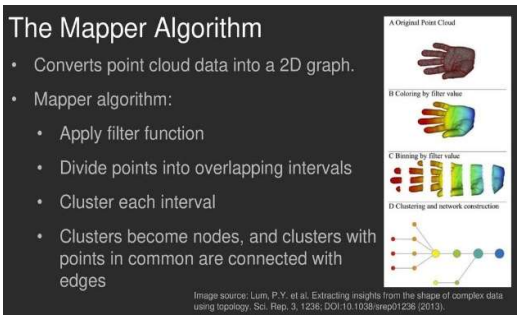

Figure 3 Mapper algorithm – steps

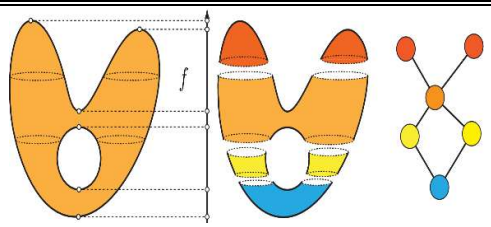

Figure 4. How works the Mapper algorithm – an illustration

Next, it is given a more precise description of the algorithm.

Given: X point cloud, |X| = N,

filter function f : X → R.

Assume we can always compute inter point distances.

Let I denote the "range" of f: explicitly I = [m, M] ⊂ R where m = $\min_{x\in X}$ {f (x)}, M = $\max_{x\in X}$ {f (x) }

Divide I into a set S of smaller intervals (of uniform length) which overlap. Obtain two resolution controlling parameters: *l* the length of the intervals, and *p* the percentage overlap between successive intervals.

- For each interval $I_j \in S$, let $X_j := \{x : f(x) \in I_j\}$. Then the collection of all such X_j is a covering of X.
- (2) For each X_j , perform a clustering algorithm to obtain clusters $\{X_{jk}\}$.
- Each cluster defines a vertex of our simplicial complex: draw an edge between vertices whenever $X_{jk} \cap X_{lm} \neq \emptyset$.

4. Application of the Mapper algorithm on the Tori (two rings) dataset

In this section, we choose 3D object form of two rings (tori), see Figure 5. It's synthetic dataset, consisted of 2048 points. We apply Mapper algorithm on that dataset.

In these experiments, made in mathematical software *R*, we use different values of the parameters:

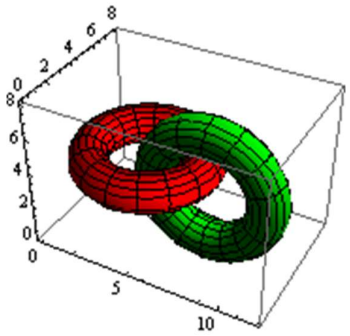

Figure 5. Tori

- *n*=number of intervals, varying between 6 and 16,
- *p*=percent of overlapping, between 20 and 80,
- *b*=number of overlapping bins when clustering, between 5 and 15.

The results from Mapper algorithm for Dvatorusi datset are given in Figure 6, Figure 7, Figure 8 and Figure 9. Every figure corresponds to a Mapper algorithm results for different parametars.

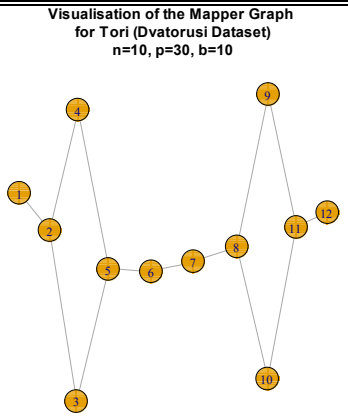

Figure 6. Mapper algorithm on Tori- 2 obtained cycles

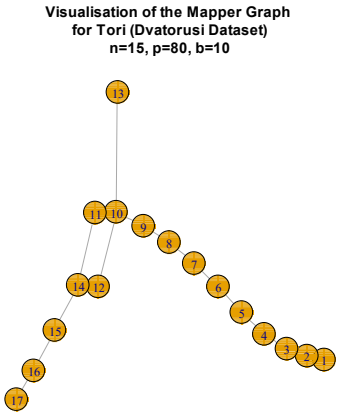

Figure 7. Mapper algorithm on Tori - 1 obtained cycle

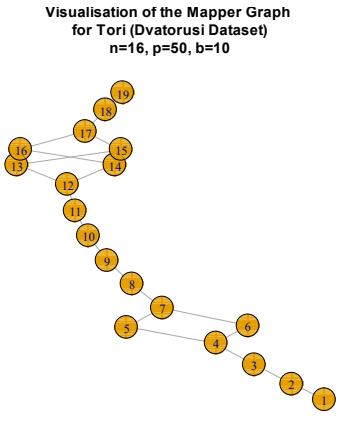

Figure 8. Mapper algorithm on Tori - 3 obtained cycles

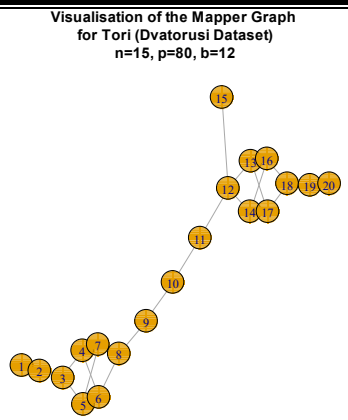

Figure 9. Mapper algorithm on Tori - 4 obtained cycles

We can conclude that there are different graphs obtained for different values of parameters. There is no one way of choosing parameters of Mapper algorithm. It depends on the subject of the research.

5. Application of the Mapper algorithm on the Torus dataset

In this section, we choose Torus- 3D object see Figure 10 and apply Mapper algorithm over the database.

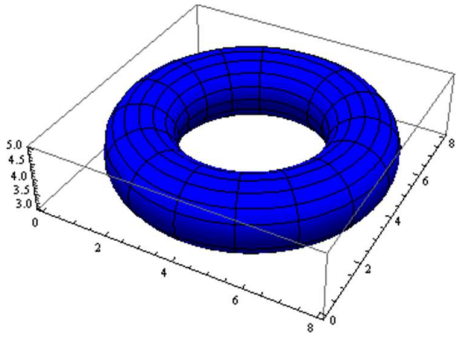

Figure 10. Torus

In these experiments, it is interesting that Mapper graphs with one dimensional filter, for all values of the different parameters, are of the same form, showed in Figure 11.

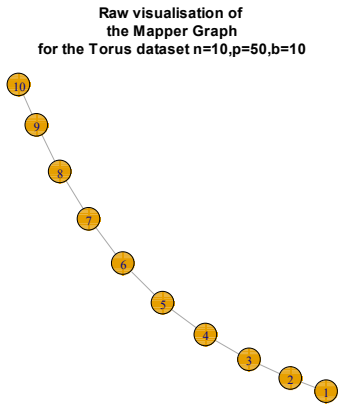

Figure 11. Mapper algorithm on Torus dataset

But, if the filter is bi-dimensional [11], the obtained Mapper graph is of the form, showed in Figure 12.

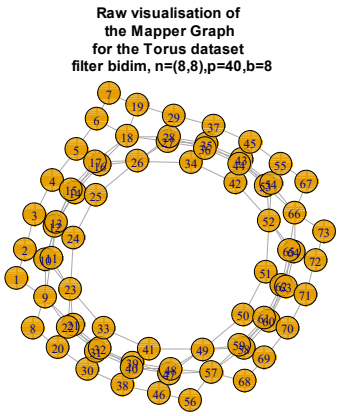

Figure 12. Mapper algorithm on Torus- bi-dimensional, filter

6. Application of the Mapper algorithm on the Diabetes dataset

In the following case, we apply Mapper algorithm on the Diabetes dataset, consists of 145 lines, with 6 attributes in each line- Miller-Reaven dataset. Reaven and Miller (1979) examined the relationship among blood chemistry measures of glucose tolerance and insulin in 145 non-obese adults [10]. They visualized the data in 3D, and discovered a peculiar pattern that looked like a large blob with two wings in different directions. In this dataset, the data is split up in three categories. Data from non-diabetic patients, data from patients with diabetes classified as overt and data from patients with diabetes classified as chemical diabetes. Overt diabetes is the most advanced stage, characterized by elevated fasting blood glucose concentration and classical symptoms. Preceding overt diabetes is the latent or chemical diabetic stage, with no symptoms of diabetes but demonstrable abnormality of oral or intravenous glucose tolerance.

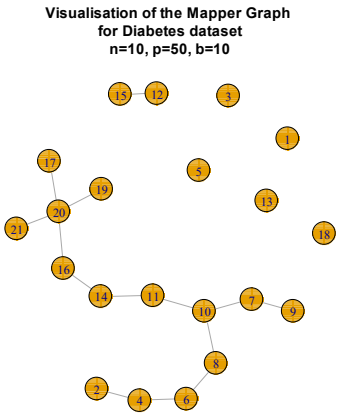

Figure 13. Mapper algorithm on Diabetes dataset (n=10)

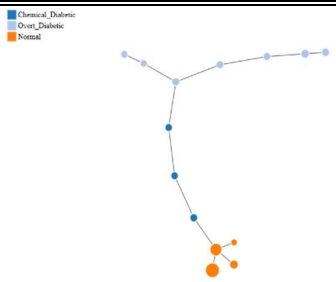

Figure 14. Colored Mapper Graph over Diabetes dataset (from Fig.13)

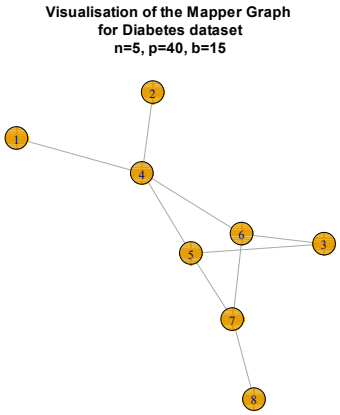

Figure 15. Mapper Graph on Diabetes data set (n=5)

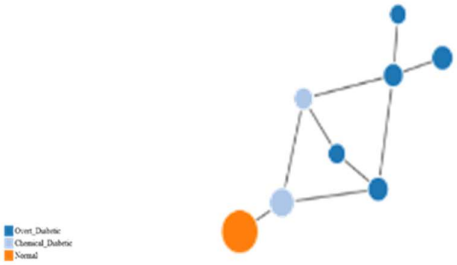

Figure 16. Colored Mapper Graph on Diabetes dataset (from Fig.15)

The peculiar pattern visualized in [10], can be seen on Figure 14 and Figure 16. The two types of diabetes are distinguished on the obtained graphs.

7. Discusion

Mapper algorithm is useful tool for visualization of datasets. There are many open problems in the process of choosing parameters, as it can be seen on the visualizations in this work. It is open research area. In the future, we like to optimize that process. Also, we plan to apply Mapper algorithm on bio-medical data and used it for categorize or group observations of some diseases.

8. Acknowledgement

This work was partially supported by the Faculty of Computer Science and Engineering at the "Ss. Cyril and Methodius University", Skopje.

Literature

[1] Gurjeet Singh, Facundo Mémoli and Gunnar Carlsson, "Topological Methods for the Analysis of High Dimensional Data Sets and 3D Object Recognition", Eurographics Symposium on Point-Based Graphics, 2007

[2] Andrew W. Herring, "The Mapper Algorithm", Western TDA Learning Seminar, Department of Mathematics, Western University, 2018

[3] Gunnar Carlsson, "Topology and data". Bulletin of the American Mathematical Society, 46 (2), 2009, pp. 255–308.

[4] J. R. Munkres, Topology. vol. 2. Upper Saddle River: Prentice Hall, 2000

[5] llen Hatcher, Algebraic topology. Cambridge University Press, 2002

[6] http://archive.ics.uci.edu/ml/datasets/statlog+(heart)

[7] Brittany Terese Fasy, Jisu Kim, Fabrizio Lecci, and Clément Maria. "Introduction to the R package tda. ", arXiv preprint arXiv:1411.1830, 2014.

[8] https://s3.amazonaws.com/cdn.ayasdi.com/wp-content/uploads/2018/11/12131418/TDA-Based-Approaches-to-Deep-Learning.pdf

[9] https://en.wikipedia.org/wiki/Topological_data_analysis

[10] Reaven, G. M. and Miller, R. G. (1979). An attempt to define the nature of chemical diabetes using a multidimensional analysis. Diabetologia, 16, 17-24.

[11] http://bertrand.michel.perso.math.cnrs.fr/Enseignements/TDA/_Mapper.html

[12] Mariam Pirashvili, Lee Steinberg, Francisco Belchi Guillamon, Mahesan Niranjan, Jeremy G. Frey, Jacek Brodzki, "Improved understanding of aqueous solubility modeling through topological data analysis", Journal of Cheminformatics, 2018

EFFECT OF THERMAL PROPERTIES OF BOUNDARIES ON STABILITY OF STEADY-STATE FLOW A LIQUID WITH HEAVY IMPURITY

Prof., Dr. Dementev O.
Chelyabinsk State University, Chelyabinsk, Russia
e-mail: dement@csu.ru

Abstract: *The results of a solution of the problem of the stability of steady convective flow in a vertical layer with thermally insulated boundaries and a comparison with the opposite limiting case of ideally thermally conducting boundaries are presented. Study is made of the effect of thermal properties of boundaries on the convective flow stability in a closed vertical layer. The numerical solution of a spectral amplitude problem for normal disturbance is presented for thermally insulated boundaries. The critical Grashof numbers are determined. A comparison with the case of ideal conducting walls shows that there is a slight effect of thermal properties on the instability criterion.*
***KEYWORDS*:** STEADY-STATE CONVECTIVE FLOW, THERMAL PROPERTIES OF BOUNDARIES, STABILITY, LIQUID, IMPURITY.

1. The results of studies of the stability of closed steady convective flow liquid with heavy impurity between vertical planes [1,4] a show that depending on the value of the Prandtl number *Pr* the instability is caused by mechanisms which differ in their physical nature. At low and moderate Prandtl number hydrodynamic disturbance leading to the formation of steady vortices at the interface of the opposing flows are responsible for the instability. At larger Prandtl number (*Pr > 12*) the instability has a wave nature and is connected with an increase in the convective fluxes of temperature waves.

The numerical results presented in [1,4,6] were obtained on the assumption that temperature disturbances vanish at the boundaries of the layer. Such boundary conditions correspond to the limiting case when the thermal conductivity of the boundaries is much greater than the thermal conductivity of the liquid and the solid masses bordering on it are comparable then temperature disturbances penetrate into the solid masses. Then the question arises of whether the relative thermal conductivity of the boundaries affects the stability of the convective flow the conjugate problem of stability of convective flow. It is clear in advance that the hydrodynamic mechanism of the instability must be little sensitive to the thermal properties of the solid masses. As for a wave instability, since it is connected with growing temperature waves it cloud be expected, generally speaking, that the properties of the solid masses have a considerable effect on the critical parameters of this instability. The results presented below, however, that the penetration of temperature disturbances into the surrounding solid masses has a weak effect on the conditions of formation of instabilities of both the hydrodynamic and the wave types.

To clarify the role of the penetration of thermal disturbances on the stability it is obviously sufficient to consider the limiting case opposite to that which one usually has in mind, namely when the thermal conductivity of the liquid is far larger than the thermal conductivity of the boundaries. In this limiting case the boundary condition of thermal insulation must be set up for temperature disturbances.

In the following, a study is made of the effect on convective flow all factors characterizing the added particles: the rate of particle settling u_s, the velocity and temperature relaxation times for the particles (or, which comes to the same thing, their size, density, and heat capacity), and the mass concentration *a* of the additive.

1. We consider a viscous incompressible fluid containing a cloud of spherical nondeformable solid particles of identical radius *r* and mass *m*. As in [2-6], we assume the liquid and impurity to be continuous media, interpenetrating and interacting with each other, and neglect interaction between the particles. The volume fraction of particles is assumed to be so low that the Einstein correction to liquid viscosity can be neglected. The density of the particle material ρ_1 is much greater than the density of the carrier medium ρ.

The displacement force acting on the particles is negligibly small, since it is proportional to the ratio $\rho/\rho_1 << 1$. Interaction between the phases as they undergo relative motion follows the Stokes law. The equations describing the behaviour of an incompressible fluid with an impurity of heavy solid particles have the form [2, 3]. Based on those equations, equations were obtained [2] in the Boussinesq approximation for the free convection of an incompressible medium with a heavy additive:

$$\frac{\partial \vec{u}}{\partial t} + (\vec{u}\nabla)\vec{u} = -\frac{\nabla p}{\rho} + \nu\Delta\vec{u} - \frac{a}{\tau_v}(\vec{u}_p - \vec{u}) + (1+a)\vec{g}\beta T, \qquad (1)$$

$$\frac{\partial \vec{u}_p}{\partial t} + ((\vec{u}_p + \vec{u}_s)\nabla)\vec{u}_p = \frac{1}{\tau_v}(\vec{u}_p - \vec{u}),$$

$$\frac{\partial T}{\partial t} + (\vec{u}\nabla)T = \chi\Delta T + \frac{ab}{\tau_t}(T_p - T),$$

$$\frac{\partial T_p}{\partial t} + ((\vec{u}_p + \vec{u}_s)\nabla)T_p = -\frac{1}{\tau_v}(T_p - T),$$

$$div\,\vec{u} = 0, \quad \frac{\partial \rho_p}{\partial t} + div\left(\rho_p(\vec{u}_p + \vec{u}_s)\right) = 0,$$

$$\rho_p = mN,\ \tau_v = \frac{m}{6\pi r\rho\nu},\ \tau_t = \frac{mb}{4\pi r\rho\chi},\ a = \frac{\rho_p}{\rho},$$

where $\vec{u}$ is the liquid velocity; *T* is temperature; *p* is pressure of the fluid measured with respect to the hydrostatic pressure renormalized because of the settling particles; *c* is the heat capacity of the fluid at constant pressure; β, ν and χ are the coefficient of volume expansion of the fluid, its kinematic viscosity, and thermal diffusivity; quantities with the subscript "*p*" refer to the particle cloud, where $\vec{u}_p$ is the velocity acquired by the particles as a result of their interaction with the moving fluid measured with respect to the rate of particle settling $\vec{u}_s$; c_1 is the heat capacity of the particle material; *N*, number of particles per unit volume; and $\vec{g}$, acceleration of gravity. The quantities τ_t and τ_v have the dimensionality of time and are, respectively, the time required for the temperature difference between fluid and particles to decrease by factor *e* and the time required for the velocity of the particles relative to the fluid to decrease by factor of *e* in comparison with its original value.

We consider convective motion of a fluid containing an additive in a plane layer between infinite parallel vertical surfaces, which are constant temperatures – Θ and Θ, respectively. The particles, the concentration of which is nonuniform, move through the fluid. We obtain a steady-state solution of the equation, describing plane-parallel convective motion and we used boundary conditions $u_0(\pm h) = 0$, $T_0(-h)=\Theta$, $T_0(h) = -\Theta$ and the closure condition for convective flow. We obtain the distribution of velocities and temperatures of the fluid and particle cloud over a section layer.

In the closed vertical layer between the plane $x = +h$ plane-parallel convective flow is established with a linear temperature profile and a cubic velocity profile:

$$T_0 = -x;\ u_0 = \frac{Gr}{6}(x^3 - x), N_0 = const,$$
$$P = \frac{\nu}{\chi},\ Gr = (1+a)\frac{g\beta\Theta h^3}{\nu^2}. \quad (2)$$

Here is u_0 and u_{p0} are the vertical velocity components and the subscript 0 indicates the steady-state solution of Eq. (1), Ga, GR, Pr are the Galileo, Grashof and Prandtl numbers; τ_v and τ_t are now dimensionless relaxation times; γ is a unit vector directed vertically upward.

The boundary conditions and closed flow condition are expressed by

$$u(\pm 1) = 0,\quad \int_{-h}^{h} u_0 dx = 0. \quad (3)$$

As is clear from Eqs. (2), presence of added particles leads to renormalization of the velocity profile of the liquid in comparison with the case of a fluid without an additive.

We investigate the stability of the steady-state motion of a medium containing a heavy additive as defined by Eqs. (1). To do this, we consider the perturbed fields of velocity, temperature, pressure and number of particles per unit volume $u_0 + u$, $T_0 + T$, $U_{p0} + u_p$, $T_{p0} + T_p$, $p_0 + p$, and $N_0 + N$, where u, u_p, T, T_p, p, and N are small perturbations. We write the equations for the perturbations in dimension form, using the following units of measurement: distance h, time h^2/ν, velocity ν/h, pressure $\rho\nu^2/h^2$, and temperature Θ. Linearizing over the perturbations, we obtain from Eqs. (1)

As in the case of a pure fluid [4], one can show for a medium containing an additive that the problem of stability with respect to spatial perturbations reduced to the corresponding problem for plane perturbations. Plane perturbations are more dangerous in case of vertical orientation of the layer, i.e., lower Grashof numbers are associated with them. Consequently, it is sufficient to confine the investigation to plane perturbations in a study of stability.

We consider plane normal perturbations

$$u_x = -\partial\psi/\partial z,\quad u_z = \partial\psi/\partial\psi, \quad (4)$$
$$\psi(x, y, z) = \phi(x)e^{ik(z-ct)},\ T(x, y, z) = \theta(x)e^{ik(z-ct)}$$
$$u_{px}(x, y, z) = v_{px}(x)e^{ik(z-ct)},\ u_{pz}(x, y, z) = v_{pz}(x)e^{ik(z-ct)}$$

where ψ is a stream function; ϕ, θ, v_{px} and v_{pz} are the amplitudes of the perturbations; k is a real wave number; $c = c_r + ic_i$ is the complex phase velocity of the perturbations (c_r is the phase velocity, c_i the decrement).

Substituting Eqs. (4) into Eqs. (1), we obtain a system of amplitude equations (primes denote differentiation with respect to x)

$$\left(\varphi^{IV} - 2k^2\varphi'' + k^4\varphi\right) + ik\left(\varphi'' - k^2\varphi\right)(u_1 - c) + iku_1''\varphi - Gr\vartheta' = 0,$$
$$\frac{1}{P}(\theta'' - k^2\theta) + ik\vartheta(u_2 - c) -$$
$$- ikT_0'\varphi\left\{1 + ab/[(1+ik\tau_v(u_0 - c))(1+ik\tau_t(u_0 - c))]\right\} = 0;$$

$$u_1 = u_0 + \frac{a(u_0 - c)}{(1+ik\tau_v(u_0 - c))},\ u_2 = u_0 + \frac{a(u_0 - c)}{(1+ik\tau_t(u_0 - c))}. \quad (5)$$

Boundary conditions are

$$x = \pm 1:\ \varphi = \varphi' = \Theta' = 0. \quad (6)$$

The boundary-value problem (5), (6) determines the spectrum of characteristic perturbations and their decrements. The complex phase velocity c depends on seven independent parameters of the problem: the Grashof, Prandtl, and Galileo numbers; the wavenumber k; the mass concentration a of the additive; and the relaxation times τ_v and τ_t. The limit of stability for a steady-state flow is determined from the condition $c_i = 0$.

The boundary problem (5), (6) determines the spectrum of the characteristic disturbances an d their decrements c_i. The solution of the problem was found numerically by the Runge-Kutta-Merson method with orthogonalization of the vector solutions by the Gram-Schmidt method at each step of integration; the orthogonalization was performed with respect to the maximum vector solution in absolute value (in the given step).

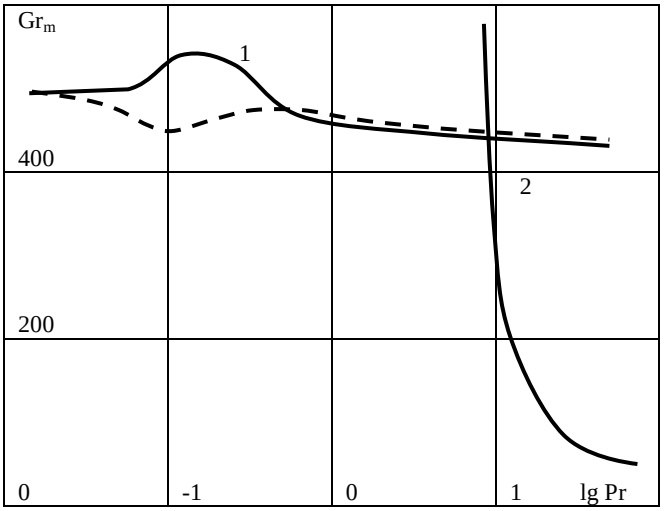

Fig. 1

The principal result of the calculations is presented in Fig. 1, where dependence of the minimum (with respect to k) critical Grashof number Gr_m on the Prandtl number Pr is shown for the hydrodynamic (1) and wave (2) branches of instability. The corresponding limits of stability for ideally conducting boundaries are shown here by a dashed line for comparison. As is seen, in both branches of instability dependences $Gr_m(Pr)$ for the two types of boundary conditions are similar. By comparison with the case of ideally conducting boundaries there is some decrease in the limiting Prandtl number Pr_* beginning with which the wave branch of instability appears (extrapolation gives a value of $Pr_* \approx 0.96$ instead of 11.4 for the case for ideally thermally conducting boundaries). In the limit of $Pr >> Pr_*$, as an asymptotic analysis shows, the some limiting law $Gr_m = 590(Pr)^{1/2}$ occurs in both cases of boundary conditions. The critical values of the wave number k_m are also similar for the two variants of the boundary conditions discussed.

Thus, the calculation shows that the thermal properties of the boundaries have a weak effect on the stability of convective flow in a vertical layer. In this sense one must emphasize the difference from the problem of the stability of equilibrium of a horizontal layer of liquid heated from below, where, as is known, there is a very strong dependence of the limit of stability and the form of the disturbances on thermal properties of the boundary solid masses.

REFERENCES

1. Gershuni, G.Z., Dement'ev O.N., Zhukhovitskii E.M. "Effect of thermal properties of boundaries on stability of convective flow in a vertical layer". Inzhenerno-Fizicheskii Zhurnal, 1976; Vol. 32, No. 6. 1062-1064.
2. Marble F. E. "Dynamics of dusty gases," *Mekhanik,*. 1970; No. 6, 397-404.
3. Sow S. "Hydrodynamics of Multiphase Systems "[Russian translation], Mir, Moscow, 1971. P. 576.
4. Gershuni, G.Z., Zhukhovitskii E.M., Nepomnjashchy A.A. "Stability of convective flows". Moscow, Nauka. 1989, P. 320.
5. Dement'ev, O. "Convective stability of a medium containing a heavy solid addutive". Zhurnal Prikladnoi Mekhaniki I Tekhnicheskoi Fiziki, No. 3. 1976, P. 105-115.
6. Gershuni G. Z., Zhukhovitskii E. M. "Convective Stability of Incompressible Fluids", Halsted Press, 1976. P. 392.
7. Abramowitz, M., Stegun, I.A. Handbook of mathematical function, National Bureau of Standards Appl. Math. ser., Moscow, Nauka, 1964, P. 830.

MATHEMATICAL AND NUMERICAL SIMULATION OF STRESSES AND DISPLACEMENTS LOCALIZATION PROBLEMS

PhD. Zirakashvili Natela
I. Vekua Institute of Applied Mathematics of Iv. Javakhishvili Tbilisi State University, Georgia

natzira@yahoo.com

Abstract: *Mathematical and numerical simulation of the non-classical problems, namely problems of localization of stresses and displacements in the elastic body, are obtained by the boundary element method. The current work examines two localization problems, which have the following physical sense: on the middle point of the segment lying inside a body parallel to the border half plane in first case a point force is applied, and we must find such value of the normal stress along the section of the border half plane, which will cause this point force, while in the second case, there is given a vertical narrow deep trench outgoing of this point, and we must find such value of the normal stress along the section of the border half plane, which will result in such a pit. By using MATLAB software, the numerical results are obtained and corresponding graphs are constructed.*

Keywords: NON-CLASSICAL PROBLEM, BOUNDARY ELEMENT METHOD, LOCALIZATION PROBLEM, HOMOGENEOUS ISOTROPIC HALF PLANE

1. Introduction

In the present work, mathematical and numerical simulation of the problems of localization of stresses and displacements in a body, are gained by the boundary element method (BEM) [1]. In a certain sense, the problem of localization of stresses in the elastic body is the inverse problem to the delocalization problem [2]. The localization problem is defined as follows: to change a sufficiently uniform stressed-deformed state of a body for a sharply expressed non-uniform stressed-deformed state (in conditions of constant external perturbations) by changing and appropriate selection of parameters of the medium.

In the theory of elasticity, there are a number of problems [3]-[10] that could be called non-classical due to the fact that boundary conditions on a part of the boundary surface or on the entire boundary surface are either over-determined or underdetermined, or the conditions on the boundary are connected with the conditions inside the body (so called non-local problems).

The current article sets and solves non-classical two-dimensional elasticity problems by using BEM, and problems of localization of stress and displacement for a homogeneous isotropic elastic half-plane are formulated based on them. The present paper examines two localization problems, which have the following physical meaning: on the middle point of the segment lying inside a body parallel to the border half plane in first case a point force is applied, and we must find such value of the normal stress along the section of the border half plane, which will cause this point force (stresses localization), while in the second case, there is given a vertical narrow deep trench outgoing of this point, and we must find such value of the normal stress along the section of the border half plane, which will result in such a pit (displacements localization).

Finally, there are test examples given showing the value of normal stress supposed to apply to the section of the half-plane boundary to obtain the pre-given localized stress or displacement at the midpoint of the segment inside the body. The numerical results of these problems are obtained and presented appropriate graphs, and mechanical and physical interpretations of the problems.

2. Formulation of problems

Let us set some non-classical static problems for homogeneous isotropic half plane (see. Fig.1).

It is known that a homogeneous system of elastic static equilibrium in displacements in the Cartesian system of coordinates has the form [16]

$$\begin{cases}(\lambda+\mu)\theta_{,x}+\mu\Delta u=0\\(\lambda+\mu)\theta_{,y}+\mu\Delta \mathrm{v}=0\end{cases}\quad \text{in } D \tag{1}$$

where $\lambda=\dfrac{\nu E}{(1-2\nu)(1+\nu)}$, $\mu=\dfrac{E}{2(1+\nu)}$ are Lamé constants, E is elasticity modulus, and ν Poissons's ratio; $\Delta(\cdot)=(\cdot)_{,xx}+(\cdot)_{,yy}$ is a Laplacian, $\theta=\operatorname{div}\vec{U}=u_{,x}+\mathrm{v}_{,y}$; $\vec{U}=(u,\mathrm{v})$ is the displacement vector; $(\cdot)_{,x}=\dfrac{\partial(\cdot)}{\partial x}$, $(\cdot)_{,y}=\dfrac{\partial(\cdot)}{\partial y}$; $(\cdot)_{,xx}=\dfrac{\partial^2(\cdot)}{\partial x^2}$; $(\cdot)_{,yy}=\dfrac{\partial^2(\cdot)}{\partial y^2}$.

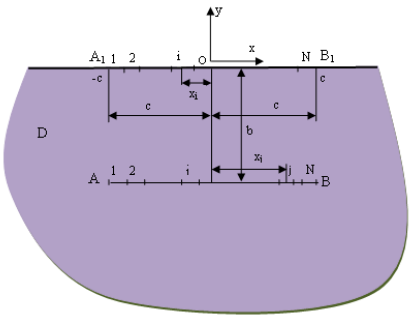

Fig. 1 *Illustration of localization problems of stresses and displacements for elastic half plane.*

2.1. Statement and solving of problem when normal stress is applied to segment inside half plane

(a) Setting. Let us consider a non-classical problem for half plane D (see Fig. 1), when the tangent stress along the entire border and normal stress along boundary segment $|x|>c,\ y=0$ equal to zero. Along segment $|x|\le c,\ y=-b$ inside the body, the value of normal stress σ_{yy} is known. So, let us find the solutions to the system of equilibrium equations (1) satisfying the following boundary conditions:

$$\begin{aligned}&\text{for } |x|<\infty \text{ and } y=0: \quad \sigma_{yx}=0,\\&\text{for } |x|>c \text{ and } y=0: \quad \sigma_{yy}=0,\\&\text{for } |x|\le c \text{ and } y=-b: \quad \sigma_{yy}=-P_0(x),\end{aligned}$$

where $P_0(x)$ is the sufficiently smooth function given along segment $[-c;c]$.

We can formulate the set problem as follows: let us find the kind of distribution of normal stress σ_{yy} along section $|x|\le c,\ y=0$ of the boundary of a half plane (see Fig. 1) so that the normal stress along segment $|x|\le c,\ y=-b$ inside the body equals to the values of given function $P_0(x)$.

If we consider function of kind $P_0(x)=P\cdot 10^{-|4x|}$ $(P=\text{constant})$, which describes a force similar to the concentrated

one, then we will have the following localization problem: we must find the kind of distribution of normal stress σ_{yy} along segment A_1B_1 to obtain the concentrated force of the given value (localization of stresses) along section AB (see Fig. 1).

(b) Solution. Let us divide segments $|x| \le c,\ y = 0$ and $|x| \le c,\ y = b$ into N segments (elements) of the same size $2a$ and smaller sizes (i.e. $a = c/N$). We mean that constant normal stresses P_y^j act on each j^{th} element of length $2a$ with center $(x^j; 0)$ of segment $|x| \le c,\ y = 0$. We need to find such values of these stresses, for which the values of the normal stresses in middle points $(x^i, -b)$ of each i^{th} segment with a length of $2a$ along segment $|x| \le c,\ y = -b$ inside body will equal to the given value of $-P_0(x^i)$.

Normal stress in the centre of the i^{th} element lying on segment $|x| \le c,\ y = -b$ will equal to following sum:

$$\sigma_{yy}(x^i, -b) = \sum_{j=1}^{N} A^{ij} P_y^j, \qquad i = 1, 2, \ldots, N,$$

where for the influence coefficients A^{ij} has the following formula

$$A^{ij} = -\frac{1}{\pi}\left[\left(\arctan\frac{b}{x^i - x^j - a} - \arctan\frac{b}{x^i - x^j + a}\right) + \frac{b\left(x^i - x^j + a\right)}{(x^i - x^j + a)^2 + b^2} - \frac{b\left(x^i - x^j - a\right)}{(x^i - x^j - a)^2 + b^2}\right].$$

Thus, we obtain the following system of N linear algebraic equations with N unknown quantities P_y^j, $j = 1, 2, \ldots, N$.

$$\sum_{j=1}^{N} A^{ij} P_y^j = P_0\left(x^i\right), \qquad i = 1, 2, \ldots, N. \tag{2}$$

If solving (2) system in relation to unknown quantities P_y^j by means of any standard method of numerical analysis (by method of Gauss in our case), then we can assume that the set problem is solved and $\sigma_{yy}^j = P_y^j, \quad j = 1, \ldots, N$.

After solving these equations, we can express the displacements and stresses at any point $\left(x^i, y^k\right)$ of the body by means of other linear combination of load P_y^j. For example, the stresses and displacements have the following form:

$$\begin{aligned}
\sigma_{xx}(x^i, y^k) &= \frac{1}{\pi}\sum_{j=1}^{N}\left[\left(\arctan\frac{y^k}{x^i - x^j + a^j} - \arctan\frac{y^k}{x^i - x^j - a^j}\right) - \frac{y^k\left(x^i - x^j + a^j\right)}{(x^i - x^j + a^j)^2 + \left(y^k\right)^2} + \frac{y^k\left(x^i - x^j - a^j\right)}{(x^i - x^j - a^j)^2 + \left(y^k\right)^2}\right] P_y^j, \\
\sigma_{yy}(x^i, y^k) &= \frac{1}{\pi}\sum_{j=1}^{N}\left[\left(\arctan\frac{y^k}{x^i - x^j - a^j} - \arctan\frac{y^k}{x^i - x^j + a^j}\right) - \frac{y^k\left(x^i - x^j + a^j\right)}{(x^i - x^j + a^j)^2 + \left(y^k\right)^2} + \frac{y^k\left(x^i - x^j - a^j\right)}{(x^i - x^j - a^j)^2 + \left(y^k\right)^2}\right] P_y^j, \\
\sigma_{xy}(x^i, y^k) &= \frac{1}{\pi}\sum_{j=1}^{N}\left(y^k\right)^2\left[\frac{1}{(x^i - x^j + a^j)^2 + \left(y^k\right)^2} - \frac{1}{(x^i - x^j - a^j)^2 + \left(y^k\right)^2}\right] P_y^j, \\
& \qquad i = 1, 2, \ldots, M_1, \quad k = 1, 2, \ldots, M_2.
\end{aligned} \tag{3}$$

$$\begin{aligned}
u_x^j(x^i, y^k) = -\frac{1}{2\pi\mu}\sum_{j=1}^{N}\Bigg\{&(1-2\nu)\left[\left(x^i - x^j - a^j\right)\arctan\frac{y^k}{x^i - x^j - a^j} - \left(x^i - x^j + a\right)\arctan\frac{y^k}{x^i - x^j + a^j} - \pi a\right] \\
&+ (1-\nu)y^k \ln\frac{(x^i - x^j - a^j)^2 + \left(y^k\right)^2}{(x^i - x^j + a^j)^2 + \left(y^k\right)^2}\Bigg\} P_y^j,
\end{aligned}$$

$$\begin{aligned}
u_y^j(x^i, y^k) = \frac{1}{2\pi\mu}\sum_{j=1}^{N}\Big\{&-y^k(1-2\nu)\left(\arctan\frac{y^k}{x^i - x^j - a^j} - \arctan\frac{y^k}{x^i - x^j + a^j}\right) \\
&+ (1-\nu)\left[\left(x^i - x^j - a^j\right)\ln\left((x^i - x^j - a^j)^2 + \left(y^k\right)^2\right)\right. \\
&- \left(x^i - x^j + a^j\right)\ln\left((x^i - x^j + a^j)^2 + \left(y^k\right)^2\right) \\
&\left.+ \left(L - x^j + a^j\right)\ln\left(L - x^j + a^j\right)^2 - \left(L - x^j - a^j\right)\ln\left(L - x^j - a^j\right)^2\right]\Big\} P_y^j.
\end{aligned}$$

2.2. Statement and solving of problem when normal displacement is applied to segment inside half plane

(a) Setting. Let us consider a non-classical problem, when along the entire border of half plane D (see Fig. 1) the tangent stress is equal to zero, and normal displacement u_y on segment $|x| \le c, \quad y = -b$ lying inside the body is known. Also, normal stress along part $|x| > c,\ y = 0$ of boundary is equal to zero. Thus, we have the following boundary conditions:

$$\begin{aligned}
&\text{when} \quad |x| < \infty \ \text{and} \ y = 0: \quad \sigma_{yx} = 0, \\
&\text{when} \quad |x| > c \ \text{and} \ y = 0: \quad \sigma_{yy} = 0, \\
&\text{when} \quad |x| \le c \ \text{and} \ y = -b: \quad u_y = -U_0(x),
\end{aligned}$$

where $U_0(x)$ is the sufficiently smooth function given along segment $[-c, c]$.

We can formulate this problem as follows: let us find the distribution of normal stress σ_{yy} along part $|x| \le c,\ y = 0$ of the boundary of the half plane when normal displacement along segment $|x| \le c,\ y = -b$ lying inside half plane D equals to $-U_0(x)$.

Let us consider this function of the following kind $U_0(x) = P \cdot 10^{-|4x|}$, $(P = \text{constant})$, which describes clearly expressed non-uniform normal displacement. Thus, we will have the following localization problem: let us find the distribution of normal stress σ_{yy} along segment A_1B_1 to obtain the pit of a given value along segment AB (displacements localization) (see Fig. 1).

(b) Solution. Let us divide segments $|x| \le c,\ y = 0$ and $|x| \le c,\ y = -b$ into N segments (elements) with equal $2a$ and smaller lengths. We mean that constant normal stresses P_y^j act on each j^{th} segment of segment $|x| \le c,\ y = 0$, each with the length of $2a$ and with centre $(x^j, 0)$. We must find such values of these stresses, for which the values of normal displacement in middle point $(x^i, -b)$ of each i^{th} element with length $2a$ of $|x| \le c,\ y = -b$ segment inside the body should equal to the given value of $-U_0(x^i)$.

Normal displacement in the centre of the i^{th} element lying on segment $|x| \le c,\ y = -b$ will be computed with the following formula:

$$u_y(x^i, -b) = \sum_{j=1}^{N} B^{ij} P_y^i, \qquad i = 1, 2, \ldots, N,$$

where we have the following formula for influence coefficients B^{ij}:

$$\begin{aligned}
B^{ij} = \frac{1}{2\pi\mu}\Bigg\{&-b(1-2\nu)\left(\arctan\frac{b}{x^i - x^j - a} - \arctan\frac{b}{x^i - x^j + a}\right) \\
&+ (1-\nu)\left[\left(x^i - x^j - a\right)\ln\left((x^i - x^j - a)^2 + b^2\right)\right. \\
&- \left(x^i - x^j + a\right)\ln\left((x^i - x^j + a)^2 + b^2\right) \\
&\left.+ \left(L - x^i + a\right)\ln\left(L - x^i + a\right) - \left(L - x^l - a\right)\ln\left(L - x^j - a\right)^2\right]\Bigg\}.
\end{aligned}$$

Thus, the set problem is reduced to solving the following system of linear algebraic equations (N equations with N unknown values):

$$\sum_{j=1}^{N} B^{ij} P_y^i = -U_0(x^i), \quad i = 1,2,...,N. \tag{4}$$

If we solve system (4) in relation to unknown values P_y^j, then the set problem can be considered as solved, like the problem set in 2.1.

3. Numerical simulation

By using MATLAB software, we obtained the numerical values of the normal stresses (problem of stresses localization) and displacements (problem of displacements localization) along segment AB (the given normal load and normal displacement) and distribution of normal stresses along segment A_1B_1 (the obtained normal stress) shown in Fig. 1 for the following data: c=1m, 2m, 3m, 4m, 15m, 18m, 20m, 30m, and b=5m, 6,5m, 8m, 10m, 15m 18m, 20m, 30m; $N = 120$; $P = 10\,kg/cm^2$. Below are graphs of some of the obtained results. Namely, Fig. 2 shows load $P_0(x)$ and Fig. 3, Fig. 4 shows normal displacement $U_0(x)$ along AB segment and distribution of obtained normal stress P_y along A_1B_1 segment, when $c = 1m$ and $b = 5m, 6{,}5m, 8m, 10m$.

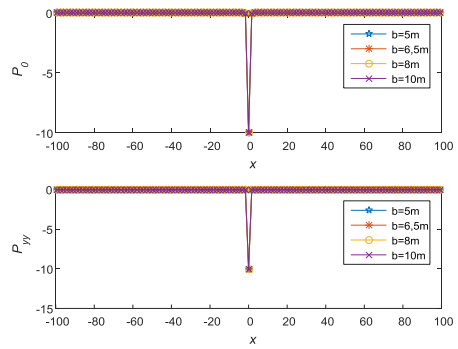

Fig. 2 *The load $P_0(x)$ along segment AB and distribution of obtained normal stress $P_{yy} := \sigma_{yy}$ along segment A_1B_1, when $c = 1m$.*

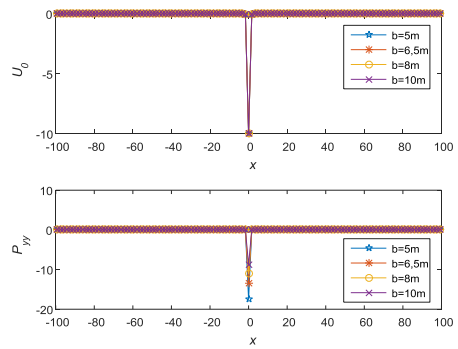

Fig.3 *Displacement $U_0(x)$ along segment AB and distribution of obtained normal stress P_{yy} along segment A_1B_1, when $c = 1m$ and $E = 2\times10^2\ kg/cm^2$, $\nu = 0.42$ (technical rubber).*

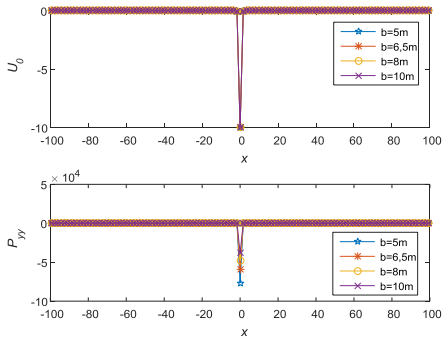

Fig. 4 *Displacement $U_0(x)$ along segment AB and distribution of obtained normal stresses P_{yy} along segment A_1B_1, when $c = 1m$ and $E = 2\times10^6\ kg/cm^2$, $\nu = 0.3$ (steel).*

Besides, represented 3D graphs of the distribution of stresses and displacements in the body section relevant to domain $-c < x < c$, $-30 < y < -10$, when $c = 1m$, $b = 30m$; for steel $E = 2\times10^6\ kg/cm^2$, $\nu = 0.3$ (see Fig. 5 and Fig. 8 for stresses localization problem, and Fig. 6 and Fig. 10 for displacements localization problem) and technical rubber $E = 2\times10^2\ kg/cm^2$, $\nu = 0.42$ (see Fig. 9 for stresses localization problem, and Fig.7, Fig.11 for displacements localization problem). Formula (3) evidences that the stresses in the stress problems do not depend on Young's modulus and Poison's ratio. As for the displacements, the normal displacement less and tangential displacement is bigger in steel than in technical rubber.

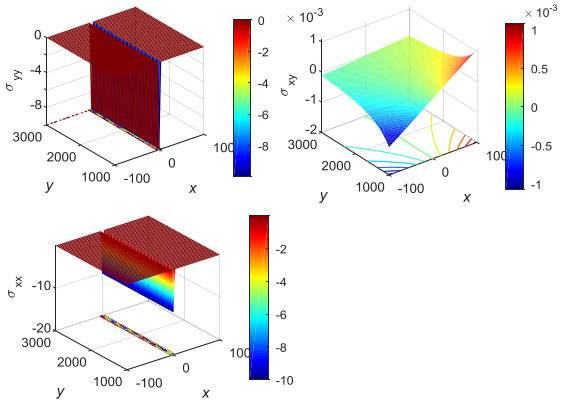

Fig. 5 *Distribution of stresses in domain $-c < x < c$, $-30 < y < -10$, when $c = 1m$, $b = 30m$, $\nu = 0.3$ (in stresses for the problem, when $P_0(x) = P\cdot10^{-|4x|}$).*

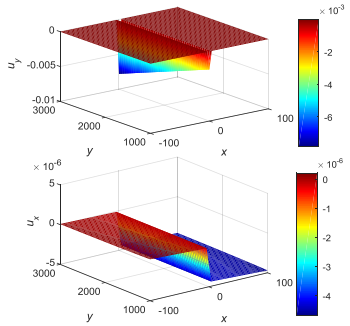

Fig. 6 *Distribution of displacements for steel in domain $-c < x < c$, $-30 < y < -10$, when $c = 1m$, $b = 30m$, $E = 2\times10^6\ kg/cm^2$, $\nu = 0.3$ (in stresses for the problem, when $P_0(x) = P\cdot10^{-|4x|}$).*

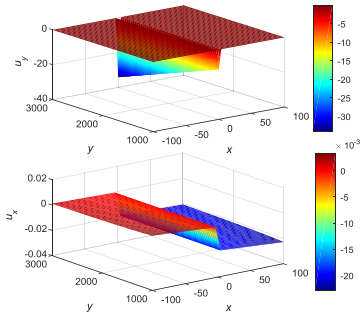

Fig. 7 *Distribution of displacements for technical rubber in domain $-c < x < c$, $-30 < y < -10$, when $c = 1m$, $b = 30m$, $E = 2\times10^2\ kg/cm^2$, $\nu = 0.42$ (in stresses for the problem, when*

$P_0(x) = P \cdot 10^{-|4x|}$).

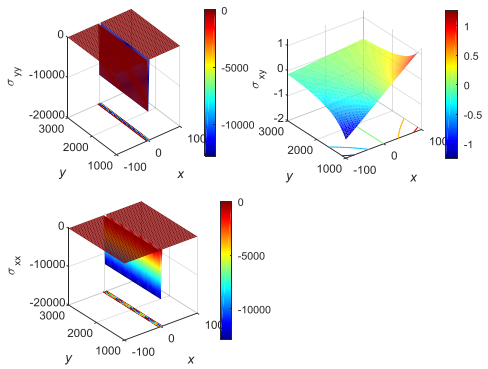

Fig. 8 *Distribution of stresses in the part of the body of steel bordered by domain* $-c < x < c,\ -30 < y < -10$, *when* $c = 1m$, $b = 30m$, $E = 2 \times 10^6\ kg/cm^2$, $\nu = 0.3$ *(in displacements for the problem when* $P_0(x) = P \cdot 10^{-|4x|}$ *).*

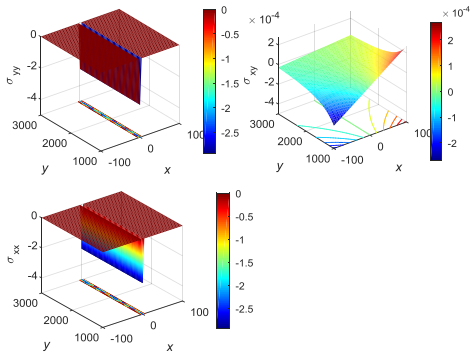

Fi. 9 *Distribution of stresses in the part of the body of technical rubber bordered by domain* $-c < x < c,\ -30 < y < -10$, *when* $c = 1m$, $b = 30m$, $E = 2 \times 10^2\ kg/cm^2$, $\nu = 0.42$ *(in displacements for the problem when* $P_0(x) = P \cdot 10^{-|4x|}$ *).*

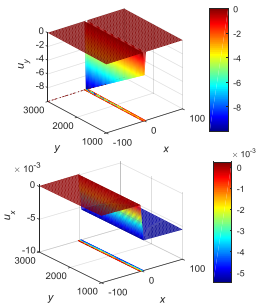

Fig. 10 *Distribution of displacements in the part of the body of steel bordered by domain* $-c < x < c,\ -30 < y < -10$, *when* $c = 1m$, $b = 30m$, $E = 2 \times 10^6\ kg/cm^2$, $\nu = 0.3$ *(in displacements for the problem when* $P_0(x) = P \cdot 10^{-|4x|}$ *).*

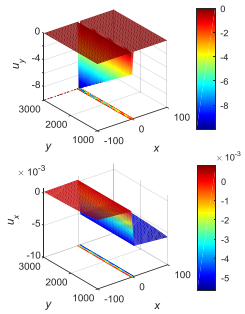

Fig. 11 *Distribution of displacements in the part of the body of technical rubber bordered by domain* $-c < x < c,\ -30 < y < -10$, *when* $c = 1m$, $b = 30m$, $E = 2 \times 10^2\ kg/cm^2$, $\nu = 0.42$ *(in displacements for the problem when* $P_0(x) = P \cdot 10^{-|4x|}$ *).*

4. Conclusion

The paper sets non-classical problems, and problems of localization of stress and displacement for a homogeneous isotropic elastic half-plane are formulated based on them. The essence of the problems is as follows: we must find the distribution of the normal stress along section A_1B_1 (see Fig. 1) of the border of the half plane so that normal stress σ_{yy} or normal displacement u_y along segment AB parallel to the border of a given length distanced from the border by b within the body should equal to the value of the given function. If we take the kind of this function, which describes the point-force applied to the middle point of section AB (e.g. $U_0(x) = C \cdot 10^{-|4x|}$, $(C = \text{constant})$), we will obtain the problem of localization of stresses and displacements. The set problems are solved by BEM [1].

By using the MATLAB's software, we obtained the numerical results and plotted the corresponding graphs showing the values of normal stress to be applied to the part of the boundary of the half plane to obtain the point force or displacement in the middle point of a segment inside the body. The paper also presents 3D graphs of distribution of stresses and displacements within the parts of the bodies of steel and technical rubber bordered by domain .

The problems considered in the work can be used in practice, e.g. in soils and rocks, materials that are susceptible to cracking and faulting when sheared, as well materials used to demolish military structures or in underground facilities.

References

[1] Crouch, S.L., Starfield A.M. Boundary element methods in solid mechanics. Allen & Unwin, London, 1983

[2] Zirakashvili, N. On the numerical solution of some two-dimensional boundary-contact delocalization problems - Meccanica, 48(7), 2013,1791–1804

[3] Agalovyan, L.A . The solution asymptotics of classical and nonclassical, static and dynamic boundary-value problems for thin bodies - J Int Appl Mech 38(7), 2002, 765–782

[4] Dehghan Mehdi. Numerical solution of a non-local boundary value problem with Neumann's boundary conditions - Commun Numer Methods Eng 19(1), 2002, 1–12

[5] Sladek, J., Sladek, V., Baant, Z.P. Non-local boundary integral formulation for softening damage - Int J Numer Meth Eng 57(1), 2003, 103–116

[6] Avalishvili, G., Avalishvili, M., Gordeziani, D. On some non-classical two-dimensional models for thermoelastic plates with variable thickness - Bull Georgian Natl Acad Sci (N.S.) 4(2), 2010, 27–34

[7] Avalishvili, G., Avalishvili, M., Gordeziani, D. On integral nonlocal boundary value problems for some partial differential equations - Bull Georgian Natl Acad Sci (N.S.) 5(1), 2011, 31–37

[8] Ma, H. M. , Gao, X. -L., Reddy, J. N. A non-classical Mindlin plate model based on a modified couple stress theory - Acta Mechanica 220 (1), 2011, 217–235

[9] Khomasuridze, N., Janjgava, R., Zirakashvili, N. Some non-classical thermoelasticity problems for a rectangular parallelepiped - Meccanica, 49(6), 2014, 1337-1342

[10] Zirakashvili, N. Numerical Simulation of Some Non-Classical Elasticity Problems for the Half-Space by the Boundary Element Method - Bulletin of TICMI, 22(1), 2018, 41-58

ABOUT NEW NONLINEAR PROPERTIES OF THE PROBLEM OF NONLINEAR THERMAL CONDUCTIVITY

Prof. Dr.ph.-math.Sci. Aripov M.M., PhD stud. Sayfullaeva M.Z.
National University of Uzbekistan, Uzbekistan
E-mail: mirsaidaripov@mail.ru, maftuha87@mail.ru

Annotation: *In this paper we are consider a problem of nonlinear heat conduction with double nonlinearity under action of a strong absorption. For which an exact analytical solution is found, analysis of which makes it possible to reveal a number of characteristic features of thermal processes in nonlinear media. The following nonlinear effects are established: an inertial effect of a finite velocity of propagation of thermal disturbances, spatial heat localization and finite time effect i.e. existence of a thermal structure in a medium with strong absorption.*

Keywords: *degenerate nonlinear, parabolic equation, not divergent, exact solution, new effects, localization, estimate.*

I. Introduction

In the investigation of the processes of energy transfer in high-temperature environments, a number of their special properties should be taken into account. For example, the dependence of heat capacity and the coefficient of thermal conductivity on temperature, it is necessary to take into account the contribution of volume radiation to the energy balance, the processes of exo and endothermic ionization, the leakage of chemical reactions, combustion, etc. The consideration of these factors determines the nonlinearity of the equation of energy transfer. Along with this, one can also take into account convective heat transfer and its influence on the evolution of the process under the investigation. The intensive development of the theory of nonlinear transfer was stimulated by studies in plasma physics [1]. Here, fundamental results have recently been obtained, and a number of nonlinear effects have been discovered, which determine the properties of inertia and localization of thermal processes [1-4]. In the [6-8] author study the properties of solutions for the following degenerate and singular parabolic equation in non-divergence form

$$\frac{\partial u}{\partial t} = u^m \nabla(\left|\nabla u\right|^{p-2} \nabla u)$$

Properties of solutions, which are different of equations in divergence form, generalizing the results of other authors . Then getting self-similar solution, we show asymptotic behavior of solutions for large time. Slow and fast diffusion cases investigated. At last, we give the results of numerical experiments of the Cauchy problem.

II. Problem formulation

Let us consider the following problem about the effect of an instantaneous concentrated source of heat in an incompressible nonlinear medium with a coefficient with double nonlinearity of thermal conductivity of temperature and its gradient in the presence of volume absorption of thermal energy in it, which power depends on the temperature and explicitly on the time according to the power law. Such a non-stationary process of heat conduction is described by the following Cauchy problem for a degenerate quasilinear parabolic equation in not divergent form

$$\frac{\partial u}{\partial t} = u^n \nabla(u^{m-1} \left|\nabla u^k\right|^{p-2} \nabla u) + div(v(t)u) - b(t)u^q,\ u(0,x) = Q_0\delta(x),\ (t>0, x \in R^N) \quad \textbf{(1)}$$

Here, *u(x, t)* — temperature , *m, k, p* — the parameter of nonlinearity of the medium: b>0, $b(t)u^q$ - is the power of volumetric heat absorption; Q_0 -the value that determines the energy of the heat source at the initial moment of time; $\delta(x)$ — Dirac's delta function that is characterizing the initial temperature distribution of a concentrated heat source placed at the beginning of the coordinate.

To investigating different qualitative properties of the solutions of the problem Cauchy and boundary value problem for particular value of numerical parameters devoted many works [1-9]. For instance in the case $m = k, \quad n = 0, \quad 0 < q < 1$ by analyzing an exact solution [2] when

$$q = \frac{p - [\mathrm{m}(p-1) - 1]}{p-1}, \quad 1 < m < 2, \quad p > m(\mathrm{p}-1) - 1$$

establish the following properties of solutions: *an inertial effect of a finite velocity of propagation of thermal disturbances, spatial heat localization and finite time localization solution effect.* Considered the problem of the effect of an instantaneous concentrated heat source in incompressible nonlinear medium with a power dependence of a coefficient of heat conduction on temperature in presence of volume absorption of thermal energy, whose power depends on temperature and explicitly on time by a power law.

Jin and Yin [5] consider the doubly degenerate diffusion Cauchy problem when *k*=0, where *m*>1, *p*>1. The authors obtained the critical exponent $q_c = p + m - 1$, namely, the solutions are global if $q < q_c$, and there exist both global and blow-up solutions if $q > q_c$. In the [9] authors study global in time existence and nonexistence conditions are found for a solution to the Cauchy problem. Exact estimates of a solution are obtained in the case of global solvability, where *k*=1, *n*=0.

In the [10] authors study the large time behavior of nonnegative solutions to the Cauchy problem for a fast diffusion equation with critical zero order absorption if $m_c := (N-2)_+ / N < m < 1$ and $q = m + 2/N$. Chunhua J., Jingxue Y. [11] study the self-similar solutions for a non-divergence form equation of the form, where $n \geq 1,\ p > 1$, This equation comes from many physical problems such as dispersal mechanisms on species survival, plasma physics, damage mechanics, curve shortening flow and so on, see for example [12-15]. If the initial value $u(x,0) = u_0(x)$ is appropriately smooth, there are papers in devoting to the solvability of the Cauchy problem of (1), one can refer to Wu-Zhao [16], Gmira[17], Yang and Zhao [18], Zhao [19], Zhao and Yuan [20], Li and Xie [21] and the references therein for details.

Let us show that with

$$q = \frac{p-[k(p-2)+n+m]}{p-1}, \quad 1<m<2 \qquad (2)$$

problem (1) has a definite one. In order to show it, we consider the class of radially symmetric solutions of the equation, obtained by following

$$u(t,x) = w(t,|\xi| = r),\ \xi = \int_0^t v(ydy) - x,\ |\xi| = (\sum\nolimits_1^N (\int_0^t v(ydy) - x_i)^{1/2},\ x \in R^N \qquad (3)$$

Then the unknown function *w (t, r)* satisfies the equation

$$\frac{\partial w}{\partial t} = w^n r^{1-N} \frac{\partial}{\partial r}(r^{N-1} w^{m-1} \left|\frac{\partial w^k}{\partial r}\right|^{p-2} \frac{\partial w}{\partial r}) - b(t) w^q,\ w(0,|x|) = u_0(x), \qquad (4)$$

Further assuming

$$w(t,r) = a(t)(f(t) - r^\gamma)_+^{\gamma_1},\ \gamma = p/(p-1),\ \gamma_1 = (p-1)/(k(p-2)+m+n-2) \qquad (5)$$

where, *a (t), f (t)*- are the functions to be defined, and through $(n)_+$, the expression of $(n)_+ = \max(0,n)$ is designated.
Calculating the derivatives of the function of *w(t, r),* we have

$$\frac{\partial w}{\partial t} = \frac{da}{dt}(f(t) - r^\gamma)^{\gamma_1} + \gamma_1 a(t) \frac{df}{dt}(f(t) - r^\gamma)^{\gamma_1 - 1},$$

$$(r^{N-1} w^{m-1} \left|\frac{\partial w^k}{\partial r}\right|^{p-2} \frac{\partial w}{\partial r}) = -(\gamma k \gamma_1)^{p-2} \gamma\gamma_1 a^{(p-2)k+m} r^N (f(t) - r^\gamma)^{(k\gamma_1 - 1)(p-2)+(m-1)\gamma_1 + \gamma_1 - 1} = \qquad (6)$$

$$= -(\gamma k \gamma_1)^{p-2} a^{k(p-2)+m-1} r^N w(t,r) \in C(Q)$$

If we choose γ_1 from (6) as

$$(k(p-2)+m+n-1)\gamma_1 - (p-1) = 0, \text{ then} \quad \gamma_1 = \frac{(p-1)}{(k(p-2)+m+n-1)}$$

$$w^n r^{1-N} \frac{\partial}{\partial r}(r^{N-1} w^{m-1} \left|\frac{\partial w^k}{\partial r}\right|^{p-2} \frac{\partial w}{\partial r}) = -(k\gamma\gamma_1)^{p-2} \gamma\gamma_1 N a^{k(p-2)+m+n} (f(t) - r^\gamma)^{(k(p-2)+m+n)\gamma_1 - (p-1)} - \qquad (7)$$

$$-[(k\gamma\gamma_1)^{p-2} \gamma\gamma_1 a^{k(p-2)+n+m-1}] \gamma_1 r^\gamma [f(t) - r^\gamma)]^{(k(p-2)+m+n)\gamma_1 - 1}$$

or considering the fact that

$$(k(p-2)+m+n)\gamma_1 - (p-1) = \gamma_1 \qquad (8)$$

Calculating

$$w^n r^{1-N} \frac{\partial}{\partial r}(r^{N-1} w^{m-1} \left|\frac{\partial w^k}{\partial r}\right|^{p-2} \frac{\partial w}{\partial r}) = -(k\gamma\gamma_1)^{p-2} \gamma\gamma_1 N a^{k(p-2)+m+n} (f(t) - r^\gamma)^{\gamma_1} +$$

$$+[(k\gamma\gamma_1)^{p-2} \gamma\gamma_1 a^{k(p-2)+n+m-1}] \gamma_1 r^\gamma [f(t) - r^\gamma)]^{\gamma_1 - 1}$$

expression (8) may be rewritten as

$$w^n r^{1-N}\frac{\partial}{\partial r}(r^{N-1}w^{m-1}\left|\frac{\partial w^k}{\partial r}\right|^{p-2}\frac{\partial w}{\partial r}) = -(k\gamma\gamma_1)^{p-2}\gamma\gamma_1 N a^{k(p-2)+n+m}(f(t)-r^\gamma)^{\gamma_1} +$$

$$+[(k\gamma\gamma_1)^{p-2}\gamma\gamma_1 a^{k(p-2)+n+m-1}]r^\gamma[f(t)-r^\gamma]^{\gamma_1-1}$$

$$w^n r^{1-N}\frac{\partial}{\partial r}(r^{N-1}w^{m-1}\left|\frac{\partial w^k}{\partial r}\right|^{p-2}\frac{\partial w}{\partial r}) - b(t)w^q = -(k\gamma\gamma_1)^{p-2}\gamma\gamma_1 N a^{k(p-2)+n+m}(f(t)-r^\gamma)^{\gamma_1} + \quad \textbf{(9)}$$

$$+[(k\gamma\gamma_1)^{p-2}\gamma\gamma_1 a^{k(p-2)+n+m-1}r^\gamma - b(t)a^q][f(t)-r^\gamma)^{\gamma_1-1}]$$

If $\gamma_1 q = \gamma_1 - 1$

Then, through substituting the calculated expressions into equation (4) we get the following:

$$\frac{da}{dt}(f(t)-r^\gamma)^{\gamma_1} + \gamma_1 a(t)\frac{df}{dt}(f(t)-r^\gamma)^{\gamma_1-1} =$$

$$= (k\gamma\gamma_1)^{p-2}\gamma\gamma_1 N a^{k(p-2)+n+m}(f(t)-r^\gamma)^{\gamma_1} + [(k\gamma\gamma_1)^{p-2}\gamma\gamma_1 a^{k(p-2)+n+m-1}r^\gamma - b(t)a^q][f(t)-r^\gamma]^{\gamma_1-1}$$

From here we have

$$[\frac{da}{dt} + (k\gamma\gamma_1)^{p-2}\gamma\gamma_1 N a^{k(p-2)+n+m}](f(t)-r^\gamma)^{\gamma_1} + [\gamma\gamma_1 a(t)\frac{df}{dt} - [(k\gamma\gamma_1)^{p-2}\gamma\gamma_1 a^{k(p-2)+n+m-1}]r^\gamma -$$

$$-b(t)a^q][f(t)-r^\gamma)]^{\gamma_1-1} = 0 \quad \textbf{(10)}$$

Now from here, to define the functions *a(t), f(t),* we obtain *a system of nonlinear differential equations*

$$-\gamma\gamma_1 a(t)\frac{df}{dt} + b(t)a^q = (\gamma\gamma_1)^p a^{k(p-2)+n+m} f(t)$$

$$\frac{da}{dt} + (k\gamma\gamma_1)^{p-2}[(\gamma\gamma_1 + N)]a^{k(p-2)+n+m} = 0$$

$$\frac{da}{dt} + (k\gamma\gamma_1)^{p-2}[(\gamma\gamma_1 + N)]a^{k(p-2)+n+m} = 0, \quad \gamma\gamma_1 = \frac{p}{k(\mathrm{p}-2)+\mathrm{n}+\mathrm{m}-1} \quad \textbf{(11)}$$

$$\gamma\gamma_1 a(t)\frac{df}{dt} - (\gamma\gamma_1)^p a^{k(p-2)+n+m} f(t) = b(t)a^q \quad \textbf{(12)}$$

And the equation (9) has the following general solution

$$a(t) = [c + 1 - (\mathrm{k}(p-2)+n+m)(\gamma\gamma_1)^{p-1}[(\gamma\gamma_1 + N)t]^{-\frac{1}{k(p-2)+n+m-1}} =$$

$$= [c + (\frac{p}{\mathrm{k}(p-2)+n+m})^{p-1}(p + (\mathrm{k}(p-2)+n+m)Nt]^{-\frac{1}{k(p-2)+n+m}}$$

where c is a constant of integration.

Rewrite equation (12) as

$$\frac{df}{dt} - b_1(t)\,f = b_2(t) \quad \textbf{(13)}$$

Then, taking into account (11) from (12), we have

$$b_1(t) = [c + (\frac{p}{\mathrm{k}(p-2)+n+m-1})^{p-1}(p + (\mathrm{k}(p-2)+n+m-1)Nt]^{-1},$$

$$b_2(t) = -\frac{\mathrm{k}(p-2)+n+m}{p} b(t)[a(t)]^{q-1}$$

$$b_1(t) = [(\frac{kp}{\mathrm{k}(p-2)+n+m})^{p-2}(p + (\mathrm{k}(p-2)+n+m-1)N]t^{-1}$$

Hence the solution tending to ∞ at $t \to 0$ has the form of

$$a(t) = [(\frac{kp}{\mathrm{k}(p-2)+n+m-1})^{p-2}(p + (\mathrm{k}(p-2)+n+m-1)N)]t^{-1/((\mathrm{k}(p-2)+n+m)-1)},$$

(14)

The equation (13) is a first order linear equation. It is integrated. Its overall solution is:

$$f(t) = [c + (\frac{p}{\mathrm{k}(p-2)+n+m-1})^{p-1}(p + (\mathrm{k}(p-2)+n+m)Nt)]^{(\frac{p}{\mathrm{k}(p-2)+n+m})^{p-1}(p+(\mathrm{k}(p-2)+n+m)N} [f_0 + \int_0^t b_2(y) e^{\int b_1(y)dy} dy]$$

When c=0, we have

$$f(t) = [(\frac{p}{\mathrm{k}(p-2)+n+m-1})^{p-1}(p + (\mathrm{k}(p-2)+n+m)Nt)]^{(\frac{p}{\mathrm{k}(p-2)+n+m})^{p-1}(p+(\mathrm{k}(p-2)+n+m)N)} [f_0 +$$

$$+ \int_0^t b_2(y) e^{\int b_1(y)dy} dy]$$

$$(\sum_1^N (\int_0^t v(y)dy - x_i)^{1/2} = [f(t)]^{(p-1)/p}$$

$$\int_0^t v(y)dy < \infty, \ f(t) < \infty, \ \forall t > 0$$

Theorem 1. Let in equation (1)

$$q = \frac{p - [k(p-2)+n+m]}{p-1}, \ u_0(x) \le z(0,x), \ x \in R^N$$

where

$$z(t,r) = a(t)(f(t) - r^{\gamma})_+^{\gamma_1}, \ \gamma = p/(p-1), \ \gamma_1 = (p-1)/(\mathrm{k}(p-2)+n+m-1),$$

where the functions *a(t), f(t)* are defined above.
Then for problem (1), the phenomenon FSP takes place.
Theorem 2. Let into an Equation (1)

$$q = \frac{p - [k(p-2)+n+m]}{p-1}, \ u_0(x) \le z(0,r), \ r \in R, \quad f(t) < \infty, \ t > 0$$

where

$$z(t,r) = a(t)(f(t) - r^{\gamma})_+^{\gamma_1}, \ \gamma = p/(p-1), \ \gamma_1 = (p-1)/(\mathrm{k}(p-2)+n+m-1),$$

and *a(t), f(t)*- are the functions defined above.
Then for problem (1), the spatial localization of the solution takes place.

Fast diffusion case: $k(p-2)+m+n<0$

Theorem 3. Let in the equation (1)

$$q = \frac{p-[k(p-2)+n+m]}{p-1},\ u_0(x) \le z(0,x),\ x \in R^N$$

where

$$z(t,r) = a(t)(f(t)+r^{\gamma})_{+}^{\gamma_1},\ \gamma = p/(p-1),\ \gamma_1 = (p-1)/(\mathrm{k}(p-2)+n+m-1),$$ *a(t), f(t)* are the functions defined above.

Then for the solution of problem (1), there is a place for the estimate.

$$u(t,x) \le z(t,r),\ r \in R,\quad t > 0$$

The finite time of the thermal impulse is due to the influence of the volume absorption of thermal energy in considered medium. Indeed, if we consider even the initial temperature distribution of the form $u\ (x,\ 0)$ and then due to the volumetric absorption of heat, the temperature of the medium will decrease by time.

The results of numerical calculations are given below.

Numerical schemes, algorithms and a set of programs for the tasks in the Python3 environment are developed, the analysis of results on the basis of the received estimates of decisions is carried out.

At $t > t_m$ volumetric heat absorption becomes the dominant factor in the energy balance, the heating wave is replaced by a cooling wave, and the width of the heat pulse begins to decrease with time. At the moment of time, the heat pulse shrinks to a point and ceases to exist.

Visualization when using a timer:

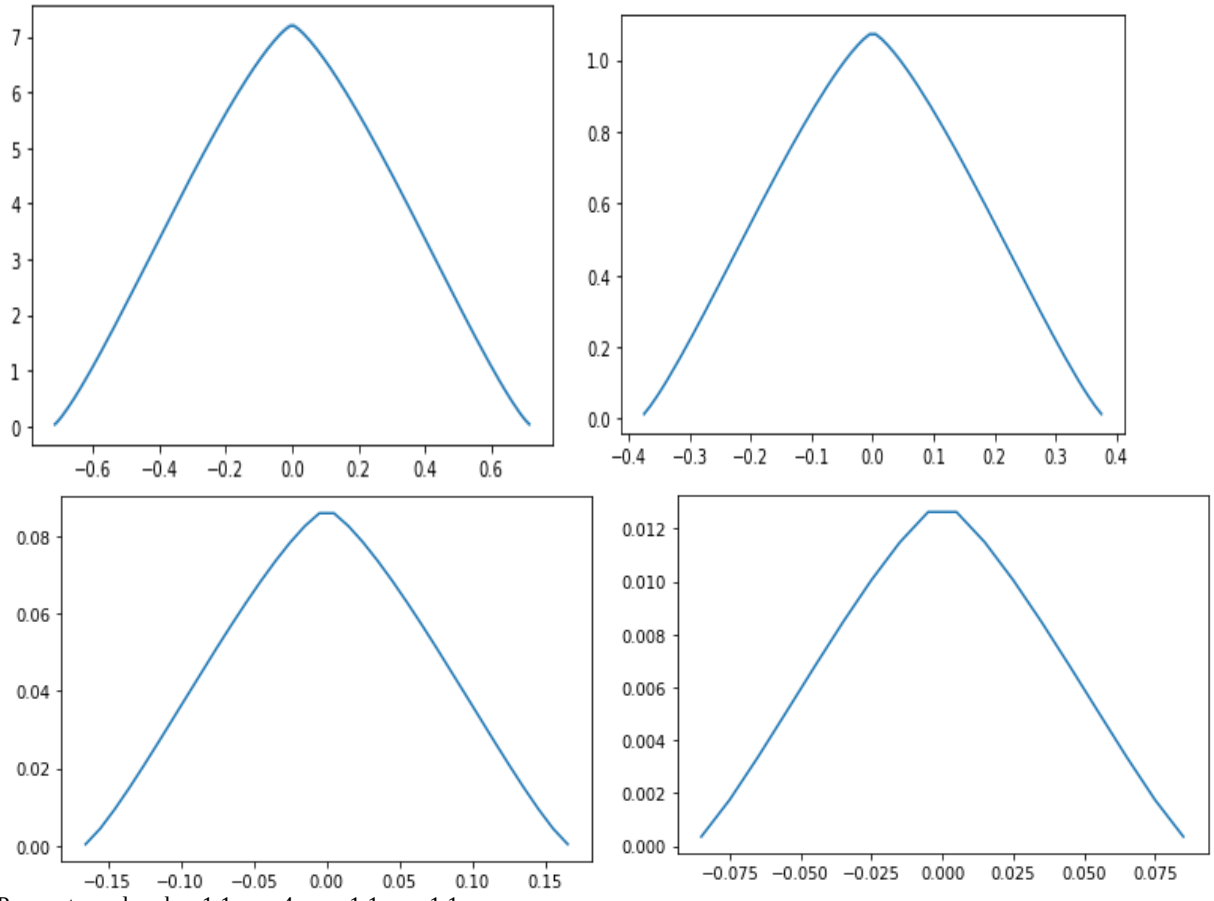

Parameter value: k = 1.1, p = 4, m = 1.1, n = 1.1,

Conclusion

In the considered problem, the following nonlinear effects observed the inertial finite speed of propagation, the effect of a spatial localization of heat, the effect of finite time of existence of a thermal structure in a medium with absorption in the case strong absorption. The analysis of solutions showed that this phenomenon is peculiar only for nonlinear problems. It is find an exact solution to these problems based on which we analyze the properties of its solution such as localization and finite time effect. The solution found is in good agreement with the processes of physics.

Acknowledgments

This work supported by scientific project F-4-30 Republic of Uzbekistan (2018)

Results of computational experiment at the initial moment of time:	Results of the computational experiment at a finite time:
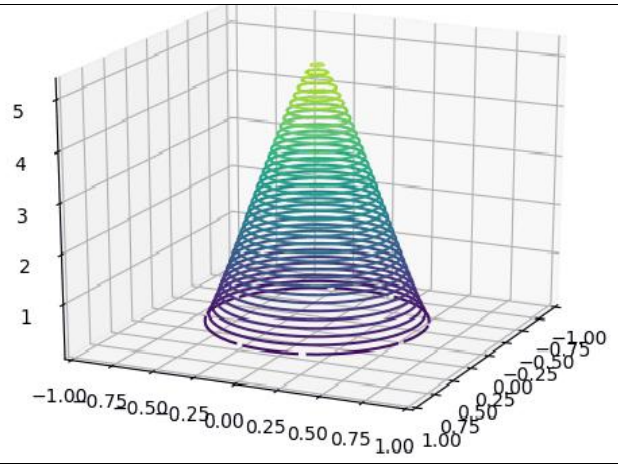	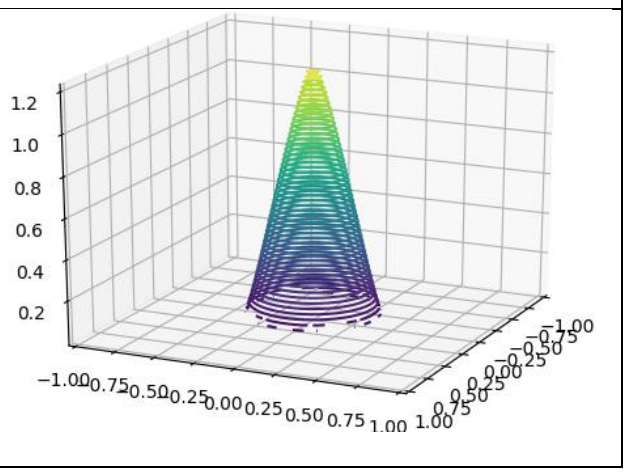

REFERENCE

1. *Aripov M. Abdullaeva Z.*, On the bottom of the exact solution of a nonlinear problem with absorption or a source. Bulletin of the TATU, №4 2016, 107-113.
2. *Martinson L. K.,* Evolution of a heat pulse in a nonlinear medium with bulk heat absorption, high temperature Thermophysics, 1983, vol. 21, i. 4, 801-803.
3. *Mersaid Aripov, Shakhlo A. Sadullaeva*. Properties of solutions to reaction-diffusion equation with double nonlinearity wih distributed parameters. Log SFU. Ser. Mat and Phys., 6: 2 (2013), 157-167.
4. *Zeldovich B. V., Raizer Yu. P.* Physics of shock waves and high-temperature hydrodynamic phenomena. M.: Science, 1966. 686 s.
5. C.Jin, J.Yin Critical exponent of a double degenerate parabolic equation in non-divergence form with nonlinear source. Chin. Ann. Math., Ser. A, 30(2009), 525-538.
6. Wang M., Wei Y. Blow-up properties for a degenerate parabolic system with nonlinear localized sources // J. Math. Anal. Appl. 343 (2008), 621--635.
7. Raimbekov J.R. The Properties of the Solutions for Cauchy Problem of Nonlinear Parabolic Equations in Non-Divergent Form with Density // Journal of Siberian Federal University. Mathematics & Physics 2015, 8(2), 192--200.
8. Mersaid Aripov, Shakhlo A. Sadulaeva, "To properties of solutions to reaction diffusion equation with double nonlinearity with distributed parameters", Jour. of Siberian Fed. Univer. Math. & Phys. 6(2013), pp. 157-167
9. P. Cianci, A. V. Martynenko, and A. F. Tedeev, "The blow-up phenomenon for degenerate parabolic equations with variable coefficients and nonlinear source," Nonlinear Analysis: Theory, Methods & Applications A, vol. 73, no. 7, pp. 2310–2323, 2010.
10. Said Benachour, Razvan Iagar, Philippe Laurencot. Large time behavior for the fast diffusion equation with critical absorption. Journal of Differential Equations, Elsevier, 2016, 260, pp.8000-8024.
11. Chunhua J., Jingxue Y. Self-similar solutions for a class of non-divergence form equations // Nonlinear Differ. Equ. Appl. Nodea. – 2013. – Vol. 20, Issue 3. – P. 873--893.
12. Friedman, A., McLeod, B.: Blow-up of solutions of nonlinear degenerate parabolic equations. Arch. Rational Mech. Anal.,96 , 55–80 (1986)
13. Wiegner, M.: Blow-up for solutions of some degenerate parabolic equations. Differ. Integral Eqs. 7, 1641–1647 (1994)
14. Bertsch, M., Bisegna, P.: Blow-up of solutions of a nonlinear parabolic equation in damage mechanics. Eur. J. Appl. Math. 8, 89–123 (1997)
15. Angenent, S.: On the formation of singularities in the curve shortening flow. J.Differ. Geom.33, 601–633 (1991)
16. Z.Wu, J.Zhao, J.Yun and F.Li, Nonlinear Diffusion Equations, New York, Singapore: World Scientific Publishing, 2001
17. A. Gmira, On quasilinear parabolic equations involving measure date, Asymptotic Analysis North-Holland, 3, 1990 pp. 43-56.
18. J. Yang and J. Zhao, A note to the evolutional P-Laplace equation with absorption, Acta. Aci. Nat.Jilin. 2, 1995, pp. 35-38
19. J. Zhao, Source-type solutions of quasilinear degenerate parabolic equation with absorption, Chin. Ann. of Math., ISB1, 1994, pp. 89-104.
20. J.Zhao and H.Yuan, The Cauchy problem of a class of doubly degenerate parabolic equation (in chinese), Chinese Ann. of Math. 16As2, 1995, pp. 1881-196.
21. Y.Li and Ch. Xie, Blow-up for p-Laplace parabolic equations, E.J.D.E. (20)2003, pp. 1-12.

INDUSTRIAL PROCESSES STABILITY MODELING

Christo Boyadjiev
Institute of Chemical Engineering, Bulgarian Academy of Sciences, Bulgaria
E-mail: chr.boyadjiev@gmail.com

Summary. *A theoretical analysis of the stability of the non-equilibrium industrial processes is presented. A unified approach is proposed for the creation of the mathematical models of the processes that allows the determination of the velocities at which the processes move to their thermodynamic equilibriums and their use for mathematical analysis of processes velocities stability. For this purpose is used mathematical stability theory, evolution (autonomous) equations, bifurcation theory (stable focuses, stable cycles), parameter eigenvalues and eigenfunctions.*
Keywords: *stepped complex, stability theory, evolution equations, bifurcation theory, stable focuses, stable cycles, parameter eigenvalues*.

Introduction

Non-equilibrium industrial systems are aggregations of physical, chemical and biological processes. They "move" to their thermodynamic equilibrium with a velocity that depends on the velocities of the individual processes. Non-equilibrium industrial systems are stable when two conditions are met:
1. The velocity of movement towards their thermodynamic equilibrium is a constant;
2. Capable of rapidly reaching their constant velocity at deviations, as a result of smooth change of external conditions.
The theoretical analysis of the stability of the non-equilibrium industrial systems consists of 2 stages:
1. Creation a mathematical model of the system, allowing the determination of the velocity at which the system moves to its thermodynamic equilibrium;
2. Mathematical analysis of system velocity stability.
The first stage is different for individual systems, while the second stage is common to all industrial systems.
An unified approach will be proposed for the creation of a mathematical model of the system, which permits to be obtained the velocity of the system movement to its thermodynamic equilibrium and mathematical analysis of the system stability.

Industrial processes kinetics

The kinetics of industrial processes depends on a set of variables. If the velocity of the industrial process is denoted by the values of these variables, the equation of the kinetic model of the industrial process will have the form:

$$y = f\left(x_1,...,x_n\right). \tag{1}$$

This function is a mathematical structure that is retained when changed the measurement system of the variable, i.e. this mathematical structure is invariant with respect to similar transformations [1]:

$$\overline{x}_i = k_i x_i, \quad i = 1,...,n, \tag{2}$$

i.e. f is a homogeneous function:

$$ky = f\left(k_1x_1,...,k_nx_n\right) = \phi\left(k_1,...,k_n\right).f\left(x_1,...,x_n\right), \quad k = \phi\left(k_1,...,k_n\right). \tag{3}$$

A short recording of (3) is:

$$f\left[\overline{x}_i\right] = \phi\left[k_i\right] f\left[x_i\right]. \tag{4}$$

The problem consists in finding a function *f* that satisfies equation (4). A differentiation of equation (4) concerning k_1 leads to:

$$\frac{\partial f\left[\overline{x}_i\right]}{\partial k_1} = \frac{\partial \phi}{\partial k_1} f\left(x_i\right). \tag{5}$$

On the other hand

$$\frac{\partial f\left[\overline{x}_i\right]}{\partial k_1} = \frac{\partial f\left[\overline{x}_i\right]}{\partial \overline{x}_1}\frac{\partial \overline{x}_1}{\partial k_1} = \frac{\partial f\left[\overline{x}_i\right]}{\partial \overline{x}_1} x_1. \tag{6}$$

From (5, 6) follows

$$\frac{\partial f\left[\overline{x}_i\right]}{\partial \overline{x}_1} x_1 = \alpha_1 \ f\left[x_i\right], \tag{7}$$

where

$$\alpha_1 = \left(\frac{\partial \phi}{\partial k_1}\right)_{k_i=1}. \tag{8}$$

The equation (7) is valid for different values of k_i including $k_i = 1 \ \left(i = 1,...,n\right)$. As a result $\overline{x}_i = x_i, i = 1,...,n$ and from (7) follows:

$$\frac{1}{f}\frac{\partial f}{\partial x_1} = \frac{\alpha_1}{x_1}, \tag{9}$$

i.e.

$$f = c_1 x_1^{\alpha_1}. \tag{10}$$

When the above operations are repeated for $x_2,...,x_n$, the homogenous function *f* assumes the form:

$$f = kx_1^{\alpha_1},...,x_n^{\alpha_n}, \quad (11)$$

i.e. the function *f* is homogenous if it represents a power functions complex and as a result is invariant with respect to similarity (metric) transformations.

The parameters $k, \alpha_1,...,\alpha_n$ are determined by experimental data of the industrial process velocity. This allows to consider the velocity of the industrial process y (phase velocity) as a point in a n-dimension space, with coordinates $x_1,...,x_n$ (phase space). Velocity projections on coordinate axes $x_1,...,x_n$ are $\frac{dx_i}{dt}\left(i=1,...,n\right)$ and satisfy the "evolution" law of the industrial process:

$$\frac{dx_i}{dt} = a_i y = a_i k x_1^{\alpha_1}...x_n^{\alpha_n}; \quad t=0, \quad x_i = x_{0i}; \quad i=1,...,n, \quad (5)$$

where $a_1,...,a_n$ represent the ratios of variable $x_1,...,x_m$ velocities and the industrial process velocity y.

The components of the phase velocity $\frac{dx_i}{dt}\left(i=1,...,n\right)$ are the coordinates of the vector field at the same phase velocity and determine the velocity of motion of the industrial process in the phase space. The points $x_i\left(t\right)\left(i=1,...,n\right)$ represent a curve (phase trajectory) in the scalar phase space.

If we use the rule to differentiate a exponent function, the derivative of the velocity of the industrial process (4) over the time has the form:

$$\frac{dy}{dt} = k\prod_{i=1}^{n}\left[x_i\left(t\right)\right]^{\alpha_i}\sum_{i=1}^{n}\left[\frac{\frac{dx_i}{dt}}{x_i\left(t\right)}\alpha_i\right]. \quad (13)$$

From this equation is possible to be obtained stability condition $\frac{dy}{dt}=0$ of the industrial process:

$$k\prod_{i=1}^{n}\left[x_i\left(t\right)\right]^{\alpha_i}\sum_{i=1}^{n}\left[\frac{\frac{dx_i}{dt}}{x_i\left(t\right)}\alpha_i\right]=0, \quad x_i\left(0\right)=x_{i0}, \quad i=1,...,n. \quad (14)$$

The solution of this set of equations allows the determination of the conditions for the stability of the industrial processes.

Mathematical Stability Theory

The velocity of the non-equilibrium industrial processes with which they "move" to their thermodynamic equilibrium is determined by the theory of the evolution equations [2-4]. Their capable of rapidly reaching their constant velocity at deviations, as a result of smooth change of external conditions, is determined by the theory of bifurcations [5].

Evolution equations

Let consider the industrial process velocity, which may be determined by the variables $x_i \ \left(i=1,...,n\right)$. This permits to consider the state of the process as a point in *n*-dimensional space with co-ordinates $x_i \ \left(i=1,...,n\right)$ (a phase space).

The changing of the process velocity over the time is a vector in the n-dimensional space. Its projections on coordinate axes $\frac{dx_i}{dt}\left(i=1,...,n\right)$ satisfy the "evolution" law of the process:

$$\frac{dx_i}{dt} = X_i\left(x_1,...,x_n,t\right), \quad x_i\left(0\right)=x_{i0}, \quad i=1,...,n. \quad (15)$$

The evolution equations (15), for processes with laws independent of the time, are termed autonomous equations:

$$\frac{dx_i}{dt} = X_i\left(x_1,...,x_n\right), \quad x_i\left(0\right)=x_{i0}, \quad i=1,...,n. \quad (16)$$

The components of the phase velocity $X_i\left(i,...,n\right)$ are the co-ordinates of the vector field of the same phase velocity and determine the velocity of the process in the phase space. The points $x_i\left(t\right)\left(i,...,n\right)$ represent a curve (a phase trajectory) in the scalar phase space (field).

For simplicity of explanation consider the autonomous equation

$$\frac{dx}{dt} = X\left(x\right), \quad x\left(0\right)=x_0. \quad (17)$$

The process is stable when the system velocity does not change over the time:

$$X(x)=0, \tag{18}$$

i.e.

$$X(a)=0. \tag{19}$$

It follows from (19) that the point $x=a$ may be considered as a stationary point (the process velocity is constant over time). If $a=x_0$ it clear that

$$x(t)\equiv a \tag{20}$$

is a solution of (17), where a is a singular point.
For simplicity will be considered the linear version of the equation (17) and its solution:

$$\frac{dx}{dt}=\lambda x, \quad x(0)=x_0, \quad x=x_0\exp(\lambda t). \tag{21}$$

It is follows from (21) that $x=0$ is a singular point, i.e. $x_0=0$ and the solution of (21) has the following features (see Fig. 1):

$$\lambda<0, \quad \lim_{t\to\infty}x(t)=0, \quad \forall x_0; \tag{22}$$

$$\lambda=0, \quad x=x_0, \quad \forall x_0; \tag{23}$$

$$\begin{aligned}&\lambda>0, \quad x=x_0, \ at \ \ t=0;\\ &\lambda>0, \quad \lim_{t\to\infty}x(t)\to\infty, \quad \forall x_0>0;\\ &\lambda>0, \quad \lim_{t\to\infty}x(t)\to-\infty, \quad \forall x_0<0.\end{aligned} \tag{24}$$

The multiformity of the solution at $\lambda>0$ is not a result of its non-uniqueness, but this due to the solution instability with respect of the small perturbation of the initial condition (x_0).

.

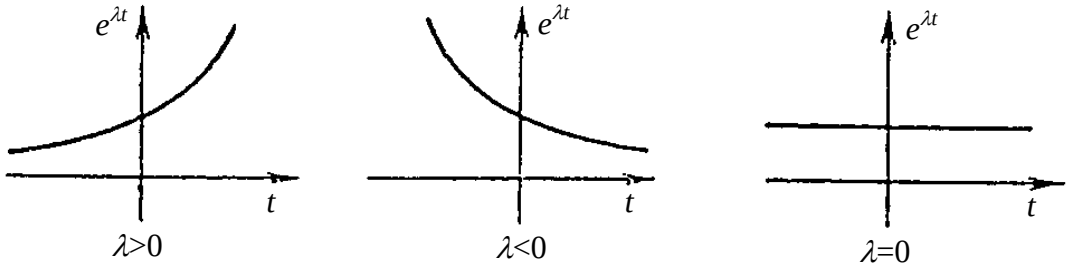

Fig.1. Solution of the equation (14)

The solution of the equation (14) leads to the following conclusions:

1. The solution (the process) is unstable at $\lambda>0$ and the small deviations of the initial state $x_0\neq 0$ lead to deviations of the solution $x=0$.

2. At $\lambda>0$ the solution is unstable for each x_0.

3. At $\lambda\le 0$ the solution is approaching to the singular point $x=0$, i.e. the stationary point become a focus of attraction of the solution (an attractor).

The linear equation (14), together with the conditions for the solution stability, are attractive because they give the basis of the kinetics models of many important processes (evolution of the organisms, nuclear processes, chemical reactions etc.) These features in the area of the real number (R) become more interesting in the complex area (C), where the equation (14) has the form:

$$\frac{dz}{dt}=\lambda z, \quad z\in C, \quad \lambda\in C, \quad t\in R, \quad z(0)=z_0, \quad z(t)=z_0\exp(\lambda t). \tag{25}$$

Bifurcation theory

The bifurcation theory [5] is wide applied for investigations of jump reactions of processes as responses of smooth changes of the external conditions. For the real processes it has been developed recently as a theory of the catastrophes. Here, the bifurcation theory will be considered in two-dimensional phase space only.

For clarity of explanation, consider that a real evolutionary process occurring in the phase plane (x,y) and the corresponding model is:

$$\frac{dx}{dt}=X(x,y,\mu), \quad \frac{dy}{dt}=Y(x,y,\mu), \quad x(0)=x_0, \quad y(0)=y_0. \tag{26}$$

The process evolution in time is represented by the phase trajectory (the trajectory of the phase point) of the process

$$F(x, y, \mu) = 0, \tag{27}$$

where $x(t)$ and $y(t)$ in (27) are determined from the solution of (26). Depending on the form of the relationships for X and Y in (26), the parameter μ and the initial conditions x_0 and y_0 various phase trajectories are possible.

The variations of the parameter μ lead to several interesting cases of the solution of (26) shown in Fig. 2. The case shown in Fig. 2a corresponds to a periodic process that is attenuating with the time and approaching to a focus (a stationary state point). If other value of μ is chosen the process might be unstable and periodic (Fig.2b). The stable periodic processes (limit cycles) have closed trajectories in the phase space (Fig.2c). The change of the initial state (y_0) of the stable processes leads to attenuating processes approaching a stable periodic state. (Fig. 2d).

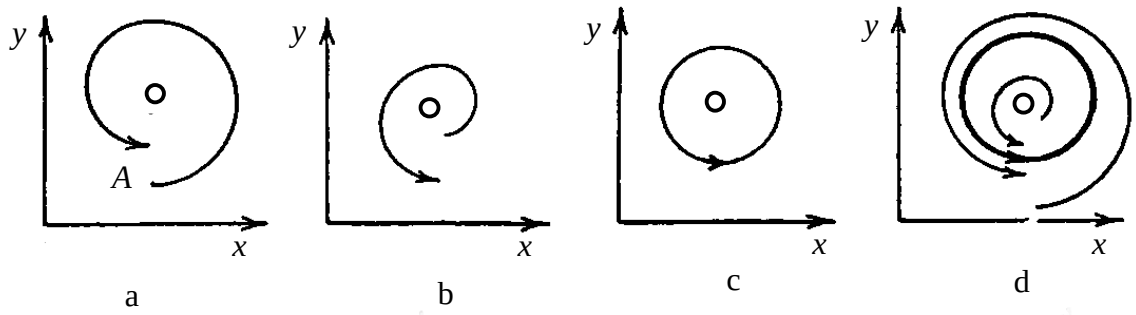

Fig. 2. Phase trajectories.

Figure 2 may be developed for more complicated cases (see Fig. 3). It is possible the existence of two limit cycles (periodic processes and solutions,), where one of them (the internal) is stable if the initial conditions are in the entire internal area of the large cycle. The internal cycle attracts all the solutions, while the external cycle is unstable (Fig. 3a).The variations of the parameter μ may lead to a junction of both cycles (Fig.3b). The junction of an unstable and a stable cycle (as these in Fig. 3a) may lead to an abnormal limit cycle (Fig. 3b). In this case the solutions go from the initial conditions in internal area, approach the cycle and then due to small perturbations may go out of the cycle, so the process becomes unstable. The further changes of μ may lead to a situation when the limit cycle disappear and the process becomes unstable (Fig. 3c).

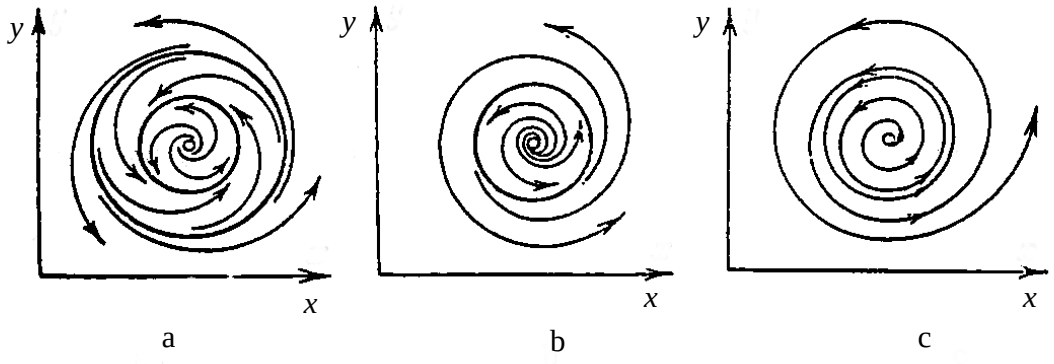

Fig. 3. Limit cycles.

The resulted obtained here show that the bifurcation theory considers qualitatively the changes of the movement of phase point as a result of a continuous variation of the model parameters. Parallel to the existence of stable points (focuses) there are stable cycles. They describe stationary periodic oscillations of the systems (self-oscillations). They differ from the free oscillations (of a pendulum for example) where the system does not interact with the environment as well as from the forced oscillations provoked by external periodic impacts.

The focuses and the limit cycles attracting the solution (the phase point) are termed *attractors*.

Figure 4 shows bifurcations of cycle transitions from focuses. The case (a) corresponds to a supercritical bifurcation (stable closed trajectories), while the case (b) presents a subcritical bifurcation (unstable and closed trajectories).

Further, Fig. 4a shows the mechanism of a transition from a stable point (focus) toward a stable orbit (cycle). This type of bifurcation is shown in Fig.5. The stages of that transition are: 1) a stable point; 2) the occurrence of a closed trajectory; 3) an increase of the closed trajectory amplitude. This order leads to the existence of stable three-dimensional torus.

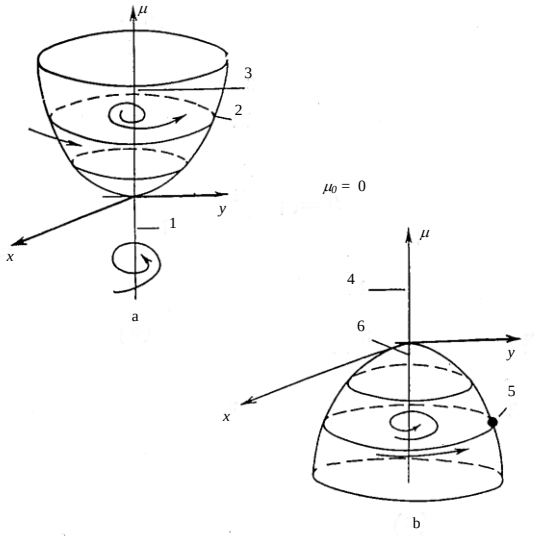

Fig.4. Bifurcation of cycle transitions from focuses.

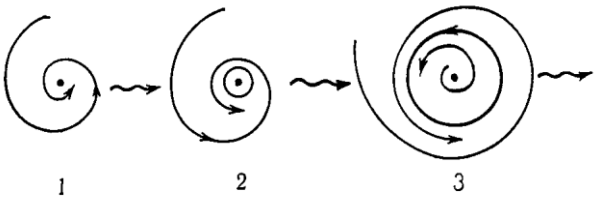

Fig. 5. Mechanism of a transition from a focus toward a cycle.

Eigenvalue problems

The presented analysis of the processes and the systems concerns its stabilities as functions of the model parameters. This requires a solution of differential equations with parameters. It is possible that the solution of the differential equation to exist at a given point (e.g. focus), only for a specific value of the parameter - "eigenvalue". For example, the second-order ordinary differential equation, when the boundary conditions are presented at two different points, can have solution for a specific value of the parameter only, i.e. this leads to eigenvalue problems. The solution to this problem will be demonstrated in a first order linear ordinary homogeneous differential equation:

$$y'+\left[f\left(x\right)+\lambda g\left(x\right)\right] y=0, \tag{28}$$

where λ is a parameter and the solution must to satisfy the condition:

$$y\left(b\right)=\alpha y\left(a\right), \quad \alpha \neq 0. \tag{29}$$

The solution of (28) is well known

$$y=C\exp\left[-\int_{a}^{x}\left(f+\lambda g\right) dx\right]. \tag{30}$$

The substitution of (30) in (29) shows that the condition (29) is satisfied, when $\lambda=\lambda_0$, only:

$$\lambda_0=-\frac{\ln\alpha+\int_{a}^{b} f dx}{\int_{a}^{b} g dx}, \tag{31}$$

well known as an eigenvalue. The substitution of (31) in (30) leads to an eigenfunction. Thus, for example at $f\equiv 0$ and $g\equiv 1$ it follows directly:

$$\lambda_0=\frac{\ln\alpha}{a-b}, \quad y=C\exp\left[-\frac{\ln\alpha\left(x-a\right)}{a-b}\right]. \tag{32}$$

It is well demonstrated in the differential equation theory [6] that if $\int_{a}^{b} g dx\neq 0$ there is an infinite set of eigenvalues:

$$\lambda_k = \lambda_0 + \frac{2k\pi i}{\int_a^b g dx}, \quad k = 0, \pm 1, \pm 2, \ldots . \tag{33}$$

The results obtained are used [7] for the theoretical analysis of the hydrodynamics stability in systems with non-linear mass transfer.

Conclusions

The presented theoretical analysis shows, that the stability of the non-equilibrium industrial processes (physical, chemical, biological and economic processes) is possible to be analyzed by the creation a mathematical model of the process, the determination of the velocity at which the process moves to its thermodynamic equilibrium and mathematical analysis of process velocity stability.

A unified approach is proposed for the creation of the mathematical models of the processes that allows the determination of the velocities at which the processes move to their thermodynamic equilibriums and their use for mathematical analysis of processes velocities stability. For this purpose is used mathematical stability theory, evolution (autonomous) equations, bifurcation theory (stable focuses, stable cycles), parameter eigenvalues and eigenfunctions.

References

1. Chr. Boyadjiev, Theoretical Chemical Engineering. Modeling and simulation, Springer-Verlag, Berlin Heidelberg, 2010, 594 pp.

2. V. I. Arnold, Ordinarily Differential Equations, Nauka, Moskow, 1984 (in Russian).

3. M. Braun, Differential Equations and their Applications, Springer-Verlag, New York, 1978.

4. D. Zwillinger, Handbook of Differential Equations (ed. II) Acad. Ress. Inc., Boston, 1957.

5. J. E. Marsden and M. McCracken, The Hopf Bifurcation and its Application, Springer-Verlag, New York, 1976.

6. E. Kamke, Differentialgleichungen, Leipzig, 1959.

7. Chr. Boyadjiev, V. N. Babak, *"Non-Linear Mass Transfer and Hydrodynamic Stability"*, Elsevier, Amsterdam, 2000.

P-BOX UNCERTAINTY QUANTIFICATION OF QUEUES USING THE TAYLOR SERIES EXPANSION

M.Sc. Ouazine S. PhD.[1], Prof. M.Sc. Abbas K. PhD.[2]
Applied Mathematical Laboratory (LMA), Department of Mathematics , Faculty of Exact Sciences –University of Bejaia, Algeria [1]
Research Unit LaMOS, Department of Operation Research, Faculty of Exact Sciences –University of Bejaia, Algeria [1]
wazinesofi@gmail.com

Abstract: *In this work, firstly we opted, for the global sensitivity analysis using the first order Sobol indices of simulated by the Monte Carlo method, to see and determine the parameters to which the stationary distribution of model GI/M/1/N with negative arrivals is sensitive. Secondly, we used the Monte Carlo method to propagate the uncertainty of the parameters of the stationary distribution of GI/M/1/N queuing model with negative arrivals, while estimating its statistics (expectation and variance).*

Keywords: GI/M/1/N QUEUE, NEGATIVE ARRIVALS, SOBOL'S INDICES, PARAMETRIC UNCERTAINTY.

1. Introduction

The sensitivity analysis is currently receiving considerable interest in the area of the performance evaluation of diff erent stochastic models. The sensitivity analysis consists on investigating which individual input parameter drives most of the uncertainty on the model output. In this regard, we estimate the Sobol's indices for global sensitivity analysis of stationary distribution in the GI/M/1/N queueing models. Specifically, when we estimate the Sobol's indices, we consider the more influents parameters are uncertains. In this case, we estimate the expectation and the variance of the stationary distribution under the uncertainty.

Recently there has been a rapid increase in the literature on queueing systems with negative arrivals. Queues with negative arrivals, called G-queues, were first introduced by Gelenbe [5]. When a negative customer arrives, it immediately removes an ordinary (positive) customer if present. Negative arrivals have been interpreted as inhibiter and synchronization signals in neural and high speed communication network. For example, we can use negative arrivals to describe the signals, which are caused by the client, cancel some proceeding. There is a lot of research on queueing system with negative arrivals. But most of these contributions considered continuous-time queueing model: Boucherie and Boxma [6], Jain and Sigman [8], Bayer and Boxma [2], Harrison and Pitel [9] all of them investigated the same M/G/1 model but with the diff erent killing strategies for negative customers; Harrison, Patel and Pitel [10] considered the M/M/1 G-queues with breakdowns and repair; Yang [11] considered GI/M/1 model by using embedded Makov chain method.

The remainder of this paper is organized as follows. In Section 2, we introduce the necessary notations: the sensitivity analysis and uncertainty analysis. In Section 3, we outline description of the model and we finish by the numerical framework to illustrate the applicability of this analysis. Concluding remarks are provided in Section 4.

2. Sensitivity Analysis

Mathematical models always approximate the real phenomena. The uncertainty of their input parameters described the incapacity to envisage precisely her issues, from which the uncertainty also of the output parameters.

Thus, the precision of the output parameters will depend on the quality of the available information. These uncertainties often correspond to the errors made by measuring instruments, manufacturing processes or limited data.

There are several types of sensitivity analysis. We satisfies in this work on one precise method, it is the method of analysis of the global sensitivity. This method studies the influence of the variability of the input parameter in the output parameters. We can't speak about the sensitivity analysis without citing the Sobol's indices.

If we consider a mathematical model

$$\begin{aligned} f: \ \mathbb{R}^m &\longrightarrow \mathbb{R} \\ X &\longmapsto Y = f(X), \end{aligned}$$

Where $X = (X_1, ..., X_m)$ is the vector of the input parameters, Y is the output parameter.

The purpose of this analysis is to estimate the Sobol's indices of sensitivities by this formula:

$$S_i = \frac{V(E[Y/X_i])}{V(Y)}, \quad i = 1, ..., m.$$

In general way, the compute of the first order Sobol's indices proves so difficult or impossible in some case, that returns to the complexity of the function f, from which the obligation of using of the simulation methods. The Monte Carlo method seems the appropriate for this kind of problem.

3. Queueing Model Description

We investigate the GI/M/1/N queue with negative customers, where N is the capacity of the system including the one who is in service.

Assume that customer arrivals occur at discrete-time instants τ_k, where $\tau_0 = 0$ customers arrive at the system according to a renewal process with interarrival time distribution $G(t)$ and mean $1/\lambda$ .The service time T_s of each server is assumed to be distributed exponentially with service rate μ. It's density function is given by

$$s(t) = \mu e^{-\mu t}, \quad t \geq 0.$$

Additionally, we assume that there is another kind of customers, namely RCH, arriving in the system according to an independent Poisson process of parameter ζ. Let L_k denote the number of customers left in the system immediately after the kth departing

customer. A sequence of random variables $L_k; k = 1, 2, \ldots, N$ constitutes a Markov chain. Its transition probabilities matrix is given by:

$$P = \begin{pmatrix} b_0 & a_0 & 0 & 0 & 0 & \ldots & 0 \\ b_1 & a_1 & a_0 & 0 & 0 & \ldots & 0 \\ b_2 & a_2 & a_1 & a_0 & 0 & \ldots & 0 \\ b_3 & a_3 & a_2 & a_1 & a_0 & 0 & 0 \\ . & & . & . & . & . & . \\ . & & . & . & . & . & . \\ . & & . & . & . & . & . \\ b_{N-1} & a_{N-1} & a_2 & a_{N-3} & a_{N-4} & \ldots & a_0 \\ b_{N-1} & a_{N-1} & a_2 & a_{N-3} & a_{N-4} & \ldots & a_0 \end{pmatrix}_{(N+1)\times(N+1)}$$

Where $$a_j = \int_0^{+\infty} e^{-(\mu+\zeta)t} \frac{[(\mu+\zeta)t]^j}{j!} dG(t)$$

$$b_j = 1 - \sum_{i=0}^{j} a_i.$$

4. Numerical Results

Consider this application

$$\begin{aligned} \pi_l : \quad \mathbb{R}^m &\longrightarrow \mathbb{R} \\ \theta &\longmapsto \pi_l(\theta), \end{aligned}$$

where $\pi_l, l = 0, 1, \ldots, N$ is the stationnary distribution of a such model, and $\theta = (\theta_1, \theta_2, \ldots, \theta_m)$ is a vector of all parameters of the model. The first order Sobol's indices are compute by this formula

$$S_i = \frac{V(E[\pi_l/\theta_i])}{V(\pi_l)}, \quad i = 1, \ldots, m \quad ; \quad l = 0, 1, \ldots, N.$$

The M/M/1/4

Consider the M/M/1/4 system with negative arrivals, where the inter-arrivals times and the service times are exponentials.

Let the input vector parameters

$$\theta = (\theta_1, \theta_2, \theta_3) = (\lambda, \mu, \zeta).$$

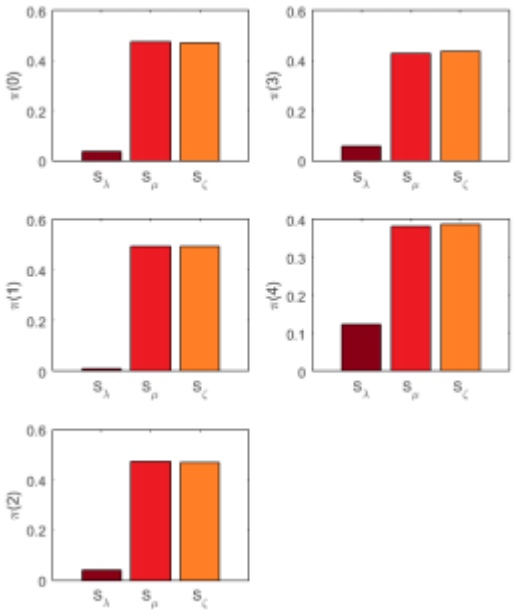

Figure 1: Sobol's indices for the M/M/1/4 model

According to this figure, we note that the values of the highest indices those, which correspond to the parameters μ and ζ, therefore these two last, are more influents on the stationary distribution, and as the parameter λ is less influent, so it is considered deterministic (constant).

The H2/M/1/4

Consider the H2/M/1/4 system with negative arrivals, where the inter-arrivals times are hyper-exponentials and the service times are exponentials.

Let the input vector parameters

$$\theta = (\theta_1, \theta_2, \theta_3, \theta_4) = (\lambda_1, \lambda_2, \mu, \zeta).$$

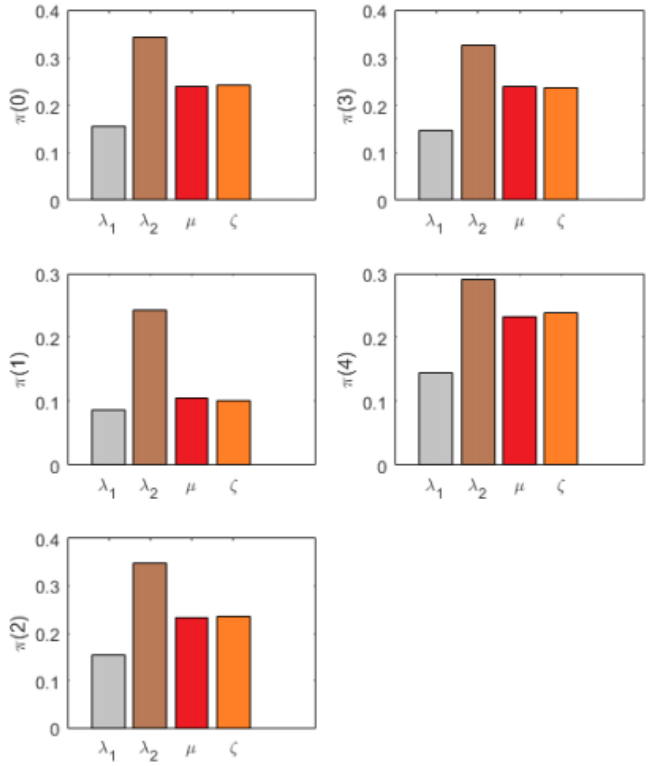

Figure 2: Sobol's indices for the H2/M/1/4 model

According to this figure, we note that the values of the highest indices those, which correspond to the parameters λ_2, μ et ζ and ζ, therefore these two last, are more influents on the stationary distribution, and as the parameter λ_1 is less influent, so it is considered deterministic (constant).

According to the analysis carried previously, we obtained μ and ζ like the most influential parameters for each component πl, l = 0, 1…, 4 of the stationary distribution π (μ, ζ), and the parameter λ is considered like a deterministic parameter.

To simulate the expectation and the variance of the stationary distribution, we present a new formula the two parameters μ and ζ:

$$\mu = \overline{\mu} + \sigma_\mu \epsilon_\mu,$$

$$\zeta = \overline{\zeta} + \sigma_\zeta \epsilon_\zeta,$$

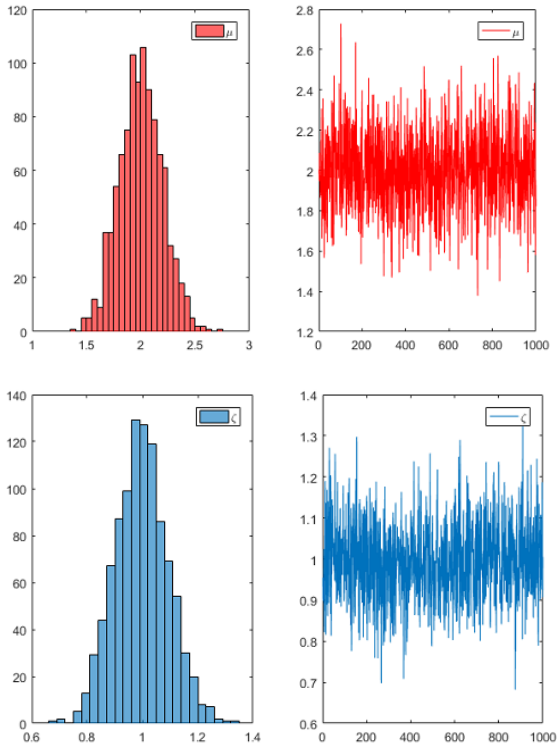

	Simulation Monte Carlo	$\pi(0)$	$\pi(1)$	$\pi(2)$	$\pi(3)$	$\pi(4)$
$M/M/1/N$	Expectation	0.6682	0.2232	0.0749	0.0252	0.0085
	Variance $\times 10^{-04}$	4.6370	0.5840	0.5770	0.1840	0.0420

According to the analysis carried in this table, we note that a disturbance of 10% of each input parameter involve a maximum variance of 4.63 × 10E(-04), which proves the robustness of the M/M/1/4 model with negative arrivals, compared to the uncertainty inflicted in the influential parameters. In other words, a small disturbance on the input parameters generates a small disturbance in the output parameter.

5. References

[1] Abbas, K., Heidergott, B. and Aïssani, D. A Functional Approximation for the M/G/1/N Queue. Discrete Event Dynamic Systems , pages 93–104, 2013.

[2] Bayer, N., Boxma, O.J.WienerHopf analysis of an M/G/1 queue with negative customers and of a related class of random walks, Queueing Syst.23 (1996) 301316.

[3] Boucherie, R.J. , Boxma, O.J. The workload in the M/G/1 queue with work removal, Probab. Eng.Inform.Sci.10 (1995) 261277.

[4] Cao, X.R. Realization Probabilities: The Dynamics of Queueing Systems, Springer Verlag, New York, 1994.

[5] Gelenbe,E. Product-form queueing networks with negative and positive customers, J.Appl. Probab.28 (1991) 656663.

[6] Boucherie, R.J. , Boxma, O.J. The workload in the M/G/1 queue with work removal, Probab. Eng.Inform.Sci.10 (1995) 261277.

[7] Heidergott, B., Hordijk, A.: Taylor series expansions for stationary Markov chains. Advances in Applied Probability 35, 1046–1070 (2003).

[8] Jain, G., Sigman, K. A pollaczek-Khintchine formula for M/G/1 queues with disasters, J.Appl. Probab.33 (1996) 11911200.

[9] Harrison, P.G., Pitel, E. The M/G/1 queue with negative customers, Adv. Appl Probab. 28 (1996) 540566.

[10]. Harrison, P.G., Patel, N.M. Pitel, E. Reliability modelling using G-queues, Eur. J. Oper. Res. 126 (2000) 273287.

[11] Yang, W.S., Chae, K.C. A note on the GI/M/1 queue with poisson negative arrivals, J. Appl. Probab.38 (2001) 10811085.

MODELING THE NUMBER OF ERRORS THAT THE CODE SURELY DETECTS

Prof. Ilievska N. PhD.
Faculty of Computer Science and Engineering, "Ss. Cyril and Methodius" University, Skopje, R. N. Macedonia
natasa.ilievska@finki.ukim.mk

Abstract: *The codes for error control (error-detecting and error-correcting codes) are extremely important part of the communication systems and storage devices, ensuring reliable data transmission and storage. In this paper using simulations, we analyze an error-detecting code. More specifically, we will be focused on the error-detecting capability of the code. Namely, using simulations we will obtain the number of errors that the code detects for sure, as an important parameter of every error-detecting code.*

Keywords: ERROR-DETECTING CODE, CODED BLOCK, SYMBOL, ALPHABET

1. Introduction

When data is transmitted through or stored on some medium, due to the noises in the medium or other external influences, there is a possibility of errors. This means that the data received by the recipient may not be identical to those sent through the communication channel or data recorded on the storage. Therefore, there is a need to check that the data is correct. Checking is done using the codes for error control. There are two basic types of these codes: error-correcting and error-detecting codes. While the first ones have ability to correct up to some number of incorrectly transmitted bits, there are slower in their work. The error-detecting codes are faster and are in advantage in networks where errors rarely occur. There are various error-detecting codes: from very simple as parity bit ([1]) and repetition code ([2]) to more complex as checksum ([3], [4]), CRC ([5], [6]), etc. In our previous work we have also defined some error-detecting codes ([7], [8], [9]).

All error-detecting codes add redundant symbols on the input blocks, which are later used by the receiver in order to check whether there are errors in transmission. If the code detects that some data is incorrectly transmitted, it asks for retransmission of that data [10].

For every error-detecting code it is possible that there will be errors in transmission that the code will not detect. Therefore, before any code is implemented, it is important to know the ability of the code to detect errors. In this regard, it is important to know up to which number of incorrectly transmitted bits, the code will detect the error for sure. In this paper we will analyze an error-detecting code in the light of this parameter - the number of errors that the code surely detects. The number of errors that the code surely detects is the maximum number of incorrectly transmitted bits up to which the code will surely detect the error in transmission.

2. Definition of the Error-Detecting Code

Let A and B be non-singular binary matrices of order $s\times s$, and let C be a binary matrix of order $1\times s$. The alphabet is $\sum=\{0, 1, \ldots, 2^s-1\}$. We choose the parameter r of the model, which should be a non-negative integer.

Let the input block be $a_0a_1\ldots a_{n-1}$, where all symbols a_i are from the alphabet $\sum$. Then the redundant symbols are defined using the following equation:

$$(1)\ \boldsymbol{d_i} = \boldsymbol{a_i}A^{n-2} + \sum_{j=1}^{n-2} \boldsymbol{a_{i+j}}BA^{n-j-2} + C\sum_{j=0}^{n-3} A^j,\ \ i=0, 1, \ldots, r$$

where n is the length of the input block, r is the model's parameter that is an integer which satisfies the condition $1\le r\le n-1$. Bolded symbols are the binary representations of the corresponding symbols as $1\times r$ vectors, i.e., $\boldsymbol{a_i}$ is the binary representation of the information symbol a_i, $i=0, 1, \ldots, n-1$, while $\boldsymbol{d_i}$ is the binary representation of the redundant symbol d_i, $i=0, 1, \ldots, r$. A, B and C are the binary matrices that are used for coding. The operation + is binary addition and all operations in indexes are modulo n.

After calculating the redundant symbols, the binary form of the input block $\boldsymbol{a_0a_1\ldots a_{n-1}}$ is extended into a block $\boldsymbol{a_0a_1\ldots a_{n-1}d_0d_1\ldots d_r}$. With this is obtained the binary form of the coded block, which is transmitted through the binary symmetric channel.

From the above definition of the model we can see that this code always adds $r+1$ redundant symbol on each input block, regardless of its length. As we can see from the constrains for the parameter of the code r, the length of redundancy must not exceed the length of the input block.

When the receiver receives the output block, in order to ensure that it has a correct block, it calculates the redundant symbols using equation (1). If the calculated symbols are identical with the received ones, it accepts the block as correctly transmitted. In opposite, the receiver concludes that the block is not correctly transmitted. It that situation, the receiver asks the sender to send the block once again. But, there is always a small chance to have errors in transmission and at a same time the calculated by the receiver symbols to be equal to the received redundant symbols. This means that it is possible to have undetected errors in transmission. Therefore, it is important to know up to which number of incorrectly transmitted bits, the code will surely detect the error, which is exactly the subject of this paper.

But, first let see the coding procedure in the following example.

Example: In this example we will demonstrate the coding procedure. Let the following binary matrices of order 3×3 are used for coding:

$$A=\begin{bmatrix}1&0&1\\0&1&1\\1&1&1\end{bmatrix}, B=\begin{bmatrix}0&1&1\\1&1&1\\1&0&1\end{bmatrix}, C=[0\quad 0\quad 0]$$

The alphabet is $\sum=\{0, 1, 2, 3, 4, 5, 6, 7\}$.

Let suppose that the parameter of the model is $r=2$ and input block $a_0a_1a_2a_3a_4=46320$ of length $n=5$ symbols from the alphabet is coded. Then, the binary representations of the information symbols are $\boldsymbol{a_0}=[1\ 0\ 0]$, $\boldsymbol{a_1}=[1\ 1\ 0]$, $\boldsymbol{a_2}=[0\ 1\ 1]$, $\boldsymbol{a_3}=[0\ 1\ 0]$ and $\boldsymbol{a_4}=[0\ 0\ 0]$. The redundant symbols are calculated using (1), i.e.:

$\boldsymbol{d_i}=\boldsymbol{a_i}A^3+\boldsymbol{a_{i+1}}BA^2+\boldsymbol{a_{i+2}}BA+\boldsymbol{a_{i+3}}B$, $i=0, 1, 2$.

First, we obtain the matrices:

$$A^3=\begin{bmatrix}0&1&1\\1&0&1\\1&1&1\end{bmatrix}, BA^2=\begin{bmatrix}1&0&1\\1&1&1\\0&1&1\end{bmatrix}, BA=\begin{bmatrix}1&0&0\\0&0&1\\0&1&0\end{bmatrix}$$

Now,

$$\boldsymbol{d_0}=\boldsymbol{a_0}A^3+\boldsymbol{a_1}BA^2+\boldsymbol{a_2}BA+\boldsymbol{a_3}B=[1\ 0\ 0]\begin{bmatrix}0&1&1\\1&0&1\\1&1&1\end{bmatrix}+$$

$$[1\ 1\ 0]\begin{bmatrix}1&0&1\\1&1&1\\0&1&1\end{bmatrix}+[0\ 1\ 1]\begin{bmatrix}1&0&0\\0&0&1\\0&1&0\end{bmatrix}+[0\ 1\ 0]\begin{bmatrix}0&1&1\\1&1&1\\1&0&1\end{bmatrix}=$$

$$=[1\ 0\ 1]$$

$$\boldsymbol{d_1}=\boldsymbol{a_1}A^3+\boldsymbol{a_2}BA^2+\boldsymbol{a_3}BA+\boldsymbol{a_4}B=[1\ 1\ 0]\begin{bmatrix}0&1&1\\1&0&1\\1&1&1\end{bmatrix}+$$

$$[0\ 1\ 1]\begin{bmatrix}1&0&1\\1&1&1\\0&1&1\end{bmatrix}+[0\ 1\ 0]\begin{bmatrix}1&0&0\\0&0&1\\0&1&0\end{bmatrix}+[0\ 0\ 0]\begin{bmatrix}0&1&1\\1&1&1\\1&0&1\end{bmatrix}=$$

$$=[0\ 1\ 1]$$

$$\boldsymbol{d_2}=\boldsymbol{a_2}A^3+\boldsymbol{a_3}BA^2+\boldsymbol{a_4}BA+\boldsymbol{a_0}B=[0\ 1\ 1]\begin{bmatrix}0&1&1\\1&0&1\\1&1&1\end{bmatrix}+$$

$$[0\ 1\ 0]\begin{bmatrix}1&0&1\\1&1&1\\0&1&1\end{bmatrix}+[0\ 0\ 0]\begin{bmatrix}1&0&0\\0&0&1\\0&1&0\end{bmatrix}+[1\ 0\ 0]\begin{bmatrix}0&1&1\\1&1&1\\1&0&1\end{bmatrix}=$$

$$=[1\ 1\ 0]$$

The redundant symbol $\boldsymbol{d_0}$ over the alphabet $\sum$ is d_0=5, the symbol $\boldsymbol{d_1}$ over the alphabet $\sum$ is d_1=3 and the symbol $\boldsymbol{d_2}$ is d_2=6. With this we obtained the coded block $a_0a_1a_2a_3a_4d_0d_1d_2$=46320536, while the binary form is $\boldsymbol{a_0a_1a_2a_3a_4d_0d_1d_2}$=10011001101000010101111O. This coded block in binary form is transmitted through the binary symmetric channel.

Let suppose that the 14th information bit is incorrectly transmitted. This means that if we denote the output block that receiver receives with $\boldsymbol{a_0'a_1'a_2'a_3'a_4'd_0'd_1'd_2'}$, then $\boldsymbol{a_0'=a_0}$, $\boldsymbol{a_1'=a_1}$, $\boldsymbol{a_2'=a_2}$, $\boldsymbol{a_3'=a_3}$, $\boldsymbol{a_4'}$=[0 1 0]≠ $\boldsymbol{a_4}$, $\boldsymbol{d_0'=d_0}$, $\boldsymbol{d_1'=d_1}$, $\boldsymbol{d_2'=d_2}$. The receiver checks whether the block is correctly transmitted, i.e., using (1) it calculates the redundant symbols for the received block $\boldsymbol{a_0'a_1'a_2'a_3'a_4'}$.

$$\boldsymbol{d_0'}=\boldsymbol{a_0'}A^3+\boldsymbol{a_1'}BA^2+\boldsymbol{a_2'}BA+\boldsymbol{a_3'}B=[1\ 0\ 1]$$

$$\boldsymbol{d_1'}=\boldsymbol{a_1'}A^3+\boldsymbol{a_2'}BA^2+\boldsymbol{a_3'}BA+\boldsymbol{a_4'}B=[1\ 0\ 0]$$

$$\boldsymbol{d_2'}=\boldsymbol{a_2'}A^3+\boldsymbol{a_3'}BA^2+\boldsymbol{a_4'}BA+\boldsymbol{a_0'}B=[1\ 1\ 1]$$

Since $\boldsymbol{d_1}\neq\boldsymbol{d_1'}$ (also $\boldsymbol{d_2}\neq\boldsymbol{d_2'}$), the receiver concludes that there are errors in transmission, i.e., the received block is not identical with the block sent by the sender. Therefore, it demands retransmission of the block.

3. Results from the Simulation Procedure

In this paper, using simulations we will obtain the number of errors that the code surely detects. In the simulation process for a given n and r, we transmit through a simulated binary symmetric channel a large number of coded input blocks of length n over the alphabet $\sum$. For each i from 1 to the length of the coded input blocks in binary form, we calculate the percentage of transmitted coded blocks with i incorrectly transmitted bits in which the error in transmission is not detected. The number of errors that the code detects for sure is the largest integer v such that the percentage of incorrectly transmitted coded blocks with i incorrectly transmitted bits in which the error is not detected is equal to 0% for all i from 1 to v. In order to obtain reliable and accurate results, we chose the probability of bit-error in the simulated binary-symmetric channel such that the number of incorrectly transmitted coded blocks with i incorrectly transmitted bits to be large number for small values of i, i.e., values of i smaller than or equal to v.

In the coding procedure, we use the following binary matrices A, B and C:

$$A=\begin{bmatrix}1&0&1\\0&1&1\\1&1&1\end{bmatrix}, B=\begin{bmatrix}0&1&1\\1&1&1\\1&0&1\end{bmatrix}, C=[0\quad 0\quad 0]$$

The alphabet is $\sum$={0, 1, 2, 3, 4, 5, 6, 7}. We will consider the cases when the parameter of the model r=2, r=3 and r=4.

Since the length of the redundancy is r+1 symbol, follows that in the case when r=2, the length of the redundancy is 3 symbols from the alphabet $\sum$. Since the length of the input block must be greater than or equal to the length of the redundancy, in this case the length of the input block n must be greater than or equal to 3 symbols from the alphabet $\sum$ (Fig. 1). Each element from the alphabet of order 8 is presented with 3 bits in the binary representation. Therefore, in this case the redundancy has length 9 bits.

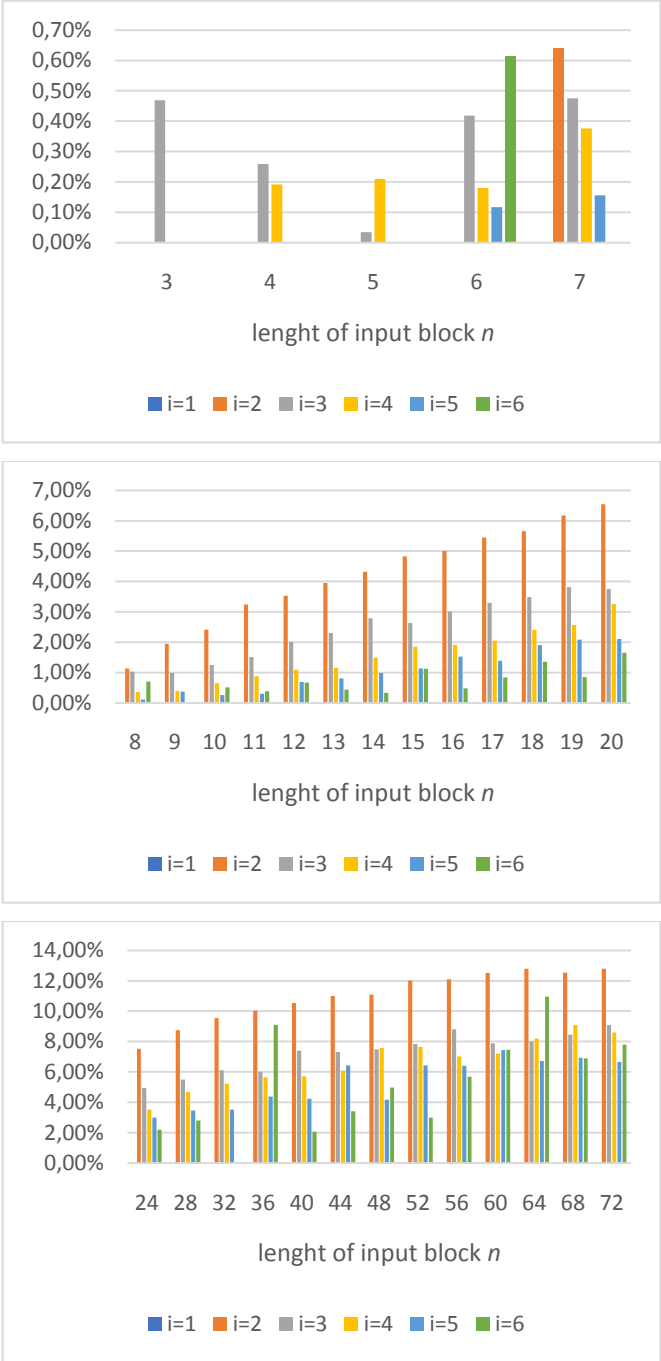

Fig. 1 *Percentage of undetected incorrectly transmitted coded blocks with i incorrectly transmitted bits when input blocks have length n symbols from the alphabet* $\sum$ *in the case when the redundancy is 9 bits.*

In Fig. 1 are given the percentages of incorrectly transmitted coded blocks in the simulation process in which i≤6 bits are incorrectly transmitted and the error in transmission is not detected in the case when the redundancy is 9 bits (r=2). The length of the input blocks n is expressed in a number of symbols from the alphabet $\sum$. Please note that the scaling of the y-axis is different on the three graphs. For small values of the length of the input block n, the percentages of undetected incorrectly transmitted blocks with i incorrectly transmitted bits are very small. In order the results to be visible they are separated in the first figure from Fig. 1. Since the percentages of undetected incorrectly transmitted blocks with i incorrectly transmitted bits increase when n increases, the scaling of the second and third image from Fig. 1 is adjusted accordingly.

As we can see from Fig. 1, when the length of the input blocks is n=3 symbols from $\sum$, the percentage of undetected incorrectly

transmitted blocks with i incorrectly transmitted bit is different than 0% only for i=3. Since the code detected all incorrectly transmitted blocks with 1 or 2 incorrectly transmitted bits, but there are blocks with 3 incorrectly transmitted bits in which the error is not detected, the number of errors that the code surely detects when the length of the input blocks is n=3 symbols from $\sum$ is 2. Also, in the case when the length of the input blocks is n=4, the smallest value of i for which the percentage of undetected incorrectly transmitted blocks with i incorrectly transmitted bits is different than 0% is 3. Therefore, we conclude that in this case the code surely detects also up to 2 incorrectly transmitted bits. The same conclusion holds also in the cases when the length of the input block n is 5 or 6 symbols from the alphabet $\sum$. For input blocks with length greater than or equal to 7 symbols, the percentage of undetected incorrectly transmitted blocks with 2 incorrectly transmitted bits is positive (there is the orange pillar), from where follows that in this case the code surely detects 1 incorrectly transmitted bit.

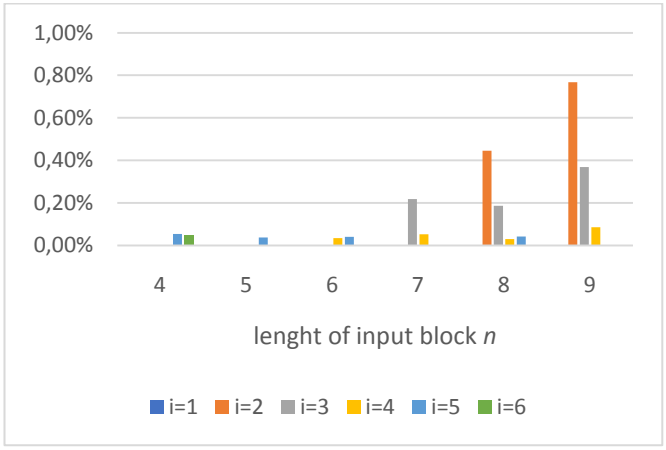

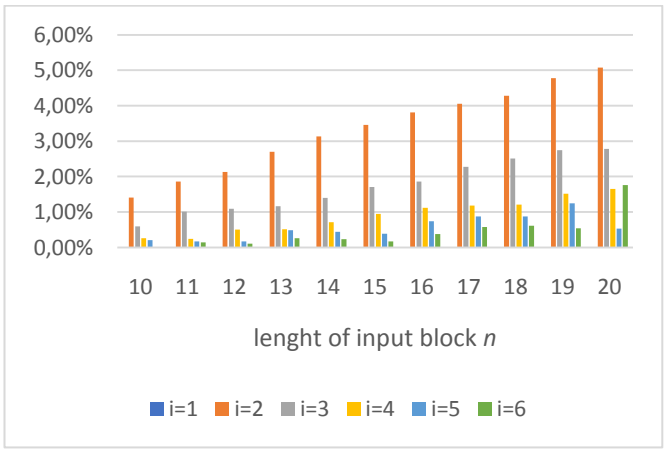

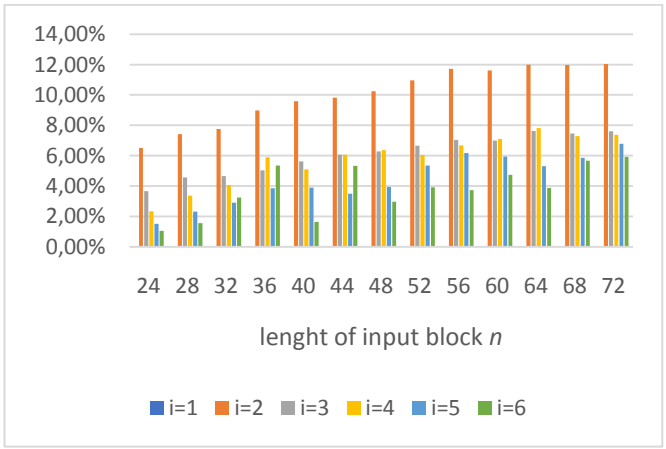

Fig. 2 *Percentage of undetected incorrectly transmitted coded blocks with i incorrectly transmitted bits when input blocks have length n symbols from the alphabet $\sum$ in the case when the redundancy is 12 bits.*

The results when r=3 are given in Fig. 2. In this case the length of the redundancy is 4 symbols from the alphabet $\sum$ (i.e., 12 bits in the binary representation). Therefore, in this case the length of the input block must be greater than or equal to 4 symbols from $\sum$. From Fig. 2, we can see that in the case when the redundancy is 12 bits, the code surely detects up to 4 incorrectly transmitted bits when the length of the input block is 4 or 5 symbols from $\sum$. When the input block has length 6 symbols, the code surely detects up to 3 incorrectly transmitted bits, while when the input block has length 7 symbols, the code surely detects up to 2 incorrectly transmitted bits. When the input block has length greater than or equal to 8 symbols, the code surely detects 1 incorrectly transmitted bit.

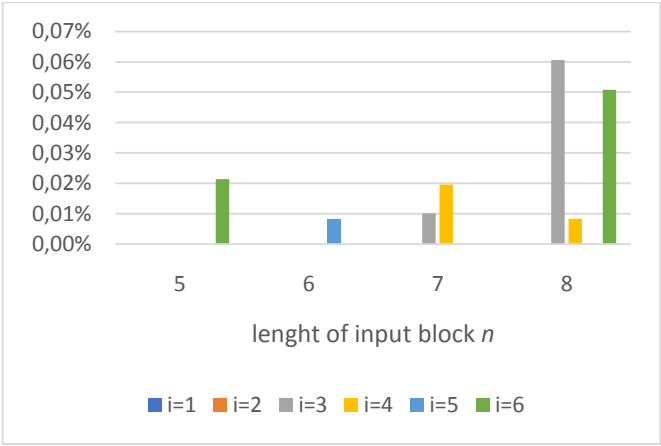

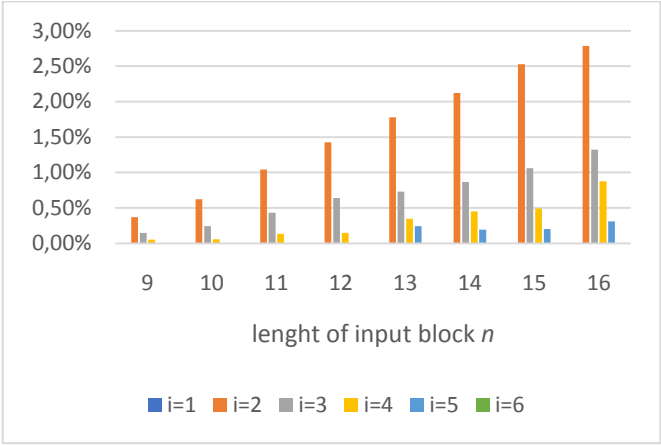

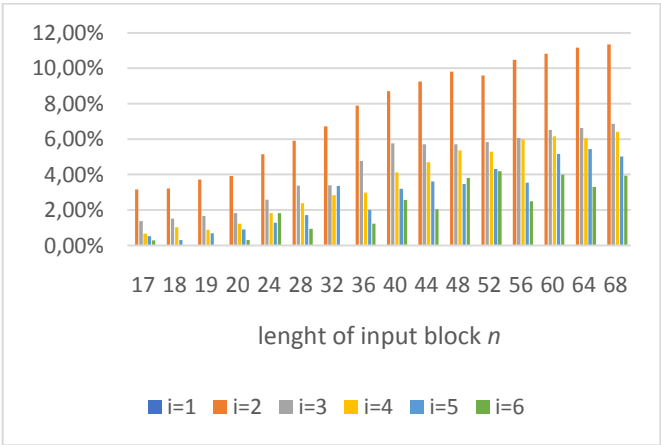

Fig. 3 *Percentage of undetected incorrectly transmitted coded blocks with i incorrectly transmitted bits when input blocks have length n symbols from the alphabet $\sum$ in the case when the redundancy is 15 bits*

Similarly, when the parameter r=4, the redundancy is 5 symbols from $\sum$ (i.e., 15 bits in the binary representation) and the length of the input blocks $n \geq 5$ (Fig. 3). When the length of the input block is 5 symbols, the code surely detects up to 5 incorrectly transmitted bits, while when the length of the input block is 6 symbols, the code

surely detects up to 4 incorrectly transmitted bits. For input blocks with length 7 or 8 symbols, the code surely detects up to 2 incorrectly transmitted bits. When the length of the input block is greater than 8 symbols, the code detects for sure 1 incorrectly transmitted bit.

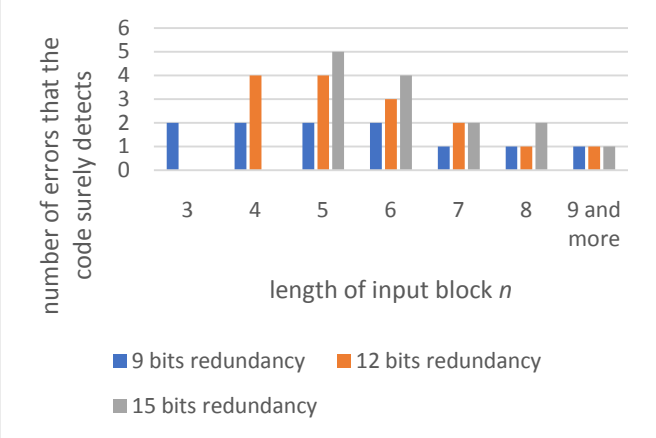

Fig. 4 *Number of incorrectly transmitted bits that the code surely detects when the length of the input blocks is n symbols from the alphabet ∑ and the redundancy is 9, 12 and 15 bits.*

In Fig. 4 and Fig. 5 are presented the numbers of incorrectly transmitted bits that the code surely detects when the redundancy is 9, 12 and 15 bits. On *x*-axis in Fig. 4 is given the length of the input block, on *y*-axis is given the number of errors that the code surely detects, while the color of each pillar represents the length of the redundancy.

From Fig. 4 we can see that when the length of the input block is fixed, if longer redundancy is added to the input blocks, then the number of incorrectly transmitted bits that the code detected for sure is greater or at least equal to the number of surely detected incorrectly transmitted bits when a shorter redundancy is added. This is expected result since longer redundancy means that each information symbol is controlled by more redundant symbols.

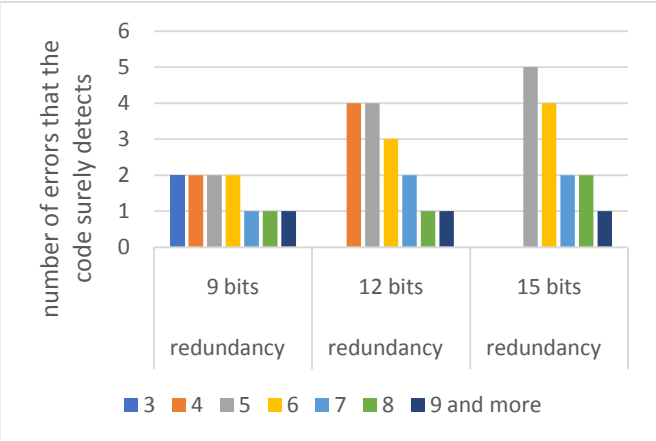

Fig. 5 *Number of incorrectly transmitted bits that the code surely detects when the length of the input blocks is n symbols from the alphabet ∑ and the redundancy is 9, 12 and 15 bits.*

On Fig. 5 on *x*-axis is given the length of the redundancy, while the length of the input blocks *n* is represented with the color of the pillars. As we can see from Fig. 5, regardless of the length of the redundancy, when the length of the input block increases and the length of the redundancy is fixed, the number of errors that the code surely detects decreases or remains the same.

As we can see from Fig. 4 and Fig. 5, the best result from the aspect of the number of errors that the code surely detects is achieved when the length of the input blocks is 5 symbols from the alphabet ∑ and the redundancy has length 15 bits. This means that from the aspect of the number of errors that the code surely detects, it is best to divide the input message into blocks of length 5 symbols from ∑ and to code these blocks such that the redundancy is 15 bits (i.e., to choose the parameter *r* in the model to be 4). In this case the code will detect for sure every incorrectly transmitted coded block with up to 5 incorrectly transmitted bits.

4. Conclusion

The results for the number of errors that the code surely detects when the given binary matrices *A*, *B* of order 3×3 and zero matrix *C* of order 1×3 are used for coding are the following:

In the case when the redundancy has length 9 bits, the code surely detects up to 2 incorrectly transmitted bits when the length of the input block is smaller than or equal to 6 symbols from ∑. For input blocks with length greater than or equal to 7 symbols, the code surely detects 1 incorrectly transmitted bit.

When the redundancy is 12 bits, the code surely detects up to 4 incorrectly transmitted bits when the length of the input block is 4 or 5 symbols from the alphabet ∑, up to 3 incorrectly transmitted bits when the input block has length 6 symbols, up to 2 incorrectly transmitted bits when the input block has length 7 symbols and 1 incorrectly transmitted bit when the input block has length greater than or equal to 8 symbols.

When the redundancy has length 15 bits, the code surely detects up to 5 incorrectly transmitted bits when the length of the input block is 5 symbols, up to 4 incorrectly transmitted bits when the length of the input block is 6 symbols, up to 2 incorrectly transmitted bits when the length of the input blocks is 7 or 8 symbols. The code surely detects 1 incorrectly transmitted bit when the length of the input block is greater than or equal to 9 symbols.

When the length of the input blocks is fixed, the number of errors the code surely detects does not decrease with increasing redundancy length. If the length of the redundancy is fixed, then when the length of the input block increases, the number of errors that the code surely detects decreases or remains the same.

In order to achieve largest number of surely detected incorrectly transmitted bits, the input message should be divided into blocks of length 5 symbols and each block to be coded separately such that the parameter of the model is *r*=4.

5. References

[1] Ziemer R. E., Tranter W. H., "Principles of communication: systems, modulation, and noise," Wiley, 2014.
[2] Bossert M., "Channel Coding for Telecommunications," Wiley, 1999.
[3] Fenwick P., "Checksums and Error Control," Introduction to Computer Data Representation, Bentham Science Publishers, 2014.
[4] Verhoeff, J., "Error Detecting Decimal Codes (Tract 29)," The Mathematical Centre, Amsterdam, 1969.
[5] Peterson W. W., Brown D. T., "Cyclic Codes for Error Detection," Proceedings of the IRE. 49 (1), 1961, pp. 228–235.
[6] Koopman P., "32-Bit Cyclic Redundancy Codes for Internet Applications," Proceedings of The International Conference on Dependable Systems and Networks, 2002, pp. 459–468.
[7] Bakeva V., Ilievska N., "A probabilistic model of error-detecting codes based on quasigroups", Quasigroups and Related Systems, vol. 17, 2009, pp. 135-148.
[8] Ilievska N., "Proving the probability of undetected errors for an error-detecting code based on quasigroups," Quasigroups and Related Systems, vol. 22, 2014, pp. 223 – 246.
[9] Ilievska N., Gligoroski D., "Simulation of some new models of error-detecting codes," Proceedings of the 22nd Telecommunications Forum Telfor, Belgrade, Serbia, pp. 395-398, 2014.
[10] Klove T., "Codes for Error Detection," World Scientific, 2007.

STUDY OF STRESS-STRAIN STATE AND TEMPERATURE FIELD DURING ROLLING UNDER THE NEW SCHEME WITH ALTERNATING AND SHEAR DEFORMATIONS

Abdrakhman Naizabekov, d.t.s., professor[1], Sergey Lezhnev, c.t.s., associate professor[1], Evgeniy Panin, PhD, associate professor[2]
Rudny industrial Institute, Rudny, Kazakhstan[1]; Karaganda state industrial University, Temirtau, Kazakhstan[2],
email: naizabekov57@mail.ru, sergey_legnev@mail.ru, cooper802@mail.ru

Abstract: *In this paper, a computer simulation of a new technology of thick-sheet rolling, including rolling in rolls with a relief surface followed by rolling on rolls with a smooth barrel to the desired size. The analysis of effective plastic deformation, hydrostatic pressure and temperature field was carried out according to the results of modeling. According to the results of the analysis of effective strain, maximum of processing in the first pass receives the ridge area, but after the second pass observed alignment distribution of this parameter over the cross section. The study of the temperature field showed that the greatest temperature difference in the cross section occurs when rolling in relief rolls, in the future when rolling in smooth rolls due to the increase in the contact surface area, this difference decreases. Analysis of hydrostatic pressure showed the presence of both compressive and tensile stresses in the deformation zone. Such distribution is caused by the presence of a relief surface after 1 pass in the further alignment of the strip profile, which occurs both in the longitudinal and transverse directions.*

Keywords: ROLLING, SHEAR DEFORMATION, SIMULATION, TEMPERATURE, STRESS-STRAIN STATE.

1. Introduction

Obtaining high-quality products, i.e. products that fully meet the needs of the consumer, realizing the greatest economic effect and having the highest technical, economic and operational indicators, in metallurgical and machine-building production is mainly associated with the development of new technological processes. Thus, one of the primary and most urgent tasks of metallurgical production is to obtain high-quality cast billets, as well as the modernization of existing and development of new technological schemes of rolling capable of providing the study of the cast structure, a high level of mechanical properties and performance of the finished product. Currently, the use of technological processes of rolling with the use of classical tools and existing deformation schemes do not fully provide the required level of mechanical and operational properties due to the uneven distribution of the degree of deformation in the metal volume. Therefore, a promising direction to improve the quality of finished products is the development of new deformation schemes, including those implementing intensive shear or alternating deformation in the entire volume of the processed metal.

For introduction into production, a new technological scheme for rolling thick-sheet blanks was proposed, which implements intensive shear deformation without significant changes in the geometric parameters of the original workpiece. This technological scheme includes rolling in rolls with a relief surface followed by rolling of relief blank in rolls with a smooth barrel to the desired size. The technological scheme is presented in figure 1.

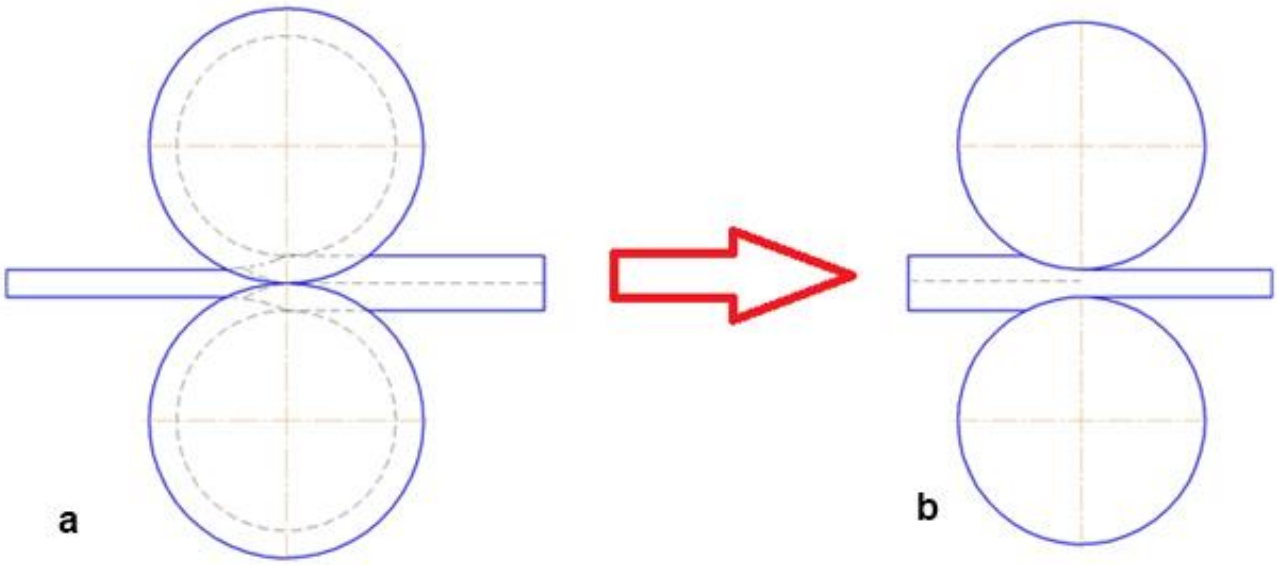

a) rolling in rolls with a relief surface; b) alignment and subsequent rolling in rolls with a smooth barrel
Fig. 1 *Scheme of rolling according to the proposed technology*

The surface of the relief rolls is made in the form of annular grooves forming projections and depressions of trapezoidal shape along the entire length of the roll barrel and located at an angle of 90° degrees to the rolling axis [1]. At rolling in rolls with a relief surface there is an introduction of trapezoidal segments of protrusions in the workpiece and due to features of the form there is a displacement of a part of metal in deepening of hollows. As a result, the intensification of shear deformation along the section of the workpiece is carried out with the formation of alternating protrusions and depressions on the surface of the workpiece in the form of trapezoidal segments. During the subsequent rolling of the workpiece in smooth rolls, conditions are created to ensure the alternating flow of metal when alignment the surface of the roll with the preservation of the original geometry of the workpiece.

The purpose of this work is to study the influence of the proposed deformation scheme on the stress-strain state of the metal and the distribution of the temperature field over the cross-section of the workpiece.

2. Computer model of process

The use of only theoretical methods of analysis of technological processes can not be effective for a number of reasons. To implement an objective and more accurate analysis, in addition to theoretical calculations, it is necessary to resort to new innovative technologies. One of the most effective technologies productive in the development and research of materials processing pressure is computer modeling. One of the most productive and popular is the Simufact Forming software package - a specialized software package designed to simulate the processes of metal forming.

Based on previous studies [2], when modeling a new technological scheme of rolling, including rolling in relief rolls, it was decided to use relief rolls with an unequal ratio of the protrusion to the cavity, providing the same values of the roll gap at different points (figure 2a). The use of such rolls allows to implement a simple shift scheme, which most favorably affects the preservation of the original dimensions of the workpiece than the use of rolls with an equal ratio of the protrusion to the cavity (figure 2b), where in addition to the shift is carried out and compression on the inclined sections of the rolls.

a) 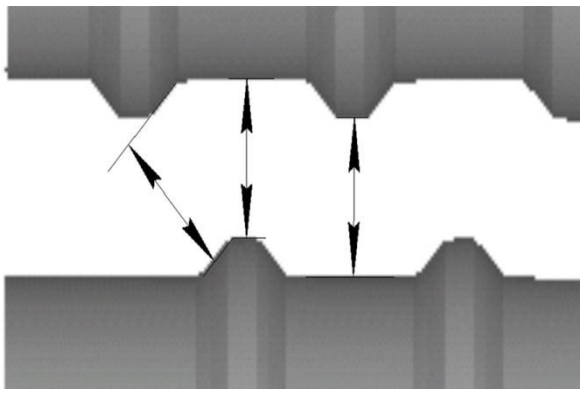 b) 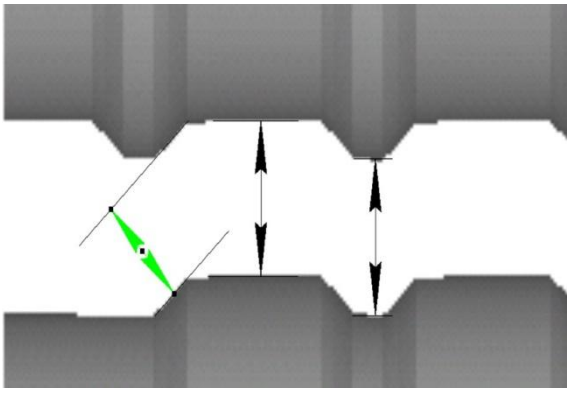

a) unequal ratio of the protrusion to the cavity; b) equal ratio of the protrusion to the cavity.

Fig. 2 *Variants of ratio of the protrusion to the cavity*

When constructing the geometry of relief rolls for modeling, the following dimensions were adopted:

- diameter of the proposed roll-embossed surface for the clamps is 200 mm;
- barrel length 380 mm (these values correspond to the geometric dimensions of rolls for existing laboratory mill DUO 200);
- depth of the depression is equal to the height of the protrusion is 10 mm.
- bevel groove on the projections and depressions is 45°.

The design of the gap in the relief rolls is shown in figure 3. The total gap between the two opposite cavities of the roll was 20 mm.

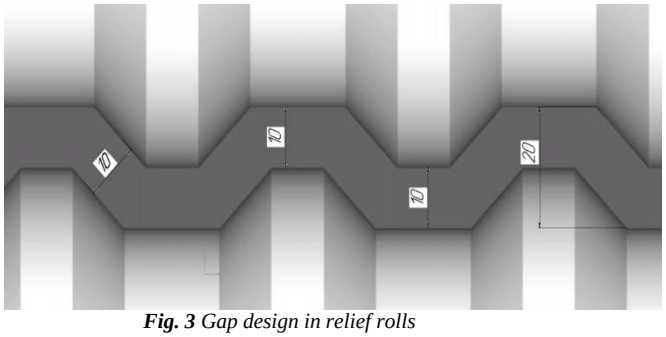

Fig. 3 *Gap design in relief rolls*

The following technological parameters in computer modeling of the process were used:

Rolling was carried out at room temperature (20°C);

The temperature of the workpiece before rolling was 1000°C;

The thermal conductivity coefficient was 7000 $W/(m^2 \cdot ℃)$;

The Siebel friction model (the contact stress exceeds the yield strength);

Friction coefficient was 0.7;

The rolling speed was 1.25 rad/s.

The initial blank is a thick sheet of rectangular shape with dimensions h x b x l = 10 x 140 x 200 mm. Material for the workpiece the steel AISI 1015 was selected.

Smooth rolls were made with geometric dimensions: the diameter of the barrel rolls is 200 mm, barrel length is 380 mm.

After importing the geometry files into the Simufact Forming, a computer model was obtained (figure 4) consisting of 3 consecutive rolling stands: the first stand with relief rolls, where the workpiece undergoes shaping and shear deformation, the second and third - with rolls with a smooth barrel. The second and third stands serve to align the relief shape of the workpiece obtained in the first pass to its original geometric shape (flat form), while the alternating deformation is realized in the metal, contributing to a more intensive study of the original metal structure.

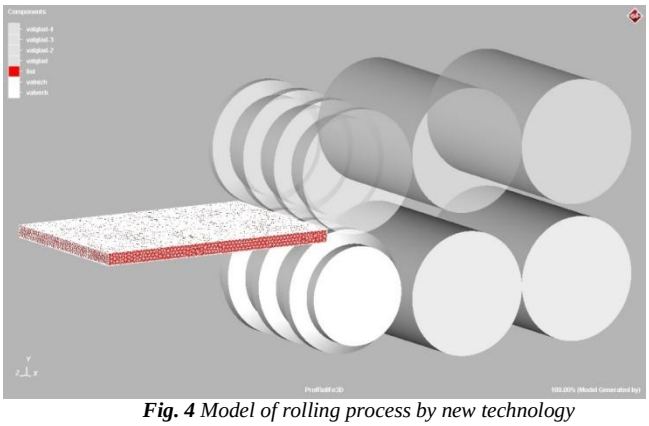

Fig. 4 *Model of rolling process by new technology*

3. Simulation results

The whole rolling process can be divided into three main stages. At the first stage, the preheated to the temperature of rolling beginning the workpiece is fed into the roll gap of the proposed design and a single compression in the first pass is carried out until the cavity of the rolls is completely filled with metal (figure 5a). After rolling in the 1st stand on the workpiece surface the alternating protrusions and depressions in the form of trapezoidal segments are formed. This stage is characterized mainly by shear deformation, but there is also a high-altitude deformation at the junction of the projections, contributing to the capture of the

workpiece. In order to align the surface of the profiled workpiece after rolling in relief rolls, it is rolled in stands equipped with rolls with a smooth barrel (figure 5b-c) (second and third stage). In this case the conditions are created to ensure the alternating flow of metal when alignment the metal surface when rolling in smooth rolls with the preservation of the original shape of the workpiece.

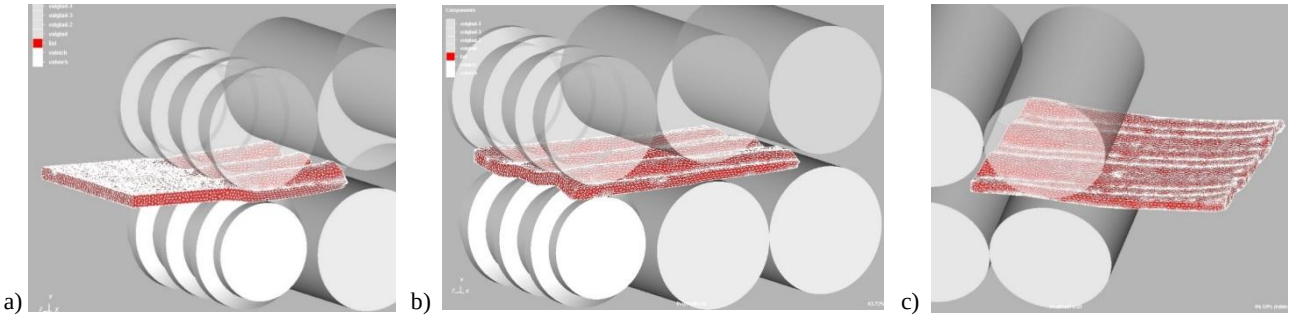

Fig. 5 *Stages of the rolling process*

In the study of any metal forming process, the key step before laboratory or industrial testing is the study of the stress-strain state (SSS). It will allow to reveal distribution of stresses and strains in the considered process, and also to define their critical values that will give the chance to check the working tool on durability.

Effective plastic strain shows the intensity of the workpiece throughout its cross-section. This parameter also allows you to track the degree of accumulated deformation, which is cumulative. When studying the strain state, it is necessary not only to provide a high level of equivalent strain required for the formation of a fine-grained structure, but also a uniform distribution of this parameter over the section of the workpiece.

At the first stage (figure 6a) deformation develops during rolling in the deformation center in relief rolls. From the results obtained, it was revealed that the maximum value of effective plastic strain is concentrated at the junction of the roll ridges and is 0.4. Also, the cross-section of the workpiece is observed shear deformation, its value is in the range of 0.25-0.35. The difference in equivalent strain values was 62.5 %. At the second stage (alignment of the workpiece in smooth rolls) there is a further increase in the equivalent deformation (figure 6b). There is also a cross-section alignment of the deformation, as evidenced by a decrease in the difference in the values of the equivalent deformation to 50 %. From the results at stage 3, it can be said about the uniform distribution of accumulated deformation (figure 6c). The difference in equivalent strain values is less than 20 %.

Also, in the SSS study, it is very useful to study the temperature conditions of the process, since the change in the temperature of the deformed metal significantly affects the energy-power parameters of deformation.

Figure 7a shows the temperature distribution on the surface and in the cross section of the workpiece when rolling in relief rolls. In the center of deformation during the process there is an increase in temperature to 1070°C, which improves the plastic properties of the workpiece. In other parts of the workpiece is maintained uniform temperature distribution. According to the laws of thermodynamics, the cooling of the surface layers is faster than the internal, so the temperature of the end parts of the workpiece has decreased to 970°C.

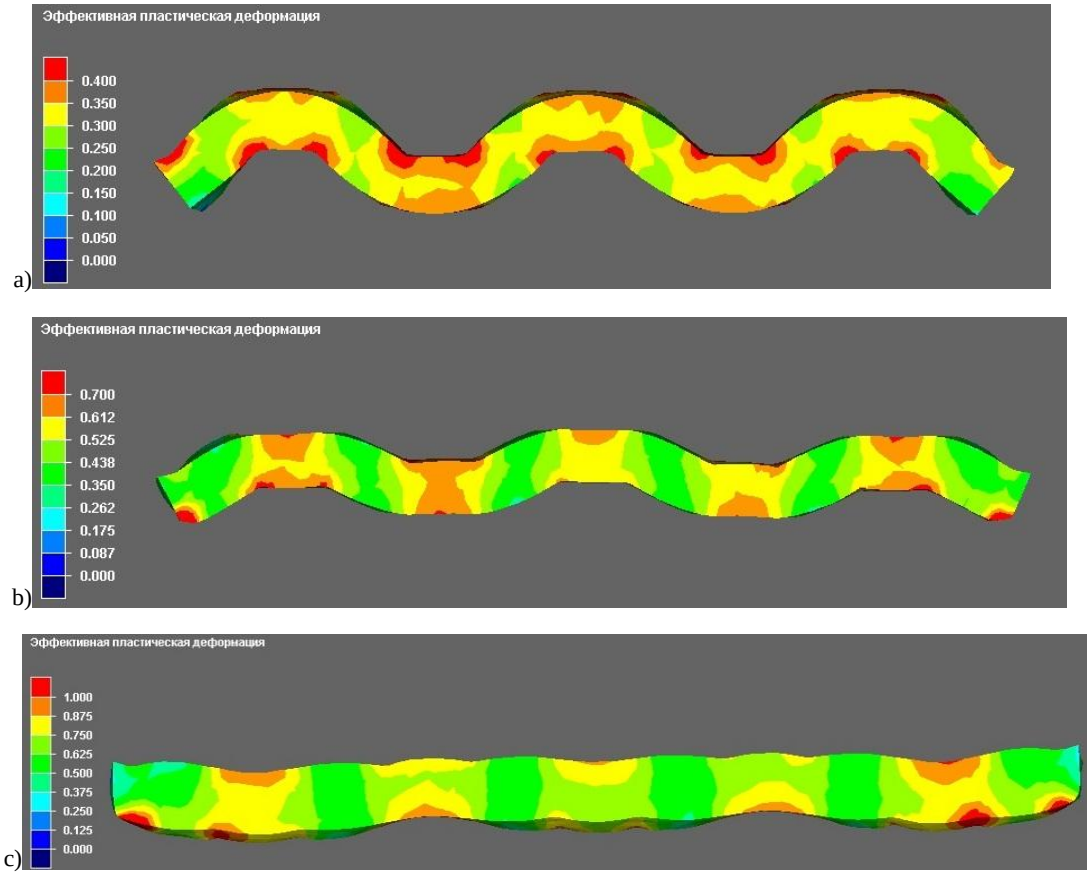

Fig. 6 *Effective plastic strain of the workpiece by passes*

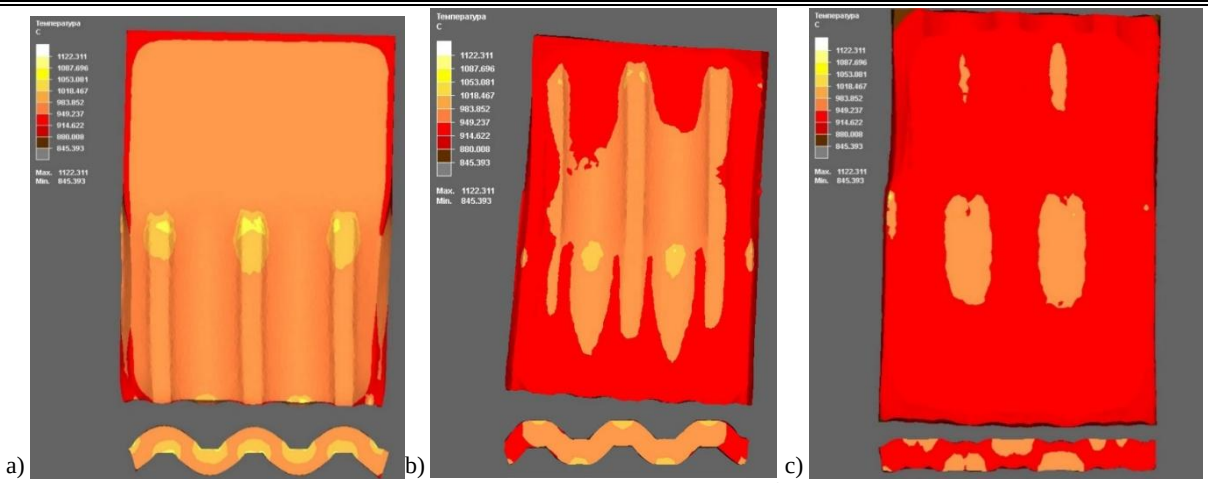

a) b) c)

Fig. 7 *Temperature distribution at each stage of rolling*

In the second stage (figure 7b), most of the surface cools to temperatures of 950°C and only in the deformation center the temperature reaches 1040°C. At the third stage of rolling (figure 7b), almost the entire surface of the workpiece, in addition to the deformation center, cools to 920°C. On the cross section, the temperature difference of the workpiece layers can be clearly observed.

Another important component in the SSS study is hydrostatic pressure. Hydrostatic pressure shows the intensity of compressive and tensile stresses across the workpiece section, i.e. the value of the stress can take both positive and negative values. By analyzing this parameter, it is possible to identify those zones that are exposed to tensile stresses, i.e. are the most dangerous from the point of view of defects. From the results obtained, it can be concluded that at the first stage of rolling (figure 8a) at the point of contact of the roll with the workpiece, the hydrostatic pressure fluctuates between -150÷-100 MPa. The compressive nature of stresses is due to the fact that in addition to shear deformation in the place of formation of ridges and troughs, a certain proportion of high-altitude deformation occurs. In the undeformed zone of the workpiece, a pressure value within 30÷50 MPa is observed. The tension of the central layers of the workpiece remained unchanged.

At the second stage (figure 8b) in the process of the workpiece alignment on smooth rolls in the zone of the deformation center, a hydrostatic pressure within -350÷-300 MPa is created. In places the top of the ridge there are tensile stresses.

In the center of deformation at the secondary alignment of the workpiece on smooth rolls (figure 8c), the value of hydrostatic pressure reaches -450÷-500 MPa. The cross-section of the workpiece clearly shows the accumulation of compressive stress at the base (origin) of the ridges, this is due to the occurrence of backpressure during the lateral flow of the metal (there is a collision of the lateral flows of the metal flow during the alignment of the ridges). The voltage in this area reaches 130 MPa.

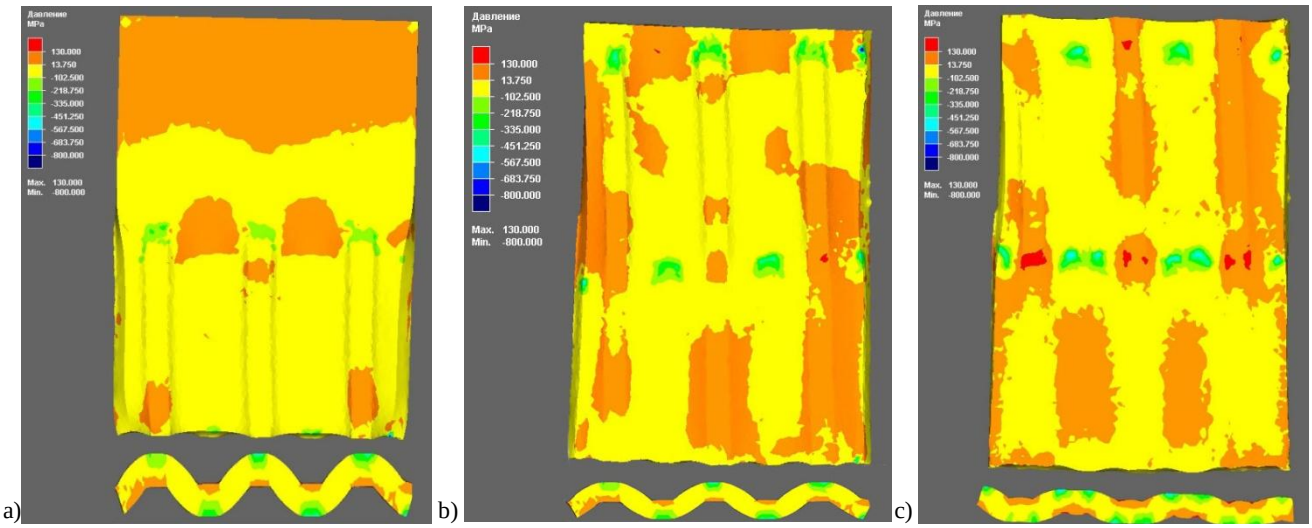

a) b) c)

Fig. 8 *Hydrostatic pressure distribution*

Conclusions

In this paper, a computer simulation of a new technology of thick-sheet rolling, including rolling in rolls with a relief surface followed by rolling on rolls with a smooth barrel to the desired size. The analysis of effective plastic deformation, hydrostatic pressure and temperature field was carried out according to the results of modeling. According to the results of the analysis of effective strain, maximum of processing in the first pass receives the ridge area, but after the second pass observed alignment distribution of this parameter over the cross section. The study of the temperature field showed that the greatest temperature difference in the cross section occurs when rolling in relief rolls, in the future when rolling in smooth rolls due to the increase in the contact surface area, this difference decreases. Analysis of hydrostatic pressure showed the presence of both compressive and tensile stresses in the deformation zone. Such distribution is caused by the presence of a relief surface after 1 pass in the further alignment of the strip profile, which occurs both in the longitudinal and transverse directions.

References

1) Патент РК № 14791. Валки для прокатки толстых листов. Найзабеков А.Б., Лежнев С.Н. 2007, Бюл. № 22.

2) A. Naizabekov, S. Lezhnev, E. Panin, T. Koinov, I. Mazur. Research and development of technology for rolling of high-quality plates of non-ferrous metals and alloys in relief rolls. Journal of Chemical Technology and Metallurgy, 51, 4, 2016, 363-370.

MULTIPARAMETER HYBRID NEURAL NETWORK METAMODEL OF EDDY CURRENT PROBES WITH VOLUMETRIC STRUCTURE OF EXCITATION SYSTEM

Trembovetska R., PhD Eng., Assoc. Prof .; Halchenko V., Dr.Sc. Eng., Prof .; Tychkov V., PhD Eng., Assoc. Prof.
Faculty of Electronic Technologies and Robotics – Cherkasy State Technological University, Ukraine

r.trembovetska@chdtu.edu.ua

Abstract: *A multiparameter metamodel of the eddy current probe with the volumetric excitation structure is constructed. As variable parameters of the metamodel, the spatial coordinates of the testing zone, the radii of the excitation coils and the height of their location above the testing object were used. Due to the use of hybrid construction of multiple neural networks using decomposition of the search space, an acceptable metamodel's error of the eddy current probe with volumetric excitation structure is obtained.*

Keywords*:* EDDY CURRENT PROBE, UNIFORM SENSITIVITY, VOLUMETRIC EXCITATION STRUCTURE, EDDY CURRENTS DENSITY, NEURAL NETWORKS, HYBRID RBF-METAMODEL

1. Introduction

Some difficulties associated with the non-uniform sensitivity of the probe in the testing zone are characteristic for the defectometry problems solution by the eddy current method. The non-uniform sensitivity is due to the exponential eddy currents density distribution (ECDD) in the testing object (TO) and is inherent in any type of excitation coils, so their using in this case is not effective. In defectometry the best sensitivity characteristic in the testing zone is considered to be uniform, the so-called P-shaped. In this case, the effect of the dependence of the probe sensitivity to the location of the defect in the testing zone is reduced. Thus, there is a need to create eddy current probes (ECP) with uniform sensitivity, and, consequently, the uniform ECDD in the TO zone. One of the ways to solve this kind of problem is the optimal surrogate synthesis of the excitation system (ES) of ECP. Using parametric non-linear synthesis, a sectioned excitation coil system is created and takes into account the shape, electrophysical parameters of the TO and a priori given uniform sensitivity characteristic.

In [1] the problem of the linear synthesis of ECP with a given structure of the excitation field in the TO zone is considered. In addition, since the linear values of the ECDD were obtained with the help of linear synthesis, the practical implementation of such ECP's is complicated. The cases, when the given field structure is obtained with non-linear parameters of the probe are not considered in these work.

The non-linear synthesis problem was solved in [2]. The problem solution for the optimal placement of the section coils and their geometric dimensions provided the fixed value of the excitation current density in them is obtained. The structural-parametric synthesis method of the source of the electromagnetic field [3] allows us to solve the problem of choosing the structure of the ES ECP. However, the presence of a conductive medium and the speed effect, i.e. at motionless ECP relatively TO is not taken into account.

2. Background and means to solve the problem

A number of works by the authors of [4–6] are devoted to solving the problems of the non-linear, in the general case, synthesis of non-coaxial circular EDP's with a planar ES structure. A characteristic feature of a planar ES structure is the presence of M coils of radii r_k $(k = 1...M)$ with their uniform $\Delta r = const$ or non-uniform $\Delta r = var$ arrangement, which are at the same height z_0 above the TO [7] and switched on counter or consensually "across the field" (Fig. 1). For such task the synthesis parameters are three variables $J=f(x, y, r)$: spatial coordinates x, y of the testing zone and the radii of the excitation coil sections r.

Moreover, the obtained ES of planar design with a uniform or un- uniform arrangement of coils provides a value of the reduced error in the uniform of the ECDD in the testing zone from 9 to 11 %, which is not an entirely acceptable result, and leaves the desire to further improve the structure of the ES [4-8].

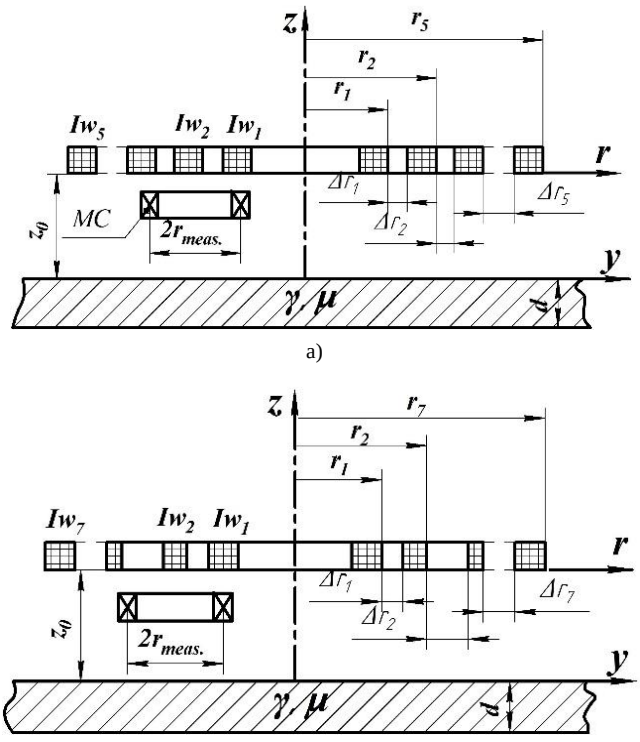

Fig. 1 *Variants of the arrangement of the coil sections of the surface ECP with a planar ES structure: a) uniform Δr = const; b) un-uniform Δr = var; MC - measuring coil*

3. The solution to the problem

As a result, there is a need to study probes with a volumetric structure of ES, both of a homogeneous and heterogeneous structure (Fig. 2).

The arrangement of coils of surface ECP's of a volumetric ES can be either uniform when $\Delta r = const$, $z_1 = z_k = const$, or non-uniform $\Delta r = const$, $z_1 \neq zk$ (Fig. 3).

In contrast to the planar structure of the ES, the number of parameters of the synthesis problem increases, i.e. the height of the coils above TO z_0 is added $J=f(x, y, r, z_0)$. As in the simpler case of the planar design of the probe, one cannot do without the ECP metamodel $\hat{J}=f(x, y, r, z_0)$, which significantly reduces the calculation time and it becomes possible to solve the synthesis problem.

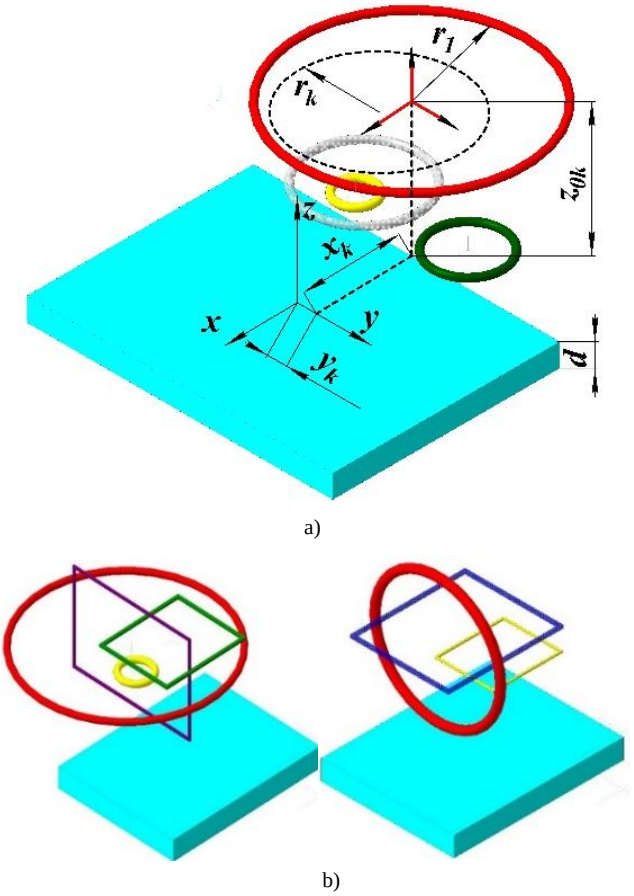

Fig. 2 *Volumetric structures of ES ECP: a) homogeneous; b) heterogeneous*

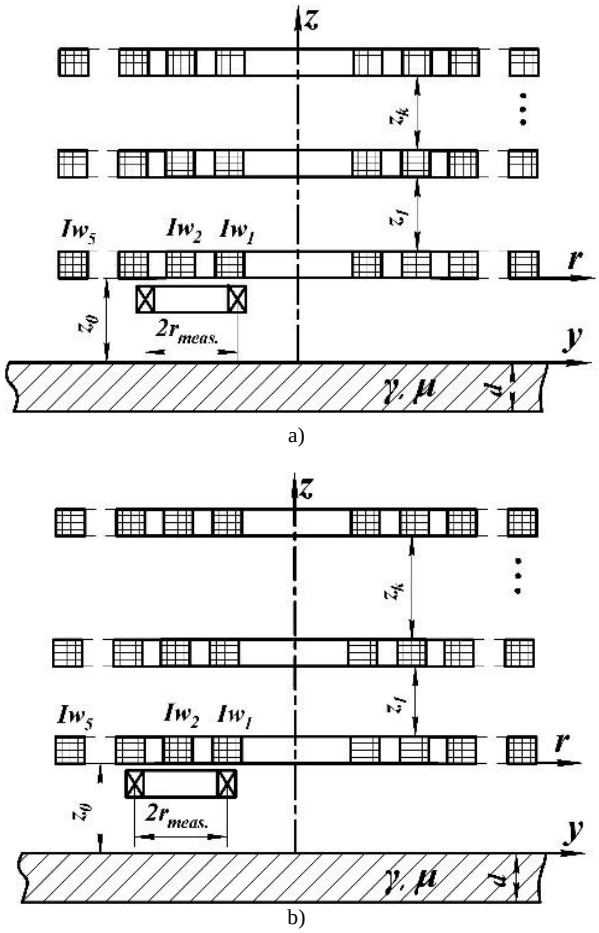

Fig. 3 *Arrangement of sections of coils of surface ECP's of a volumetric homogeneous structure ES: a) uniform Δr = const, $z_1 = z_k$ = const; b) un-uniform Δr = const, z1 ≠ zk*

The aim of the work is constructing a multiparameter hybrid RBF-metamodel of eddy current probes with volumetric homogeneous excitation structure.

On the basis of a mathematical model of a moving surface ECP, which was obtained analytically by solving the direct problem of electrodynamics in the form of Maxwell's differential equations [6], a neural network metamodel that takes into account the change in four parameters simultaneously $\hat{J}=f(x, y, r, z_0)$ was constructed. The metamodel for the moving structure of the ES ECP in the form of ampere-coils located at different heights above the TO (Fig. 3) with the following initial data: TO thickness d = 10 mm; excitation current frequency f = 5 kHz; electrophysical parameters of the material TO $\sigma = 3{,}745 \cdot 10^7$ Sm/m, $\mu_r = 1$, the speed of the probe relative to TO $\vec{v} = (40, 0, 0)$ m/s was constructed. Variable model parameters are: spatial coordinates of the testing zone x = -45 ... 45 mm; y = 0 ... 35 mm; the radii of the coils ES r = 2 ... 15 mm; their height above TO z_0 = 2 ... 5 mm.

Next, the construction of a metamodel of a moving surface ECP in accordance with the algorithm proposed in [6, 7] is performed. It is advisable to approximate the multidimensional response surface using the heuristic method based on artificial neural networks. This method has some significant advantages in comparison with to well-known methods [9]. An RBF-neural network with a Gaussian activation function as a multidimensional approximator was used. However, unlike the simpler case of an optimization problem with three variables, a number of difficulties arise in this case. Firstly, the response surface has a complex topography, which imposes certain limitations associated with the need to use a big data array in the procedure of training a neural network. Secondly, there is a big range of ECDD values in the range of radius changes. This is especially true for the region beyond the ES, which entails an un-uniform distribution of the ECDD values at the points of the experiment plan (Fig. 4), which necessitates the decomposition of the search space. All this greatly complicates the constructing of a multiparameter metamodel and it is almost impossible to implement it on the simplest, so-called single RBF-neural networks.

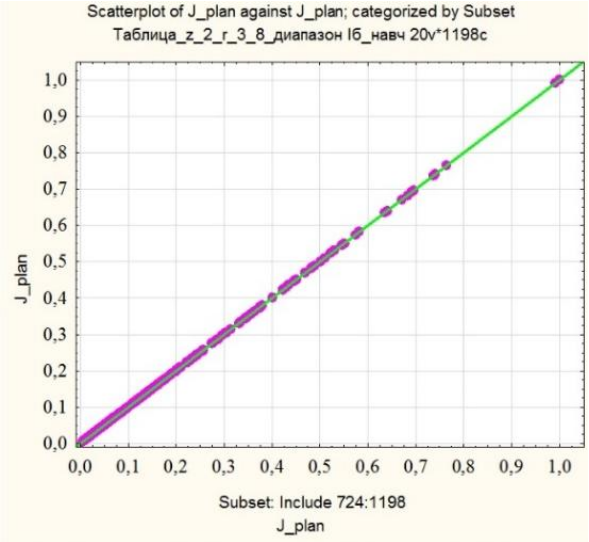

Fig. 4 *Normalized ECDD values for the subregion I_z - III_r of the testing zone beyond the ES*

The decomposition along the height of the probe and along the radius manages to partially level a number of these difficulties. The decomposition along the height of the probe above the TO is performed into three subregions: I_z ($2 \le z \le 3$ mm), II_z ($3 < z \le 4$ mm), III_z ($4 < z \le 5$ mm). The decomposition along the radius of the coil turns is performed into six subregions: I_r ($2 \le r \le 3$ mm), II_r ($3 < r \le 5$ mm), III_r ($5 < r \le 8$ mm), IV_r ($8 < r \le 10$ mm), V_r ($10 \le r \le 12$ mm), VI_r ($12 < r \le 15$ mm). Additionally, if necessary, the radius of the search space is further divided into two subregions - directly under the turns of the coil

sections and beyond them. In order to construct the metamodel as accurately as possible, the number of points of the experiment plan at which the eddy current density is calculated is set different for the area under the turns of the coil sections and beyond them. Thus, it is possible to simplify the architecture of a single RBF-neural network and achieve a certain balance between the accuracy of the construction of the metamodel and the number of points in the experiment plan of the $N_{training}$. In this case, not classical methods of experiment planning are used, but computer methods of homogeneous filling with search points of hyperspace, namely, points of the Sobol's LP$_\tau$-sequence $\xi_1, \xi_2, ..., \xi_{52}$ [10]. So, for example, for the subregion Iz_0 and all subregions along the radius I_r - VI_r where such LP$_\tau$-sequences as $\xi_1, \xi_2, \xi_3, \xi_4$ in the region immediately under the coil sections, and $\xi_1, \xi_3, \xi_4, \xi_2$ realized beyond it. Those, we have the arrangement of points of the LP$_\tau$-sequence in a multifactorial space, respectively, in the x and y coordinates of the testing zone, in the radius r of the excitation coils and the height of their location above the TO z_0 (Fig. 5). The number of points for each subregion is set individually depending on the size of the excitation coil and, accordingly, the size of the region under it. Accounting the symmetry of the ECDD concerning to the coordinate axes also influences the choice of the number of points, i.e. for a moving probe they are specified for I and II quadrants. For example, for I_z - II_r the size of the testing area directly under the coil is x = - 17...17 mm; y = 0...13.5 mm. For the most accurate description of the behavior of the response surface, the number of points for the training sample was chosen $N_{training}$ = 1749 (Fig. 6), while beyond the region - $N_{training}$ = 1198.

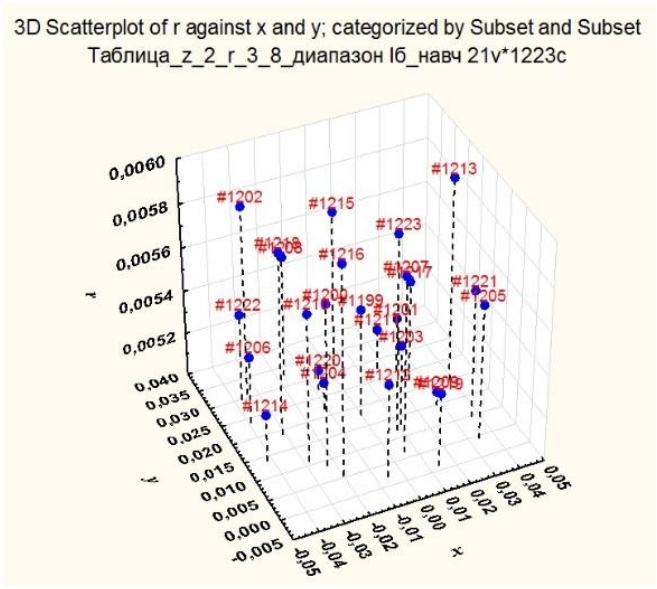

Fig. 5 *Arrangement of points of the LP τ-sequence $\xi_1, \xi_3, \xi_4, \xi_2$ in three-dimensional factor space for r = 5...6 mm at a fixed height z = 2 mm*

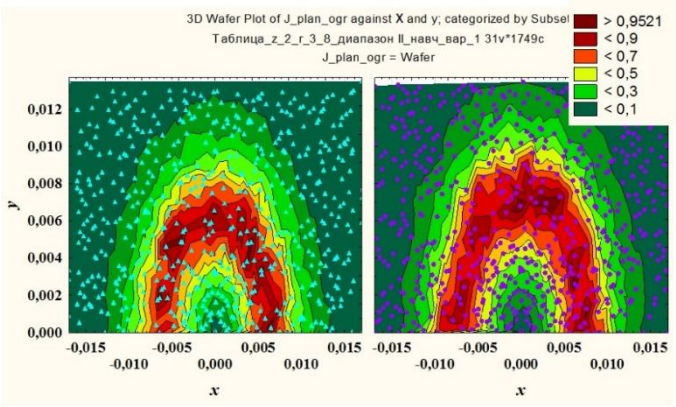

a) b)

Fig. 6 *A training sample, presented in the form of lines of ECDD, with points of the LP τ-sequence for the I_z - III_r subregion: a) r = 6 - 7 mm; b) r = 7 – 8 mm*

Acceptable accuracy of the metamodel was obtained using hybrid neural network construction. This implies the construction of several cascades of neural networks with subsequent additional application at each committees cascade (Fig. 7) [6]. As a function of activation of neurons in a hidden layer of an RBF-network the Gauss function is used. Then the output of the neural network is formed by a linear combination of the outputs of the neurons of the hidden layer and is described by the formula:

$$\hat{J}(x,y,r,z) = \sum_{i=1}^{m} w_i \cdot \exp\left(-\frac{\left(x-c_{x_i}\right)^2 + \left(y-c_{y_i}\right)^2 + \left(r-c_{r_i}\right)^2 + \left(z-c_{z_i}\right)^2}{a_i^2} \right),$$

where m is the number of neurons in the hidden layer; w_i is the weighting coefficient of the output neuron with the i-th neuron of the hidden layer; c_{xi}, c_{yi}, c_{ri}, c_{zi} are coordinates of the center of the i-th neuron; a_i - the width of the i-th neuron.

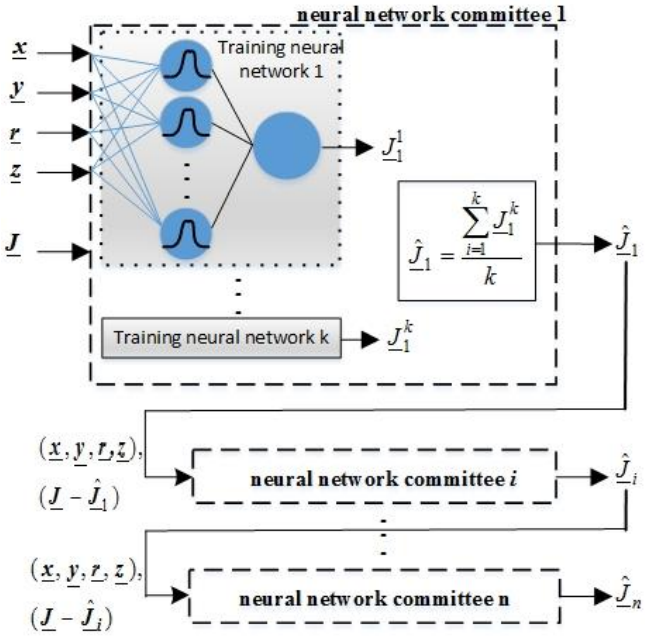

Fig. 7 *Hybrid construction of a neural network metamodel*

For the network's committee only networks with the productivity of the training, testing, and controlling samples of more than 90 % are used. The number of cascades is determined by the obtained value of the mean absolute percentage error MAPE, %. The best models were selected according to a combination of objective statistical indicators [10] and a subjective assessment of dispersion diagrams and histograms of residues.

Table 1 shows the obtained values of MAPE, % at the stage of training and reconstitution of neural networks for several decomposition subregions.

4. Results and discussion

Verification of the metamodel was carried out by checking the correctness of reconstitution of the response surface in all subregions on the sample, which has a bigger number of points than during training, i.e. $N_{reconstitution} > N_{trainina}$. To illustrate this, Fig. 8 shows the dispersion diagrams of the values of the multidimensional approximation function for one of the I_z-III_r subregions at the stages of training the neural network and its reconstitution.

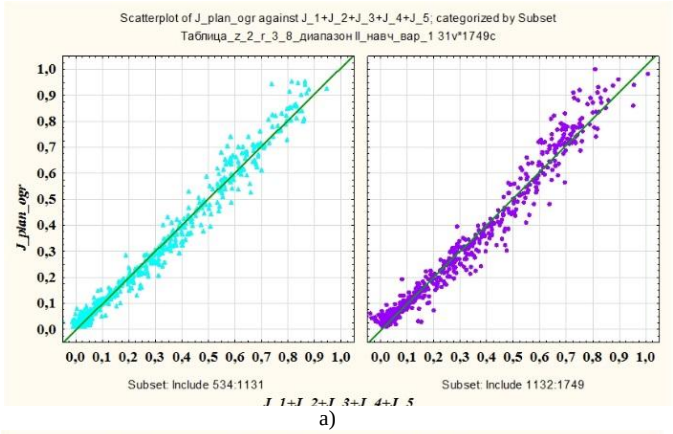

a)

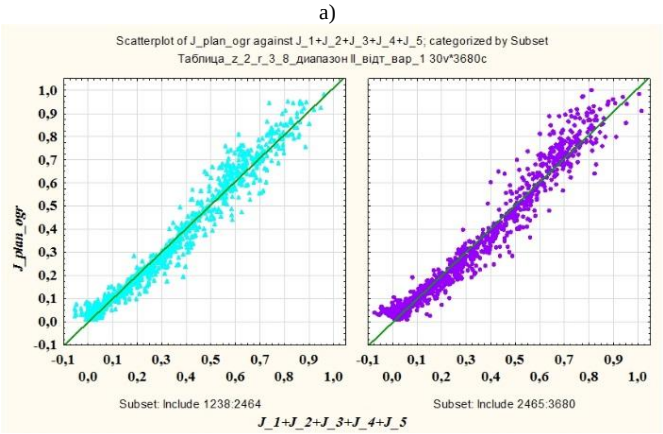

b)

Fig. 7 *Diagram of the dispersion of the values of the multi-dimensional approximation function for the subregions I_z-III_r: a) the stage of training the neural network; b) the stage of reconstitution*

The adequacy of the obtained metamodel was evaluated according to the statistical F-criterion based on the following indicators: the sum squares of the regression and residues ones; the average square of the regression and residuals at a significance level of 5 % [10]. The information content of the constructed metamodel is controlled by the coefficient of determination.

Table 1: *Values of MAPE,% of the obtained multi-parameter hybrid neural network metamodel of ECP for several decomposition subregions.*

Decomposition subregions	$N_{training}$ / $N_{reconstitution}$	MAPE,%	
		stage training	stage reconstitution
I_z-III_r (beyond coil)	1198/2186	16,72	21,17
I_z-III_r (under coil)	1749/3680	19,09	21,31
II_z-I_r (under coil)	900/1250	4,35	6,22

Thus, due to the use of hybrid construction of multiple neural networks using decomposition of the search space, an acceptable error in the metamodel of the volumetric structure of the ES EDP is obtained.

5. References

[1] Steblev, Yu. I. Synthesis of eddy current probes with a given structure of the excitation field in the testing zone. Defectoscopy, 1986, issue 4, pp. 58-64.

[2] Halchenko, V. Ya., Pavlov, O. K., Vorobyov, M. O. Nonlinear synthesis of magnetic fields of excitation of eddy-current probes of flaw detectors. Methods and instruments of quality testing, 2002, issue 8, pp. 3-5.

[3] Gal'chenko, V. Ya., Vorob'ev, M. A. Structural synthesis of attachable eddy-current probes with a given distribution of the probing field in the test zone. Russian Journal of Nondestructive Testing, 2005, vol. 41, issue 1, pp. 29-33. doi:10.1007/s11181-005-0124-7.

[4] Halchenko, V. Ya., Trembovetska, R. V., Tychkov, V. V. Linear synthesis of non-axial surface eddy current probes. International Journal "NDT Days", 2019, vol. 2, issue. 3, pp. 259-268.

[5] Trembovetska, R. V., Halchenko, V. Ya., Tychkov, V. V. Optimal surrogate parametric synthesis of surface circular non-axial eddy-current probes with uniform sensitivity in the testing zone. Visnyk of Kherson National Technical University, 2019, vol. 69, part 2, issue 2, pp. 118-125.

[6] Halchenko, V. Ya., Trembovetska, R. V., Tychkov, V. V., Storchak A. V. Nonlinear surrogate synthesis of the surface circular eddy current probes. Przegląd elektrotechniczny, 2019, vol. 95, issue 9, pp. 76-82. doi:10.15199/48.2019.09.15

[7] Halchenko, V. Ya., Trembovetska, R. V., Tychkov, V. V. Development of excitation structure RBF-metamodels of moving concentric eddy current probe. Electrical engineering & electromechanics, 2019, issue 2, pp. 28-38. doi: 10.20998/2074-272X.2019.2.05.

[8] Trembovetska, R. V., Halchenko, V. Ya., Tychkov, V. V., Storchak A. V. Estimation of accuracy of neuro-network metamodels of surface eddy current probes. Visnyk Cherkassy State Technological University. Seriia: Tehnichni nauky, 2019, issue 2, pp.18-29. doi:10.24025/2306-4412.2.2019.171272

[9] Haykin Simon. Neural Networks: A Complete Course. Moscow, Williams Publ. House, 2006. 1104 p.

[10] Halchenko, V. Ya., Trembovetska, R. V., Tychkov, V. V. The neurocomputing using of the development metamodels stage in the optimal surrogate antennas synthesis process. Visnyk NTUU KPI. Seriia - Radiotekhnika Radioaparatobuduvannia, 2018, vol. 74, pp. 60-72. doi:10.20535/RADAP.2018.74.60-72.

MODELING AND SIMULATIONS OF AN UPPER LIMB EXOSKELETON DESIGNED FOR REHABILITATION AND TRAINING

Assoc. Prof. Chakarov D.[1], Assoc. Prof. Veneva Iv.[1], Assist. Prof. Tsveov M.[1], Eng. Venev P.[1]
[1]Institute of Mechanics, BAS, Acad. G. Bonchev str., Block 4, Sofia 1113, Bulgaria

Abstract: *The work presents a study of an upper limb exoskeleton designed for rehabilitation and training. While in the first stages of rehabilitation, when the patient is unable to move alone, the exoskeleton must be rigid, in the next stages it should be able to respond to any movement made by the patient. The key feature here is transparency: the robot must be able to "hide" if the patient is able to make the movement without assistance. The aim of the work is to identify and evaluate an appropriate solution of the upper limb exoskeleton that provides transparency and natural safety on the one hand, and force impact and performance on the other. In the paper, the mechanical model of the exoskeleton was shown. The mechanical structure is similar to the structure of the human arm. Through the kinematic model, the direct and inverse tasks of kinematics are solved using the Octave matrix software. The upper limb exoskeleton is designed as a haptic device that can perform tasks in virtual reality. Simulations of the interaction force between the patient and the exoskeleton were conducted also using the Octave software. Here, an assessment of the interaction force was made as a result of the exoskeleton passive impedance and the active control of the exoskeleton. Finally, conclusions and development recommendations are given.*

Keywords: EXOSKELETON, REHABILITATION, PASSIVE IMPEDANCE, INTERACTION FORCE, SIMULATIONS

1. Introduction

The exoskeleton must be capable of both: to generate a high level of forces to sustain, assist, and/or to perturb the motor capabilities of the patient; and without perturbing to follow human movements which have large velocity and acceleration peaks, thus requiring a high level of dynamic interaction [1], [2].

As soon as the patient has recovered a minimal amount of motor capacity [3], [4], shared control of movement must be possible. Therefore, one key feature that rehabilitation exoskeletons have to exhibit is transparency: the robot must be able to "hide" if the patient is able to make the movement without assistance [5]. The forces that must be overcome when moving the robot are produced by mechanical impedance of the robot including inertia, friction and stiffness. Gravity forces must be added to these forces as well.

There are two main approaches to reduce the device impedance: the active and the passive approaches. A more feasible way is to use active control. This compensation can take the form of the model feedforward [6] or feedback control [7]. The passive approach which is independent of the servo-responses provides increased safety and maintains the transparency.

Various approaches are known to implement passive impedance. All of them require the use of a passive or natural compliant element. The so-called "serial elastic actuation" [8], [9] is the most well-known approach to realize passive compliance. The values of the high impedance are limited to the values of the elastic link stiffness.

One of the most common approaches to implement natural compliance is the usage of pneumatic artificial muscles (PAM), [10]. Compared to other actuation systems, high power/weight and power/volume ratios allow pneumatic muscles to be a good solution for lightweight actuation design.

The aim of the work is to reveal the results of modelling and simulation of an upper limb exoskeleton for rehabilitation and training that ensures transparency and natural safety on the one hand and force impact and performance on the other.

2. Mechanical structure and actuation of exoskeleton arm

One way to achieve the design goal is to build an exoskeleton developing the passive approach. This means having extremely light attachments to the limbs, and putting all the heavy exoskeleton components on the torso or the ground. Thus an exoskeleton with light segments was developed. The exoskeleton mechanical structure (Fig.1a) consists of two arms L and R, each consisting of four movable segments 1, 2, 3, 4. The two arms are mounted on a rigid structure that is fixed to the base behind the operator's back as shown in Fig.1.

All segments of the arm are made of aluminium, they have adjustable length, thus allowing quick and easy adjustment according to the user's size. Each arm has four active joints J1, J2, J3 and J4 resembling the natural motion of the human arm from shoulder to elbow. A CAD view of the exoskeleton prototype is shown in Fig. 1 b). The summed masses of the four main segments of the arm calculated from the CAD program are ***M1=0.302kg***, M2=0.303kg, M3=0.271kg and M4=0.122kg. The lengths of the exoskeleton arm and forearm in the initial setup are L1=0.286 m and L2=0.370 m respectively. The exoskeleton is designed so, that it covers the requirements of "Activities of daily living" (ADLs) as they have been assessed in [11]. The ranges of exoskeleton joints are: J1(110°), J2(120°), J3(150°), J4(135°).

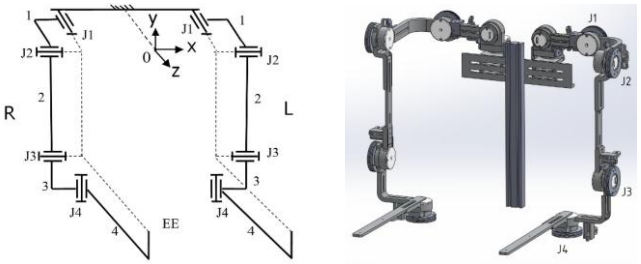

a) *b)*

Fig. 1 *Exoskeleton arms: a) mechanical structure; b) CAD view of the prototype.*

The actuation system of exoskeleton arm should have the following advantages: excellent power/weight ratio with inherent safety, natural compliance, low cost. Self-made braided pneumatic muscle actuators (PMA) are used to achieve these advantages. The muscles are used not only singly, but also in parallel groups as bundles [12]. Joint motion/torque on the exoskeleton arm is achieved by antagonistic actions through cables and pulleys, driven

by the pneumatic bundles. All actuators are mounted on the exo-shell on the operator's back. A selection of bundles with different number of muscles for every joint is performed to ensure nominal torques in the joints.

3. Mechanical model of exoskeleton arm

The mechanical model of the exoskeleton arm was build up, according to the kinematics scheme shown in Fig. 1. The kinematics structure includes 4 rotation joints with h = 4 DoF. Independent parameters for evaluation are the rotations in the four joints $\boldsymbol{q_1}$, $\boldsymbol{q_2}$, $\boldsymbol{q_3}$ and $\mathbf{q_4}$, corresponding to the four basic motions of the upper limb: shoulder abduction/adduction, shoulder flexion/extension, elbow flexion and shoulder med./lat. rotation.

$$\mathbf{q} = [q_1,..., q_h]^T \tag{1}$$

The coordinates of the end-effector (EE) are presented by the vector

$$\mathbf{X} = [X_1,..., X_\nu]^T, \nu \le 6 \tag{2}$$

Jacobian matrix is built using the *Octave Software*,

$$\mathbf{J} = \left[\frac{\partial \mathbf{X}}{\partial \mathbf{q}}\right] \tag{3}$$

The direct task of kinematics is solved regarding positions and velocities. Assuming that the operator hand is connected to a point EE (end effector), we will further consider exoskeleton positions only, and we will accept the operating space as 3 dimensional (v=3). The vector of end-effector coordinates (2) will be (3 x 1) dimensional, and Jacobian (4) will be (3x4) dimensional.

Using the pseudoinverse of the Jacobian [J +] in the *Octave Software* and an iterative procedure using small position deflection on the selected path, inverse kinematics is solved and the corresponding angles and velocities of the joint are found:

$$\dot{\mathrm{q}} = \mathrm{J}^{+}\dot{\mathrm{X}} \tag{4}$$

Denote by

$$\mathbf{Q} = [Q_1,...,Q_h]^T \tag{5}$$

the (h x 1) vector of the generalized torques in the joints in the basic chain corresponding to the generalized parameters (1) and by

$$\mathrm{F} = [F_x, F_y, F_z]^T \tag{6}$$

the (3 x 1) vector of the external forces applied at the end effector and corresponding to the coordinates (2) of the end effector. The link between the external forces (6) and the effective generalized torques (5) can be defined according to the principle of virtual work as follows

$$\mathbf{Q} = \mathbf{J}^{\mathbf{T}}\mathbf{F} \tag{7}$$

In virtual reality tasks, the vector of the external forces (6) represents the desired force on the end effector, when the user is in contact with a virtual surface.

The gravity of exoskeleton links and the gravity of human arm influences on the behaviour of the end-effector. The (4 x 1) vector

$$\mathbf{G} = [G_1,...,G_4]^T \tag{8}$$

is the vector of gravity torques, generated at the exoskeleton joints. Its components are determined by the mass of the links and their centre of mass positions in the base frame.

4. Interaction "patient– exoskeleton" as a result of the exoskeleton passive impedance

If a rehabilitation robot is completely transparent, the interaction force initiated by the patient between him and robot is zero. The subject of the present simulations is to evaluate the interaction force between the patient and the exoskeleton as a result of the exoskeleton passive impedance. As rehabilitation robotics, especially upper limb robotics, operate at high torques at low velocity, the interaction force includes mainly gravitational forces, elastic forces and frictional forces.

An experiment has been conducted on the influence of gravitational forces on the end effector motion in a curvilinear path, such as a circle, in the *OXY* plane. (Fig. 2a). At the points of the circular trajectory, the inverse kinematics problem (4) is solved by the *Octave Software* and the corresponding joint angles are found. For each point in the procedure, the joints torques (8) generated by the gravitational forces are calculated. From these torques, the inverse solution of (7) is made and the equivalent force of EE (6) is calculated. Fig. 2 a) depict graphically the change of this force, and Fig. 2 (b) shows the change of its components along the axes of the Cartesian coordinate system *OXYZ*.

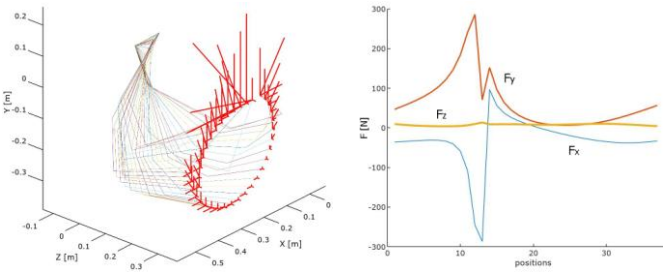

a) *b)*

Fig. 2 *Gravitational influence in guiding the end effector in a circle with radius 0.18 m: (a) change in the interaction force; (b) modification of the components of the interaction force.*

Fig. 3 shows the results of a similar experiment when the arm is in a different configuration and the end effector moves in a circle with smaller radius. Fig. 3 a) depict graphically the change of end effector force, and Fig. 3 (b) shows the change of its components along the axes of the Cartesian coordinate system *OXYZ*. Joint moments as a result of arm gravity are shown in Fig.3 c).

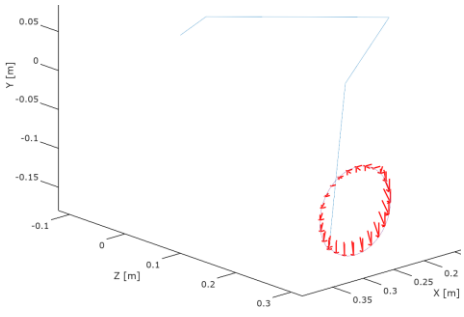

a)

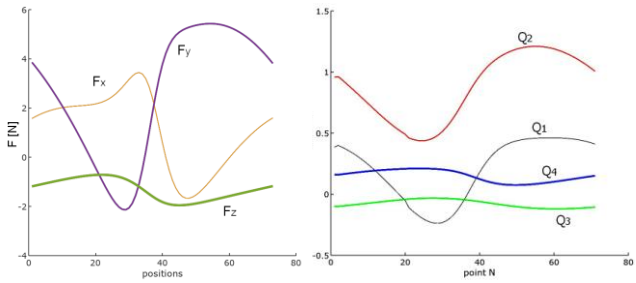

b) *c)*

Fig. 3 *Gravitational influence in guiding the end effector in a circle with radius 0.05 m: (a) change in the interaction force; (b) modification of the components of the interaction force; (c) joint moments as a result of arm gravity.*

In motion initiated by the patient to maintain the end effector trajectory, in cases without feedback or without mechanical model compensation, the force exerted by the patient depends on the configuration of the arm. As can be seen from the graphs, in some configurations this force is limited in size. In other configurations and special positions, the interaction forces are multiplied several times. Ensuring transparency in these situations can be achieved through active control, by changing the exoskeleton arm configuration, by changing contact points, and more.

At the initial moment of "patient - exoskeleton" contact, the interaction force is mainly the result of elastic displacement. The exoskeleton passive elasticity is determined by the compliance of the pneumatic drive. For selected design parameters such as: number of muscles in each bundle m = 7, wheel radius r = 0.04 [m], maximum feed pressure of 600 kPa, joints compliances reache values B_{pii} = 0.031 [rad / Nm], i = 1, ..., 4, [12].

The exoskeleton compliance in Cartesian space represents a function of the joint compliance and joint positions, involved in Jacobian J:

$$\boldsymbol{B} = \boldsymbol{J}\boldsymbol{B}_{\boldsymbol{p}}\boldsymbol{J}^{\boldsymbol{T}} \tag{9}$$

Above, $\boldsymbol{B}$ represents a (3x3) symmetric matrix of end effector linear compliance and $\boldsymbol{B_p}$ represents (4x4) diagonal matrix of joint compliance.

The end effector compliance (11) is calculated for the specified values of joint compliances in the four joint $\boldsymbol{B_{pii}}$. The calculations are consistent with changing situations in the four joints of the arm respectively in 0, 55^0.30^0, 30^0 in the range of joint motions. The results are shown in Fig. 4 using a compliance ellipsoid. The experiment shows that there are large differences between compliance at different points, as well as between compliance in different directions from a given point. Transparency is directly dependent on the type of compliance represented by compliance ellipsoid with a certain shape.

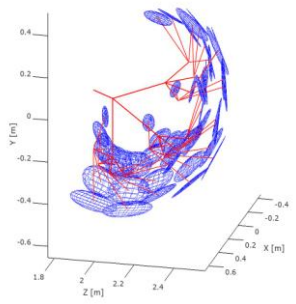

Fig.4. *End effector passive compliance at workspace points.*

5. Interaction "patient– exoskeleton" as a result of active control

The passive impedance of the pneumatic actuation takes care of the initial response in order to provide security and ensure the transparency but the active impedance creates a subsequent response that is generated by the position feedback and feed-forward compensations.

An open-loop impedance controller with feedforward gravity compensation is selected [2]. This type of force control is called open-loop because there is no force feedback from the device to the controller to regulate the force output of the exoskeleton end effector as it is illustrated by the control block diagram in Fig. 5.

Virtual Engine in the controller on Fig. 5 according to reference impedance value K_d generates a desired force command F_d used to calculate force command in the exoskeleton joints. A software block G(q) is introduced in order to take into consideration the effects of the exoskeleton weight. Generalized torques in the joints as joint force commands are given by the following equation

$$\Delta Q = J^T F_d + G(q) - Q_H \tag{10}$$

Forces that human exerts on the exoskeleton end effector $\boldsymbol{Q_H}$ represent a physical, not control input to the device.

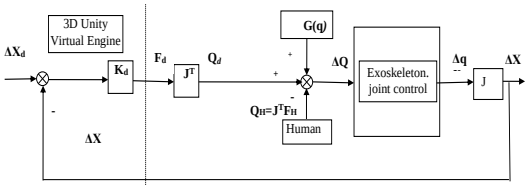

Fig.5. *Block scheme of impedance control with feedforward gravity compensation.*

In the next experiment, a simulation is made for the case where the patient leads the hand in a circle as shown in Fig. 3, and the exoskeleton assures transparency with active control. The force commands to the joint according to (10) are formed only by the gravitational compensation command (8) ΔQ = G, as shown in Fig. 3c). In this case the desired force of the end effector is zero (Q_d = 0). In each position, the compensated arm deviates as a result of gravitation and pneumatic actuator passive compliance. In a series of points on the trajectory elastic deviation in the joints $\Delta q = B_p \Delta Q$, and the corresponding deviation of the end effector $\Delta X = J\Delta q$ are calculated. Fig. 6a) shows the end effector trajectory after elastic deviations as result of gravity. When the patient is leading the hand, he applies force $Q_h = J^T F_h$ to the end effector, which according to (10) changes the joint torques. As a result, the elastic exoskeleton arm deviates further.

The task of the impedance controller shown in Fig. 5 is to provide transparency with low stiffness K_d, to reduces errors in joint torque in order to reset the interaction force F_h. Due to low sensor resolution or other factors as a result of active control, the patient-initiated force may be different from 0. The magnitude of this force is determined by the passive impedance of the exoskeleton. In the experiment, the elastic deviation of the end effector at trajectory points was calculated when a setpoint of the interaction force $F_h = [-5, -5, -5]^T$N was chosen. In Fig. 6b) arm deviations are shown as result of the set interaction force. In Fig. 7a) components of the EE deviation vector dXa dYa dZa are shown as a result of the set interaction force. The joint moments nd as a result of set interaction force are shown in Fig.7 b). The results obtained show the relationship between the deviations from the desired trajectory and the uncompensated interaction force as a result of the elasticity of the exoskeleton arm.

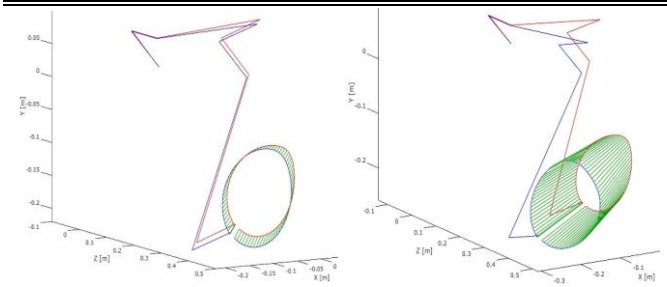

a) *b)*

Fig. 6. *Deviations as a result of: a) gravity and b) as a result of interaction force.*

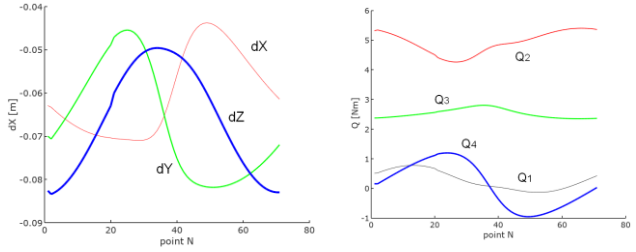

a) *b)*

Fig. 7. *Motion parameters along the selected trajectory: a) components of the EE deviation vector dX, dY, dZ as a result of the set interaction force; b) joint moments as a result of interaction force.*

The calculated values of the EE deviations determine the transparency as a result of passive compliance. Of course, this transparency depends on the amount of passive compliance and the speed and accuracy of active control. The experiment was conducted for a minimum value of passive compliance. By controlling the pressure of the pneumatic actuators, the passive compliance in the joints can be increased, thus increasing the transparency and safety of the interaction.

6. Conclusion

The work presents a study of an upper limb exoskeleton designed for rehabilitation and training. The aim of the work is to identify and evaluate an appropriate solution of upper limb exoskeleton that provides transparency and natural safety on the one hand and force impact and performance on the other.

In the paper, the choice of a mechanical structure is shown to be equivalent to the structure of the human arm. A mechanical model of the exoskeleton arm was built. Through the kinematic model direct and inverse tasks of kinematics are solved using the Octave matrix software.

The upper limb exoskeleton is designed as a haptic device that can perform tasks in virtual reality. Simulations of interaction force between patient and exoskeleton are conducted using the Octave software. Here an assessment of the interaction force as a result of the exoskeleton passive impedance and as a result of exoskeleton active control is made.

It has been shown that for this arm structure the transparency in some positions and directions is higher than in others. Ensuring transparency in the extreme and singular positions can be achieved through active control, by changing the exoskeleton arm configuration, by changing the contact points "patient - exoskeleton", etc. We can also select structure of the arm with more degrees of mobility and wide working area than the human arm.

Acknowledgements: This work is partially supported by the National Science Fund, Call 2016, through Project AWERON - No. DN 07/9 and by the National Scientific Program "Information and Communication Technologies for a Single Digital Market in Science, Education and Security (ICTinSES)", contract No DO1–205/23.11.2018, financed by the Ministry of Education and Science in Bulgaria.

References

[1] Jarrasse, N., T. Proietti, V. Crocher, J. Robertson, A. Sahbani, G. Morel, A. Roby-Brami. Robotic Exoskeletons: A Perspective for the Rehabilitation of Arm Coordination in Stroke Patients, Frontiers in Human Neuroscience, · November 2014, DOI: 10.3389/fnhum.2014.00947, (2014).

[2] Lynch, D., Ferraro, M., Krol, J., Trudell, C. M., Christos, P., and Volpe, B. T. (2005). Continuous passive motion improves shoulder joint integrity following stroke. Clin. Rehabil. 19, 594–599. doi:10.1191/0269215505cr901oa

[3] Patton, J. L., and Mussa-Ivaldi, F. A. (2002). Robot assisted adaptative training: custom force fields for teaching movement patterns. IEEE Rev. Biomed. Eng. 51, 636–646. doi:10.1109/TBME.2003.821035

[4] Hogan, N., Krebs, H. I., Rohrer, B., Palazzolo, J. J., Dipietro, L., Fasoli, S. E., et al. (2006). Motions or muscles? Some behavioral factors underlying robotic assistance of motor recovery. J. Rehabil. Res. Dev. 43, 605–618. doi:10.1682/JRRD. 2005.06.0103

[5] Nef T., P. Lum, Improving backdrivability in geared rehabilitation robots, Med. Biol. Eng. Comput. 47(4), 441–447, DOI 10.1007/s11517-009-0437-0.

[6] Hogan, N., Impedance Control: An Approach to Manipulation, *ASME J. Dynamic Systems Meas. & Control*, 107: 1-24, (1985)

[7] Bergamasco, M., B. Allotta, L. Bosio, L. Ferretti, G. Perrini, G. M. Prisco, F. Salsedo, G. Sartini, An Arm Exoskeleton System for Teleoperation and Virtual Environment Applications, IEEE Int'l Conf. Robot. Automat., vol. **2**, 1449–1454, (1994).

[8] Pratt G. and Williamson, Series elastic actuators, In: *Proc. of IEEE/RSJ International Conference on Intelligent Robots and Systems*, Pittsburgh, 1, 399-406, 1995.

[9] Veneman, J.F., R. Ekkelenkamp, R. Kruidhof, F.C.T. van der Helm, and H. van der Kooij, A series elastic- and bowden-cable-based actuation for use as torque actuator in exoskeleton-type robots, *The International Journal of Robotics Research*, vol. 25(3), pp. 261-281, 2006.

[10] Daerden Fr., D. Lefeber, Pneumatic Artificial Muscles: actuators for robotics and automation. European Journal of Mechanical and Environmental Engineering, 47, 1, 1–11, (2002).

[11] Perry, J., Rosen J, Burns S., Upper-limb powered exoskeleton design. IEEE/ASME Transactions on Mechatronics. Vol.12, No. 4, 408–417, (2007).

[12] Chakarov, D., Veneva, I., Tsveov, M., Venev, P. Powered upper limb orthosis actuation system based on pneumatic artificial muscles, Journal of Theoretical and Applied Mechanics (Bulgaria), 48 (1), pp. 23-36, (2018).

THE FORMATION OF INVESTMENT PORTFOLIOS BASED ON FORECASTED INCOME WITH THE USE OF FRACTAL MODELS

ФОРМИРОВАНИЕ ИНВЕСТИЦИОННЫХ ПОРТФЕЛЕЙ НА БАЗЕ ПРОГНОЗНЫХ ДОХОДНОСТЕЙ С ПРИМЕНЕНИЕМ ФРАКТАЛЬНЫХ МОДЕЛЕЙ

PhD. student Garafutdinov R.[1], PhD. Gurova E.[2]
Perm State National Research University – Perm, Russia[1,2]
Institute of Economics of the Ural Branch of the Russian Academy of Sciences – Yekaterinburg, Russia[2]

rvgarafutdinov@gmail.com[1], eg555a@yandex.ru[2]

Abstract: *The article proposes an approach to the formation of optimal investment portfolios according to the criteria of profitability and risk based on the predicted returns of assets obtained using fractal econometric models. It has been hypothesized that this method allows you to create more profitable and low-risk portfolios than in the optimization of historical returns. To test the approach and test the hypothesis, an attempt was made to form various portfolio options from the shares of two Russian issuers. The results obtained allow us to conclude that the proposed approach is promising, and further research is needed.*

Keywords: INVESTMENT PORTFOLIO, INCOME, STANDARD DEVIATION, FINANCIAL INSTRUMENT, FRACTAL MODELS, ARFIMA

1. Introduction

The most important way to generate income in a market economy is investing, which implies the rejection of current consumption in order to profit in the future. At present, the greatest interest in the Russian financial sector is caused not by investing in bank deposits (this tool is characterized by a practically single probability of the risk of loss of funds due to the comparability, or even exceeding, of inflation rates offered by banks on deposit interest rates), but investing in the IT sector, venture capital investment and the formation of investment portfolios on stock exchanges. Now, it is more important not just to generate income, but to guarantee it in conditions of instability along with hedging financial risks. An important role is played by the development of innovative methods of portfolio formation that can provide a more accurate forecast of the financial result.

Despite its considerable age, the most widely accepted theory of the optimal investment portfolio is authored by G. Markowitz, based on maximizing the return on investment while minimizing risk [2]. The risk is usually expressed by the standard deviation of return. The optimization problem is solved, and the portfolio structure is selected in such a way as to ensure the best values of its indicators calculated based on historical returns on assets. It is assumed that in the future the probabilistic characteristics of the price of these assets (mathematical expectation, standard deviation) will remain unchanged, prices will behave in a similar way.

However, investors are not interested in past returns, but in the future. In practice, a portfolio optimized by historical price values will be optimal if the future yield dynamics is a constant. Of course, in real life, in an unstable economy, dynamically changing market conditions, financial crises, such a premise is not feasible. We suggested that if we extrapolate the price series of assets included in the portfolio and calculate the target function not by historical returns, but by forecast , then the resulting portfolios should have more attractive characteristics (higher profitability with less risk) than when applying the classical model of average dispersion.

There are many methods for forecasting the dynamics of the rates of financial instruments. According to some authors, the most adequate mathematical apparatus for studying the complex behavior of financial indicators was developed based on fractal theory [5],[9]. There are extensions of widely used econometric models (such as linear ARIMA, non-linear GARCH) that consider the fractal properties of market time series. Researches have shown higher efficiency of such models compared to classical ones [6]. In this paper, we decided to predict the returns of financial instruments that make up the portfolio, apply the ARFIMA long memory model.

Thus, the purpose of this study is to test the hypothesis that the formation of an investment portfolio based on forecasted returns using fractal models can improve the characteristics of the portfolio in comparison with the approach to calculating the characteristics of historical returns only. To achieve the goal, the following tasks were set: to carry out a literature review on the research topic, describe the input data and the research methodology, make the necessary calculations, analyze the results and outline the directions for further work.

The problem of applying and developing the theory of portfolio investment has been dealt with by many researchers. So, in the work of E. Gubanova and a group of authors proposed a methodology for the formation of the most effective portfolio of securities, considering the current situation on the market (aggressive, passive or balanced) [4]. The models of W. Sharp and J. Tobin are used, which are a development and alternative to the classical model of G. Markowitz. I. Agarysheva et al. proposed an original methodology for selecting the instruments included in the portfolio [1]. Article by B. Aouni et al. discusses approaches to optimizing the portfolio according to several criteria different from average profitability and variance [2]. Moreover, in all the studied works, portfolios are invariably formed according to the historical profitability of the instruments.

The use of fractal analysis to predict financial time series is not paid much attention to by researchers. G. Caporale [3], S. Zhelyazkova [8], P. Simonov and R. Garafutdinov [6] and others dealt with this problem. Their researches show that financial series have a long memory and can be well described by various fractal modifications of econometric models. In article [6], on a large data set, the advantages of such models over classical forecasts in accuracy are demonstrated.

2. The solution to the problem

We describe the input data and state the research methodology. It was decided to consider the dynamics of asset prices from January 2008 to February 2019. Since the portfolio, as a rule, is formed in order to generate income for a sufficiently long time, the annual return on asset R_y calculated by formula (1) and the annual standard deviation were taken as optimized characteristics of the portfolio.

$$R_y = \frac{P_1 - P_0}{P_0}, \quad (1)$$

where P_1 is the closing price of the asset at the beginning of the month of a certain year, P_0 – the closing price of the asset at the beginning of the month of the previous year.

The initial sample of instruments included ordinary shares of 51 issuers traded on the Moscow Exchange from the list of securities for customers with a standard risk level. Of these, two instruments with a rather low level of correlation of annual returns (0.309) were selected as the base for portfolio formation: ordinary shares of PJSC "Aeroflot – Russian Airlines" (ticker AFLT) and PJSC "Acron" (ticker AKRN).

The mathematical formulation of the investment portfolio optimization problem is described in many works, for example, in [1]. Optimized variables are the shares of assets in the portfolio. Additional limitation: the sum of shares must be equal to one. In the framework of this study, we will perform optimization according to three criteria: maximizing profitability; risk minimization; maximizing the profitability to risk ratio. Since it is necessary to compare the portfolios obtained in the new and classical ways, we will form portfolios in two ways. In the first case, the objective function is calculated based on the average annual return on assets (to calculate the average annual return on an asset and estimate its standard deviation, annual returns for 2009–2018 are used, only 10 values). In the second case, according to the predicted annual returns in 2019 (the annual return on the asset is forecasted, and the standard deviation is estimated by several historical annual returns her with the addition of predicted returns, only 11 values). The criteria for comparing the portfolios obtained by both methods are the actual annual portfolio return in 2019 and the standard deviation of its annual return calculated from the series of historical annual asset returns with the actual added in 2019.

To model predicted returns, it is necessary to use not annual historical returns, but monthly ones, since at least several tens of values are required to identify the parameters of the ARFIMA model. Monthly returns are calculated similarly to annual ones by formula (1) – with the only difference being that the interval between prices P_0 and P_1 is not a year, but a month. To switch from monthly returns to annual R_y, the formula is used:

$$R_y = \sum_{i=1}^{12}(1+R_{mi}) - 1, \quad (2)$$

where R_{mi} is the monthly yield of the asset, i – the serial number of the month. Table 1 shows the obtained annual returns ($E(R_v)$ is the average annual return of the asset, σ_y – the standard deviation of the annual return).

Table 1: *Historical annual returns on portfolio assets.*

Year	AFLT	AKRN
2009	-0.7574	-0.7541
2010	1.4916	1.5806
2011	0.3767	0.4044
2012	-0.3513	0.0022
2013	0.0660	0.0170
2014	0.4870	-0.1886
2015	-0.5333	1.0235
2016	0.4668	0.5613
2017	2.1952	-0.0402
2018	-0.2266	0.1776
$E(R_y)$	0.3215	0.2784
σ_y	0.9216	0.6572

The methodology for using ARFIMA(p,d,q) models is described in [6]. The fractional differentiation operator d is calculated through the Hurst exponent of the time series. To assess the fractal dimension of the series and the Hurst indicator, it was decided to use the so-called dimension of the minimum coverage, since only a few dozen observations are required to calculate it sufficiently accurately [7]. In order to obtain adequate models suitable for forecasting, that is, satisfying the distribution normality Lilliefors test) and the lack of autocorrelation of residues (according to the Ljung-Box test) and the significance of the coefficients (at least half of the coefficients should be significant at the 5% level), etc. It was necessary to change the length of the training interval, cutting off the values from the front. Among the models satisfying all the conditions, the models with the lowest values of the BIC were selected. Table 2 presents the characteristics of the constructed models (n is the length of the interval on which the model was trained, that is, the number of monthly returns in a row).

Table 2: *ARFIMA Forecast Models the return on each asset in the portfolio.*

AFLT	AKRN
ARFIMA(1, -0.007408, 1) n = 100 BIC = -151.71	ARFIMA(0, -0.068203, 2) n = 103 BIC = -180.49

Figure 1 shows the graphs of the monthly returns of both instruments from February 2008 to February 2019, as well as their forecast from March 2018 to February 2019.

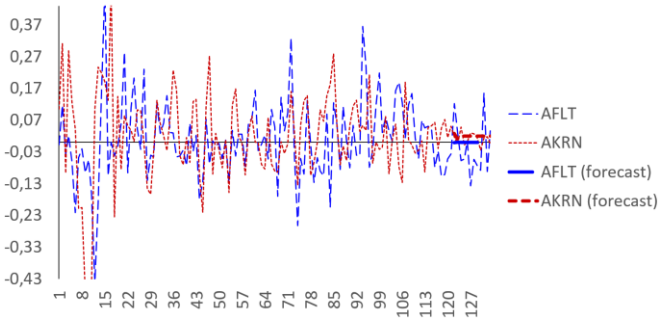

Fig. 1 *Actual and forecast graphs of monthly asset returns.*

3. Results and discussion

As you can see, forecasts tend to the mathematical expectation of instrument returns and very weakly model their volatility. In the framework of this study, the most interesting are the characteristics of the portfolio, the structure of which is optimized based on these forecasts.

As an optimizer, the Solver tool in Microsoft Excel was used. Optimization method was GRG Nonlinear. Before each start of the optimization process, the values of the variables were set to 0.5. Six portfolios with various objective functions were formed, the results are summarized in table 3 (R_{ph} is annual portfolio historical return, σ_{ph} – standard deviation of historical portfolio annual return, R_{pp} – annual portfolio return forecast, σ_{pp} – standard deviation of portfolio annual forecast, R_{pf} – annual portfolio return actual, σ_{pf} – standard deviation of annual portfolio return, taking into account the actual).

Table 3: *Characteristics of portfolios formed in various ways.*

Portfolio number	Target function	Share AFLT	Share AKRN	Portfolio characteristics
0	–	0.5	0.5	R_{pf} = -0.0461 σ_{pf} = 0.6191 R_{pf} / σ_{pf} = -0.0744
1	$R_{ph} \rightarrow max$	1	0	R_{pf} = -0.2226 σ_{pf} = 0.8896 R_{pf} / σ_{pf} = -0.2502
2	$\sigma_{ph} \rightarrow min$	0.27	0.73	R_{pf} = 0.0352 σ_{pf} = 0.5789 R_{pf} / σ_{pf} = 0.0607
3	R_{ph} / $\sigma_{ph} \rightarrow max$	0.33	0.67	R_{pf} = 0.0140 σ_{pf} = 0.5824 R_{pf} / σ_{pf} = 0.0240
4	$R_{pp} \rightarrow max$	0	1	R_{pf} = 0.1305 σ_{pf} = 0.6251 R_{pf} / σ_{pf} = 0.2087
5	$\sigma_{pp} \rightarrow min$	0.27	0.73	R_{pf} = 0.0364 σ_{pf} = 0.5788 R_{pf} / σ_{pf} = 0.0628
6	R_{pp} / $\sigma_{pp} \rightarrow max$	0	1	R_{pf} = 0.1305 σ_{pf} = 0.6251 R_{pf} / σ_{pf} = 0.2087

As you can see, the parameters of portfolios that are optimized according to historical and forecast data differ. A balanced

portfolio, which includes equally shares of both issuers (portfolio 0), is expected to have mediocre characteristics: negative return (-5%) and high volatility (62%). However, portfolio 1, maximizing historical profitability, in practice turned out to be even more unprofitable and risky. Portfolio 4, which maximizes projected returns, showed returns 35% higher and volatility 26% lower. Portfolios that minimize historical and forecast risks (2 and 5) are practically the same (portfolio 5 has slightly better parameters, and the coincidence of its structure with the structure of portfolio 2 is due to rounding). This is because the series of asset returns for estimating the forecast standard deviation differ from the series of historical returns by adding a single forecast value. However, as you can see, even this single value slightly improves portfolio parameters. Portfolio 6, which maximizes the forecast profitability to risk ratio, showed 12% greater profitability and 4% greater volatility than portfolio 3, which can also be considered an improvement in performance.

It turned out that the hypothesis that the use of fractal models for forecasting returns and the formation of investment portfolios based on projected returns allows us to improve the characteristics of portfolios is not rejected. The only experiment conducted showed that the parameters of the portfolio, at least, do not deteriorate. Therefore, we can talk about a new method of forming investment portfolios as a possible application of a fractal approach to forecasting financial series. In any case, start its discussion. Moreover, the technique used in this study has several limitations. Firstly, the classic, simplest method of forming optimal portfolios, proposed by G. Markowitz, was applied. As part of the first testing of our methodology, this approach is justified, but it would be more interesting to try more advanced portfolio models with other performance criteria (for example, the risk measure can be expressed by the VaR indicator). Secondly, the choice of securities for inclusion in the portfolio was carried out arbitrarily and their number was only two, while a well portfolio with well-diversified risk can contain up to a dozen instruments. Such a primitive approach to the selection of assets led to the fact that the portfolios turned out to be quite low-yield and high-risk. In addition, the optimizer in some cases completely preferred to leave the only asset in the portfolio, which does not even allow talking about portfolio investment. Thirdly, ARFIMA linear models were used to predict returns, while no predictive analysis of the fractal properties of the price series of the selected assets was made and no conclusion was made on the appropriateness of using such models to predict these series. All these limitations indicate that it makes sense to continue the study of our proposed method of forming portfolios, to develop an idea that at this stage exists almost in the form of a concept.

4. Conclusion

Thus, in our opinion, the proven approach to portfolio formation looks promising and deserves attention. Modeling the expected dynamics of portfolio returns using modern mathematical methods instead of using the simplest expected value as predicted returns allows us to more adequately describe real market processes and, as a result, to create more profitable and less risky portfolios. The directions of future research, due to the shortcomings of the methodology used, may be the following:

- application of a more sensible methodology for choosing financial instruments to form the portfolio base, increasing the number of assets in the portfolio;
- performing a prediction analysis of the series and the use of other, more suitable predictive models (for example, fractal modifications of the GARCH);
- use of more advanced portfolio models and non-classical indicators of its effectiveness.

5. References

1. Agarysheva, I., K. Zaalishvili and S. Kudymov. Methodology for the formation of investment portfolios from several instruments. Bulletin of modern research, no. 7 (22), 2018, 7–11.

2. Aouni, B., M. Doumpos, B. Pérez-Gladish and R. Steuer. On the increasing importance of multiple criteria decision aid methods for portfolio selection. Journal of the Operational Research Society, vol. 69, 2018, 1525–1542.

3. Caporale, G. and M. Škare. Long memory in UK real GDP, 1851–2013: An ARFIMA-FIGARCH analysis. DIW Berlin Discussion Paper, no. 1395, 2014. doi: 10.2139/ssrn.2459806.

4. Gubanova, E., I. Sokolova and S. Solovieva. The use of financial instruments in the formation of an effective portfolio of securities. Bulletin NGIEI, no. 9 (64), 2016, 123–137.

5. Ostapenko, E. and T. Dunaeva. Forecasting time series with long memory using ARFIMA models. Bulletin of the Kiev National University of Technology and Design, no. 7, 2010, 270–273.

6. Simonov, P. and R. Garafutdinov. Modeling and forecasting the dynamics of the courses of financial instruments using econometric models and fractal analysis. Bulletin of Perm University. Series “Economics”, vol. 14, no. 2, 2019, 268–288.

7. Starchenko, N. and M. Dubovikov. Econophysics and fractal analysis of financial time series. Advances in Physical Sciences, vol. 181, no. 7, 2011, 779–786.

8. Zhelyazkova, S. ARFIMA-FIGARCH, HYGARCH and FIAPARCH Models of Exchange Rates. Izvestia Journal of the Union of Scientists – Varna. Economic Sciences Series, vol. 7 (2), 2018, 142–153.

9. Zinenko, A. R/S analysis in the stock market. Business Informatics, no. 3 (21), 2012, 24–30.

MODELING OF TEMPERATURE DEPENDENCIES TO DETERMINE THE CONTENT OF SOLUBLE ELEMENTS IN THE BASIS OF DISPERSIONLY-HARDENING ALLOYS

Ass. Prof., Dr. Eng. Khristenko V., Ass. Prof., Dr. Eng. Donii O., Dr. Eng. Kotliar S., M.Sc. Boguk Ju.

National Technical University of Ukraine "Kyiv Polytechnic Institute named after Igor Sikorsky" - Kyiv, Ukraine

Email: dosha@iff.kpi.ua

Abstract: The possibility of assessing of the temperature stability of the hardening phases of dispersion-hardened alloys with the help of polytherms of electrical resistance is experimentally confirmed. For alloys compositions of which belong to the quasi-binary Cu - Ni_2Si cross section of the state diagram of the Cu - Ni - Si system, a procedure has been developed for calculating of the content of elements dissolved in the phase, based on copper, using data on temperature dependences of the electrical resistivity on temperature, presented in the form of regression equations. In the future, it is possible to use the developed model to assess the temperature stability of dispersed phases in alloys of more complex systems (for example, such as Cu - (Ni - Si) - (Fe - Cr - C)).

KEYWORDS: *HARDENING PHASES, POLYTHERMS OF ELECTRICAL RESISTANCE, REGRESSION EQUATIONS*

1. Introduction

Dispersion-hardening bronzes are among the best hardened conductive alloys (for example, heat- and electrically conductive ones) [1, 2]. However, the upper temperature limit at which such materials retain acceptable mechanical and conductive properties is restricted by the stability of inclusions of the hardening phase. Therefore, when developing new dispersion hardening alloys which are capable to maintain acceptable characteristics of performance at elevated temperatures, the problem of a fairly simple and effective assessment of the temperature stability of the hardening phases with respect to dissolution in the base remains relevant. Temperature dependencies of the content of dissolved elements in the base can serve as one of the indicators of such stability.

Preliminary studies [3] established interconnection between the configurations of solvus line and the polytherm of the electrical resistivity of the alloy as a whole for nickel-silicon bronzes belonging to the quasi-binary Cu – Ni_2Si cross section of the state diagram of the Cu – Ni – Si system. For bronze K1H3 (Ukraine), the composition of which belongs to the indicated cross section, the temperature dependencies of the electrical resistivity were experimentally obtained [3]. Therefore, it seems appropriate to develop a mathematical model to determine the temperature dependence of the composition of the phase based on copper on the polytherms of resistance in order to assess the stability of the hardening phases, based on the available information.

2. Background and means to solve the problem

For dispersion hardening copper conductive alloys, due to a rather small volume fraction of the dispersed phase, one can assume that indicators of the electrical resistivity are determined mainly by the resistance of the base (for K1H3 bronze - of a copper-based solid solution), and the effect of the dispersed phase is minor. Therefore, in the framework of the classical theory of electrical conductivity, the value of the electrical resistivity of the alloy at a given temperature can be represented as the result of the combined action of the following factors:

1. Interference to the movement of charge carriers (electrons) created by copper atoms, oscillating regarding to the nodes of the crystal lattice of the solid solution. This resistance R depends linearly on temperature t, as follows from the equation for the temperature dependence of the resistance of pure metals $R(t) = R_0(1 + \alpha t)$, where α is the temperature coefficient of resistance (K^{-1}).

The atoms of nickel and silicon, which are part of the solid solution based on copper, violate the regular arrangement of atoms in the crystal lattice, and thereby create additional obstacles to the movement of charge carriers. At the same time, there is Vegard's empirical law, which states a linear correlation between the properties of the crystal lattice of the alloy and the concentration of its individual elements at a constant temperature [4]. If this is correct and the content of impurity in the crystal lattice of the solid solution is small, we can assume that the obstacles to the flow of charge carriers due to the presence of lattice distortions created by nickel and silicon atoms linearly depends on the total content of these atoms in the solid solution.

3. Thermal vibrations of nickel and silicon atoms in the crystal lattice of a solid solution create additional obstacles to the movement of electrons. In the general case, the intensity of the influence of thermal vibrations of impurity atoms on the value of electrical resistance of a solid solution cannot be considered as equivalent to the intensity of the influence of thermal vibrations of copper atoms. However, the same as in the case with copper atoms, it increases linearly along with increasing of temperature. Therefore, the increase of electrical resistance created by thermal vibrations of impurity atoms is determined by the composition and temperature of the solid solution. The intensities of the influence of thermal vibrations of nickel and silicon atoms on the value of electrical resistance are not equivalent. But for alloys of the quasibinary Cu – Ni_2Si cross section of the state diagram (when the transition to a solid solution of one of silicon atom is accompanied by the transition of two nickel atoms), one can consider only the total content of nickel and silicon in the solid solution (in [5] this concept for alloys belonging to the quasibinary cross section is indicated by the term "solubility of Ni_2Si silicide in copper").

Within the framework of these assumptions, the temperature dependence of the electrical resistivity of the alloy can be represented as:

$$\rho(t) = \rho_0 + \alpha_t t + \alpha_x [x(t) - x_0] + \alpha_{xt} [x(t) - x_0] t, \quad (1)$$

where ρ_0 is the electrical resistance of the alloy in equilibrium state at 0 ^{0}C (Ohm·m), which takes into account, inter alia, obstacles to the movement of charge carriers due to the presence of impurities in the solid solution at 0 ^{0}C; α_t is the coefficient which takes into account obstacles to the movement of the electron flux caused by the thermal vibrations of copper atoms at temperatures other than 0 ^{0}C (Ohm·m/^{0}C); t is the value of temperature (^{0}C); α_x is the coefficient which takes into account obstacles to the movement of charge carriers caused by distortions in the crystal lattice of copper created by the presence of impurity atoms (nickel and silicon) in it at temperatures other than 0 ^{0}C (Ohm·m /%); $x(t)$ is the "Ni_2Si silicide content" in a copper-based solid solution at temperature t (wt.%); x_0 is the "Ni_2Si silicide content" in a copper-based solid solution at 0 ^{0}C (wt.%); α_{xt} is the coefficient which takes into account obstacles to the flow of charge carriers due to thermal vibrations of impurity atoms (nickel and silicon) in the crystal lattice of the solid solution at temperatures other than 0 ^{0}C (Ohm·m / (^{0}C·%)).

3. Solution of the problem under consideration

It is often difficult to bring the alloy at a temperature of 0 °C to a state which is close to equilibrium state as much as possible in order to determine experimentally the value of ρ_0. In this case, it is possible to provide calculations in a relative coordinate system, which implies determining of the content of elements dissolved in the base at a given temperature relative to their content at some randomly selected ("reference") temperature t_{01}. Obviously, the value of the ("reference") temperature should be chosen based on the convenience of achieving of the state of the solid solution which is the closest to equilibrium one at this temperature.

To shift the reference point of the values of resistivity to temperature t_{01}, expression (1) is reduced to the form

$$\rho(t) = \rho_{01} + \alpha_t(t - t_{01}) + \alpha_x[x(t) - x_0] + \\ + \alpha_{xt}[x(t) - x_0](t - t_{01}), \qquad (2)$$

where x_{01} is the "content of silicide Ni_2Si" in a solid solution based on copper at t_{01}; ρ_{01} is the value of the specific electrical resistance of the alloy determined by the polytherm at the "reference" temperature t_{01}. This addendum takes into account the influence of all the above mentioned factors on the movement of charge carriers at temperature t_{01}.

For K1H3 bronze, it is convenient to take t_{01} = 550 °C as the "reference" temperature (the optimal temperature of artificial aging of the hardened alloy [5]). For this temperature x_{550} = 1.59 wt. % [5] and $\rho_{550} = 11.718 \cdot 10^{-8}$ Ohm·m [3].

4. Results and discussion

The values of the coefficients, α_t, α_x and α_{xt} were determined by substituting in (2) the values of the specific electrical resistance of bronze K1H3 ($\rho(t)$) which were experimentally determined in [3], and also the equilibrium compositions of the solid solution, which were determined from the state diagram [5], at the corresponding temperatures.

To ensure a more complete verification of the adequacy of the obtained results, the group of data used in the calculation of the coefficients did not include information on the electrical resistivity and composition of the solid solution for temperatures lower than t_{01} = 550 °C. It should be emphasized that the number of obtained equations exceeds significantly the number of sought-for unknowns. Therefore, an overdetermined system of equations was solved by minimizing the residuals using the least-squares method. The calculated results give the following values of parameters: α_t = $0.0077 \cdot 10^{-8}$ Ohm·m/^{0}C; α_x = $2{,}5004 \cdot 10^{-8}$ Ohm·m /%; α_{xt} = $0.00346 \cdot 10^{-8}$ Ohm·m/(^{0}C·%).

The value of α_t = $0.0077 \cdot 10^{-8}$ Ohm·m/^{0}C is close to the tabular value of the absolute temperature coefficient of the specific electrical resistance of pure copper (according to [6] α_t = $0.00736 \cdot 10^{-8}$ Ohm·m/^{0}C). Even with the above assumptions, the calculation error is 4.6%. The results of comparison show a good coincidence between the experimentally determined temperature dependences of the electrical resistivity of K1H3 bronze and those ones which were calculated analytically using (2) (Fig. 1), including results for temperatures below 550 °C, which were not used for determining of the parameters of the model.It is also worth to pay attention on the accuracy of model's predictions (2) of the linear cross section of the polytherm of the K1H3 bronze electrical resistance at temperatures exceeding the solvus temperature (843 °C), although the experimental points lying on this segment also

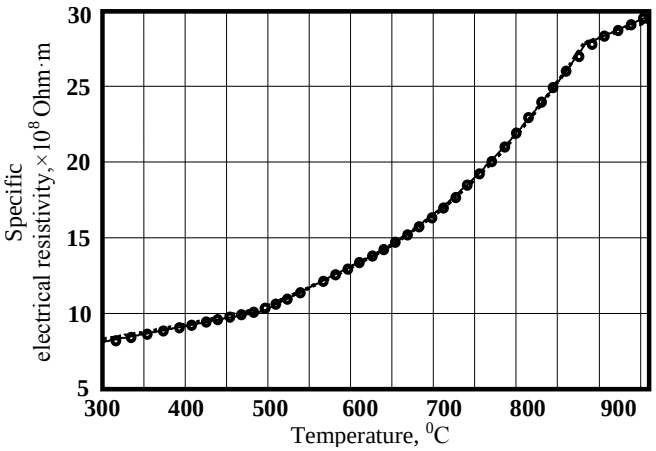

Figure 1 - Temperature dependence of the specific electrical resistivity of the bronze K1H3.
o - according to experimental data
. . – calculated by the equation (2)

were not used in calculations of the model parameters. The presence of this segment is associated with the completion of dissolution of the components of nickel silicide in the base. Ni_2Si phase which is a source of saturation of the copper-based solid solution with nickel and silicon is already absent in the structure of K1H3 bronze at temperatures above 843 °C (these elements are already completely dissolved in the base). Therefore, upon further heating, the specific resistance of the alloy increases only due to an increase of the average amplitude of atomic vibrations at the nodes of the crystal lattice. The action of only one factor, the intensity of the influence of which on the resistance value depends linearly on temperature, leads to the appearance of an almost rectilinear site on the polytherm.

However, the determination of the contents of dissolved elements in a phase based on copper (for equilibrium conditions of the coordinates of points lying on the solvus line) with the usage of experimental data on the polytherms of the electrical resistivity of the alloy is of the greatest practical interest. For this purpose, expression (2) should be submitted in the form:

$$x(t) = \frac{\rho(t) - \rho_{01} - \alpha(t - t_{01})}{\alpha_x + \alpha_{xt}(t - t_{01})} + x_{01}\ , \qquad (3)$$

Literature data on the coordinates of points belonging to the solvus line of the quasibinary Cu – Ni_2Si cross section of the state diagram of the Cu – Ni – Si system [5] are in good correlation with the

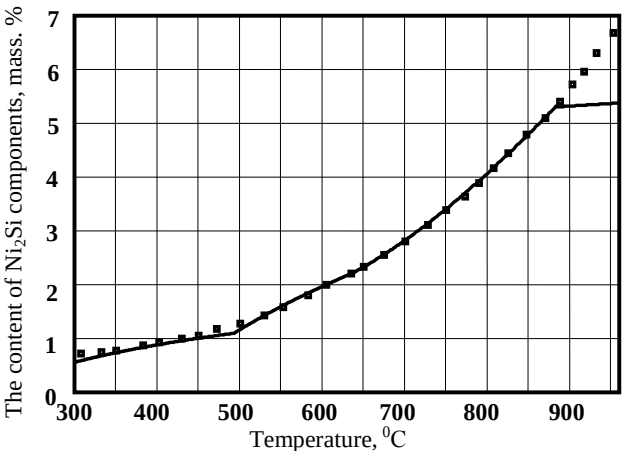

Figure 2 - Temperature dependence of the Ni_2Si content in copper based solid solution on alloys belonging to the quasibinary cross section of the Cu - Ni - Si system
□ □– experimental data [4]
- – calculated for K1H3 bronze according to the temperature dependence of resistivity

values of calculated electrical resistivity [3] (according to expression (3)) (Fig.2). It should be noted that there is a good coincedence between the data on the compositions of the solid solution at temperatures up to 550 °C, information about which was not used in the calculation of the coefficients of the model.

It should be noted that (3) can also be used to assess the temperature stability of dispersed phases in alloys of more complex systems (e.g., Cu - (Ni - Si) - (Fe - Cr - C)) for which state diagrams are absent in literature sources (therefore, it is not possible to obtain a priori information on the equilibrium composition of the solid solution at a "reference" temperature). Although in this case, expression (3) allows to obtain only the differences $x(t)-x_{01}$, however, this may be quite sufficient to estimate the temperature stability of the dispersed phases.

5. Conclusions

The aggregate of the above mentioned facts allows to assume that the developed model describes quite adequately the interrelation between the value of the electrical resistivity of the alloy and the content of dissolved elements in the base. Therefore, the presence of empirical data on the polytherms of electrical resistivity allows to determine analytically the content of elements dissolved in the base of alloy at various temperatures. Having made additional assumptions, it is possible to use the developed model in the future to assess the temperature stability of the dispersed phases in alloys of more complex systems (for example, such as Cu - (Ni - Si) - (Fe - Cr - C)).

6. References

1. Nikolaev A.K. Alloys for electrodes of contact welding. M., Metallurgy, 1978, 96 p. (Nikolaev A.K., Rosenberg V.M.) (Russion)

2 Nikolaev A. K. Chrome bronzes. M., Metallurgy, 1983, 176 p.(Nikolaev A.K., Novikov A.I., Rosenberg V.M.) (Russion)

3. Khristenko V.V. Effect of the content of dissolved elements in the copper-based phase on the polytherm of the electrical resistance of quasi-binary Cu - Ni_2Si alloys of the cross section of the state diagram of the Cu - Ni - Si system.- Casting processes, 2012, № 2, p. 73 - 77. (Khristenko V.V., Kirievsky B.A, Trubachenko L.N.) (Russion)

4. A.R. Denton. Vegard's law.- Phys. Rev., 1991, A, 43, p. 3161–3164. (A.R. Denton, N.W. Ashcroft).

5. Suchkov D. I. Copper and its alloys. M., Metallurgy, 1967, 248 p. (Russion)

6. Ed. Samsonova. Properties of the elements. Part 1. Physical properties. Directory. M., Metallurgy, 1975, 600 p. (Russion)

THEORETICAL MODELING OF THE MAGNETIC STATES OF SYNTHESIZED $FE_3O_4 – FE_{3-X}TI_XO_4$ PARTICLES

Prof. Dr. Kharitonskii P.V.[1], Ph.D. Kosterov A.A.[2], B. Sc. Gurylev A.K.[1], Anikieva Y.A.[1], Zolotov N.A.[1], M. Sc. Kirillova S.A.[1], Ph.D. Gareev K.G.[1]

Saint Petersburg Electrotechnical University ‘‘LETI”, Saint Petersburg, Russia[1]
Saint Petersburg State University, Saint Petersburg, Russia[2]
Email: gurylev.tosha@yandex.ru

Abstract: A system of two-phase particles ($Fe_3O_4 – Fe_{3-x}Ti_xO_4$) has been obtained using the sol-gel method followed by hydrothermal treatment. It is shown that the synthesis conditions favor forming composites that contain titanomagnetite in very low concentration. A theoretical analysis of the magnetic properties of system was performed using the model of clusters consisting of magnetostatically interacting particles. The theoretical value of the saturation magnetization and the experimental values of the coercive force can be explained by the presence of two different magnetic phases.

Keywords: *MICROMAGNETIC MODELING, TWO-PHASE NANOSTRUCTURES, MAGNETOSTATIC INTERACTION, DEMAGNETIZATION COEFFICIENTS, COMPOSITES “MAGNETITE – TITANOMAGNETITE”*

1. Introduction

Magnetic nanoparticles, especially in the superparamagnetic state, are often used to filter heavy metals, to isolate nucleic acids and proteins, in target drug delivery and in magnetic hyperthermia [1-3]. In addition, magnetic nanoparticles are of interest in the context of environmental magnetism providing valuable information on paleoclimate [4, 5].

In this work, we present experimental data on the synthesized $Fe_3O_4 – Fe_{3-x}Ti_xO_4$ composites and the theoretical modeling of their magnetic properties. The complexity of modeling such structures stems from both magnetic and chemical inhomogeneity of particles. This requires the use of micromagnetic modeling taking into account the dipole – dipole interaction and magnetic granulometry data.

Results of theoretical calculations are in good agreement with the experimental results obtained using X-ray diffractometry, X-ray fluorescence, electron microscopy, vibration sample and SQUID-magnetometry.

2. Solution of the examined problem

2.1 Theoretical model

Let us consider a chemically inhomogeneous two-phase particle whose magnetic states can be described using a model developed previously [6-8].

To simplify the mathematical treatment, we assume that each phase of the particle (Fig. 1) is a uniformly magnetized uniaxial ferrimagnet with spontaneous magnetizations M_{s1} и M_{s2} and dimensionless first-order crystallographic anisotropy constants K_{11} и K_{12}, respectively. The inter-phase boundary is parallel to the *XZ* plane and divides the particle into two parallelepipeds having volumes $qa^3(1-\varepsilon-\delta)$ for the first phase and $qa^3\varepsilon$ for the second phase. We consider the case when the external field is parallel to the *Z*-axis. This allows us to describe the orientation of the magnetic moment of each phase using the single angle θ counted from the *Z*-axis (the magnetization vector lies in the *XZ* plane).

To find magnetic states and construct magnetization curves, free energy was minimized, including the exchange, magnetocrystalline, magnetostatic, and Zeeman energies. Free energy of the particle is written as ($\delta = 0$):

$$E = qa^3(N_{13}M_{s1}^2 + N_{33}M_{s2}^2 + \left(N_{11} - N_{13} + K_{11}(1-\varepsilon)\right) \times$$
$$\times M_{s1}^2 sin^2\theta_1 + (N_{31} - N_{33} + K_{12}\varepsilon)M_{s2}^2 sin^2\theta_2 + N_{21}M_{s1}M_{s2} \times$$
$$\times sin\theta_1 sin\theta_2 + N_{23}M_{s1}M_{s2}cos\theta_1 cos\theta_2 - H(1-\varepsilon)M_{s1}cos\theta_1 -$$
$$- H\varepsilon M_{s2}cos\theta_2), \qquad (1)$$

where H is the Zeeman field, N_{ij} are shape anisotropy coefficients. If $\delta \neq 0$, then the free energy can be calculated considering the change in the magnetic characteristics at the boundary [7].

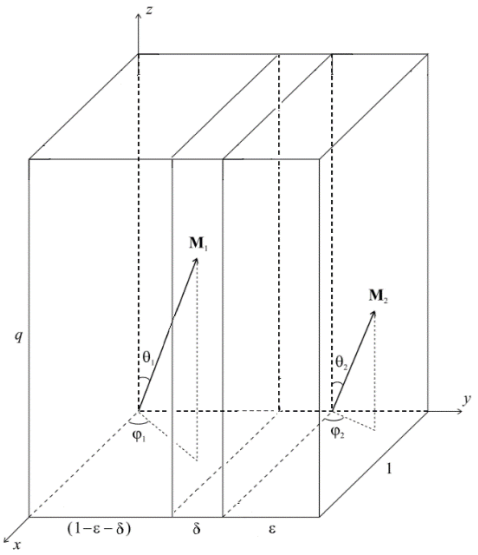

Fig. 1. *A model of a two-phase particle with a boundary of finite width δ. The characteristic particle size a, elongation q, width of the second phase ε*

In our calculations, we use a model in which the inter-phase boundary between chemically different regions is infinitely thin due to the proximity of their magnetic and structural characteristics. In the case of grains containing few domains (pseudo-single-domain), we consider the domain wall as an extended one, so that chemical inhomogeneity is taken into account by introducing effective parameters.

In this model, a particle can be in four states (indices 1 and 2 number the first and second phases, respectively): 1) $\theta_1 = 0$, $\theta_2 = 0$; 2) $\theta_1 = \pi$, $\theta_2 = \pi$, 3) $\theta_1 = 0$, $\theta_2 = \pi$, 4) $\theta_1 = \pi$, $\theta_2 = 0$. Applying an external magnetic field H (parallel to the *Z*-axis) does not produce the additional equilibrium states, but only makes the existing ones more or less advantageous.

Thus, an ensemble can contain four types of particles. These will determine the critical fields of magnetization reversal for a given two-phase grain. In the case of an ensemble of identical particles, the expression for magnetization has the form [9]:

$$I(q, \varepsilon, H) = c\left[M_{s1}(1-\varepsilon)\frac{n_1 - n_2 + n_3 - n_4}{n_0} + M_{s2}\varepsilon\frac{n_1 - n_2 - n_3 + n_4}{n_0}\right], \qquad (2)$$

where c is the volume concentration of two-phase particles in a non-magnetic matrix, $n_k = n_k(H)$ is the number of particles in the k^{th} state, determined from the statistical Boltzmann distribution.

In the case of an ensemble of magnetostatically interacting particles distributed randomly in a nonmagnetic matrix, an interaction field H_{int} produced by all the particles in the ensemble acts on each particle. Let the random interaction fields H_{int} be uniformly distributed in the interval ($-H_{max}$; $+H_{max}$) [10]:

$$H_{max} \approx 5c[M_{s1}(1-\varepsilon) + M_{s2}\varepsilon], \text{ if } c<0.07,$$
$$H_{max} \approx 1.3\sqrt{c}[M_{s1}(1-\varepsilon) + M_{s2}\varepsilon], \text{ if } c\geq 0.07. \quad (3)$$

In addition, we use the approximation assuming that when the external field changes, all the moments that change direction turn over simultaneously and independently of each other, i.e. the rotation of one moment does not affect the distribution of the interaction fields [9]. The magnetization of the ensemble of interacting particles is then written as:

$$I(H) = \frac{1}{2H_{max}} \int_{-H_{max}}^{+H_{max}} I(H - H_{int}) dH_{int}. \quad (4)$$

The values of magnetization and magnetization reversal fields obtained using the ensemble model of two-phase particles were further consistent with theoretical estimates of the hysteresis parameters and characteristics of anhysteretic remanent magnetization calculated on the basis of the approach used in [11].

The use of these models can reveal the characteristic features associated with chemical heterogeneity. It is however pointless to determine the fine structure of magnetization without detailed information about the structure of particles. Thus, the aim of this study is to develop general understanding of the magnetic structure of chemically inhomogeneous particles. Simplified structures found in such a study can then be used as initial approximations for subsequent more realistic calculations.

2.2 Synthesis of $Fe_mO_n - TiO_2$ composites

Synthesis of composites based on the $Fe_mO_n - TiO_2$ system was carried out by precipitation of magnetite in a suspension of TiO_2 powder [12]. 4 g of $FeCl_3 \cdot 6H_2O$ and 2 g of $FeSO_4 \cdot 7H_2O$ (molar ratio 2:1), were dissolved in 100 ml of distilled water. After that (0.5, 1, 2 g) of the TiO_2 powder was dispersed in the solution for samples T05L and T05H, T10L, T20L accordingly. Then 10 ml of ammonia solution was added to the suspension, and the magnetic precipitate has been washed using Nd-Fe-B permanent magnet for particle extraction until pH = 7 was reached and chloride and sulfate ions were absent. Finally, powders were dried at room temperature. After that, three powders with different Ti content were hydrothermally treated in distilled water at 240°C and 50 MPa for 4 hours. Sample T05H was treated at 470°C and 42 MPa, respectively, also for 4 hours.

2.3 Methods for the study of physicochemical and magnetic characteristics

Phase composition of the samples was determined by X-ray phase analysis using a DRON-3M diffractometer (JSC IC "Burevestnik", Russia). Peak identification on the diffractogram was performed using PDWin 4.0 and Crystallographica Search-Match software packages. Based on X-ray powder diffractograms, average crystallite size corresponding to regions of coherent scattering and the parameters of the crystal lattice unit cell have been calculated. Samples elemental composition was determined by electron probe microanalysis using a Hitachi S-570 scanning electron microscope (Hitachi Ltd., Japan), equipped with Bruker Quantax 200 microprobe system (Bruker Corp., USA). Qualitative and quantitative elemental analysis of the samples was carried out using a portable X-ray fluorescence crystal diffraction scanning spectrometer Spectroscan MAX-GF2E with built-in software ("Spectroscan" Ltd., Russia).

To determine the grain size, the specific surface area (SSA) was estimated using the instrument SORBI N.4.1 (CJSC "META", Russia). The volume of adsorbate gas absorbed by the test sample was compared to the standard sample with a known specific surface area using the thermal desorption method. Nitrogen was used as the adsorbate gas. Determination of the specific surface area has been carried out according to the 4-point BET method. The obtained data were subsequently confirmed by scanning electron microscopy (SEM) using a Hitachi S-3400N microscope (Hitachi Ltd., Japan).

Hysteresis characteristics were measured at room temperature using a PMC 3900 vibrating sample magnetometer (Lake Shore Cryotronics, USA). Demagnetization curves of the anhysteretic remanent magnetization (ARM) were measured using an SRM-755 SQUID magnetometer (2G Enterprises, USA), also at room temperature.

3. Results and discussion

3.1 Physicochemical characteristics

Figure 2 shows the SEM images of the sample. As seen in Figure 1, particles with average size of 100–200 nm form aggregates as large as a few micrometers.

Figure 3 shows X-ray diffraction patterns for four samples, with peak designation according to the PDF-2 database.

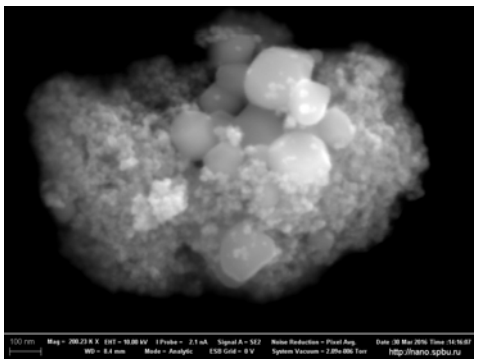

Fig. 2. *SEM images of the sample T05H*

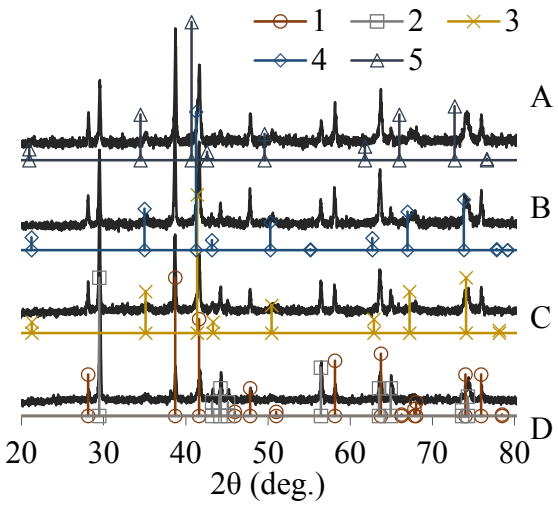

Fig. 3. *X-ray diffraction patterns of the samples T05H (A), T05L (B), T10L (C), and T20L (D). 1 – α-Fe_2O_3 Hematite 33-664, 2 – TiO_2 Anatase 21-1272, 3 – Fe_3O_4 Magnetite 19-629, 4 – $Fe_{2.75}Ti_{0.25}O_4$ Titanomagnetite 75-1373, 5 – Fe_2TiO_4 Ulvöspinel 34-177*

Particle sizes are distributed over a relatively wide range from few tens to hundreds of nm. Particles are often combined into agglomerates (clusters) of submicron to micron size. Judging from the X-ray data, samples may contain at least three magnetic minerals: magnetite, titanomagnetite and hematite.

3.2 Magnetic characteristics

Figure 4 shows the hysteresis loop for the T05H sample. Hysteresis curves of other samples have a similar shape.

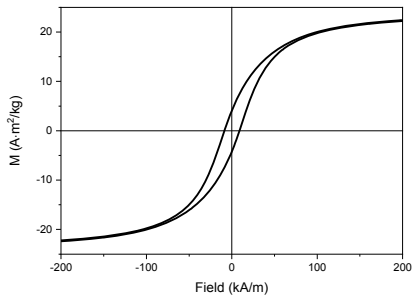

Fig. 4. *Hysteresis loop for the sample T05H. Only the central part of the loop is shown for clarity*

Saturation magnetization and remanent saturation magnetization of the T05H sample are 23.8 $A \cdot m^2/kg$ and 4.2 $A \cdot m^2/kg$, respectively. Coercive force and remanent coercivity are 8.8 kA/m and 18.4 kA/m. Ratios of the remanent magnetization to saturation magnetization (M_{rs}/M_s) and the remanent coercivity to coercive force (H_{rc}/H_c) amount respectively to 0.18 and 2.1. Experimental data for magnetite [13] show that such values correspond to particles containing few domains (pseudo-single-domain) with characteristic size > 100 nm. Alternatively, these may be due to magnetostatically interacting superparamagnetic particles, combined into clusters with the same characteristic size.

In a model of ARM of single-domain particles [14], it is assumed that an alternating field of a given amplitude magnetizes magnetic particles having remanent coercivity H_{rc} approximately equal to that amplitude. Therefore, the ARM demagnetization curve by alternating field can be regarded as a proxy for the remanent coercivity spectrum. Thus, the obtained data make it possible to use demagnetization curves to describe the distribution over H_{rc} and to reveal the effective particle size distribution [14].

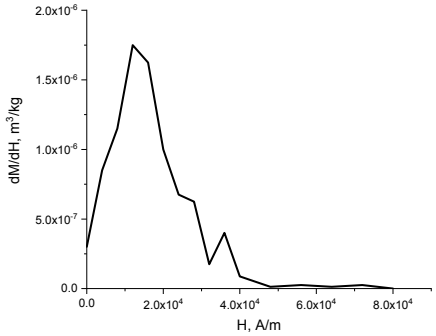

Fig. 5. *The coercive spectrum of the T05H sample*

Differentiating the ARM demagnetization curve, we obtain the coercive spectrum of our sample shown in Fig. 5. For this sample, the coercive spectrum has a maximum around 3 maxima (~ 12, 28, and 36 kA/m) can be seen. Moreover, the curve is clearly asymmetric, so that the main fraction of particles has coercivities between 8–24 kA/m.

3.3 Theoretical modeling

Changes in the composition and structure on the surface of magnetic particles associated with the diffusion of titanium atoms into the crystal lattice of magnetite and/or the formation of vacancies and stresses result in their chemical inhomogeneity. For simplicity, we further consider a model of an ensemble of two-phase magnetic particles of the "magnetite-titanomagnetite" type. The contribution to the remanent magnetization of hematite can be neglected, since its spontaneous magnetization is two orders of magnitude smaller than that of magnetite.

The T05H sample obtained in the high-temperature conditions (470°C, 42 MPa) has the most interesting magnetic properties. Particles and/or agglomerates of three types represent its particle size distribution: several microns in size, submicron and smaller (of the order of ten or less nanometers).

To match the models in terms of size and concentrations of magnetic nanoparticles, we assume their volume distribution s in the sample to be lognormal [15]. The fraction of the area under the lognormal distribution curve for a certain range of volumes corresponds to the fraction of particles having these volumes. Fig. 6 shows an approximate lognormal distribution curve of magnetic nanoparticles in the selected T05H sample.

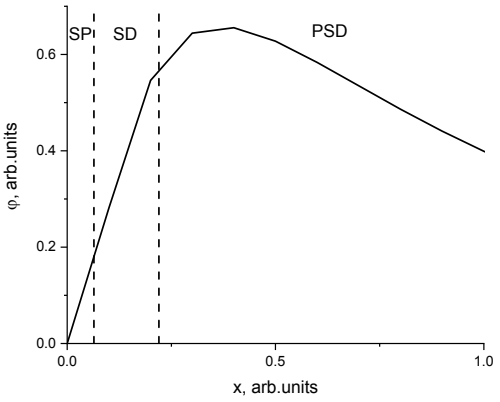

Fig. 6. *Log-normal density function $\varphi(x)$, $x=v/v_p$ ($v_p = (\pi/6)\cdot(d_p)^3$, $d_p \approx 50$ nm)*

Assuming a lognormal distribution of particle volumes, three groups were identified during the simulation: superparamagnetic (SP), single domain (SD) and pseudo single domain (PSD) particles with average sizes (diameters) of about 18, 27 and 60 nm, respectively.

To estimate the spontaneous magnetization, saturation magnetization, coercivity, concentration, and fraction of the second phase in a two-phase particle, the model described in section 2.1 was used. In this case, it was assumed that the fraction of the second (titanomagnetite) phase is approximately 0.5 for SP and SD particles and 0.01 for PSD (due to the small specific surface area). A small remanent magnetization and nonzero coercivity of the SP particles are explained by their interaction in clusters.

Fig. 7 shows the coercive spectra for different groups of particles obtained using the two-phase grain model.

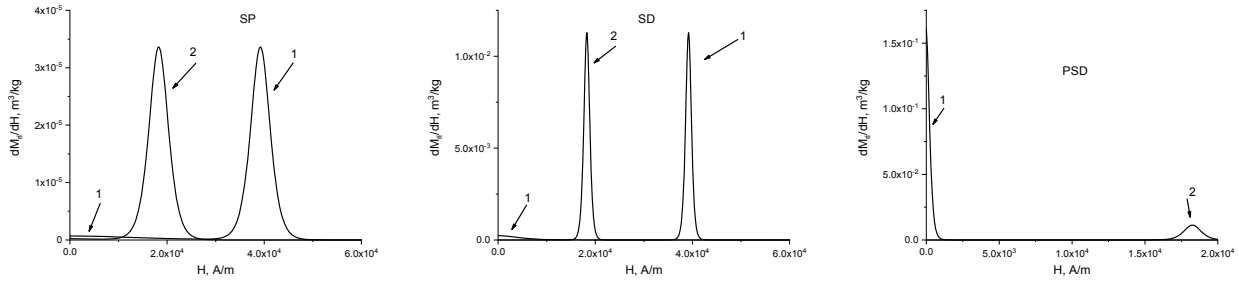

Fig. 7. *Coercive spectra of two-phase particles after simulation: 1 and 2 - spectra of particles without interaction and taking into account the interaction, respectively*

Notably, the main peaks (1) of the curves not taking into account the interaction (Fig. 7) agree well with the experimental ARM spectrum (Fig. 5). The expanded width of the peak in the experimental spectrum may be due to a greater diversity in the $n_k(H)$ particle types, which can lead to a broadening in H_{rc}. Presence of near-zero fields of magnetization reversal for SP and SD is caused by a transition to intermediate states. For non-interacting PSD particles, small coercivities are due to the emergence of a domain structure. In large fields, all magnetic moments enter the ground state, their orientations being along the external field. The peaks (2) calculated for interacting case (Fig. 7), are close to the average H_{rc} for the ensemble of all particles (SP, SD, PSD).

4. Conclusion

Theoretical modeling of a system of two-phase magnetostatically interacting particles of synthesized composites allows us to draw the following conclusions.

The magnetic characteristics of the composites calculated within the framework of the proposed model agree well with the experimental data.

The presence of a titanomagnetite phase appears quite likely, which should significantly affect the magnetic properties, especially of SP and SD particles. Simulation results best correspond to experimental data at characteristic sizes of 18, 27, and 60 nm and volume concentration of 10^{-5}, 10^{-3}, and $3.3 \cdot 10^{-2}$ for SP, SD, and PSD particles, respectively.

Theoretical and experimental coercive spectra show similar ranges of critical fields. Magnetostatic interaction between particles can result in a spread of critical fields and thus to a broadening of the coercive spectra.

References

1. Giakisikli G. and Anthemidis A. Magnetic materials as sorbents for metal/metalloid preconcentration and separation. A review. Analytica Chimica Acta, Vol. 789, 2013, pp. 1–16.
2. Sadighian S., Rostamizadeh K. [et al]. Doxorubicin-conjugated core–shell magnetite nanoparticles as dual-targeting carriers for anticancer drug delivery. Colloids Surf B Biointerfaces, Vol. 117, 2014, pp. 406–413.
3. Ding Q, Liu D. [et al]. Shape-controlled fabrication of magnetite silver hybrid nanoparticles with high performance magnetic hyperthermia. Biomaterials, Vol. 124, 2017, pp. 35–46.
4. Maher, B. A., & Thompson, R. Quaternary climates, environments and magnetism. Cambridge University Press, 1999.
5. Liu, Q., Roberts, A. P. [et al]. Environmental magnetism: Principles and applications. Rev. Geophys., Vol. 50, 2012, P. RG4002.
6. Ralin A. Yu. and Kharitonskii P. V. Magnetic metastability of small inhomogeneous ferrimagnetic particles. Physics of metals and metal science, Vol. 78, 1994, pp. 38–43.
7. Ralin A. Yu. and Kharitonskii P. V. Features of the domain structure of small two-phase chemically inhomogeneous particles. Physics of metals and metal science, Vol. 102, 2006, pp. 133–138.
8. Kharitonskii P., Rudnev V. [et al]. Peculiarities of Magnetic States of Iron-Cobalt Coatings Formed on Aluminum by Plasma Electrolytic Oxidation. Journal of Superconductivity and Novel Magnetism, Vol. 31, 2018, pp. 1933–1940.
9. Afremov L. L., Ralin A. Yu. [et al]. Features of the magnetization curves of an ensemble of chemically inhomogeneous two-phase grains. Physics of the solid Earth, Vol. 6, 1995, pp. 80–84.
10. Shcherbakov V.P. On the distribution function of molecular fields in systems with randomly distributed interaction centers. Physics of metals and metal science, Vol. 48, 1979, pp. 1134-1137.
11. Kharitonskii P. Kamzin A. [et al]. Magnetic granulometry and Mössbauer spectroscopy of Fe_mO_n–SiO_2 colloidal nanoparticles. JMMM, Vol. 461, 2018, pp. 30–36.
12. Bogachev Yu. V., Gareev K. G. [et al]. Study of magnetite nanoparticle suspensions by photometry and NMR relaxometry. Physics of the Solid State, Vol. 55, 2013, pp. 2431–2435.
13. Day R., Fuller M. [et al]. Hysteresis properties of titanomagnetites: grain-size and compositional dependence. Physics of the Earth and planetary interiors, Vol. 13, 1977, pp. 260-267.
14. Kirschvink J.L., Jones D.S., MacFadden B.J. Magnetite Biomineralization and Magnetoreception in Organisms. A New Biomagnetism, N.-Y.: Plenum Press, 1985.
15. Ajitkumar J., Lin-Sien H. and Lum, Stanley D. NIST Recommended Practice Guide: Particle Size Characterization. Washington.: U.S. Government Printing Office, 2001.

This work was partly supported by the Russian Foundation for Basic Research, grants No. 18–05– 00626 and No. 19–05–00471)

MODELING OF OVERLAP AREA OF POWDER FILTER MATERIALS

МОДЕЛИРОВАНИЕ ЗОНЫ ПЕРЕКРЫТИЯ ПОРОШКОВЫХ ФИЛЬТРУЮЩИХ МАТЕРИАЛОВ

Prof., Dr. Eng., Cor. Member of NAS of Belarus Ilyushchanka A.[1, 2],
Head of the Lab. Charniak I.[2], Res. Zhehzdryn D.[2], Dr. Eng., Docent Kusin R.[3],
State Research and Production Powder Metallurgy Association[1] – Minsk, Republic of Belarus
State Scientific Institution "O.V. Roman Powder Metallurgy Institute" [2] – Minsk, Republic of Belarus
Belarusian State Agriculture Technical University [3] – Minsk, Republic of Belarus
E-mail: alexil@mail.belpak.by, irinacharniak@tut.by, 2312444@mail.ru, lerakor1974@mail.ru

Abstract: *A model for calculating the permeability of two-layer powder filter materials (PFMs) is proposed taking into account the overlap area. Examples of calculating the permeability of PFMs on real powder structures are given.*
KEYWORDS: TWO-LAYER POWDER FILTER MATERIALS, CALCULATION MODEL, PERMEABILITY, OVERLAP AREA.

1. Introduction

Despite the widespread use of polymeric, paper, and ceramic materials in engineering, powder filter materials compete worthy with them, especially in cases where it is necessary to realize the physico-chemical properties typical for metals and alloys from which PFMs consist. PFMs are successfully used to solve various problems: for aeration of the air flow in order to saturate the air-culture fluid with oxygen when growing aerobic microorganisms in bioreactors; for dispergation of the ozone-containing air mixture flow in order to decontaminate the fish habitat (including young fish) in recirculating aquaculture systems (RAS) and uniform distribution of vapor flow over the volume of coolant (water) to control the temperature in working tanks during heat treatment of milk, milk mixtures and technological media used in milk treatment; air, water vapor, and oil purification, as well as for other purposes [1–5].

In practice, two-layer materials are widely used to increase the operational properties of PFM. One layer is formed by fine particles and provides the necessary fineness of cleaning. The second layer if formed by coarse particles and provides sufficient strength and high permeability of PFM [6, 7]. The problem in this case is the appearance of the intermediate layer at the boundary of the layers, the so-called "overlap area", in which smaller particles fill the pore space formed by coarse particles [8]. One of the effective ways to improve the properties of two-layer PFMs is to reduce the thickness of the fine layer [8]. In this regard, the calculation of the influence of the overlap area on the properties of two-layer PFMs is of great interest.

The purpose of this work is modeling of PFM "overlap area" and calculation of the permeability of this area.

2. Results and discussion

When two-layer materials are produced by co-molding powders of different fractions in the area of the layer boundary, smaller powder particles partially fill the pore space formed by larger particles, making, as noted above, an intermediate layer (overlap area). Figures 1 and 2 illustrate examples of the formation of such structures in the production of two-layer materials based on titanium and copper powders. We determine the effect of the overlap area on the permeability of two-layer PFMs.

To calculate the permeability taking into account the overlap area, we consider the case when the porous material consists of two layers and the overlap area. The first and second layers are respectively formed from powder particles with sizes D_1 and D_2, with $D_1 > D_2$. The overlap area (conditionally it can be considered as the third layer), located between the first and second layers. It consists of particles of these two sizes. Small particles with sizes D_2 are located between large particles with size D_1. We denote the thicknesses of the first layer (substrate), the intermediate layer (overlap area) and the second layer (fine powder) by h_1, h_{12} and h_2, and the flow rate of the filtered medium through the PFM per unit time by Q.

Fig. 1 The structure of a two-layer PFM made of titanium powders with a particle size of (minus 1000 + 400) and (minus 100 + 40) μm

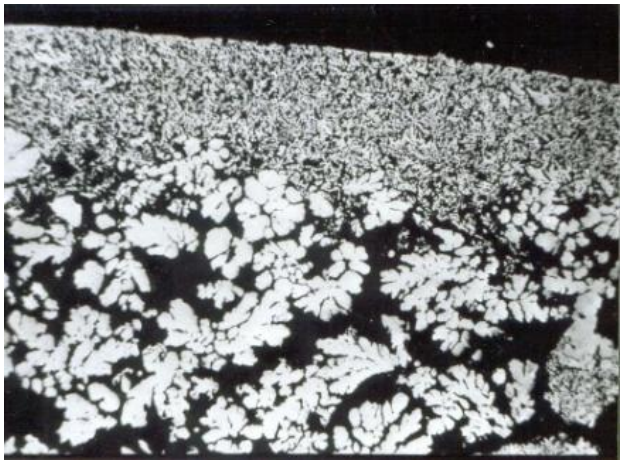

Fig. 2 The structure of a two-layer PFM made of copper powders with particle sizes (minus 315 + 200) and (minus 80 + 40) μm

Considering the flow of a liquid or gas through the whole material, it is possible to write the following according to Darcy's law [9]:

$$Q = \frac{k\Delta p}{\mu h} S, \qquad (1)$$

where k – coefficient of permeability; Δp – differential pressure on PFM; S – filtration area; μ – viscosity of filtered medium; h – thickness of PFM.

For each layer separately, equation (1) can be written as follows:

$$Q_1 = \frac{k_1 \Delta p_1}{\mu h_1} S, \quad (2)$$

$$Q_{12} = \frac{k_{12} \Delta p_{12}}{\mu h_{12}} S, \quad (3)$$

$$Q_2 = \frac{k_2 \Delta p_2}{\mu h_2} S, \quad (4)$$

where Δp_1, Δp_{12}, Δp_2, - respectively, differential pressure on each of the layers with thicknesses h_1, h_{12}, h_2;

S – the filtration area of all layers (the first layer is the substrate; the intermediate layer is the overlap area and the second layer is fine powder).

Obviously, the flows of the filtered medium passing through the whole material Q and through each layer separately Q_1, Q_{12}, Q_2, are equal to each other:

$$Q = Q_1 = Q_{12} = Q_2, \quad (5)$$

and differential pressure on PFM and its thickness are:

$$\Delta p = \Delta p_1 + \Delta p_{12} + \Delta p_2, \quad (6)$$

$$h = h_1 + h_{12} + h_2. \quad (7)$$

Based on (1–4), taking into account (5–7), it is possible to obtain the following equations:

$$\frac{\Delta p_1}{\Delta p} = \frac{k h_1}{k_1 h}, \quad (8)$$

$$\frac{\Delta p_{12}}{\Delta p} = \frac{k h_{12}}{k_{12} h}, \quad (9)$$

$$\frac{\Delta p_2}{\Delta p} = \frac{k h_2}{k_2 h}. \quad (10)$$

Summing up the left and right sides of equations (8–10), we obtain the equation for calculating k:

$$1 = \frac{k h_1}{k_1 h} + \frac{k h_{12}}{k_{12} h} + \frac{k h_2}{k_2 h}, \quad (11)$$

from which:

$$k = \frac{h}{\frac{h_1}{k_1} + \frac{h_{12}}{k_{12}} + \frac{h_2}{k_2}}. \quad (12)$$

To determine the coefficient of permeability in the overlap area, we have the following considerations. Surface sections blocked by large particles with sizes D_1 are excluded from the filtering process of this layer, and therefore its throughput capacity is determined by the pore space areas of the substrate filled with fine powder with an area of $S_{12} < S$. Accordingly, the coefficient of permeability of these areas can be taken equal to k_2.

Then, on the basis of the continuity condition of the flow (5), the value of Q_{12} can be represented as:

$$Q_{12} = \frac{k_2 \Delta p_{12}}{\mu h_{12}} S_{12}. \quad (13)$$

Equating the right sides of equations (3) and (13) to each other, we obtain:

$$k_{12} = k_2 \frac{S_{12}}{S}. \quad (14)$$

To calculate S/S_{12} value, we use the elementary cell model, according to which the properties of each PFM element are determined by the elementary cell parameters in the form of a parallelepiped selected from the regular laying of 8 powder particles joined by interparticle contacts [9]. Then the value of S_{12} within such a cell varies from a minimum value equal to:

$$S_{12\min} = D_1^2 - \frac{\pi}{4} D_1^2, \quad (15)$$

to the maximum value:

$$S_{12\max} = D_1^2. \quad (16)$$

To calculate S_{12}, we take the average value of this quantity:

$$S_{12cp} = D_1^2 - \frac{\pi}{8} D_1^2. \quad (17)$$

Given that:

$$S = D_1^2, \quad (18)$$

then:

$$\frac{S}{S_{12}} = \frac{1}{1 - \frac{\pi}{8}}. \quad (19)$$

The resulted equations (11), (14) and (15) make it possible to calculate the coefficient of permeability of a two-layer PFM taking into account the overlap area between layers, knowing the values of the coefficients of permeability of the substrate and the fine layer.

Table 1 shows the results of calculations of the PFM permeability coefficients for two-layer materials, the structures of which are shown in Figures 1 and 2, and their experimental values. The values of the permeability coefficients of the substrate and the fine layer, as well as the thickness of the overlap layer are determined experimentally.

Table 1

The calculated and experimental values of the permeability coefficients of two-layer PFMs

Initial material	Powder particle size, μm		Thickness, mm			Coefficient of permeability, m^2, $\times 10^{13}$				
						Experimental values			The calculated value of two-layer PFM	
	Sub-strates	of fine layer	Sub-strates	of overlap area	of fine layer	Sub-strates	of fine layer	of two-layer PFM	with over-lap area	without overlap area
Titanium powder	minus 1000 +400	minus 100 +40	3	1,0	1,5	180,0	7,0	14,2	11,8	23,3
Copper powder	minus 315 +200	minus 80 +40	1,7	0,3	1,0	70,0	2,16	4,17	4,19	6,1

The analysis of the data presented in the table shows, firstly, a satisfactory coincidence of the calculated and experimental data and, secondly, a significant negative effect of the overlap area on the permeability of two-layer PFMs: its presence reduces the permeability by 1.46 – 1.98 times when comparing the resulted calculations and by 1.46 – 1.64 times when comparing the results of

calculations with experimental values. This effect can be reduced by reducing the thickness of the fine layer.

Figure 3 shows the calculated dependences of the permeability coefficients of two-layer PFMs based on titanium (1) and copper (2) powders on the layer thickness of fine powder at a constant total thickness of the porous material, which, when compared with the calculated data presented in the table, indicate that, for example, a three-fold decrease in the thickness of the fine layer leads to an increase in the permeability of PFM based on titanium by 1.4 times, and based on copper – by 1.8 times. In the second case, the permeability coefficient of the material is higher than the value of the permeability coefficient of PFM with the initial thickness of the fine layer, calculated without taking into account the overlap area.

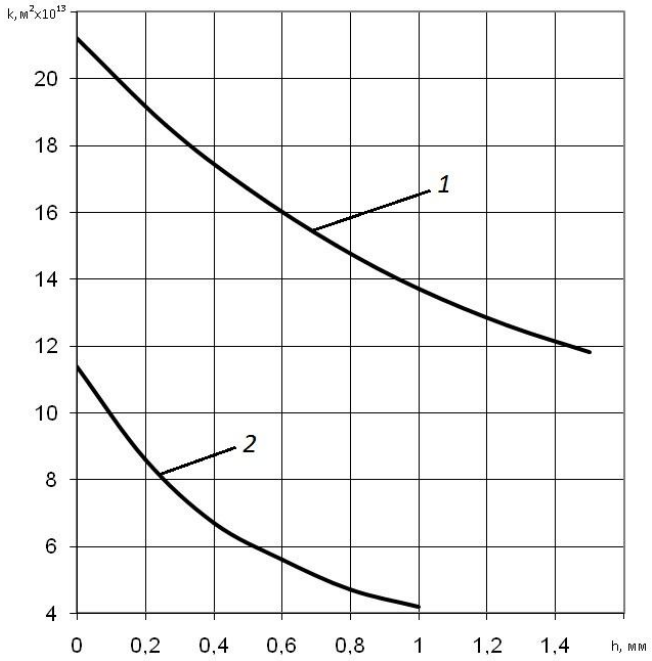

Fig. 3 The dependence of the permeability coefficient of two-layer PFM on the thickness of the fine layer:
1 – titanium-based PFM, 2 – copper-based PFM

4. Conclusion

With reference to the abovementioned, it is possible to state that the quotation obtained for calculating the permeability coefficient of two-layer PFMs with the overlap area satisfactorily agrees with experimental data. The negative effect of this area on the permeability coefficient of the porous material is shown, which, due to its presence, decreases by more than 1.46 times. It was found that this effect can be compensated by a decrease in the fine powder layer.

5. References

[1] Ilyushchanka, A.Ph. The use of powder filter materials in the processes of cultivation of aerobic microorganisms in the processing of milk whey and heat treatment of dairy products in agro-industrial complex. – Porous permeable materials: technologies and products based on them, October 19–20, 2017, Minsk, Belaruskaya Navuka, pp. 437–442. (in Russian)

[2] Kusin, R.A. The use of porous powder materials as gas flow distributors at enterprises of agro-industrial complex. – Current problems of the implementation of new equipment, technologies, technical service organization in the agro-industrial complex, June 7–8, 2017, Minsk, BSATU, pp. 91–96. (in Russian)

[3] Ilyushchanka, A.Ph. The use of powder dispersants for water ozonation in recirculating aquaculture systems. – Porous permeable materials: technologies and products based on them, Minsk, Belaruskaya Navuka, 2014, pp. 236–239. (in Russian)

[4] Kaptsevich, V.M. Refining of industrial oils by means of powder filter materials. – Actual problems of mechanization of agricultural production, October 12–14, 2001, Gorki, BSAA, 2001, Part 2, pp. 103–108. (in Russian)

[5] Kaptsevich, V.M. The use of porous powder material for filtering drinking water. – Actual problems of mechanization of agricultural production, October 12–14, 2001. Gorki, BSAA, 2001, Part 2, pp. 26–28. (in Russian)

[6] Vityaz, P.A. Porous powder materials: history, current state and promising developments, 50 years old to powder metallurgy in Belarus. History, achievements, prospects, Minsk: SRP PMA, 2010, pp. 251-320. (P. Vityaz). (in Russian)

[7] Ilyushchanka, A.Ph. Advanced materials in agricultural engineering, Minsk: BSATU, 2009, p. 256 (A. Ilyushchanka, V. Kaptsevich, R. Kusin, A. Yarkovich, A. Kusin). (in Russian)

[8] Kusin, A.R. Improving the efficiency of two-layer powder permeable materials. – New materials, equipment and technologies in industry, Mogilev, State Institution of Higher Professional Education “Belarusian-Russian University”, 2005, p. 100). (in Russian)

[9] Vityaz, P.A. Filter materials: properties, fields of applications, manufacturing technology, Minsk: “Research Institute of Powder Metallurgy with Pilot Production”, 1999, p.304. (P. Vityaz, V. Kaptsevich, R. Kusin). (in Russian).

SIMULATION OF THE THERMAL STABILITY AND MELTING OF THE Ag@Pd, Au@Pd BIMETALLIC NANOPARTICLES

МОДЕЛИРОВАНИЕ ТЕРМИЧЕСКОЙ СТАБИЛЬНОСТИ И ПЛАВЛЕНИЯ БИМЕТАЛЛИЧЕСКИХ НАНОЧАСТИЦ Ag@Pd, Au@Pd

Sen. Lect., PhD Shvets U., Assoc. Prof., PhD Borysiuk V., PhD Stud., Natalich B.
Sumy State University, Sumy, Ukraine
E-mail: ul.shvec@mss.sumdu.edu.ua, v.borisyuk@phe.sumdu.edu.ua, bvnatalich94@gmail.com

Abstract: *Within the framework of the molecular dynamics methods the simulation of the temperature stability of the metallic nanoparticles with the core-shell structure was performed and the melting temperature of the sample was determined. During the simulation of the dynamic behavior of nanoparticle the calculation of forces of interatomic interactions was carried out within the embedded atom method. To simulate the melting process the temperature of the sample was gradually increased by scaling the corresponding atomic velocities using the Berendsen thermostat. The Lindemann index was used as a numerical parameter describing changes in the structure of the nanoparticle. According to the results of the study, the temperature dependences of the Lindeman index and the average potential energy were obtained, as well as the radial distribution functions for the nanoparticles. From the simulation results, atomistic configurations of the sample were built and the dynamics of changes in its structure was investigated. Spatial distribution of the atoms on Lindeman index within the volume of the sample around melting temperature was also calculated.*
KEYWORDS: MOLECULAR DYNAMICS, CORE-SHELL, METALLIC NANOPARTICLE, MELTING, LINDEMANN INDEX

1 Introduction

Bimetallic nanoparticles are given considerable attention by researchers of nanoscale systems, since they allow the design of new structures with individual properties that are not observed in monometallic and bulk materials [1–3]. Particularly in demand from theoretical and practical aspects were nanomaterials with a core@shell structure, due to the wide range of applications in optoelectronics, semiconductors, quantum dots, biological marking, and nanocatalysis [4–6].

Among the objects of nanosystems are different types of forms and structures [1]. It is known that by changing the type and parameters of a shell, one can control the properties of these systems, at the same time as the shell, in turn, protects the kernel from external influence [7]. Thus, by correlating the structure and properties of the core and shell material, especially the shape and size, the expansion of the functionality of these nanosystems is ensured [8]. As a material for core-shell nanostructures, a wide range of combinations of inorganic and organic materials is used.

The development and production of nanoparticles with individual characteristics requires an understanding of their structural and thermodynamic properties [9–11]. Numerous methods of synthesis of nanoparticles with different structure, size and shape were proposed [1, 5]. However, some experimental techniques that are widely used in material science, not always can be applied to investigate the structure and behavior of the nanoscale objects [12], thus, various theoretical and computational investigations [13, 14] can be an additional tool in studying of nanostructures.

The purpose of this work was to study the behavior of bimetallic nanoparticles Ag@Pd, Au@Pd (Ag/Au is core; Pd is shell) during melting within molecular dynamics methods.

2 Model and simulation configuration

Within the framework, Ag@Pd and Au@Pd nanoparticles were investigated, which had a spherical shape with a core (Ag/Au)-shell (Pd) structure. In the experiment the total number of atoms was 16 757 for Ag@Pd, where 14 634 (87.3 %) atoms were palladium and 2 123 (12.7 %) atoms were silver, and the total number of atoms was 46 049 for Ag@Pd, where 40 274 (87.5 %) atoms were palladium and 5 775 (12.5 %) atoms were aurum for Au@Pd. The initial diameters of Ag@Pd and Au@Pd nanoparticles were 7.4 nm (core diameter ~4.0 nm) and 13.0 nm (core diameter ~7.0 nm), respectively. The simulation was performed with the support of an ideal vacuum at free boundary conditions in three directions. OVITO software package was used to obtain images of atomistic configurations [15]. For example, the initial atomic configuration of the Ag@Pd modeled nanoparticle is presented in Fig. 1.

During the simulation of the melting process, the sample temperature was gradually increased by scaling the corresponding atomic velocities using the Berendsen thermostat in the temperature range of 250–3000 K [16]. Recording of atomic configurations of

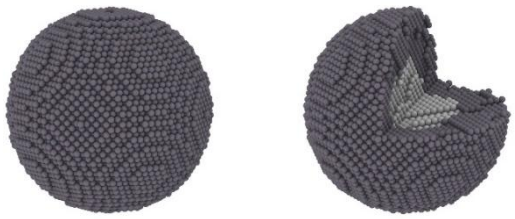

Fig. 1. *Initial atomistic configuration of Ag@Pd core-shell nanoparticle: overall view (left panel) and cross-section (left panel). Pd atoms (shell) are shown in dark gray color; Ag atoms (core) are shown in light gray color.*

the system and calculation of parameters were realized after the temperature reached equilibrium value.

The modified embedded-atom method (MEAM) was used to calculate the forces of interatomic interaction [17]. MEAM is known to reliably reproduce the basic properties of materials and is widely used in the metal alloys modelling by classical molecular dynamics (MD) techniques. The simulation was performed using the LAMMPS software package [18].

The complete algorithm for particle motion calculations used in molecular dynamics simulations involves obtaining analytical expressions for the forces of interatomic interaction $F(r)$, based on the given dependences for the potential energy, through the equation

$$F(r) = -\frac{\partial U}{\partial r} \tag{1}$$

and further numerical integration of the equations of motion

$$m\frac{d^2 r_i}{dt^2} = F_i(r_i) = -\frac{\partial U}{\partial r} \tag{2}$$

for each atom i.

Within the MEAM, the total potential energy of a metallic crystal can be presented as a sum of two components, each of which describes the corresponding mechanisms of interaction:

$$U = \frac{1}{2}\sum_{i,j,i\neq j} \varphi(r_{ij}) + \sum_i F(\rho_i), \tag{3}$$

where $\varphi(r_{ij})$ is the pair energy between atoms i and j at a distance

r_{ij}; $F(\rho_i)$ is the local embedding energy of the i-atom in the space domain, that is characterized by the electronic density ρ_i.

For each term in equation (3), the analytical expression was proposed through approximating the data obtained from the calculations from the first principles [19]. Thus, the pair energy of the interatomic interaction can be written in the form

$$\varphi(r) = \frac{Ae^{-\alpha\left(\frac{r}{r_e}-1\right)}}{1+\left(\frac{r}{r_e}-\kappa\right)^{20}} - \frac{Be^{-\beta\left(\frac{r}{r_e}-1\right)}}{1+\left(\frac{r}{r_e}-\lambda\right)^{20}}, \quad (4)$$

where r_e is the equilibrium distance between the two atoms of the given type; A, B, α, β are the approximation parameters; κ, λ are the additional parameters for ensuring zero energy of interaction at significant interatomic distances.

The local embedding energy as a function of electron density $F(\rho_i)$ is calculated in several steps. Firstly, the electronic density ρ_i is calculated as

$$\rho_i = \sum_{i,j\neq i} f(r_{ij}), \quad (5)$$

where $f(r_{ij})$ is the local electron density in the atomic region of atom i, calculated through the following expression

$$f(r_{ij}) = \frac{f_e e^{-\beta\left(\frac{r}{r_e}-1\right)}}{1+\left(\frac{r}{r_e}-\lambda\right)^{20}}, \quad (6)$$

that has the same form as the second term in formula (4) with the same values of parameters β and λ. Then the electronic density function $F(\rho_i)$ should be calculated from three following equations, depending on the value of ρ_i

$$F(\rho) = \sum_{i=0}^{3} F_{ni}\left(\frac{\rho}{\rho_n}-1\right), \quad \rho < \rho_n, \quad \rho_n = 0.85\rho_e, \quad (7)$$

$$F(\rho) = \sum_{i=0}^{3} F_i\left(\frac{\rho}{\rho_e}-1\right), \quad \rho_n < \rho < \rho_0, \quad \rho_0 = 1.15\rho_e, \quad (8)$$

$$F(\rho) = F_e\left(1-\ln(\frac{\rho}{\rho_e})^{\eta}\right)\cdot(\frac{\rho}{\rho_e})^{\eta}, \quad \rho_0 \leq \rho. \quad (9)$$

Such method for determining the electronic density function $F(\rho_i)$ is necessary for the realistic approximation of the embedding energy and for reproducing the properties of the material in a wide range of values ρ.

The forces between different types of atoms can be calculated using the MEAM model for alloys [19]. Within mentioned approach the pair energy $\varphi^{ab}(r_{ij})$ between atoms of type a i b can be calculated as

$$\varphi^{ab}(r) = \frac{1}{2}\left(\frac{f^b(r)}{f^a(r)}\varphi^{aa}(r) + \frac{f^a(r)}{f^b(r)}\varphi^{bb}(r)\right). \quad (10)$$

Thus, using equations (1)–(10), it is possible to investigate the dynamics of metallic nanoparticles under the external influences.

The description of changes in nanoparticle structure was based on the use of the Lindemann numerical parameter [20]. The local Lindeman index of the i-th atom was determined through the following formula:

$$q_i = \frac{1}{N-1}\sum_{j\neq i}\frac{\sqrt{\langle r_{ij}^2\rangle - \langle r_{ij}\rangle^2}}{\langle r_{ij}\rangle}, \quad (11)$$

where r_{ij} is the distance between i and j atoms; corner brackets are time averaging at a constant temperature value.

The quantitative characterization of the changes in the sample structure is carried out by the calculated radial density functions $g(r_n)$, which are defined as the relative probability of finding a pair of atoms at some distance from each other. $g(r_n)$ was calculated through the equation [21]:

$$g(r_n) = \frac{Vh_n}{2\pi N_m^2 r_n^2 \Delta r}, \quad (12)$$

where V_n is the volume of the sample; h_n is the number of atomic pairs (i,j) for which the condition $\left((n-1)\Delta r \leq r_{ij} \leq n\Delta r\right)$ is satisfied; N_m is the total number of atoms; Δr – parameter of sampling of interatomic distances (Δr has sufficiently small values); $r_n = (n-1/2)\Delta r$ is the value of the interatomic distances.

3 Results

Temperature dependences of the Lindemann index calculated for the Au@Pd and Ag@Pd nanoparticles under investigation are shown in Fig. 2. As it can be seen from the figure, the obtained values on the dependences $Q(T)$ and $E(T)$ increase monotonically in the temperature range $T \leq 1\,500$ K. After that, the Lindemann index and the potential energy start to rise rapidly at a temperature value of $T \approx 1\,600$ K, which may be a start of the melting process. The value of the Lindemann index for the Ag@Pd nanoparticles

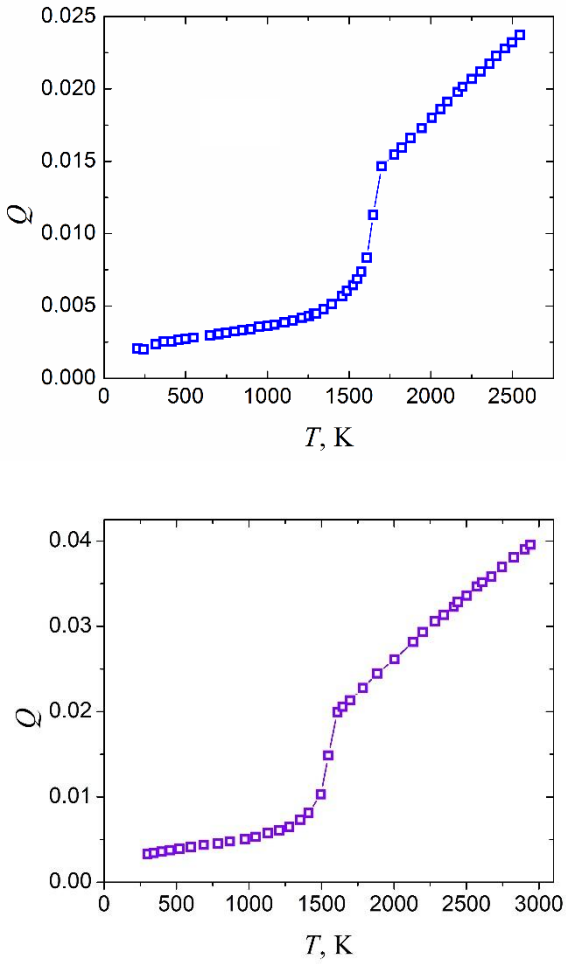

Fig. 2. *Temperature dependence of the Lindemann index for Au@Pd (top panel) and Ag@Pd (bottom panel) core-shell nanoparticles.*

was $Q_c \approx 0.01$ and for the Au@Pd nanoparticles was $Q_c \approx 0.015$. At temperatures $T > 1\,700$ K, there is a slow, almost linear increase in the values of Q and E (Fig. 2, Fig. 3).

To detect the changes in the structure of the nanoparticles, the radial distribution functions were calculated at the initial temperature of 300 K (Fig. 4, Fig. 5). As can be seen from the figure for Ag@Pd, at temperatures T = 300 K and T = 1 050 K, the sample has clearly expressed peaks corresponding to the crystalline structure of silver and palladium. At T = 1 050 K, the $g(r_n)$ is

characterized by a decrease in the height (intensity) of the peaks. At T = 2 000, only the first peak corresponding to the equilibrium

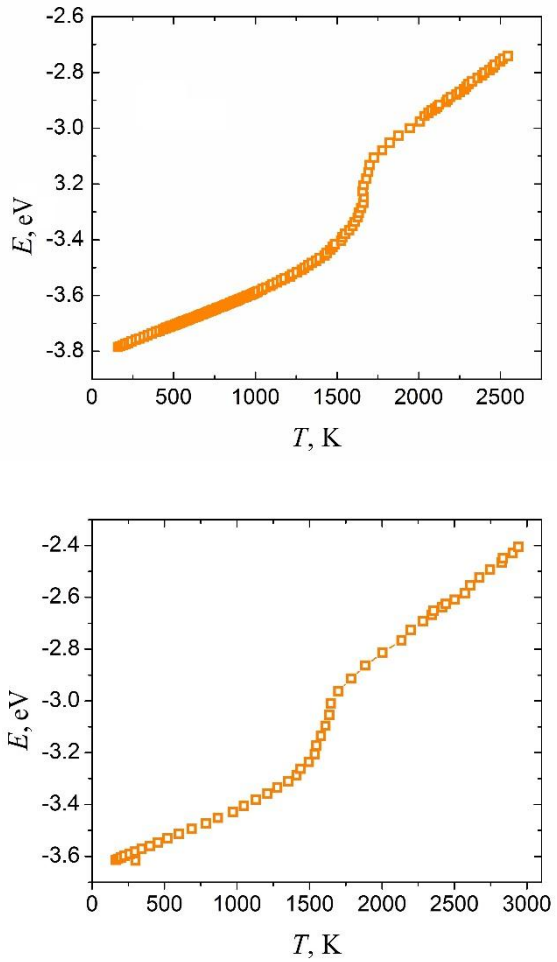

Fig. 3. *Temperature dependence of averaged potential energy for Au@Pd (top panel) and Ag@Pd (bottom panel) core-shell nanoparticles.*

distance between atoms is visible on the radial distribution function, and there are no other peaks. This kind of radial distribution function is typical of an amorphous state.

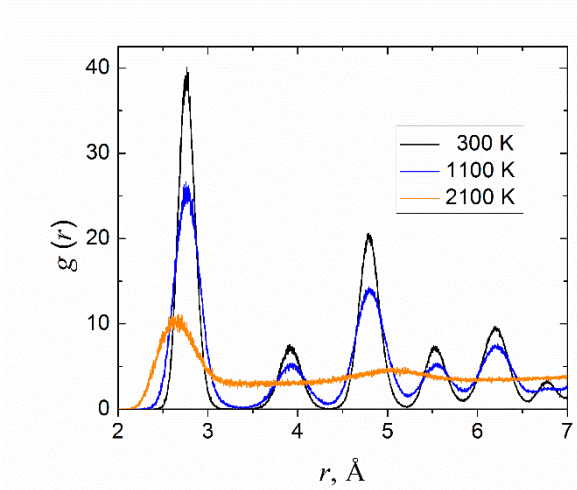

Fig. 4. *Radial distribution functions for Au@Pd core-shell nanoparticle at different temperatures.*

The cross sections and general views of the Ag@Pd nanoparticle at the melting point and the maximum temperature of the computer experiment are shown in Fig. 6. As it follows from visual analysis, temperature growth lead to increasing spacing between atoms, resulting in destruction of the initial crystal structure. It is noticeable that above the melting temperature core-shell structure of the nanoparticle is also destroyed, due to the

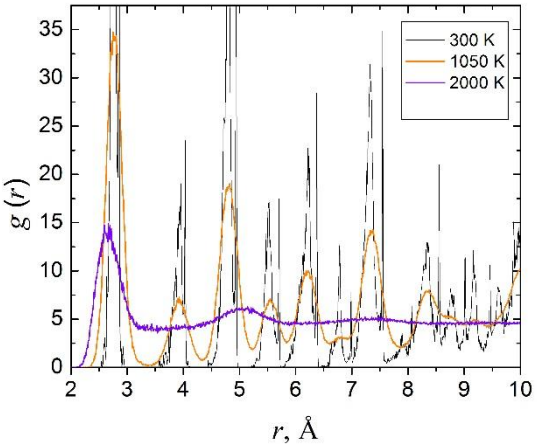

Fig. 5. *Radial distribution functions for Ag@Pd core-shell nanoparticle at different temperatures.*

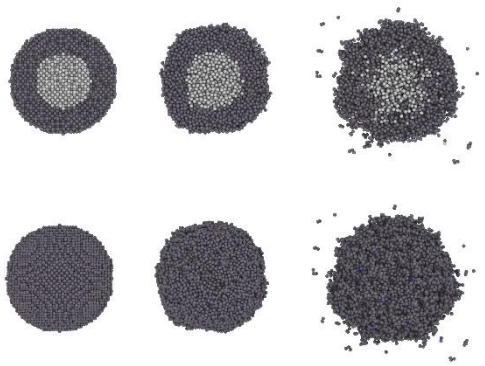

Fig. 6. *Atomistic configurations of Ag@Pd core-shell nanoparticles at 1 210; 1 650; 2 950 K (from left to right): cross-section (top panel) and overall (bottom panel).*

increased velocity of the diffusion processes.

4 Conclusion

In the work melting behavior of the bimetallic Ag@Pd, Au@Pd nanoparticles with core-shell structure investigated by classical molecular dynamic simulations. According to the simulation results, the numerical parameters were obtained for the samples and the dynamics of the structural changes were analyzed. The approximate melting point for nanoparticles was 1 600 K. At that point the Lindemann indexes exceed the critical values $Q_c \approx 0.01$ and $Q_c \approx 0.015$ for Ag@Pd, Au@Pd respectively. Initial core-shell structure of the nanoparticle is preserved up to the melting point. With the temperature growth, the volume of the nanoparticle is also increasing due to the larger spacing between atoms, which lead to the destruction of the initial crystal structure and the core-shell diffusion became more intense. It should be noted that the model presented here allows us to investigate the behavior of nanoparticles of another chemical composition during heating and melting (depending on the presence of a parameterized interatomic interaction potential), size and shape.

5 Acknowledgements

Authors are grateful to the Ministry of Education and Science of Ukraine for financial support (Project № 0117U003923).

6 Literature

1 Chaudhuri R. Gh. Core/shell nanoparticles: classes, properties, synthesis mechanisms, characterization, and applications / R. Gh. Chaudhuri, S. Paria // Chem. Rev. – 2012. – Vol. 112, № 4. –P. 2373–2433.

2 Alayoglu S. Surface composition and catalytic evolution of Au_xPd_{1-x} (x = 0.25, 0.50 and 0.75) nanoparticles under CO/O_2 reaction in torr pressure regime and at 200°C / S. Alayoglu, F. Tao, V. Altoe [et al.] // Catal. Lett. – 2011. – Vol. 141, № 5. – P. 633–640.

3 Yu W. Y. Selective hydrogen production from formic acid decomposition on Pd-Au bimetallic surfaces / W.-Y. Yu, G. M. Mullen, D. W. Flaherty [et al.] // J. Am. Chem. Soc. – 2014. – Vol. 136, № 31. – P. 11070–11078.

4 Mejia-Rosales S. J. Two-stage melting of Au-Pd nanoparticles / S. J. Mejia-Rosales, C. Fernandez-Navarro, E. Perez-Tijerina [et al.] // Phys. Chem. B. – 2006. – Vol. 110, № 26. – P. 12884–12889.

5 Tsuji M. Crystal Structures and growth mechanisms of Au@Ag core-shell nanoparticles prepared by the microwave-polyol method / M. Tsuji, N. Miyamae, S. Lim [et al.] // Cryst. Growth Des. – 2006. – Vol. 6, № 8. – P. 1801–1807.

6 Baek S. W. Au@Ag core-shell nanocubes for efficient plasmonic light scattering effect in low bandgap organic solar cells / S. W. Baek, G. Park, J. Noh [et al.] // ACS Nano. – 2014. – Vol. 8, № 4. – P. 3302–3312.

7 Мудрак І. М. Електрофізичні та теплофізичні властивості наносистеми із структурою «ядро-оболонка» AgI/SiO_2 / І. М. Мудрак, Л. П. Сторожук, С. М. Махно [та ін.] // Наносистеми, наноматеріали, нанотехнології. – 2012. – Т. 10, № 4. –P. 819827.

8 Abdel-Fattah W. I. Synthesis of biogenic Ag@Pd core-shell nanoparticles having anti-cancer/anti-microbial functions / W. I. Abdel-Fattah, M. M. Eid, Sh. I. Abd El-Moez [et al.] // Life Sci. – 2017. – Vol. 183. – P. 28–36.

9 Borysiuk V. Atomistic simulation of the melting behavior of the Au-Ag nanoparticles with core-shell structure / V. Borysiuk, I. Lyashenko // IEEE 35th International Conference on Electronics and Nanotechnology (ELNANO-2015), 2015, Kyiv – P. 155–157.

10 U. Shvets. Elastic Properties of Au, Ag, and Core-shell Au@Ag Nanorods from Molecular Dynamics Simulations // U. Shvets, B. Natalich, V. Borysiuk / J. NANO- ELECTRON. PHYS. – 2019. – Vol. 11, – P. 04026:1–5.

11 Наталіч Б. Моделювання термічної стабільності та плавлення біметалевої наночастинки Ag@Pd / Б. Наталіч, У. Швець, В. Борисюк // Вісник Львівського університету. Серія фізична. – 2019. – № 56. – С. 91–102.

12 Yang Zh. Molecular dynamics simulation of the melting behavior of Pt-Au nanoparticles with core-shell structure / Zh. Yang, X. Yang, Zh. Xu // J. Phys. Chem. C. – 2008. – Vol. 112, № 13. – P. 4937–4947.

13 Lyashenko I. A. Statistical analysis of self-similar behavior in the shear induced melting model / I. A. Lyashenko, V. N. Borysiuk, N. N. Manko // Cond. Matt. Phys. – 2014. – Vol. 17. – P. 23003: 1–11.

14 Olemskoi A. I. Hierarchical condensation near phase equilibrium / A. I. Olemskoi, O. V. Yushchenko, V. N. Borisyuk [et al.] // Physica A: Statistical Mechanics and its Applications. – 2012. – Vol. 391, P. 3277–3284.

15 Stukowski A. Visualization and analysis of atomistic simulation data with OVITO – the open visualization tool / A. Stukowski // Modelling Simul. Mater. Sci. Eng. – 2010. – Vol. 18, № 1. – P. 015012.

16 Berendsen H. J. C. Molecular dynamics with coupling to an external bath / H. J. C. Berendsen, J. P. M. Postma, W. F. van Gunsteren [et al.] // J. Chem. Phys. – 1984. – Vol. 81, № 8. – P. 3684.

17 Baskes M. I. Modified embedded-atom potentials for cubic materials and impurities / M. I. Baskes // Phys. Rev. B. – 1992. – Vol. 46, № 5. – P. 2727.

18 Plimpton S. Fast parallel algorithms for short-range molecular dynamics / S. Plimpton // J. Comput. Phys. – 1995. – Vol. 117, № 1. – P. 1–19.

19 Zhou X.W. Atomic scale structure of sputtered metal multilayers / X. W. Zhou, H. N. G. Wadley, R. A. Johnson [et al.] // Acta Mater. – 2001. – Vol. 49, № 19. – 4005–4015.

20 Zhang K. Melting and premelting of carbon nanotubes / K. Zhang, G. M. Stocks, J. Zhong // Nanotechnology. – 2007. – Vol. 18, № 28. – P. 285703.

21 Rapaport D. C. The art of molecular dynamics simulation / D. C. Rapaport // NY: Cambridge University Press. – 2004.

MATHEMATICAL MODELING OF ATOM-MOLECULAR DEPOSITION BY MAGNETRON SPUTTERING

МАТЕМАТИЧЕСКО МОДЕЛИРАНЕ НА АТОМНО-МОЛЕКУЛНО НАСЛОЯВАНЕ ЧРЕЗ МАГНЕТРОННО РАЗПРАШАВАНЕ

Ass. Prof. Dr. Georgi Evt. Georgiev, Prof. Dr. Luben Lakov, Ass. Prof. Dr. Petio Ivanov, Dr. Michaela Alexandrova
Institute of Metal Science, Equipment and Technologies with Hydro-aerodynamics Centre "Akad. A. Balevski"-BAS

***Abstract**: The thickness distribution of thin films deposited by the magnetron sputtering technique is studied with the means of mathematical modelling. A mathematical model describing the process of atomic or molecular sputtering followed by deposition process in a RF/DC magnetron equipment is proposed. It has enough comprehensiveness to describe the sputtering of metals, insulating materials or semiconductors. An algorithm has been developed to solve the equations of the model, which is implemented in the form of a computer program. With the help of this program model solutions have been received and presented by different configurations and parameters of the magnetron system. An optimal solution has been also found, where the non-homogeneity of the coating is minimal.*

KEY WORDS: MATHEMATICAL MODELLING, ATOM-MOLECULAR DEPOSITION, MAGNETRON SPUTTERING

***Резюме:** Формирането на тънки материални слоеве с помощта на магнетронно разпрашаване е изследвано със средствата на математическото моделиране. Представен е математически модел на процеса на атомно или молекулярно разпрашаване, последвано от наслояване, протичащ във високочестотен или постоянно токов магнетрон. Моделът притежава достатъчна степен на общност за да опише наслояване на метали, изолационни материали или полупроводници. Създаден е алгоритъм за решаване на уравненията на модела във формата на компютърна програма. С нейна помощ са получени и представени моделни решения за процеса на наслояване при различни конфигурации и параметри на магнетронната система. Намерено е и оптимално решение, при което дебелината на слоя е с минимални разлики.*

КЛЮЧОВИ ДУМИ: МАТЕМАТИЧЕСКО МОДЕЛИРАНЕ, АТОМНО И МОЛЕКУЛЯРНО НАСЛОЯВАНЕ, МАГНЕТРОННО РАЗПРАШАВАНЕ

1. Увод

Магнетронното разпрашаване е многофункционална техника за приготвяне на тънки филми за приложения в широк диапазон. Що се отнася до качеството на основния филм, от решаващо значение е постоянната дебелина на нанесеното покритие, тъй като пряко засяга физическите свойства и следователно производителността на устройството. Изработване на много равномерни покрития на големи отлагателни площи и контролирането на дебелината им е обект на изследване в много публикации [1-4].

Дебелината на покритието се определя основно от геометрията и взаимното разположение на мишената спрямо субстрата. През годините симулационните модели помогнаха да се промени разположението на целта спрямо субстрата за постигане на по-висока хомогенност. На Фиг.1 е показана схема на конструкцията на реален магнетрон в неговото напречно сечение.

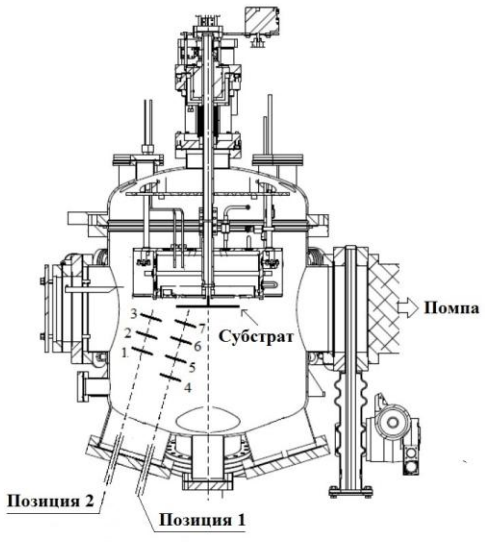

Фиг.1. Схема на RF/DC магнетрон в сечение.

В [6] е демонстрирано, че неаксиалният магнетронен източник и неговата ротация подобряват равномерността на дебелината на филма в сравнение с конвенционалните магнетронни източници, където източникът на разпрашаване споделя една и съща ос на симетрия със субстрата.

Други фактори, влияещи върху разпределението на дебелината на нанесения филм са характеристиките на разряда (мощност, налягане и т.н.), източникът на магнетрона и относителните движения на източника спрямо субстрата [5]. През последните няколко десетилетия са извършени много изследвания на различни видове разпрашителни системи за прогнозиране на неоднородностите в дебелината на филма. Въпреки това, тъй като разпределението на дебелината на филма е функция от множество променливи, не е възможно да се изведе общо, не-интегрално уравнение, което описва разпределението на дебелината въз основа на всички основни фактори [5]. Въпреки това, компютърни симулации и полу-емпирични формули са разработени въз основа на аналитични модели за по-добро обяснение на профилите за разпределение на дебелината.

Симулационните модели също така спомогнаха за оптимизация на профила на магнитното поле, на геометрията и разположението на магнетронните източници за да се получи най-доброто използване на целта за хомогенизиране на слоя върху субстрата.

В настоящата разработка е формулиран математичен модел за прогнозиране на разпределението на дебелината на покритието върху кръгов субстрат посредством радиочестотна (RF) кръгова магнетронна разпрашителна система. Разработена е специална компютърна програма за поучаване на решенията на модела. Предложеният подход може да бъде приложен и към други магнетронно разпрашителни системи.

2. Математичен модел

За целите на математичното моделиране геометрията и взаимното разположение на мишената и субстрата следва да бъдат подходящо дефинирани. Възприетата конфигурация е показана на Фиг.2. На нея са обозначени и основните определящи конфигурацията параметри. По време на процеса на разпрашаване, в мишената се формира ерозионен жлеб, чиято форма зависи от профила на магнитното поле на

източника на разпрашаване. По време на процеса на разпрашаване ерозионният профил се променя и влияе върху разпределението на дебелината на покритието върху субстрата. В разглеждания случай формата на ерозионния жлеб е пръстен и неговият радиус е означен с A на Фиг.2 и Фиг.3.

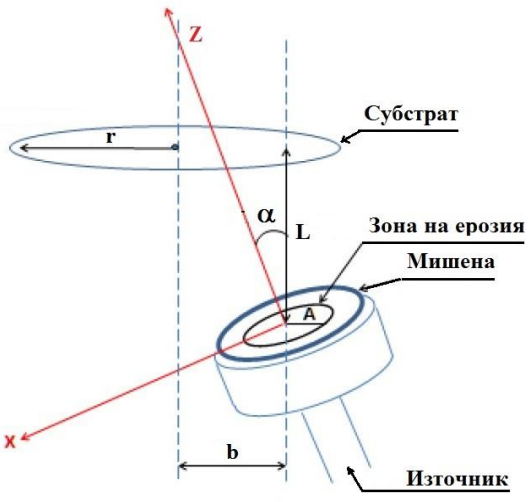

Фиг.2. Конфигурация на системата за магнетронно разпрашаване

2.1. Основни положения

В по-нататъшните разглеждания са възприети следните ограничения:

1. Всички избити от ерозионния пръстен частици напускат мишената. Този пръстен е концентричен спрямо мишената и има постоянен радиус;
2. Предполага се, че налягането в магнетрона е достатъчно ниско, така че средният свободен пробег на разпръсканите атоми става равен или по-голям от разстоянието до субстрата. Така, сблъсъците между разпръсканите атоми, аргоновите атоми или аргоновите йони могат да бъдат пренебрегнати. В резултат на това разпръснатите атоми се движат по права линия след както напуснат мишената. Ще предположим още, че средният свободен пробег на избитите от мишената атоми се дава от формулата:

$$\lambda = \frac{1}{\pi n (r_1 + r_2)^2}\ , \qquad (1)$$

където r_1 и r_2 са атомните радиуси на избитите от мишената атоми и атомите на газа, съответно. n е числената плътност на газа;

3. Предполага се, че бомбардиращите йони удрят мишената перпендикулярно;
4. Дифузията, отражението и повторното избиване на разпръснатите атоми от повърхността на субстрата също се пренебрегват.

2.2. Основни уравнения на модела

Дебелината на покритието във всяка точка на субстрата е пропорционална на масовия поток от разпрашени частици, попадащ в тази точка. Ето защо задачата за разпределението на нанесеното покритие е тясно свързана с определяне именно на този поток. Схемата, използвана за неговото пресмятане е представена на Фиг.3.

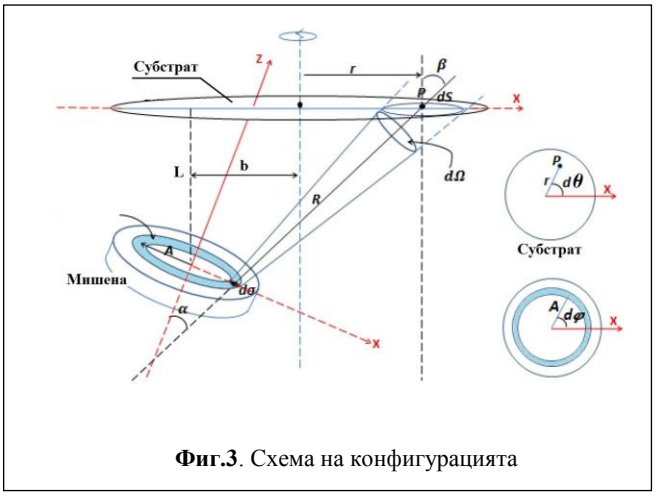

Фиг.3. Схема на конфигурацията

Нека с N да означим броя на частиците, напускащи площта $d\sigma$ за единица време във всички посоки. Тогава броят на частиците, които преминават в пространствения ъгъл $d\Omega$, определен от ъгълът α за единица време, следва да се изчисли по формулата

$$dN = CNf(\alpha)d\omega, \qquad (2)$$

където $f(\alpha)$ е функция на разпределението на интензитета на разпръскваните частици по ъгъла α. C е нормиращ множител, определен чрез уравнението

$$\int dN = N, \qquad (3)$$

отразяващо закона за запазване на масата, който изисква сумата от частиците по всички направления да е равна на общия им брой N. Използвайки зависимостите

$$d\omega = d\Omega/R^2, d\Omega = dS\cos\beta,\ d\Omega = \frac{dS\cos\beta}{R^2}, \qquad (4)$$

където R е разстоянието от разглежданата точка на източника до точка P на субстрата и замествайки в (2) получаваме уравнението

$$\frac{dN}{dS} = \frac{CNf(\alpha)\cos\beta}{R^2}, \qquad (5)$$

което ни дава частиците, достигащи областта dS , сключваща ъгъл β с направлението на емисията при точка P. Потокът в точка P от целия диск на ерозията следва да се пресметне с интегриране по него, т.е. по азимутния ъгъл φ, както следва

$$F_{loc}(P) = CN\int_0^A \int_0^{2\pi} Q(\rho)\frac{f(\alpha)\cos\beta}{R^2} d\rho d\varphi, \qquad (6)$$

където с $Q(\rho)$ е означена функцията, представяща бомбардираната повърхнина на мишената. Ако субстратът се върти около своята централна ос, то всички точки на субстрата на разстояние r от центъра ще получат същия поток. Така общият поток в даден момент ще има вида

$$F_{lux}(r) = \frac{1}{2\pi}\int_0^{2\pi} F_{loc}(P)d\theta = \frac{1}{2\pi}CN\int_0^A \int_0^{2\pi}\int_0^{2\pi} Q(\rho)\frac{f(\alpha)\cos\beta}{R^2} d\varphi d\theta d\rho. \qquad (7)$$

където θ е азимутният ъгъл на dS. Тъй като дебелината на нанесения слой е пропорционална на потока, то тя следва да се представи от вида (7) с една нова константа отпред. Тогава обединявайки всички константи за дебелината на слоя можем да напишем

$$T_h(r) = C_{of}\int_0^A \int_0^{2\pi}\int_0^{2\pi} Q(\rho)\frac{f(\alpha)\cos\beta}{R^2} d\varphi d\theta d\rho. \qquad (8)$$

Константата C_{of} най-често се определя чрез идентификация на базата на експериментални данни. За получаване на конкретни значения на функцията от (8) е разработена компютърна

програма на езика FORTRAN. Тя пресмята значенията на $T_h(r)$ при конкретни значения на параметрите *b*, *L*, *A* и r, съгласно координатната система на Фиг.3. Ъгловото разпределение $f(\alpha)$ може да се задава както аналитично, така и чрез експериментални данни в дискретни точки.

2.3. Ъглово разпределение на бомбардиращите атоми

Съществуват множество теоретични разработки, посветени на създаването на подходящ физически модел на ъгловото разпределение при магнетронното разпрашаване. От най-значимите следва да се отбележи теорията на Зигмунд-Томпсън [8,9]. За някои конкретни процеси те са в добро съвпадение с експерименталните резултати [10]. Най-добро съвпадение с повечето експериментални резултати е показало предложеното от Ямамура [10,11]

$$f(\alpha) = \cos(\alpha)\,[1 + k\cos^2(\alpha)], \qquad (9)$$

където k е свободен за фитиране параметър. Видът на такова разпределение при k=-0.7 е показан на Фиг.4.

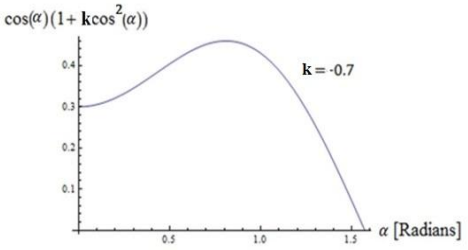

Фиг.4. Разпределение по Ямамура

Ямамура в своите теоретични разработки предлага и формула за пресмятане на параметъра k от вида

$$k = \frac{\frac{5}{3}\left(\frac{E_p}{E}\right)^{\frac{1}{2}}}{1-\left(\frac{E_p}{E}\right)^{\frac{1}{2}}} \qquad (10)$$

където E е енергията на бомбардиращия йон, E_p е енергетичния бариер за откъсване от повърхността на материала на мишената.

3. Получени резултати

За получаване на решения на изложения в т.2 математичен модел бе създаден алгоритъм и бе изготвена компютърна програма на FORTRAN, която го реализира. С нейна помощ са получени решения за дебелината на покритието при различни набори от параметри на модела и ъглови разпределения на процеса на разпрашаване. Те са показани на Фиг.5-8. На Фиг. 5-8.1 са представени

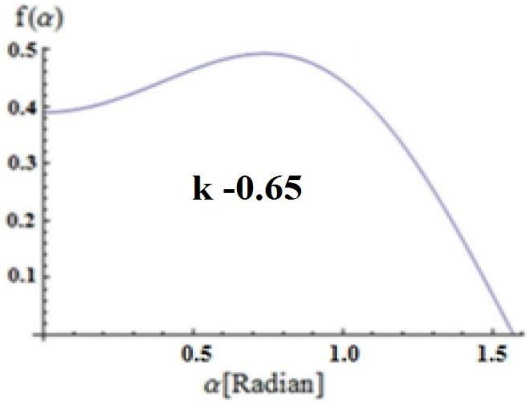

Фиг.5.1. Разпределение на Ямамура. Позиция 1.

Използваните разпределения на Ямамура, при които са получени съответните резултати за дебелината на покритието, представени на Фиг. 5-8.2, съответно. Групата от използвани параметри е изобразена на самите фигури. Резултатите на Фиг.5.2 и Фиг.6.2 съответстват на Поозиция 1 на мишената в магнетрона (виж Фиг.1), а тези на Фиг.7.2 и Фиг.8.2 на Позиция 2.

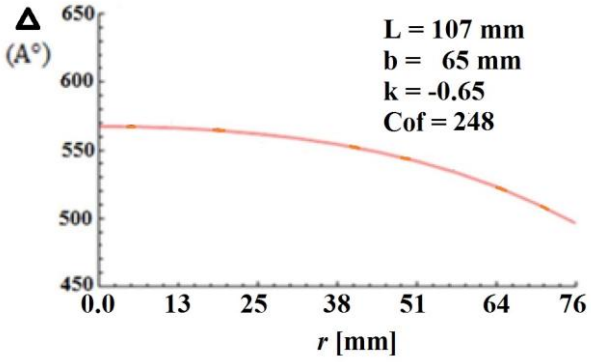

Фиг.5.2. Разпределение на дебелината на покритието. Позиция 1.

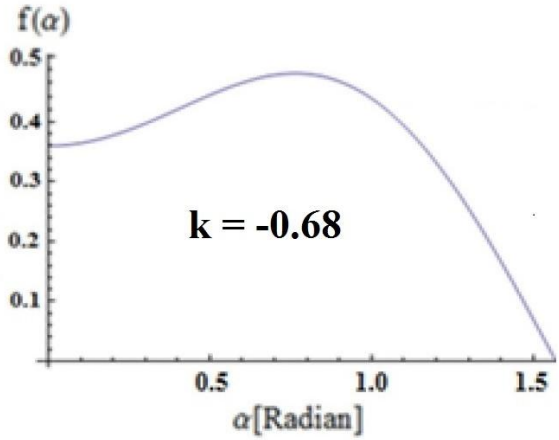

Фиг.6.1. Разпределение на Ямамура. Позиция 1.

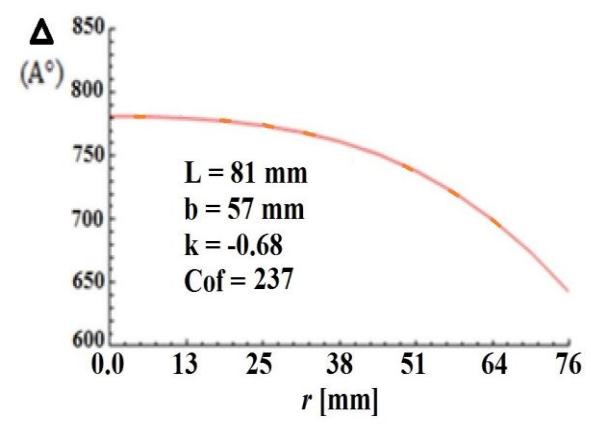

Фиг.6.2. Разпределение на дебелината на покритието. Позиция 1.

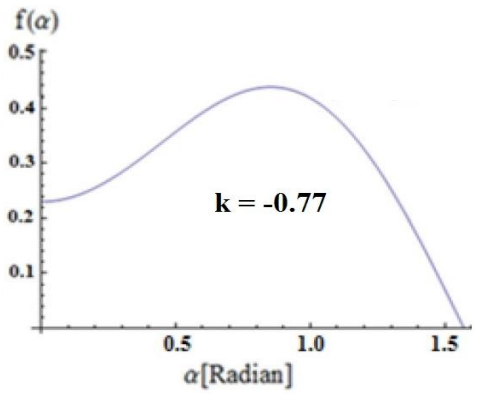

Фиг.7.1. Разпределение на Ямамура. Позиция 2.

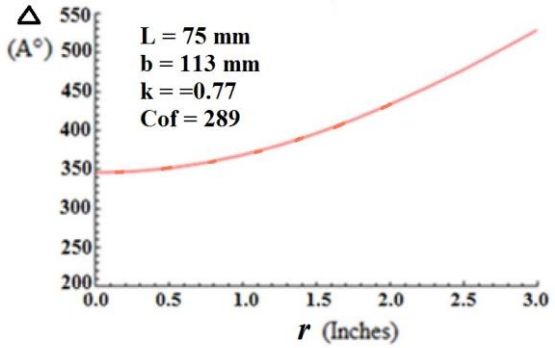

Фиг.7.2. Разпределение на дебелината на покритието. Позиция 2.

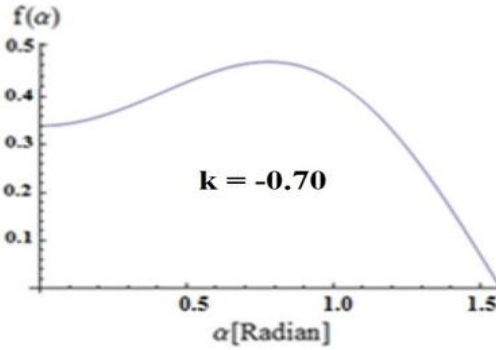

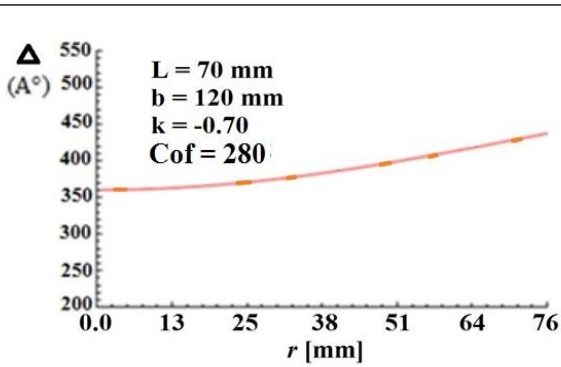

Въртенето на субстрата осигурява хомогенност на дебелината на покритието по азимутният му ъгъл на въртене, но при всички варианти от фигури 5-8 се наблюдава нехомогенност в радиална посока. С помощта на интерактивно – итеративен метод бяха варирани позицията на мишената и параметрите на модела, така, че да се получи най-хомогенно покритие. Такова бе намерено при варианта, показан на Фиг.9.

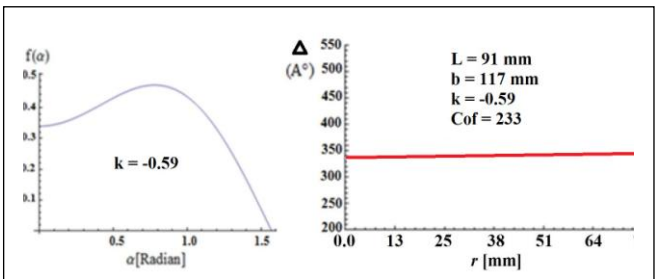

Фиг.9. Вариант, осигуряващ максимално хомогенно покритие

4. Заключение

В настоящата разработка е представен математичен модел на разпрашаване чрез йонно бомбардиране в магнетрон. Използвани са фундаменталните закони и зависимости, публикувани в [1,6,7]. Създадена е компютърна програма, с която могат да се получават конкретни решения на модела. С нейна помощ при моделни значения на параметрите е намерен вариант с хомогенно разпределение на дебелина на покритието.

Моделът може да намери приложение в различни съвременни технологии за оптимизация на процесите на нанасяне на метални и неметални покрития. Например, той би могъл да се приложи успешно както при формирането на силициеви покрития за полупроводникови изделия, така и за нанасянето на тънки изолационни покрития от керамични материали за нуждите на технологиите, предназначени за създаването на свръх мощни кондензатори за нуждите на енергетиката и автомобилостроенето.

5. Литература

1. Lieberman, M. A, A. J. Lichtenberg, Principles of Plasma Discharges and Materials Processing, Wiley Interscience, New York, 1994, pp 8-10.
2. Mahan, John E., Physical Vapor Deposition of Thin Films, John Wiley & Sons, New York, 2000.
3. "Sputter Deposition", Oxford Vacuum Science, accessed December 4, 2014.
4. Mark J.Maou, Fundamentals of Microfabrication: The Science of Miniaturization, Second Edition, CRC Press, Florida, 2002.
5. X. S. Du, Y. D. Jiang, J. S. Yu, J. Li, and G. Z. Xie, Quantitative evaluation of film thickness uniformity: Application to off-axis magnetron source onto a rotating substrate, Journal of Vacuum Science & Technology A 25, 215 (2007).
6. Swann, S., S. A. Collett, and I. R. Scarlett, Film thickness distribution control with offaxis circular magnetron sources onto rotating substrate holders: Comparison of computer simulation with practical results, Journal of Vacuum Science & Technology A8, 1299 (1990).
7. Rashidi, F, A Study of Thickness Distribution and Crystal Structure of Sputter-deposited Silicon Thin Films, Work for Degree of Master of Science, Simon Fraser University, pp.27-31,2015.
8. Thompson, M. W., Philos. Mag. 18 (1968).
9. Sigmund, P., Theory of Sputtering. I. Sputtering Yield of Amorphous and Polycrystalline Targets, Phys. Rev. 184 (2), 383 (1969).
10. Y. Yamamura, Radiation Effects and Defects in Solids 55 (1-2), 49 (1981).
11. Y. Yamamura, T. Takiguchi, and M. Ishida, Radiation Effects and Defects in Solids 118 (3), 237 (1991).

DESIGN AND ANALYSIS OF A NOVEL SEALING UNIT FOR PACKING MACHINES

M.Eng. Numan Irmak[1], M.Sc. Onur Cimen [1], Prof. I.Etem Saklakoglu PhD.[2]
[1]Kansan Wetwipe Machinery R&D Center, Izmir, Turkey

[2]Ege University Faculty of Engineering Mechanical Engineering Department, Izmir, Turkey

numanirmak@kansanmak.com

Abstract: *Packaging machines using for wet wipes operate at high speeds and the demand for speed in the relevant market is constantly increasing. The most important difficulty to faster operation of these machines is the relative slowness of the units used for sealing the packages. In this study, it is aimed to design a unique mechanism that can work at 160 packages per min instead of sealing unit which is still operating at 120 packages per min, and to verify the design by mechanical analysis. For this purpose; instead of the existing sealing unit driven by a single servo motor, the horizontal and vertical movements are separated and driven by two servo motors to achieve %33 more speed.*

Keywords: PACKAGING MACHINES, WET WIPES, SEALING

1. Introduction

Nowadays, the standard application for sealing the packages in packaging machines is provided for a fixed time, at a constant temperature, with spring compression and due to the standard cam geometry, adhesive bonding under variable pressure forces during the application period. This results in higher energy consumption on the one hand, while limiting the type of material that can be bonded on the same machine.

There is no automatic adjustable machine both in our company and in the global market. In this study, it is aimed to develop a user friendly and energy efficient machine which can work with all kinds of polymer packaging materials at high speed and efficiency.

2. Definition of Problem

The jaw unit in our standard packaging machine is capable of bonding at a constant time and pressure. This causes problems in the adhesion of some of the packaging materials developed recently and slows down the speed of the machine. Therefore D-Cam movement obtained by single servo motor in the jaw module of our standard packaging machine was improved. D-Cam movement will be provided by using 2 different cam movements by means of 2 independent servo motors. One motor will be control the vertical movement of the jaws, while the other motor will control the horizontal movement, ie the synchronous movement with the package. To do this, it have been worked on formulating the jaw movement that was occur by using 2 different mechanisms on the automation side and added into the equation. Therefor an easily adjustable adjustment screen that can be understood by the operator was designed.

Horizontal movement of the sealing jaws (movement in the direction of the flow of the package) was provided by separation of the horizontal and vertical movement.

While the horizontal movement is limited to 60mm fixed value in the current system, it is planned to increase this movement up to 100mm in the system to be developed and be able to change it from the operator panel without any mechanical adjustment.

It is also aimed to increase the contact time of the sealing jaws to the package by increasing the horizontal movement and to achieve better adhesion quality at lower temperatures.

In the design of the movement mechanism of the jaw unit, the choice of cam bearing according to the loads to be formed, determination and design of the closed cam form, dimensioning the connecting mechanism to be designed according to the jaw stroke movement were studied.

Both mechanical and automation measures was taken to protect the jaw unit against mechanical jams. When driving the horizontal movement of the jaw unit, torque limiter coupling was used in the system.

Automation measures was taken in order to detect the phase misalignment that may occur in the system. So that the sealing jaws do not press on the wet wipes which do not center the package.

A graphical image of the movements that can be obtained with standard D-Cam and adjustable D-CAM mechanisms is given in figure 1.

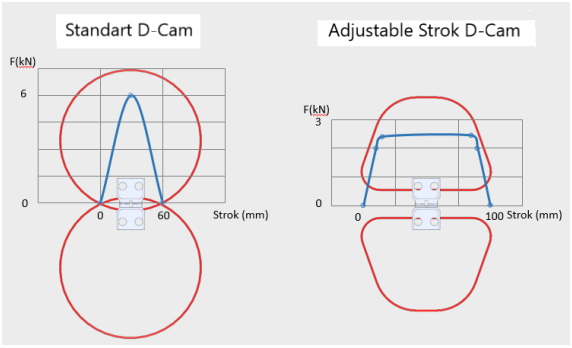

Fig. 1 *Standard and Adjustable Strok D-Cam*

The design of the movement obtained with a single servo motor in the jaw module of our standard packaging machine is shown in figure 2.

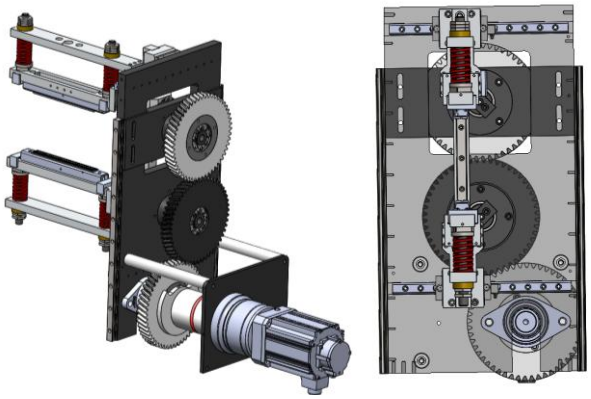

Fig. 2 *Isometric and front view of single servo motor in the jaw module*

3. Variable Stroke Jaw Design

While the horizontal movement is limited to 60mm fixed value in the current system, it is planned to increase this movement up to 100mm in the system to be developed and be able to change it from the operator panel without any mechanical adjustment.

It is aimed to increase the contact time of the sealing jaws to the package by increasing the horizontal movement and to achieve better adhesion quality at lower temperatures.

In the design of the movement mechanism of the jaw unit, the choice of cam bearing according to the loads to be formed, determination and design of the closed cam form, dimensioning the connecting mechanism to be designed according to the jaw stroke movement were studied. Figure 3 shows the variable stroke jaw mechanism designed by us

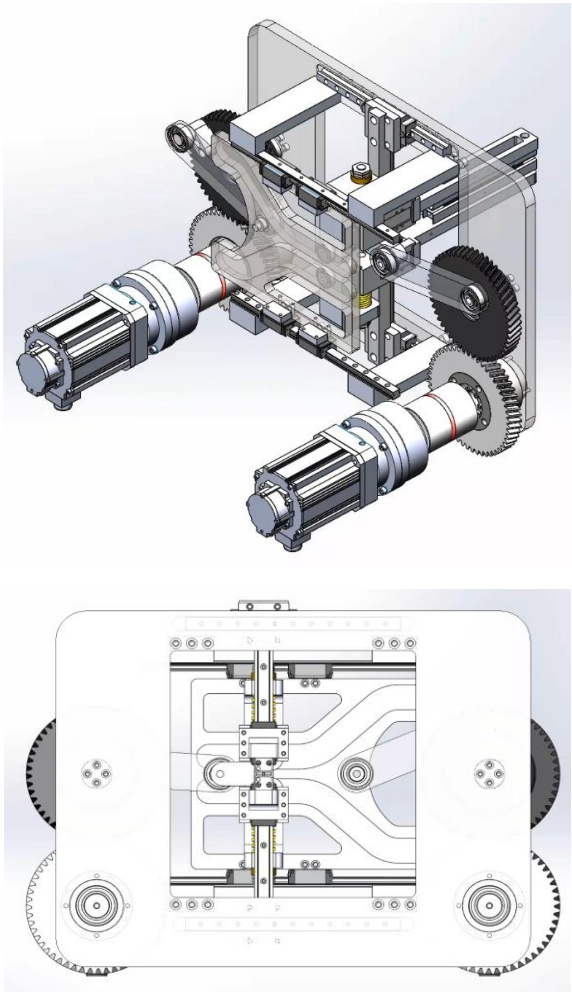

Fig. 3 *Isometric and front view of single servo motor in the jaw module*

4. Variable Stroke Jaw Position Equations

In order to provide axis movements in the two-motor design, the geometric positions formed during the movement of the mechanism must be calculated and formulated so that the automation system can control the positions.

Figure 4 shows the initial state of the closed cam positions.

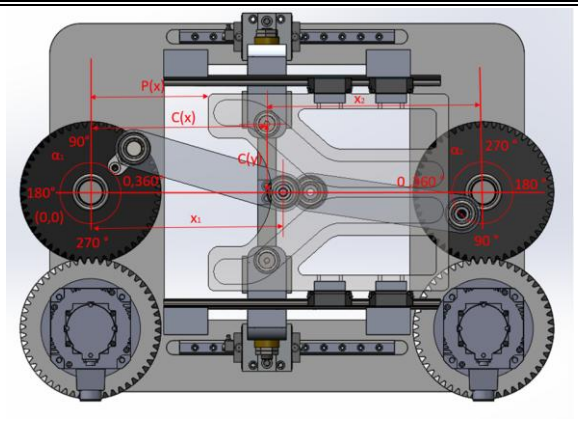

Fig 4. *Initial state of the closed cam positions.*

The calculations related to the location analyzes performed below are given.

$$\boldsymbol{x_1}$$

$$l_1 = 100mm$$

$$l_2 = 253mm$$

$$\cos\alpha_1\,(0{,}360)$$

$$x_1 = \frac{{l_1}^2 - {l_2}^2 + {x_1}^2}{2 \times l_1 \times \cos\alpha_1}$$

$$x_1 = \frac{100^2 - 253^2 + {x_1}^2}{2 \times 100 \times \cos\alpha_1}$$

$${x_1}^2 - (200\cos\alpha_1)x_1 - 54009 = 0$$

$$\Delta = b^2 - 4ac, \qquad a = 1, b = -200\cos\alpha_1, c = -54099$$

$$x_1 = \frac{-b + \sqrt{\Delta}}{2a}$$

$$\boldsymbol{x_2}$$

$$l_3 = 50mm$$

$$l_4 = 249mm$$

$$\cos\alpha_2\,(0{,}360)$$

$$x_2 = \frac{{l_3}^2 - {l_4}^2 + {x_2}^2}{2 \times l_3 \times \cos\alpha_2}$$

$$x_2 = \frac{50^2 - 249^2 + {x_2}^2}{2 \times 50 \times \cos\alpha_2}$$

$${x_2}^2 - (100\cos\alpha_2)x_2 - 59501 = 0$$

$$\Delta = b^2 - 4ac, \qquad a = 1, b = -100\cos\alpha_2, c = -59501$$

$$x_2 = \frac{-b + \sqrt{\Delta}}{2a} + 71mm$$

(+71 mm; added length of part connected to l4)

$$\boldsymbol{C(x_2);}$$

Position of the jaw on the x axis relative to the center α1

$C(x_2) = 640 - x_2$

$C(x)$;

Position of the jaw on the x axis relative to the origin

C(x)=640-(((100*COS(RADYAN(I2))+SQUAREROOT((-100*COS(RADYAN(I2)))^2-4*(-59501)))/2)+71)-270

$P(x_1)$; Position of the cam plate horizontally (x) relative to the origin

$P(x_1) = x_1 - 122$

$P(x_1)$ =((200*COS(RADYAN(A2))+SQUAREROOT((-200*COS(RADYAN(A2)))^2-4*(-54009)))/2)-122

Vertical movement of the jaw

Fig 5. shows the vertical movement of the jaw

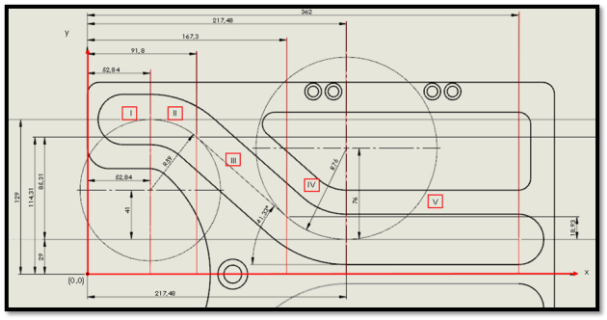

Fig 5. *Vertical movement of the jaw*

$x_ç = C(x_2) - P(x_1)$; The horizontal position of the jaw relative to the cam plate

Region-I

$0 \le x_ç < 52{,}84$

$y_ç = 100 + 29 = 129mm$

Region-II

$52{,}84 \le x_ç < 91{,}8$

$a_1 = 52{,}84mm, \quad b_1 = 41mm, \quad r_1 = 59mm$

$(x_ç - a_1)^2 - (y_ç - b_1)^2 = {r_1}^2$

$$y_ç = \sqrt{3481 - \left(x_ç - 52{,}84\right)^2} + 41 + 29$$

Region-III

$91{,}8 \le x_ç < 167{,}3$

$y_ç = \left(167{,}3 - x_ç\right)\tan 41{,}33 + 18{,}93 + 29$

Region-IV

$167{,}3 \le x_ç < 217{,}48$

$a_2 = 217{,}48mm, \quad b_2 = 76mm, \quad r_2 = 76mm$

$(x_ç - a_2)^2 - (y_ç - b_2)^2 = {r_2}^2$

$$y_ç = 76 - \sqrt{577{,}6 - \left(x_ç - 217{,}48\right)^2} + 29$$

Region-V

$217{,}48 \le x_ç < 362$

$y_ç = 29$

To solve the problem, equations of origin moved to the center of the jaw stroke. Fig 6. shows the coordinates which origin moved to the center of the jaw stroke

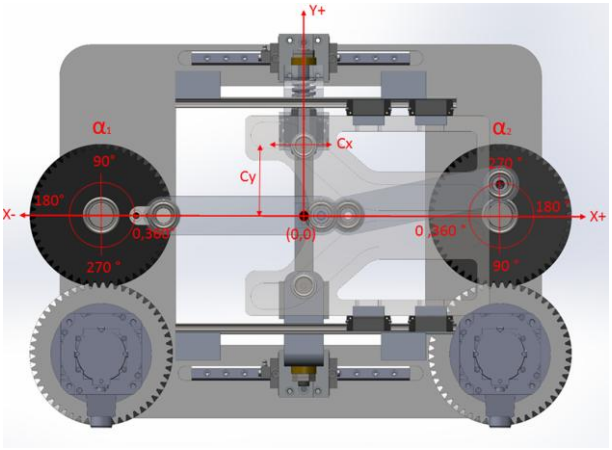

Fig 6. *The coordinates which origin moved to the center of the jaw stroke*

C(x)=640-(((100*COS(RADYAN(I2))+SQUAREROOT((-100*COS(RADYAN(I2)))^2-4*(-59501)))/2)+71)-320

C(x)=(-50,+50)mm

x_ç=C(x_2)-P(x_1); The horizontal position of the jaw relative to the cam plate

x_ç=(640-(((100*COS(RADYAN(J2))+SQUAREROOT((-100*COS(RADYAN(J2)))^2-4*(-59501)))/2)+71)-(((200*COS(RADYAN(A2))+SQUAREROOT((-200*COS(RADYAN(A2)))^2-4*(-54009)))/2)-122))

It is the combined state of the equation that gives the jaw y values according to the cam plate. U2 represents the main formula xç. By entering U2 into the equation, the equation that gives the jaw height to A2 EXCEL (X, Y) formula; Equation that gives coordinates in form (X, Y). As a result, a single equation in excel were created as follows.

="("&ROUNDUP(((640-(((100*COS(RADYAN(B1))+SQUAREROOT((-100*COS(RADYAN(B1)))^2-4*(-59501)))/2)+71)-320));2)&":"&ROUNDUP(IF((640-(((100*COS(RADYAN(B1))+SQUAREROOT((-100*COS(RADYAN(B1)))^2-4*(-59501)))/2)+71)-(((200*COS(RADYAN($A309))+SQUAREROOT((-200*COS(RADYAN($A309)))^2-4*(-54009)))/2)-122))<52,84;100+29;IF(VE((640-(((100*COS(RADYAN(B1))+SQUAREROOT((-100*COS(RADYAN(B1)))^2-4*(-59501)))/2)+71)-(((200*COS(RADYAN($A309))+SQUAREROOT((-200*COS(RADYAN($A309)))^2-4*(-54009)))/2)-122))>52,84;(640-(((100*COS(RADYAN(B1))+SQUAREROOT((-100*COS(RADYAN(B1)))^2-4*(-59501)))/2)+71)-(((200*COS(RADYAN($A309))+SQUAREROOT((-200*COS(RADYAN($A309)))^2-4*(-54009)))/2)-122))<91,8);SQUAREROOT(3481-((640-(((100*COS(RADYAN(B1))+SQUAREROOT((-100*COS(RADYAN(B1)))^2-4*(-59501)))/2)+71)-(((200*COS(RADYAN($A309))+SQUAREROOT((-200*COS(RADYAN($A309)))^2-4*(-54009)))/2)-122))-52,84)^2)+41+29;IF(VE((640-(((100*COS(RADYAN(B1))+SQUAREROOT((-

100*COS(RADYAN(B1)))^2-4*(-59501)))/2)+71)-
(((200*COS(RADYAN($A309))+SQUAREROOT((-
200*COS(RADYAN($A309)))^2-4*(-54009)))/2)-
122))>91,8;(640-(((100*COS(RADYAN(B1))+SQUAREROOT((-
100*COS(RADYAN(B1)))^2-4*(-59501)))/2)+71)-
(((200*COS(RADYAN($A309))+SQUAREROOT((-
200*COS(RADYAN($A309)))^2-4*(-54009)))/2)-
122))<167,3);(167,3-(640-
((100*COS(RADYAN(B1))+SQUAREROOT((-
100*COS(RADYAN(B1)))^2-4*(-59501)))/2)+71)-
(((200*COS(RADYAN($A309))+SQUAREROOT((-
200*COS(RADYAN($A309)))^2-4*(-54009)))/2)-
122)))*(TAN(RADYAN(41,33)))+18,93+29;IF(VE((640-
(((100*COS(RADYAN(B1))+SQUAREROOT((-
100*COS(RADYAN(B1)))^2-4*(-59501)))/2)+71)-
(((200*COS(RADYAN($A309))+SQUAREROOT((-
200*COS(RADYAN($A309)))^2-4*(-54009)))/2)-
122))>167,3;(640-
(((100*COS(RADYAN(B1))+SQUAREROOT((-
100*COS(RADYAN(B1)))^2-4*(-59501)))/2)+71)-
(((200*COS(RADYAN($A309))+SQUAREROOT((-
200*COS(RADYAN($A309)))^2-4*(-54009)))/2)-
122))<217,48);76-SQUAREROOT(5776-((640-
(((100*COS(RADYAN(B1))+SQUAREROOT((-
100*COS(RADYAN(B1)))^2-4*(-59501)))/2)+71)-
(((200*COS(RADYAN($A309))+SQUAREROOT((-
200*COS(RADYAN($A309)))^2-4*(-54009)))/2)-122))-
217,48)^2)+29;IF((640-
(((100*COS(RADYAN(B1))+SQUAREROOT((-
100*COS(RADYAN(B1)))^2-4*(-59501)))/2)+71)-
(((200*COS(RADYAN($A309))+SQUAREROOT((-
200*COS(RADYAN($A309)))^2-4*(-54009)))/2)-
122))>217,48;29;0)))));2)&")"

As a result of all the location analyzes and calculations performed in excel, point cloud showing the position status in excel environment was created. Figure 7 shows a graphical representation of these points.

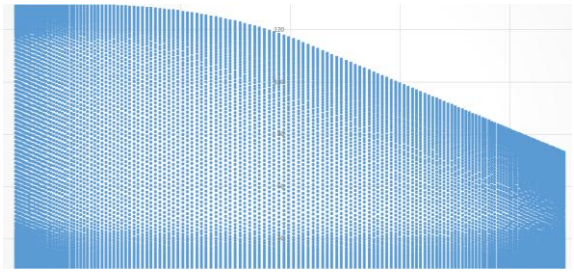

Fig 7. *A graphical representation of cloud showing the position status*

5. FEM Analysis

In the study, mechanical analysis of the critical loads was performed. This ensures safe operation of the machine parts. Figure 8 shows examples of analysis of the selected carrier pin and pin socket.

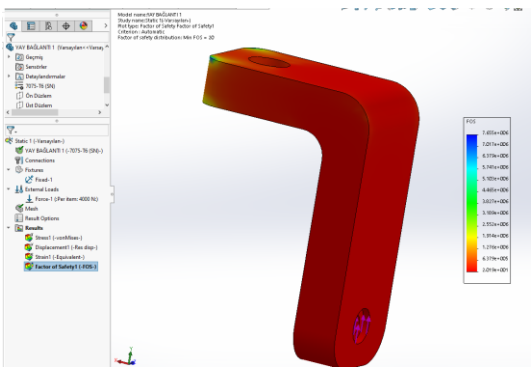

Fig 8. a*. Carrier pin socket*

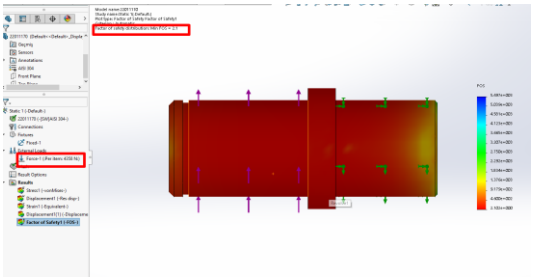

Fig 8. a*. Carrier pin*

Fig 8. *Examples of analysis of the selected carrier pin and pin socket*

6. Conclusion

In this study, instead of the existing sealing unit driven by a single servo motor, the horizontal and vertical movements were separated and driven by two servo motors. To have position control it has been analyzed the geometric positions and to have stiffness mechanical analyses were performed for critical parts of machine. It is designed a unique mechanism for sealing unit that can work at 160 packages per min instead of 120 packages per min.

7. Acknowledgment

Some of the applications presented in this study were supported by TUBITAK-TEYDEB (The Scientific and Technological Research Council of Turkey-Technology and Innovation Support Programs) with project number 3181073.

8. References

[1] Prab Bhatt, Programming the Dynamic Analysis of Structures, CRC Press Published June 13, 2002, ISBN 9780419156109

[2] Doyle, J.F. Static and Dynamic Analysis of Structures with An Emphasis on Mechanics and Computer Matrix Methods, ISBN 978-94-011-3420-0, Springer Netherlands

[3] Sondipon Adhikari, Structural Dynamic Analysis with Generalized Damping Models: Analysis, ISBN:9781848215214, 2014 by John Wiley & Sons, Inc.

[4] Bucalem M.L., Bathe KJ. (2011) Mathematical models used in engineering structural analysis. In: The Mechanics of Solids and Structures - Hierarchical Modeling and the Finite Element Solution. Computational Fluid and Solid Mechanics. Springer, Berlin, Heidelberg

[5] Mathematical Modelling in Solid Mechanics, Editors: dell'Isola, Francesco, Sofonea, Mircea, Steigmann, David (Eds.) ISBN 978-981-10-3764-1, Springer Singapore

[6] K. F. Riley, M. P. Hobson, S. J. Bence Mathematical Methods for Physics and Engineering: A Comprehensive Guide, Cambridge University Press

[7] John W. Dettman, Mathematical Methods in Physics and Engineering, Dover Pup. Inc

[8] Bernard Liengme, Keith Hekman, Liengme's Guide to Excel 2016 for Scientists and Engineers,Academic Press, Elsevier

MATHEMATICAL MODELLING OF THE CRYSTALLIZATION OF AN ALUMINIUM CASTING MODIFIED WITH NANOPARTICLES

МАТЕМАТИЧНО МОДЕЛИРАНЕ НА КРИСТАЛИЗАЦИЯТА НА ОТЛИВКА ОТ АЛУМИНЕВА СПЛАВ, МОДИФИЦИРАНА С НАНОЧАСТИЦИ

Ass. Prof. Sasho Popov, Ass. Prof. Georgi Evt. Georgiev, Ass. Prof. Valentin Manolov, PhD Pavel Kuzmanov, Chief Assistant Angel Velikov
Institute of Metal Science, Equipment and Technologies with Hydro-aerodynamics Centre "Akad. A. Balevski"-BAS

Abstract: The insertion of nanoparticles into the melt of the metal alloys leads to an increase in the mechanical properties and fragmentation of the macro- and microstructure To give the answer the question what is the mechanism of interaction between nanoparticles and alloy during the transition from liquid to solid state is a priority for scientists working in this field.. In this paper, a mathematical model for heat transfer and crystallization of an aluminium alloy casting with nanoparticles inserted therein is presented. As a result of the model solution and the application of the MAGMASOFT software package, the dependences of the temperature field, the average grain size and the values of the undercooling are obtained. The influence of the number of crystallization centres on these quantities is investigated.

KEY WORDS: MATHEMATICAL MODELLING, CRYSTALLIZATION OF ALLOYS, NANOMODIFICATION

Резюме: Въвеждането на наноразмерни частици в металните сплави води до повишаване на механичните свойства и издребняване на макро- и микроструктурата. Да се отговори на въпроса какъв е механизмът на взаимодействие на наночастиците и сплавта в процеса на преход от течно в твърдо състояние е приоритет на учените, работещи в тази област.В настоящата работа е представен математичен модел за топлообмен и кристализация на отливка от алуминиева сплав с въведени в нея наночастици. В резултат от решаването на уравненията на модела и съвместното с използване на софтуерния пакет MAGMASOFT са получени зависимостите на температурното поле, средния радиус на зърната и преохлаждането. Изследвано е влиянието на броя на центровете на кристализация върху посочените величини.

КЛЮЧОВИ ДУМИ: МАТЕМАТИЧЕСКО МОДЕЛИРАНЕ, КРИСТАЛИЗАЦИЯ НА ОТЛИВКИ, НАНОМОДИФИЦИРАНЕ

1. Въведение

Въвеждането на различни видове наночастици в металните сплави води до повишаване на механичните свойства и издребняване на макро- и микроструктурата [1,2,3]. За разкриване на механизма на взаимодействие на наночастиците и сплавта се използват както експериментални така и теоретични, моделни изследвания. В настоящата работа е представен математичен модел, отчитащ влиянието наличните наночастици върху зародишообразуването по време на кристализацията. Това позволява да се анализира тяхното влияние върху формирането на структурата на сплавта.

2. Описание на математичния модел

В работа [4] е представен подхода за формулиране на математичния модел. Тук ще приведем основните уравнения, които са включени в него.

2.1. Уравнение за топлообмен в интервала от началната температура T_0 до температурата на ликвидуса T_L

$$\frac{dT}{dt} = \frac{q}{R_0 \rho C_p}. \qquad (1)$$

2.2. Уравнение за топлообмен и кристализация в интервала от T_L до температурата на евтектиката T_E

$$\frac{dT}{dt} = \frac{L}{C_p}\frac{df_E}{dt} + \frac{q}{R_0 \rho C_p}. \qquad (2)$$

2.3. Уравнения за топлообмен и кристализация в интервала от T_E до температурата на пълно затвърдяване T_S, която се определя от условието $f = f_\alpha + f_E = 1$

$$\frac{dT}{dt} = \frac{L_E}{C_p}\frac{df_E}{dt} + \frac{q}{R_0 \rho C_p}. \qquad (3)$$

2.4. Уравнение за топлообмен на сплавта след нейната кристализация в интервала от T_S до T_f. Тук се използва уравнвние (1).

Уравнения (1)-(3) са получени за случая на относително малък обем метал V_o, за който е в сила обемна неизотермична кристализация и температурата му зависи само от времето. Тук величините f_α, f_E и f означават съответно относителните обеми на α-твърдия разтвор, на евтектиката и на сумарната твърда фаза в интервала от T_L до T_S.

Величината $q(t)$ е топлинния поток от обема метал към околната среда, L е топлина на кристализация на сплавта, L_E е топлна на евтектическата кристализация, C_p - топлинен капацитет, R_0 е отношението на обема V_o на метала към неговата повърхност, ρ - плътност на сплавта, t - време, T - температура.

Според Колмогоров [5] обемът на кристализиралия метал V при време t може да се определи от:

$$V = V_0\left[1 - \exp(-\omega)\right] \qquad (4)$$

$$\omega = \varphi N\left(\int_0^t u(\tau)d\tau\right)^3, \qquad (5)$$

където φ е параметър на формата на кристала, като за сферичен кристал $\varphi = 4/3\pi$, $u(\tau)$ е скорост на кристализацията, N е броят на центровете на кристализация. Скоростта на кристализация при зародиш с радиус $R(t)$ е:

$$u = \frac{dR}{dt} = K_V \Delta T, \qquad (6)$$

където K_V е коефициент, равен на линейната скорост на нарастване на кристала при преохлаждане 1°C. Така получаваме:

а) За интервала $T_L > T > T_E$ уравненията

$$u = \frac{dR_\alpha}{dt} = K_\alpha(T_L - T) \qquad (7)$$

$$f_\alpha = 1 - \exp\left(-\frac{4}{3}\pi N R_\alpha^3\right) \qquad (8)$$

$$\frac{df_\alpha}{dt} = 4\pi N K_\alpha (1 - f_\alpha) R_\alpha^2 (T_L - T) \qquad (9)$$

б) За интервала $T_E > T > T_S$ уравненията

$$u = \frac{dR_E}{dt} = K_E (T_E - T) \qquad (10)$$

$$f_E = 1 - \exp\left\{-\frac{4}{3}\pi N\left(R_E^3 - R_\alpha^3\right)\right\} \qquad (11)$$

$$\frac{df_E}{dt} = 4\pi N R_E^2 K_E (T_E - T) \exp\left\{-\frac{4}{3}\pi N\left(R_E^3 - R_\alpha^3\right)\right\} \qquad (12)$$

Тук с $R_\alpha(t)$ и $R_E(t)$ са означени радиусите на кристалното зърно за α-твърд разтвор от R=0 до $R=R_\alpha(t)$ и за евтектиката от $R_\alpha(t)$ до $R_E(t)$ съответно. В [6] също е използвано приближението за сферични кристали, които нарастват по закона (7).

3. Метод на решение на математичния модел съвместно със софтуерния пакет MAGMASOFT

Математичният модел (1)-(12) се решава съвместно с софтуерния пакет MAGMASOFT за съответния обект на изследване. В нашия случай това е отливка от сплав AlSi7Mg с условно наименование "Клема". На Фиг. 1 е показан общият вид на отливката. След това тя е разрязана на определена височина, показана на Фиг. 1 и от метала е изработено пробно тяло за определяне на средния диаметър на макрозърната чрез количествена металография. Така е получена информация за тази величина за отливка без въведени наночастици и за отливка с въведени наночастици.

Както е известно MAGMASOFT е програмен продукт, който служи за пресмятане на спрегнати задачи за топлобмен и кристализация на отливки от различни сплави и сложна тримерна форма. В резултат от решаването им се получава информация за разпределението на температурата, на средния размер на кристалните зърна и на много други величини, характеризиращи леярския процес. В последно време с цел издребняване на структурата в технологиите за леене се прилага модифициране на стопилката чрез въвеждане на наноразмерни частици. Очаквано е част от тях да изпълнят функцията на нови кристализационни зародиши. В резултат на това, общия брой на зародишите нараства (нови + съществуващи естествено). Така по-големият брой зародиши води до издребняване на кристалните зърна в сравнение с тези в немодифисираната структура. MAGMASOFT не предлага възможност да извърши пресмятане на затвърдяването на отливка, в която са въведени допълнителни центрове на кристализация. Математичният модел (1)-(12) може да даде информация за влиянието на броя на въведените наночастици върху средния диаметър на зърната, ако се интегрира с MAGMASOFT.

От решението на задачата за топлообмен и кристализация на отливката с използване на MAGMA може да се получи топлинният поток q, който присъства в уравнения (1)-(3). Това позволява да получим за всяка точка от отливката зависимостта на температурата от времето и функциите $R_\alpha(\tau)$, $R_E(t)$, $f_\alpha(t)$, $f_E(t)$, и $T(t)$.

Математичният модел (1)-(12), представен по-горе, описва процеса на непрекъснато охлаждане на сплавта, включващ както нейното течно състояние, така и кристализацията й. За числено решаване на диференциалните уравнения е използван метода на Рунге-Кута, реализиран чрез оператора “dsolve” от програмата Maple. Първо се решава уравнение (1) с начално условие $T(0) = T_0$
.От него намираме кога се достига температурата на ликвидуса T_L, т.е. определяме момента време t_L.

За интервала $T_L > T > T_E$ използваме уравнение (2), което, за случая на многокомпонентна сплав, може да се преобразува във вида

$$\frac{d\Delta T}{dt} = \frac{q}{R\rho C_P} - \left[\frac{L}{C_P} + (1-k)(e^{-\omega})^{k-2}\sum_i \beta_i C_i\right] e^{-\omega}\frac{d\omega}{dt} \qquad (13)$$

$$R = \frac{V_0}{F}, \quad \omega = \varphi N\left(\int_{t_L}^{t} K_V \Delta T d\tau\right)^3,$$

където α - коефициент на топлопредаване; T_f - температура на формата; F - площ на отливката; C_i - концентрация на i-та компонента в сплавта; T_A - температура на топене на чистия метал; β_i - модул на коефициента на наклона на линията на ликвидуса от диаграмата на състояние за i-та компонента и основния метал, k - коефициент на разпределение. Тук индексът f на T_f се отнася за топлофизичните характеристики на формата.

За начално условие на уравнението (13) е избрано

$$\Delta T(t_L) = 0, \qquad (14)$$

където t_L е времето, при което стопилката достига температурата на ликвидуса T_L.

За решаване на уравнение (13) с начално условие (14) се налага да се направи смяна на зависимата променлива ΔT, тъй като дясната страна на (13) съдържа интеграли от ΔT. За целта е въведена нова зависима променлива съгласно формулата

$$Q = \int_{t_l}^{t} \Delta T d\tau \cdot \qquad (15)$$

Следователно за ω и нейната производна имаме

$$\omega = \varphi N K_V^3 Q^3, \quad \frac{d\omega}{dt} = 3\varphi N K_V^3 Q^2 \frac{dQ}{dt}, \qquad (16)$$

а (15) води до

$$\Delta T = \frac{dQ}{dt} \text{ и } \frac{d\Delta T}{dt} = \frac{d^2Q}{dt^2}. \qquad (17)$$

След заместване на получените величини в (13) се получава следното диференциално уравнение от втори ред

$$\frac{d^2Q}{dt^2} = \frac{\alpha}{R\rho C_P}\left[T_A - T_f - \frac{dQ}{dt} - e^{-(k-1)\varphi N K_V^3 Q^3}\sum_i \beta_i C_i\right] \qquad (18)$$
$$-\left[\frac{L}{C_P} + (1-k)e^{-(k-2)\varphi N K_V^3 Q^3}\sum_i \beta_i C_i\right] e^{-\varphi N K_V^3 Q^3} 3\varphi N K_V^3 Q^3 \frac{dQ}{dt}.$$

Отчитайки (15) и (17) за началните условия на уравнение (18) имаме

$$Q(t_l) = \int_{t_l}^{t_l} \Delta T d\tau = 0 \quad \text{и} \quad \left.\frac{dQ}{dt}\right|_{t=t_l} = \Delta T(t_l) = 0 \cdot \qquad (19)$$

След числено решаване на уравнение (18) при начални условия (19) определяме функцията $Q(t)$, а чрез нея и температурата $T(t)$. За целта използваме формула (вж. [7])

$$T = T_A - \Delta T - f_l^{k-1}\sum_i \beta_i C_i ,$$

която вече има вида

$$T = T_A - \frac{dQ}{dt} - e^{-(k-1)\varphi N K_V^3 Q^3}\sum_i \beta_i C_i .$$

За интервала $T_E > T > T_S$ решаваме системата от три диференциални уравнения с неизвестни функции $T(t)$, $_{RE(t)}$ и fE(t), т.е. уравнения (3), (10) и (12). Началните условия тук са:

$$T(t_E) = T_E ,\ R_E(t_E) = R_\alpha ,\ f_E(t_E) = 0 ,$$

където

$$R_\alpha = \int_{t_L}^{t_E} K_\alpha [T_L - T(\tau)]d\tau .$$

За интервала $T_S > T > T_f$ използваме уравнение (1) с начално условие $T(t_S) = T_S$.

4. Резултати от математичното моделиране.

Задачата, включваща уравнения (1)-(12) е решена при следните значения на физическите константи: V=8 10^{-9}m^3, S=2.4 10^{-7}m^2, R=3.33 10^{-4}m, ρ =2500kg/m^3, C=1220 J/(kgK), T_o=988K, T_L=886.8K, L=430518 J/kg , $\varphi = 4\pi/3$, N=2.7 10^{10} 1/m^3 и 2.7 $10^9$1/m^3 K_V=0.001 m/(s·K),, T_A=933K, T_E=850K, L_{Si} =3.2 10^5 J/kg, r_p=0.5 10^{-7}, K_E=0.005 m/(s·K).

На Фиг.2 е показано разпределението на температурата на отливката в сечение перпендикулярно на вертикалната ос z на отливка „Клема“ при t=10сек., получено посредством компютърно симулиране на затвърдяването на отливката със софтуера MAGMAsoft.

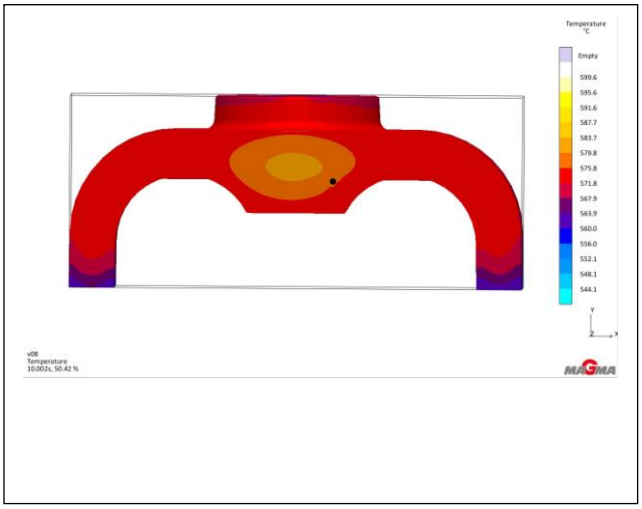

Вижда се, че централната част на обема на отливката има най-висока температура. Подобно е температурното поле и при t=18сек., показано на Фиг.3.

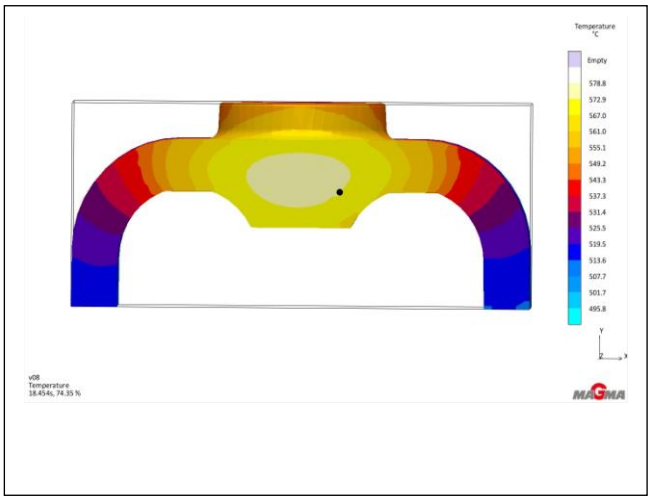

В резултат на топлообмена между по-студената метална форма и отливката температурата на отливката се понижава. На Фиг.4 е показано надлъжно сечение на отливката и нейното температурно поле. Вижда се, че най-висока е температурата в зоната на мъртвата глава, която има функция да подхранва затвърдяващите слоеве под нея.

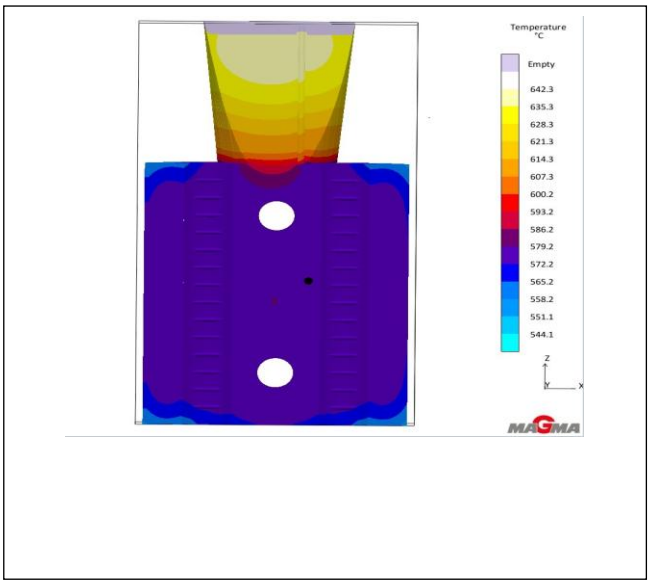

На следващата Фиг.5 е показана температурната зависимост от времето в точката, обозначена на Фиг.3 и Фиг.4.

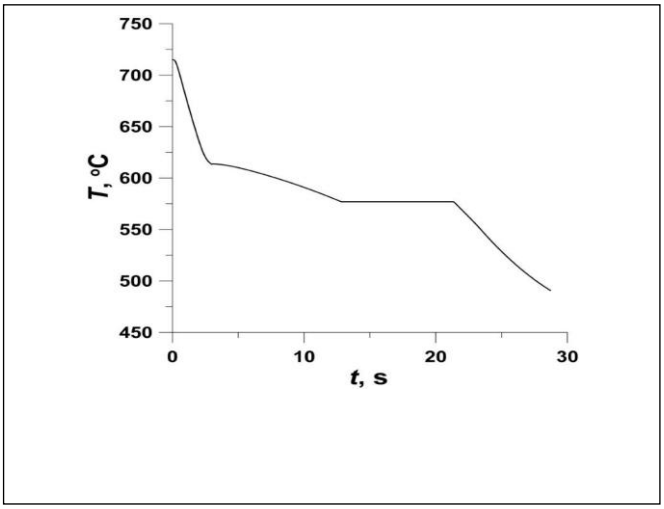

Пресмятането е извършено със системата уравнения (1)-(12) и с използване на топлинния поток $q(\tau)$, определен от решението за затвърдяване на отливката с MAGMAsoft. Температурната крива има следните характерни области: първа- бързо понижение на температурата до ликвидуса, втора- забавяне на темпа на охлаждане с отделяне на топлината на кристализация на α-твърдия разтвор в интервала $[T_E, T_L]$, трета- почти постоянна с температура равна на T_E , когато се отделя топлината на кристализация на евтектиката и последна - област на охлаждане на твърдата фаза.

На следващата Фиг.6 е предствено влиянието на броя на центровете на кристализация върху величината на минимума на температурата на сплавта при ликвидуса или величината на преохлаждането в резултат на който започва нарастването на твърдата фаза върху центровете на кристализация. Вижда се, че с увеличаване на броя на центровете N=2.7.10^9 1/m^3 до N=2.7.10^{10} 1/m^3 преохлаждането намалява.

Както беше казано, от математичния модел може да се определи средния радиус на кристалните зърна при

предположение, че те имат сферична форма. От решението на модела с а определени зависимостите $R(\tau)$ за двата разгледани случаи за N. Те са показани на Фиг. 7

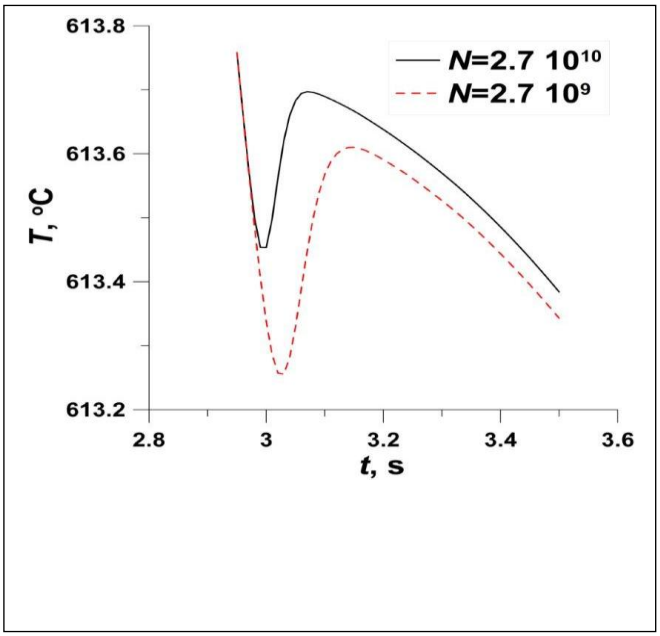

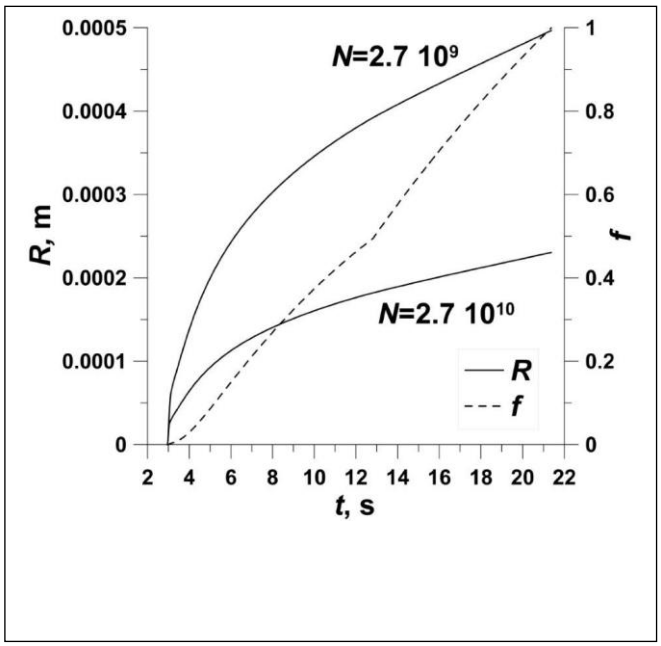

От графиката се вижда, че на по-големия брой зародиши съответства по-малка стойност на $R(\tau)$. На същата фигура е показана зависимостта от времето на частта на твърдата фаза в двуфазната зона $f(t)$. Тя е получена от решението на системата уравнения(1)-(12). Функцията $f(t)$ се изменя от 0 до 1 и има почти линеен характер. Момента от време, в който е затвърдял целия обем Времето на пълна кристализация на обема стопилка се определя от условието $f(\tau)$=1. В нашия случай това е t=21сек.

От две отливки „ клема ‘’, отляти при еднакви начални условия без и с наночастици и чрез металография са определени средните диаметри и съответно средните радиуси на кристалите R_{met}, mm в съответното сечение. В таблицата по-долу са показани изчислените с модела средни радиуси R_E,на зърната за две значения на N и измерените радиуси R_{met} чрез количествена металография.

Табл. 1 Радиуси на зърната, измерени чрез металография R_{met}, и изчислени с модела (1)-(12) R_E при различен брой центрове на кристализация и среден размер на зърната D, прогнозиран от MAGMAsof.

N, 1/m^3	$R_{E,\ mm}$	R_{met}, mm	D,mm
2.7 10^{10}	0.2305	0.196 с наночастици	
2.7 10^{9}	0.4967	0.283 без наночастици	0.802

В същата таблица е показан прогнозирания с помощта на програмата MAGMAsoft срсден размер D на зърната. Вижда се, че порядъка на величините е един и същ, но измерените величини са по-малки от изчислените. Въпреки тази разлика може да се счита, че е разработен математичен модел даващ възможност да се прогнозират размерите на кристалните зърна, температурната зависимост от времето и преохлаждането в зависимост от броя на кристализационните центрове в стопилката.

6.Заключение

Предложен е математичен модел за кристализация на отливка от сплав А356, модифицирана с наноразмерни частици. Моделът е интегриран със софтуерния продукт MAGMAsoft. Изчислени са зависимостите на температурата от времето, частта на твърдата фаза в двуфазната зона, средния радиус на кристалните зърна и преохлаждането. Изследвано е влиянието на броя на наночастиците върху преохлаждането и средния радиус на зърната. Направено е сравнение на изчислените размери на зърната с експериментално определените размери на зърната чрез металография на образци от отливки ,,клема‘’ без и с наночастици. Получено е удовлетворително съвпадение.

7. Използвана литература

1.Borodianskiy, Konstantin & Kossenko, Alexey & Zinigrad, Michael, 2013, Improvement of the Mechanical Properties of Al-Si Alloys by TiC Nanoparticles, Metallurgical and Materials Transactions A, 44A, 10.1007/s11661-013-1850-4

2.Pavel Kuzmanov, Rosica Dimitrova, Rumyana Lazarova, Anatoly Cherepanov, Sasho Popov, Roumen Petrov and Valentin Manolov. Investigation of the structure and mechanical properties of castings of alloy AlSi7Mg, cast irons GG15 and GG25 and steel GX120Mn12, modified by nanosized powders. Journal of Nanoengineering and Nanosystems, 2014, Vol. 228(1) 11–18 (DOI: 10.1177/1740349913510295).

3.K.G.Basavakumara, P.G.Mukunda, M.Chakraborty, Influence of grain refinement and modification on microstructure and mechanical properties of Al–7Si and Al–7Si–2.5Cu cast alloys, Materials Characterization 59 (2008), pp 283-289.

4.Popov, S., V. Manolov, A. Cherepanov, Mathematical Modelling of Crystallization of Metal Alloys, Comptes rendus de l’Academie bulgare des Science, Tome 65, No 4, 441-448, 2012.

5.Колмогоров А.Н. К статистической теории кристаллизации металлов. Изв. АН СССР. Сер. мат. 1937. Вып. 3. с. 355-359.

6.V. N. Popov Simulation of the modified binary alloy droplet deformation and crystallization during spreading on the substrate AIP Conference Proceedings **2125**, 030066 (2019); https://doi.org/10.1063/1.5117448 Published Online: 26 July 2019

7. Сабуров В.П., Еремин Е.Н., Черепанов А.Н., Миннеханов Г.Н., Модифицирование сталей и сплавов дисперсными инокуляторами. Омск: изд-во ОмГТУ, 2002, 212 с.

Работата е подкрепена от проект по договор №ДН07 /20/ 15.12.2016 г., финансиран от Фонд за научни изследвания, Р. България.

MATHEMATICAL MODELING OF THE OPERATING SYSTEM OF THE CAROUSEL TYPE TRANSPLANTING MACHINE

Ass. Prof., PhD, Iurie MELNIC[1], PhD student Vladimir MELNIC[2],
[1] State Agrarian University of Moldova, Chisinau, Republic of Moldova
[2] Technical University of Moldova, Chişinău, Republic of Moldova
iu.melnic@uasm.md, vladimir.melnic@mate.utm.md

Abstract. *The main disadvantages of transplanting machine are presented in the article and the mathematical modeling of the operating system of the carousel type transplanting machine with a new method of calculation of the design parameters of the system is proposed. As a result of theoretical research of the operating system of carousel type transplanting machine the rule of motion of the point F and the mathematical model for determining initial velocity V_0 of the falling seedling have been obtained.*
KEYWORDS*: TRANSPLANTING MACHINE, SEEDLING, CAROUSEL TYPE, OPERATING SYSTEM, QUADRILATERAL, INITIAL VELOCITY.*

Introduction

The improvement and modernization of agricultural machinery and equipment is under constant development, where increasing the working speed of machines is one of the main trends in improving their construction.

For transplanting machines, increasing the speed of work is also a very important matter in increasing the working capacity of the planting units [1, 2]. The main disadvantages of the known semiautomatic machines for planting seedlings are:

- reduced working capacity;
- low quality of planting at a higher speed of the planting unit.

In order to solve these problems, an improved construction of the carousel type transplanting machine was proposed [1]. The research of the operating system of the perfected transplanting machine is of particular importance when optimizing the main parameters of the machine. That is why determining the law of the vertical rod end movement to push the fasteners on the carousel of the transplanting machine is the basic problem of the given work.

Material and method

The drive mechanism of the carousel type transplanting machine is designed based on the quadrilateral with two arms for rotating the interminable movement mechanism, the transport of the seedlings from the coulter to the gripper, water dosing and distribution in portions.

The *OACB* quadrilateral (fig. 1) is joined by a slider type *1-2*, which transforms the circular motion of the support wheel and drive of the planting machine into the "go-come" movement of the exit point 3. On the connecting rod 4 a sprocket for pushing the seedlings (point *M*) is arranged, and the vertical actuating rod (point *F*) of the transplanting machine carousel [3, 4] is arranged on the driven rocker 5.

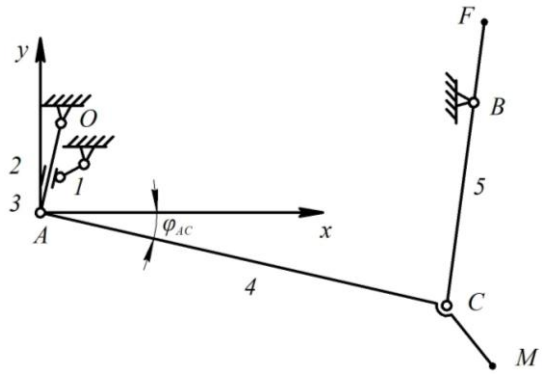

Fig.1. *Kinematic diagram of the operating system of the transplanting machine:*
AC - lower rod; CB - vertical rod; A - the output point of the drive mechanism; M - the end of the push pad; F - the end of the vertical rod.

Rezults and discussions

Let the following parameters of the drive mechanism be known: the coordinates x_0, y_0 and x_B, y_B of *O* and *B* joints, the length of the rockers $l_0=l_3$ and $l_B= l_5$, the initial φ_i and final φ_f angles of the driving rocker's return 3 with coordinates x'_M and y'_M of the point *M* located on the connecting rod 4 relative to the joint in point *O*. The coordinates $x_C(\varphi)$ and $y_C(\varphi)$ of the inner joint *C*, which belongs to the dyad ACB (or 3-4), are determined according to the turning angle φ of the driving rocker, through the system of equations of the circumferences with the radii l_{AC} and l_B [4, 5]:

$$x_C = \frac{\left(l_{AC}^2 - l_B^2 + x_B^2 - x_A^2 + y_B^2 - y_A^2\right) - 2y_C\left(y_B - y_A\right)}{2\left(x_B - x_A\right)}; \quad (1)$$

$$y_C = \frac{B - \sqrt{B^2 - AC}}{A}; \quad (2)$$

where: $A = F^2 + I$;
$B = FG - Fx_A + y_A$;
$C = (G - x_A)^2 + y^2{}_A - l_{AC}$.

In order to determine the law of motion of the end of the vertical pushing rod (point *F*) it is necessary to express the ratio of the average speeds to the free and full stroke by moving the S_F of the vertical pushing rod (point *F*):

$$k = \frac{V^F_{med.cl}}{V^F_{med.cp.}} = \frac{S_F / T_{5c.l}}{S_F / T_{5c.p.}} = \frac{T_{5c.p}}{T_{5c.l.}}; \quad (3)$$

where $T_{5c.p.}$ and $T_{5c.l.}$ - the period of time respectively at the full race and at the free race of the element 5, s.

If the crank angular velocity ω_1 is constant:

$$\frac{T_{5c.p}}{T_{5c.l}} = \frac{\varphi_{1c.p}}{\varphi_{1c.l}}; \quad (4)$$

where $\varphi_{1c.p.}$ and $\varphi_{1c.l.}$ - the values of the turning angles of the crank respectively to the full and free stroke, so

$$\varphi_{1c.p.} + \varphi_{1c.l.} = 2\pi.$$

It is obvious that the periodicity of movement of the driving element 3 and the driven element 5 is equal $T_{5c.p.} = T_{3c.p.}$ and $T_{5c.l.} = T_{3c.l.}$ As a result, the coefficient of change of the average speed k is determined only by a part of the transmission mechanism, and namely, crank-slide. On the other hand, the coefficient k can be determined by the angle β between the extreme positions of the slide:

$$k = \frac{\pi + \beta}{\pi - \beta}; \quad (5)$$

The k coefficient limit is the maximum value of the acceleration a_{Mmax} of the seedling thrust pack from the coulter in

the gripper. At the uniform rotation of the crank with the angular velocity ω_1, the acceleration a_M is equal:

$$a_M = \omega_1^2 \cdot \alpha_M, \text{ m/s}^2 \quad (6)$$

where $\alpha_M = \frac{d^2 x_M}{d\varphi_1^2}$ - the analog of the point *M* acceleration, which moves horizontally.

As

$$\alpha_M = \frac{d}{d\varphi_1^2}\left(\frac{dx_M}{d\varphi_3}\cdot\frac{d\varphi_3}{d\varphi_1}\right) = \frac{d}{d\varphi_1}\left(v_{M3}\cdot v_3\right) \quad (7)$$

where: v_{M3} - the analog of the velocity of point *M* compared to element 3 of the *OACB* quadrilateral;

v_3 - the analog of the speed of the cranked part of the drive mechanism.

Taking into account that the derivative $dv_{M3}/d\varphi_3 = \alpha_{M3}$ is analogous to the acceleration of the point *M* with respect to element 3, and $dv_{M3}/d\varphi_1 = \varphi_3$ is analogous to the acceleration of the slider, at the result of the derivation will be obtained:

$$\alpha_M = \frac{dv_{m3}}{d\varphi_1}\cdot v_3 + v_{M3}\cdot\frac{dv_3}{dv_1} = \frac{dv_{M3}}{d\varphi_3}\cdot\frac{d\varphi_3}{d\varphi_1}\cdot v_3 + v_{M3}\cdot\alpha_3;$$

$$\alpha_M = v_3^2\cdot\alpha_{M3} + \alpha_3\cdot v_{M3}.$$

Finally, the acceleration of point *M* becomes:

$$a_M = \omega_1^2\left(v_3^2\alpha_{M3} + \alpha_3 v_{M3}\right). \quad (8)$$

The kinematic characteristics of the slider as part of the driving mechanism of transplanting machine can be chosen from manuals, guidance etc [3, 4].

Then the relationship can be used to determine the velocity analog v_3:

$$v_3 = \frac{l_1}{l_3}\cos\left(\varphi_1 - \varphi_3\right); \quad (9)$$

where: l_3 - the length of the slide;

φ_3 - the angle of return of the slide.

The variable parameters l_3 and φ_3 are determined from the relation:

$$l_3 = \sqrt{l_0^2 + l_1^2 + 2l_0 l_1 \sin\varphi_1}; \quad (10)$$

$$\varphi_3 = arctg\frac{l_0 + l_1\sin\varphi_1}{l_1\cos\varphi_1}\cdot \quad (11)$$

The analog of the slide acceleration α_3 is equal:

$$\alpha_3 = -\left(\alpha_{32}^k + l_1\sin\left(\varphi_1 - \varphi_3\right)\right)/l_3; \quad (12)$$

where α_{32}^k - the analog of the Cariolis acceleration, which is determined by the relation:

$$\alpha_{32}^k = 2v_{32}^k v_3; \quad (13)$$

where $v_{32}^k = -l_1\sin\left(\varphi_1 - \varphi_3\right)$ - the analog of the relative sliding speed of the slide 3 on element 2.

From this

$$\alpha_3 = 2v_3 l_1\sin\left(\varphi_1 - \varphi_3\right)/l_3\cdot \quad (14)$$

When passing to the next dyad 4-5, it is necessary to take into account the given length l_A of the leading rocker *OA* and its position dislocated relative to the slide with a constant angle $\Delta\varphi_3$:

$$\psi_3 = \varphi_3 + \Delta\varphi_3\cdot \quad (15)$$

The formulas for determining the analogs of the angular speeds of the transmission functions v_{43}, v_{53} and the analogues of the respective angular accelerations α_{43}, α_{53} of the connecting rod 4 and of the driven rocket 5 relative to the driving one are:

$$v_{43} = -\frac{l_A\sin\left(\psi_3 - \varphi_5\right)}{l_4\sin\left(\varphi_4 - \varphi_5\right)};$$

$$v_{53} = -\frac{l_A\sin\left(\psi_3 - \varphi_4\right)}{l_5\sin\left(\varphi_5 - \varphi_4\right)}; \quad (16)$$

$$\alpha_{43} = \frac{l_A\cos\left(\psi_3 - \varphi_5\right) - v_{53}^2 l_5 + v_{43}^2 l_4\cos\left(\varphi_4 - \varphi_5\right)}{-l_4\sin\left(\varphi_4 - \varphi_5\right)}; \quad (17)$$

$$\alpha_{53} = \frac{l_A\cdot\cos\left(\psi_3 - \varphi_4\right) - v_{43}^2 l_4 + v_{53}^2 l_5\cdot\cos\left(\varphi_5 - \varphi_4\right)\cdot}{-l_5\sin\left(\varphi_5 - \varphi_4\right)} \quad (18)$$

The angular positions φ_4 and φ_5 in relations (17) and (18) are determined as follows:

$$\varphi_4 = arctg\frac{y_A - y_C}{x_A - x_C}; \quad (19)$$

From the analogs of the angular characteristics of the *OACB* quadrilateral it is easy to move to the true values of the angular velocities ω_4 and ω_5 of the angular accelerations ε_4 and ε_5 of elements 4 and 5:

$$\omega_4 = \omega_3\cdot v_{43}; \qquad \omega_5 = \omega_3\cdot v_{53}; \quad (20)$$

$$\varepsilon_4 = \omega_3^2\cdot\alpha_{43} + \varepsilon_3\cdot v_{43}; \quad \varepsilon_5 = \omega_3^2\cdot\alpha_{53} + \varepsilon_3\cdot v_{53}. \quad (21)$$

Then the speed of point *F* of the vertical rod becomes equal:

$$V_F = \omega_5 l_F = \omega_3 l_F\cdot\frac{l_A}{l_5}\cdot\frac{\sin\left(\psi_3 - \varphi_4\right)}{\sin\left(\varphi_5 - \varphi_4\right)};$$

$$V_F = \omega\cdot\frac{l_F l_A}{l_5}\cdot\frac{\sin\left(\psi_3 - \varphi_4\right)}{\sin\left(\varphi_5 - \varphi_4\right)}\cdot \quad (22)$$

Parameter V_F drives the process of dropping the seedling from the bucket into the coulter by means of the initial horizontally oriented velocity V_0. Let *AB* be the displacement path of the point *F* of the vertical rod (fig. 2).

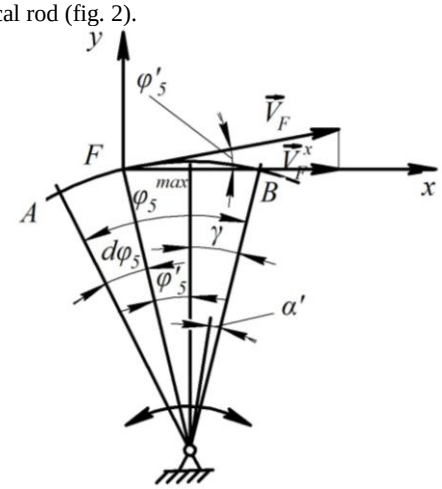

Fig.2. *The displacement path of point F and the velocities diagram*

Then the horizontal projection of the velocity of point *F* will be:

$$V_F^x = V_F\cos\varphi_5'; \quad (23)$$

where φ_5' - the angle that determines the direction of the velocity vector V_F with respect to the *x*-axis.

From Fig. 2 it is obvious that φ'_5 is equal:

$$\varphi_5' = \varphi_5^{\max} - \gamma - d\varphi_5$$

where: γ – the displacement angle of the *FC* rod in the end position relative to the vertical one, rad.

$d\varphi_5$ – changes within the limits $0...\varphi_5^{\max}$.

The function that describes the displacement path of point *F* is the folloing:

$$V_F^x(\varphi_5)=V_F\cos\left(\varphi_5^{\max}-\gamma-d\gamma_5\right). \quad (24)$$

Since the angular velocity of any point on the carousel (fig. 3) is equal to ω_{car}, then $\omega_f=\omega_r=\omega_{car}$, where ω_f and ω_r are respectively the angular velocities of the fastener of the interminable movement mechanism and of the seedling from the seedling cup , s^{-1}.

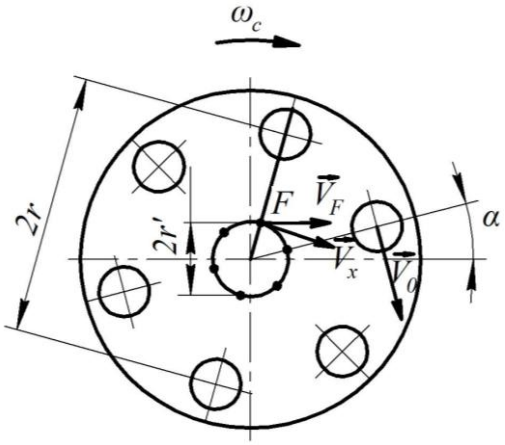

Fig.3. *The diagram of the carousel during the operation of the vertical rod on the fastener*

That's why the following relation is true:

$$\frac{V_f}{r'}=\frac{V_0}{r}, \quad \text{and} \quad V_0=\frac{V_f\cdot r}{r'}; \quad (25)$$

where: V_f – fastener speed, m/s

r – radius to the center of the cups on the carousel, m

r' – radius of the fasteners arrangement, m.

Taking into account the fact that the seedling begins its fall from the cup with an advancement equal to the angle α and velocity $V_o \neq 0$:

$$V_f(\alpha,\varphi_5)=\frac{V_F^x(\varphi_5)}{\cos\left(\frac{\pi}{n}-\alpha\right)} \quad (26)$$

where n – number of seedling cups arranged on the carousel.

The angle of the advance α of the seedlings fall from the carousel cup into the coulter can be changed in the interval $\left[2\pi/n;\ 0\right]$.

Substituting (24) and (26) into (25) the following function is obtained:

$$V_0(\alpha,\varphi_5)=\frac{rV_F\cos\left(\varphi_5^{\max}-\gamma-\varphi_5\right)}{r'\cos\left(\frac{\pi}{n}-\alpha\right)}; \quad (27)$$

where $\varphi_5^{\max}$ - the maximum return angle of element 5 compared to its initial position, rad.

Suppose that α' is the forward angle in the vertical plan, which finds the position of point *F* at a forward opening of the cup equal to the angle α, then

$$d\varphi_5=\varphi_5^{\max}-\Delta\varphi-\alpha' \quad (28)$$

where: $\Delta\varphi$ - the angle until point *F* contacts the fixer, rad;

$\varphi_5^{\max}-\Delta\varphi$ - the rotary phase of the carousel, rad.

In order to express α' through α, the following relation is used:

$$\varphi_5^{\max}-\Delta\varphi....\frac{2\pi}{n} \qquad \varphi_5^{\max}-\Delta\varphi-\alpha'....\frac{2\pi}{n}-\alpha$$

From this $\alpha'=\frac{\alpha\cdot\left(\varphi_5^{\max}-\Delta\varphi\right)n}{2\pi}$; (29)

$$\varphi_5=\varphi_5^{\max}-\Delta\varphi-\frac{\alpha\cdot\left(\varphi_5^{\max}-\Delta\varphi\right)n}{2\pi}. \quad (30)$$

Substituting φ_5 in (27) it is obtained:

$$V_0(\alpha)=\frac{rV_F\cos\left(\frac{\alpha n}{2\pi}\cdot\left(\varphi_5^{\max}-\Delta\varphi\right)-\gamma-\Delta\varphi\right)}{r'\cos\left(\frac{\pi}{n}-\alpha\right)}\cdot \quad (31)$$

As according to the projected construction the forward angle is equal to α_0, the theoretical mathematical model for determining the initial velocity V_0 of the seedling at its movement from the seed cup into the coulter of the machine has the form:

$$V_0^{\alpha_o}(\alpha)=\frac{r\cdot V_F}{r'}\cdot\frac{\cos\left(\frac{\alpha_0\cdot n}{2\pi}\cdot\left(\varphi_5^{\max}-\Delta\varphi\right)-\gamma-\Delta\varphi\right)}{\cos\left(\frac{2\pi}{n}-\alpha_0\right)}\cdot \quad (32)$$

The importance of performing the synthesis of the elaborated transplanting machine's operation system consists in the possibility of using the methodology and modeling of the operating system obtained as the result of the research.

Conclusions

1. The research of the operating system of the carousel type transplanting machine allows the determination and optimization of the essential design parameters of the improved machine.

2. There was established the law of the movement of the pushing vertical rod end of the fasteners on the carousel of the planting machine and the theoretical mathematical model for determining the initial velocity V_0 of the seedling at its movement from the seedling cup into the coulter of the machine.

3. The proposed mathematical modeling of the operating system of the carousel type transplanting machine can be used in the researching processes of the drive systems of carousel-type planters with an intermittent carousel movement.

References

1. Melnic, Iu., Bumacov, V. Maşină de plantat răsaduri. Brevet de invenţie nr.2371 din 29.02.2004. - Chişinău: BOPI nr. 2/2004.

2. Мельник Ю. Повышение рабочей скорости движения рассадопосадочного агрегата. Конструювання, виробництво та експлуатація сільскогосподарських машин. Zbirnic naukovîh praţi, випуск 39. - Кіровоград, 2009. – с. 356-362.

3. Мельник Ю. В., Бумаков В. М. Синтез заделывающего устройства рассадопосадочной машины карусельного типа. Zbirnic naukovîh praţi. - Kirovograd, 1997. – p.78...80.

4. Артоболевский И. И. Теория механизмов и машин: учебник. для втузов. - 4-е изд., перераб. и доп. - М: Наука, 1988. - 640 с.

5. Melnic, Iu. Cercetarea sistemului de acţionare a maşinii de plantat răsaduri de tip carusel. Intellectus, AGEPI, Chişinău, 2007, nr.4. – pp.75-79. ISSN 1810 7079.

КОМПЬЮТЕРНАЯ МОДЕЛЬ ПОЛЗУЩЕГО ДВИЖЕНИЯ ВЯЗКОГО СЛОЯ ПО СКЛОНУ ВОЗВЫШЕННОСТИ

COMPUTER MODEL OF THE CREEPING MOTION OF THE VISCOUS LAYER ON THE SLOPE OF THE HILL

Профессор, доктор физико-математических наук Куралбаев З.
Алматинский университет энергетики и связи, г.Алматы, Казахстан
E-mail: zaufan@mail.ru

Аннотация. *Исследование процесса возникновения оползней осадочных горных пород, находящихся на поверхности возвышенности проведено методом механико-математического моделирования, в результате которого получена математическая задача о квазилинейном уравнении параболического типа. Для решения полученной математической задачи использован конечно-разностный метод; была выбрана нелинейная неявная расчетная схема, на основе которой сформулирован алгоритм решения задачи и разработана компьютерная программа. Проведено компьютерное моделирование рассматриваемого процесса, в результате проведен численный эксперимент для различных возможных вариантов; в качестве исходных данных физических параметров взяты механические характеристики глинистых пород. Результаты исследования представлены в виде графиков и таблиц.*

КЛЮЧЕВЫЕ СЛОВА: *ОСАДОЧНЫЕ ПОРОДЫ, РЕОЛОГИЧЕСКИЕ СВОЙСТВА, ПОЛЗУЧЕСТЬ, МЕХАНИЗМ ВОЗНИКНОВЕНИЯ ОПОЛЗНЕЙ, МАТЕМАТИЧЕСКАЯ И КОМПЬЮТЕРНАЯ МОДЕЛЬ.*

1. Введение

Одной из актуальных проблем для горных районов являются исследования, связанные с таким явлением как оползни, возникающие в высокогорных областях вследствие различных причин, в частности, изменения вязкостных свойств материалов из-за природных или климатических процессов. Предполагается, что происходит движение некоторого верхнего слоя, состоящего из рыхлого грунта, который не способен выдерживать нагрузку собственного веса, поэтому происходит смещение. Такое геолого-горное явление представляет определенную угрозу сооружениям и населению, находящимся в таких районах.

При сохранении определенных геологических и климатических условий, в таких местах достаточно долгое время сохраняется устойчивое положение грунтовых материалов. Однако часто имеет место увлажнение и размытие горных пород дождевой или талой водой, что приводят к изменению вязкостных свойств материалов, составляющих верхние слои грунта. Либо под влиянием тектонических или техногенных процессов могут возникать ползущие движения верхних слоев возвышенностей под воздействием собственной тяжести. Исследования такого явления является *актуальным* по известным причинам [1,2].

Многолетние наблюдения и изучение таких процессов показывали [3,4,5], что осадочные горные породы, которые покрывают более 75% поверхности земной суши, обладают свойством ползучести. «Ползучесть – явление постепенного роста деформации во времени при постоянном напряжении и снижением прочности при длительном нагружении» [5, стр. 36]. Учитывая, что ползучесть является причиной таких явлений, как оползни, селевые потоки, течения ледников и других, в данной работе приведено теоретическое исследование их с помощью математического и компьютерного моделирования.

Данная работа посвящена компьютерному моделированию одного из вариантов механизма возникновения оползней, когда происходит опускание грунтов под воздействием собственного веса при изменении их реологических свойств. Здесь используется физическая модель «ползущих» течений в вязком слое [3,4], а для исследования рассматриваемого процесса - метод математического и компьютерного моделирования с проведением численного эксперимента.

2. Математическая модель задачи

В данном случае рассматривается вязкий слой определенной толщины (мощности), покоящийся на поверхности возвышенности и в начальный момент времени этот слой находится в устойчивом положении, отсутствует в нем какое-либо движение (Фиг.1).

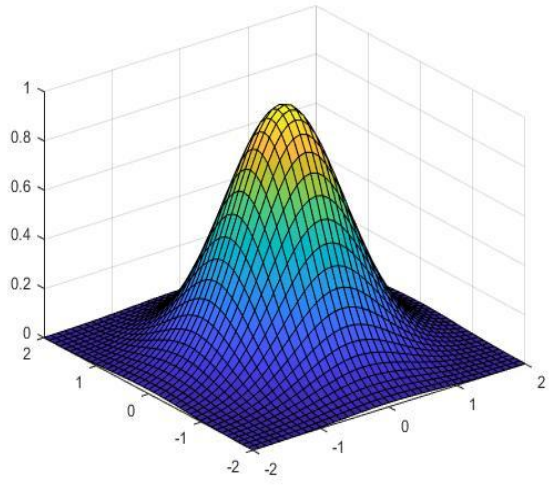

Фиг.1 *– Начальное положение возвышенности*

Предполагается, что происходит снижение значения динамического коэффициента вязкости слоя, и из-за этого происходит движение материалов слоя вниз по склону возвышенности под воздействием собственного веса. Возникает необходимость создания математической модели этого процесса, и сформулировать математическую задачу.

Для создания математической модели рассматриваемого процесса определяются основные его параметры и вводятся соответствующие обозначения. Здесь принята прямоугольная система координат, в которой x и y - горизонтальные координаты, а z — вертикальная координата; ось z направлена вверх, обратно направлению вектора силы тяжести $\vec{g}$.

Для упрощения были использованы известные из гидродинамики допущения о «мелкой воде» [4]. Для проведения расчетов на компьютере использованы

безразмерные параметры, для чего осуществлен переход к безразмерным параметрам. Проведен анализ слагаемых в безразмерных уравнениях, получены упрощенные математические зависимости, совокупность которых явилась математической моделью изучаемого процесса. Для описания свободной поверхности вязкого слоя получено следующее квазилинейное дифференциальное уравнение параболического типа в безразмерных переменных:

$$(1)\ \frac{\partial u}{\partial t} = \frac{ER}{3}\cdot[\frac{\partial}{\partial x}(u-\xi)^3\frac{\partial u}{\partial x}) + \frac{\partial}{\partial y}(u-\xi)\frac{\partial u}{\partial y})].$$

Основание вязкого слоя описано следующей функцией [6-8]:

$$(2)\ \xi(x,y) = (1-f)\cdot e^{-\frac{x^2+y^2}{b}}\cdot[1-\frac{2(x^2+y^2)}{b}],$$

где f – первоначальная толщина вязкого слоя.

В уравнении (1) имеется единственный безразмерный параметр $ER = \frac{\rho g H^3}{\eta UL}$, который зависит от физических и геометрических свойств вязкого слоя; где ρ – плотность материала и η – динамический коэффициент вязкости слоя, g – ускорение силы тяжести, U, H, L – характерные величины: скорость, вертикальный и горизонтальный размеры слоя соответственно.

Решение уравнения (1) позволяет вычислить значения скоростей движения материалов слоя по следующим формулам:

$$(3)\quad u_x = \frac{ER}{2}\cdot\frac{\partial z}{\partial x}\cdot[(z-u)^2-(u-\xi)^2],$$
$$u_y = \frac{ER}{2}\cdot\frac{\partial z}{\partial y}\cdot[(z-u)^2-(u-\xi)^2].$$

Предполагается, что в начальный момент времени (при $t=0$), когда вязкий слой находился в состоянии устойчивого положения, его свободная поверхность была описана следующей безразмерной функцией:

$$(4)\ u(x,y,0) = e^{-\frac{x^2+y^2}{b}}\cdot[1-\frac{2(x^2+y^2)}{b}].$$

Из допущения о малости характерного вертикального размера слоя в сравнении с его характерным горизонтальным размером, можно с достаточно большой точностью предположить выполнение следующего условия:

(5) $u \to 0$ при условии $x \to \pm\infty,\ y \to \pm\infty$.

Приняты следующие граничные условия:

$$x = \pm d,\ \ u(\pm d, y, t) = 0,$$

$$(6)\ y = \pm d,$$

$$u(x, \pm d, t) = 0.$$

Сформулирована постановка математической задачи (1)-(6). В качестве метода решения данной задачи использован конечно-разностный метод и алгоритм нелинейной расчетной схемы [9]:

$$(7)\quad \frac{u_i^{j+1}-u_i^j}{\tau} = \frac{ER}{3\cdot h}\cdot[(u_{i+1}^{j+1}-\xi_{i+1})^3\cdot\frac{u_{i+1}^{j+1}-u_i^{j+1}}{h} - (u_i^{j+1}-\xi_i)^3\cdot\frac{u_i^{j+1}-u_{i-1}^{j+1}}{h}],$$

$$i = 1, 2, 3, \ldots, n;\quad j = 1, 2, 3, \ldots, m,$$

где

n – количество точек по x, а m – по t.

3. Алгоритм решения задачи

В качестве нулевого приближения для метода итерации используется значение искомой функции на предыдущем слое.

Внутри итерации будут выполнены следующие операции:

1^0.Определены значения коэффициентов системы уравнений (8) по формулам (9).

2^0. В прямой прогонке определены неизвестные коэффициенты прогонки с помощью следующих формул:

$$(10)\ \alpha_1 = 1,\quad \beta_1 = 0.$$

$$(11)\ \alpha_{i+1} = \frac{A_{i+1}}{1+A_i+A_{i+1}},\quad \beta_{i+1} = \frac{v_i + A_i\cdot\beta_i}{1+A_i+A_{i+1}},$$

$i = 1, 2, 3, \ldots, n-1$.

3^0. В обратной прогонке определены значения искомой функции по формулам:

$$(12)\quad u_n = 0,\quad u_i = \alpha_{i+1}\cdot u_{i+1} + \beta_{i+1},$$
$$i = n-1, n-2, \ldots, 1.$$

4^0. Итерационный процесс продолжался до тех пор, пока не было выполнено условие точности:

$$(13)\ \max\{|\,u[i]-w[i]\,|\} < \varepsilon,$$

где ε — малое положительное число.

4. Численная реализация алгоритма

Проведен численный эксперимент с помощью разработанной компьютерной программы. В данном случае решение задачи зависит только от одного безразмерного параметра ER. Элементарные расчеты показали, что для большинства осадочных пород, в том числе, глинистых, покрывающих значительную часть земной поверхности, порядок значений безразмерного параметра ER могут быть в пределах 0,01; 0,1; 1,0; 10. Для этих значений данного параметра были проведены расчеты.

В план численного эксперимента включены следующие данные:

- для безразмерной величины ER приняты четыре значения: $ER = 0{,}01;\ ER = 0{,}1;\ ER = 1{,}0;\ ER = 10$;

- шаги по независимым переменным: $h = 0{,}02;\ \tau = 0{,}0001$;

- первоначальная толщина слоя принята постоянной и равной $f = 0{,}3$;

- для определения точности вычислений принято $\varepsilon = 0{,}0001$;

- расчеты проводились для моментов времени $0 \le t \le 10$;

- промежуток по горизонтальной переменной составил $-3 \le x \le 3$.

4.1. Результаты численного решения задачи

В результате численной реализации алгоритма решения данной задачи получены результаты, которые представлены в виде графиков. Определены положения вязкого слоя для различных моментов времени в промежутке $0 \le t \le 10$ для разных значений безразмерного параметра ER.

Из-за того, что при $ER = 0{,}01$, когда динамический коэффициент вязкости имеет достаточно большое значение,

изменение первоначального положения вязкого слоя оказалось незначительным, график для этого случая здесь не представлен.

На фиг.2-4 показаны некоторые положения вязкого слоя в момент времени $t = 10$ для значений параметра ER: 0,1; 1,0; 10.

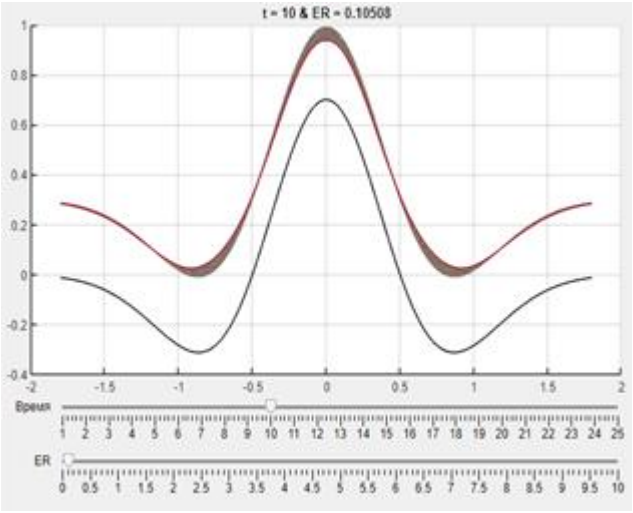

Фиг. 2 – *Положение вязкого слоя при* $t = 10$ *для* $ER = 0{,}1$

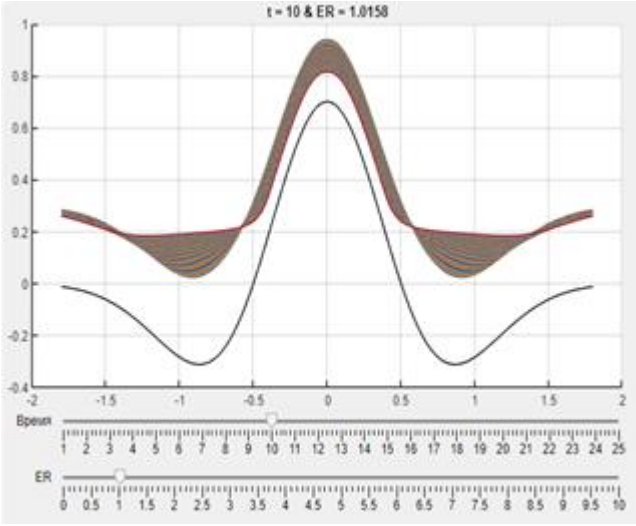

Фиг. 3 – *Положение вязкого слоя при* $t = 10$ *для* $ER = 1$

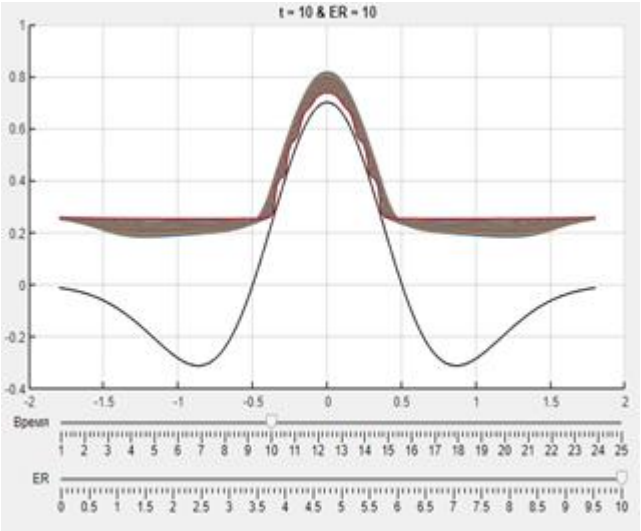

Фиг. 4 – *Положение вязкого слоя при* $t = 10$ *для* $ER = 10$

5. Анализ результатов

В связи с тем, что основным параметром, влияющим на рассматриваемый процесс, является изменение значения динамического коэффициента вязкости, изменение этого параметра было учтено в качестве основного фактора при исследовании данного процесса. Следовательно, значения параметра ER, зависящего обратно пропорционально от динамического коэффициента вязкости, были использованы для численного эксперимента.

Из анализа численных результатов следует, что при достаточно большом значении динамического коэффициента вязкости рассматриваемого слоя ($ER = 0{,}1$ и $ER = 0{,}01$) изменение первоначального состояния слоя будет незначительным. В самом деле, опускание максимальной точки (вершины) внешней поверхности слоя за промежуток времени $t = 10$ составляет для случая, когда $ER = 0{,}1$, всего на 6,15% (уменьшение от 1 до 0,9385), а для случая, когда $ER = 0{,}01$, всего на 1.09% (то же самое, от 1 до 0,9891). Для сравнения можно привести данные для $ER = 1$ и $ER = 10$. В двух последних случаях коэффициент вязкости будет иметь сравнительно небольшие значения. Опускание материалов вязкого слоя при этом будет значительным; опускание вершины слоя составит: для случая $ER = 1$ около 18%, а для $ER = 10$ - 26%.

Кроме этого следует отметить, что из-за опускания вниз материалов слоя происходит утонение верхних частей (Фиг.4), и за счет этого процесса происходит утолщение нижних частей рассматриваемой области, где накапливаются осадочные породы, толщина которых достигает значительных размеров. Утолщение слоя осадочных пород на самом нижнем уровне (на подошве) возвышенности для различных вариантов составляли значения от 13,6 % до 84,2 %.

6. Заключение

Следует отметить, что результаты решения данной задачи позволяет теоретическое (математическое) описание механизма возникновения оползней, залегающих на возвышенных местностях. Проведена оценка изменений, происходящих из-за оползней при уменьшении коэффициента вязкости осадочных пород. Полученные результаты исследования позволяют оценить масштабы катастрофических последствий из-за возникновения оползней.

7. Литература

1 Будущее прикладной математики: Лекции для молодых исследователей. От идей к технологиям/ Под ред. Г. П. Малинецкого. – М: КомКнига, 2008. - 512 с.

2 Ержанов Ж.С. Механика тектонического развития Земли // Известия АН СССР. – Серия геологическая. –М.: Наука, 1973. – № 5. -С. 35-45.

3 Bill Bruce G., Gurey Donald R., Marshal Grant A. Viscosity estimates for the crust and upper mantle from patterns of lacustire shoreline deformation in the Eastern Great Basin // Journal of Geophysical Researh. B. – 1994. 99. Vol 11. P. 46-58.

4 Ержанов Ж.С., Сагинов А.С., Гуменюк Г.Н., Векслер Ю.А., Нестеров Г.А. Ползучесть осадочных горных пород. – Алма-Ата: Наука, 1970. - 208 с.

5 Абатуров В.Г. Физико-механические свойства горных пород и породоразрушающий буровой инструмент. – Тюмень: Изд-во «Нефтегазовый университет», 2007. -238 с.

6 Остапенко В.В. О применении теории мелкой воды для моделирования волновых течений с гидравлическими борами.// Прикладная механика и техническая физика. - 2018, Том 82, Выпуск 4, С. 444-458.

7 Структруп Б. Программирование: принципы и практика использования C++. Пер. с англ. –М.: ООО «Вильямс», 2011. -1248 с.